



Sea Ice Climate Change Initiative: Phase 2



D2.1 Sea Ice Concentration Algorithm Theoretical Basis Document (ATBD)

Doc Ref: SICCI-P2-ATBD(SIC)

Version: 1.0

Date: 22 September 2017



Change Record

Issue	Date	Reason for Change	Author(s)
1.0	22 September 2017	First issue of SIC ATBD for phase 2	Rasmus Tonboe Leif Toudal Pedersen

Authorship

Role	Name	Signature
Written by:	Rasmus Tonboe (DMI) Leif Toudal Pedersen (DTU)	
Checked by:	Gary Timms	
Approved by:	Stein Sandven	
Authorised by:	Pascal Lecomte	

Distribution

Organisation	Names	Contact Details
ESA	Pascal Lecomte	Pascal.Lecomte@esa.int
NERSC	Stein Sandven, Kirill Khvorostovsky	Stein.Sandven@nersc.no; kirill.khvorostovsky@nersc.no
CGI	Gary Timms, Sabrina Mbajon, Clive Farquhar	gary.timms@cgi.com; sabrina.mbajon.njiche@cgi.com; clive.farquhar@cgi.com
MET Norway	Thomas Lavergne, Atle Sørensen	t.lavergne@met.no; atlems@met.no
DMI	Rasmus Tonboe	rtt@dmi.dk
DTU	Roberto Saldo, Henriette Skourup, Leif Toudal Pedersen	rs@space.dtu.dk; mailto:hsk@space.dtu.dk ; ltp@space.dtu.dk
FMI	Marko Mäkynen, Eero Rinne	marko.makynen@fmi.fi; eero.rinne@fmi.fi;
University of Hamburg	Stefan Kern, Lars Kaleschke, Xiangshan Tian-Kunze	stefan.kern@zmaw.de; lars.kaleschke@uni-hamburg.de; xiangshan.tian-kunze@uni-hamburg.de
University of Bremen	Georg Heygster	heygster@uni-bremen.de
MPI-M	Dirk Notz	dirk.notz@mpimet.mpg.de
Ifremer	Fanny Ardhuin	Fanny.Ardhuin@ifremer.fr
AWI	Marcel Nicolaus, Stefan Hendricks, Thomas Hollands	marcel.nicolaus@awi.de; stefan.hendricks@awi.de; thomas.hollands@awi.de

Table of Contents

1	Introduction	13
1.1	Document Structure	13
1.2	Document Status.....	13
2	Sea Ice Concentration (SIC)	14
2.1	Overview.....	14
2.2	Physical background	19
2.3	Algorithm description	22
2.4	Atmospheric noise reduction using ERA Interim and RTM.....	29
2.5	Algorithm optimisation (dynamical algorithms).....	29
2.6	Optimal estimation for sea ice concentration retrieval	32
2.7	Uncertainty model	37
2.8	Near-coast corrections	46
2.9	Gap filling by interpolation.....	46
2.10	Conclusions (will be updated in final version)	48
3	Snow algorithm	49
3.1	Overview.....	49
3.2	Calculation of Open Water, First-Year and Multiyear Ice Tie Points	50
3.3	Algorithm Description and Error Propagation.....	52
3.4	Problems	60
4	Sea Ice Type	63
4.1	Background	63
4.2	Data	64
4.3	Methods	65
4.4	Tie point selection	70
4.5	Computation of NASA-Team ice concentrations	77
4.6	Computation of MYI area	82
4.7	Conclusion and Recommendations	88
5	The SIC algorithm database	90
5.1	Overview.....	90
5.2	Physical Background	90
5.3	Algorithms description.....	103
5.4	Algorithm database computer code.....	127
6	High frequency SIC algorithm with atmospheric correction.....	142
6.1	Abstract	142
6.2	Introduction.....	142
6.3	Methodology	144
6.4	SENSITIVITY OF SIMULATED BRIGHTNESS TEMPERATURES TO ATMOSPHERIC PARAMETERS	148
6.5	SELECTING ATMOSPHERIC PARAMETERS FOR BRIGHTNESS TEMPERATURE CORRECTION	150
6.6	ASI2 VALIDATION OVER 0% AND 100% ICE CONCENTRATIONS....	152
6.7	ASI2 APPLICATION TO AMSR-E L2A BRIGHTNESS TEMPERATURES ...	157
6.8	DISCUSSION AND CONCLUSION.....	163
6.9	ACKNOWLEDGEMENT.....	165
7	References.....	166
	Appendix A The SICCI 1 algorithm – Python code.....	173

Appendix B General structure of SIC RRD **175**

List of Figures

Figure 2-1: Weights of the SIC from Bootstrap F and Bristol algorithms in the SICCI algorithm scheme.....	14
Figure 2-2: Average concentrations for datasets: SIC1 AMSR (Northern and Southern hemispheres separately) and SSM/I (both hemispheres) and thin ice (standard RRDP data set and new dataset). Standard RRDP tie-points are applied.....	15
Figure 2-3: Average concentrations for datasets: SIC1 AMSR (Northern and Southern hemispheres separately) and SSM/I (both hemispheres). RTM-adjusted tie-points are applied	15
Figure 2-4: Average concentrations for dataset SIC0 SSM/I (both hemispheres). RTM-adjusted RRDP tie-points are applied	16
Figure 2-5: Standard deviations of concentrations for datasets: SIC1 AMSR (Northern and Southern hemispheres separately) and SSM/I (both hemispheres) and thin ice (standard RRDP data set and new dataset). Standard RRDP tie-points are applied	16
Figure 2-6: Standard deviations of concentrations for datasets: SIC0 SSM/I (both hemispheres), and SIC1 AMSR (Northern and Southern hemispheres separately) and SSM/I (both hemispheres). RTM-adjusted RRDP tie-points are applied	17
Figure 2-7: Concentration biases for datasets: SIC1 AMSR (Northern and Southern hemispheres separately) and SSM/I (both hemispheres) and thin ice (new dataset). Standard RRDP tie-points are applied.....	17
Figure 2-8: Concentration biases for datasets: SIC1 AMSR (Northern and Southern hemispheres separately) and SSM/I (both hemispheres) and thin ice (new dataset). RTM-adjusted RRDP tie-points are applied.....	18
Figure 2-9: Algorithms ranking according to their mean biases and standard deviations	19
Figure 2-10: Radiative transfer model.....	20
Figure 2-11: NORSEX radiometric signatures.....	21
Figure 2-12: Example tie-point samples for Closed Ice (left) and Open Water (right), for NH (top) and SH (bottom). The colours scale with the NASA Team ice concentration.	31
Figure 2-13: Illustration of the uncertainty merging of two algorithms (BOW in green, and BICE in red)	38
Figure 2-14: Viewing geometry of AMSR-E (Wiebe et al. 2008).....	39
Figure 2-15: AMSR-E 89 GHz B-Scan ascending – descending brightness temperature differences. Left: original (JAXA) geolocation. Right: UB geolocation.....	40
Figure 2-16: Residual, random geolocation error after geolocation correction (Wiebe et al. 2008).....	40
Figure 2-17: AMSR2 Brightness temperature difference ascending – descending on 1 July 2013, 89 GHz A-scan.	43

Figure 2-18: Upper left: MODIS reference at 1 km resolution [0-1] (3000 km x 2200 km), lower left: SICCI2LF SIC [0-1], upper right: the 3 x 3 max-min proxy [0-0.5], lower right: SICCI2LF at 25 km pixel resolution and MODIS reference at 25 km pixel resolution difference [0-0.5]..... 44

Figure 2-19: The smearing error component vs. three proxies for smearing for the SICCI2LF SIC algorithm at 25 km grid.Gridding and temporal compositing 45

Figure 3-1: Scatterplot of the vertically polarised gradient ratio of the AMSR-E 18.7 and 36.5 GHz channels and the polarisation ratio of the 18.7 GHz channels. First-year ice, multiyear ice and open water areas are marked in the figure (Figure 3-3 in Spreen [2004]).50

Figure 3-2: Linear regression between OIB snow depth and the gradient ratio of the vertically polarised brightness temperatures of AMSR-E 18.7 and 6.9 GHz channels. S1 and S2 indicate sub-dataset 1 and sub-dataset 2. 59

Figure 3-3: Linear regression between OIB snow depth and the gradient ratio of the vertically polarised brightness temperatures of AMSR2 18.7 and 6.9 GHz channels. S1 and S2 indicate sub-dataset 1 and sub-dataset 2. 60

Figure 3-4: Linear regression between OIB snow depth and the gradient ratio of the vertically polarised brightness temperatures of AMSR2 18.7 and 6.9 GHz channels. The colours indicate the upper boundary of the determined NASA Team multiyear ice concentration. 61

Figure 3-5: Linear regression between gradient ratio of the vertically polarised brightness temperatures of AMSR2 18.7 and 6.9 GHz channels and surface roughness from the SICCI NERSC RRDP dataset. 62

Figure 4-1: Map of the Arctic sectors used in this study. Turquoise are regions 8 and 9 used to derive the MYI area and the MYI tie points. Orange, medium, light and dark blue counted counterclockwise from the orange region are the sectors used to derive the open water tie points. Black boxes denote the locations of the MYI regions used for the inter-sensor calibration; the white box denotes the corresponding location on the Greenland ice sheet.66

Figure 4-2: Inter-comparison of MYI-region TB from DMSP f11 and f13 for 19 GHz for horizontal (top) and vertical (bottom) polarization. Left: scatterplots, right histograms (binsize 1 K). Blue, red, and black symbols and lines denote the westernmost, easternmost and middle MYI region (see Figure 4-1). 66

Figure 4-3: As Figure 4-2 but for TB at 22 GHz. 67

Figure 4-4: As Figure 4-2 but for TB at 37 GHz. 67

Figure 4-5: Inter-comparison of MYI-region TB from DMSP f13 and f17 for 19 GHz for horizontal (top) and vertical (bottom) polarization. Left: scatterplots, right histograms (binsize 1 K). Blue, red, and black symbols and lines denote the westernmost, easternmost and middle MYI region (see Figure 4-1). 68

Figure 4-6: As Figure 4-5 but for TB at 22 GHz. 68

Figure 4-7: As Figure 4-5 but for TB at 37 GHz. 69

Figure 4-8: GR3719 histograms for selected years and months shown with the intention do demonstrate the variability of these histograms. Percentage is 50% and ratio reduction is 0.04. 72

Figure 4-9: GR3719 histograms for selected months for winter 1993/94 shown with the intention to illustrate the shift of the MYI-to-FYI transition line (vertical dashed line) during the season with different values of the ratio reduction: 0.02, 0.04, and 0.06. Percentage is 50%. 73

Figure 4-10: Monthly FYI tie points for the period January 1993 until December 2014. Shown are TB at 19 GHz, horizontal and vertical polarization, and TB at 37 GHz, vertical polarization. In total we have 154 tie points. Shown for every winter season – except 1992/93 and 2014/15 – are values for the months October to April. Small diamonds represent plus / minus one standard deviation. 75

Figure 4-11: As Figure 10 but for monthly MYI tie points. 75

Figure 4-12: As Figure 10 but for monthly OW tie points. 77

Figure 4-13: MYI sea ice concentration for the Arctic Ocean from October 1993 (top left) to April 1994 (bottom right); colors: dark blue: < 30%, yellow: 65%, orange: ~ 70%, red: 80-90%, brown: 100%. Red circles denote an area where a spurious MYI area occurs during the course of winter. Blue circles denote an area which is supposed to have 100% MYI concentration but where MYI concentration spuriously decreases over the course of winter. 79

Figure 4-14: As Figure 5-13 but for October 2009 (top left) to April 2010 (bottom right); colors: dark blue: < 30%, yellow: 65%, orange: ~ 70%, red: 80-90%, brown: 100%. Black circles denote an area where a spurious MYI area occurs at the end of winter. Blue circles denote an area which is supposed to have 100% MYI concentration but where MYI concentrations seem to be spuriously low. Red circles denote an area where both real and spurious MYI co-exist. 80

Figure 4-15: As Figure 5-14 but for October 2013 (top left) to April 2014 (bottom right); colors: dark blue: < 30%, yellow: 65%, orange: ~ 70%, red: 80-90%, brown: 100%. Red circles denote an area where both real and spurious MYI co-exist. 81

Figure 4-16: As Figure 5-15: but focusing on the low MYI concentration end. Colors: white: 0%, red-yellow: < 2%, bright green: ~ 10%, bluish-green: 20-30%, blue: > 30%.... 82

Figure 4-17: Time series of the monthly average MYI area for 1993-01 to 2014-12 computed from the monthly average MYI concentration using three different MYI concentration thresholds: 30%, 50%, and 70%. Shown are only months October to April. Black symbols: all Arctic sectors; grey symbols: only Arctic Ocean and Canadian Archipelago = sectors 8 & 9 (see Figure 4-1). 84

Figure 4-18: MYI concentration maps from SICCI (left) in comparison to ice type maps from Lindell and Long [2016] (right) for February 2000 to 2014. Colors in the maps on the left are: dark blue: < 30%, yellow: 65%, orange: 70%, red: 80-90%, brown: 100%. Circles denote a few areas of obvious differences. 86

Figure 5-1: Radiative transfer model 91

Figure 5-2: NORSEX radiometric signatures..... 92

Figure 5-3: Scatter plot the the mean melt pond fraction and cloud probability of all SIC1 pixels from June to September in 2010 and 2011 with high Tbs and cloud probability below 0.5.99

Figure 5-4: Histogram of the Tbs of RRDP SIC1 data from June to September in 2010 and 2011.100

Figure 5-5: Air temperature of data points within high peak and low peak of Tb 18H from each month.100

Figure 5-6: Histogram of the retrieved melt pond fraction based on two criteria: minimum standard deviation of melt pond on the left, and maximum number of collocated footprints on the right.101

Figure 5-7: Left panel: surface emissivity at AMSR-E frequencies with varying melt pond fraction. LMF denotes melt pond fraction below 0.15. MMF represents MPF above 0.2. HMF means MPF above 0.3. The solid lines show emissivity at vertical polarization, whereas the dashed lines are for horizontal polarization. The error bars stand for the standard deviation of emissivity. Right panel: typical surface emissivity at AMSR-E frequencies (Spreen 2008).102

Figure 5-8: Bootstrap algorithm scheme106

Figure 5-9: Flowchart of the ECICE algorithm108

Figure 5-10: MIRS data processing concept.109

Figure 5-11: Diagram depicting the MIRS sea ice algorithm.109

Figure 5-12: Usage of polarization and gradient ratios in NASA Team. Two curves for each case show limits of the value.110

Figure 5-13: Theoretical SIC(P) for Near90GHz for two tie-points sets: standard and with atmospheric correction113

Figure 5-14: Same as Figure 5-13, but for larger range of P113

Figure 5-15: Total ice concentration as function of the polarisation difference at 89 GHz before (left panel) and after (right panel) weather correction using ASI (blue solid curves) and Lin90 (red dashed lines) algorithms. The top panel are the retrieval curves for AMSR-E, and the lower panel for AMSR-2.127

Figure 6-1: Ice concentration C as a function of PD of ASI₁WF (a) and ASI₂WF (b). Tie points are marked by the vertical lines. Tie points of (a): $P_1 = 11.7$ K, $P_0 = 47$ K; of (b): $P_1 = 12.3$ K, $P_0 = 72$ K.145

Figure 6-2: Simulated brightness temperatures at 55° incidence angle with varying atmospheric parameters over (a) open water, (b) first-year ice, and (c) multiyear ice. Each color represents one varying parameter. The solid curves: vertically polarized TBs , the dashed curves: horizontally polarized TBs 150

Figure 6-3: Simulated PD to atmospheric influences over (a) open water, (b) first-year ice, and (c) multiyear ice. Each color represents one varying parameter150

Figure 6-4: Standard deviation of TBs at 89 GHz before (horizontal lines) and after correction (vertical bars) using different parameters and their combinations. Blue denotes vertical polarisation, and red denotes horizontal. Based on the pure 0% (top, SIC0) and 100% (bottom SIC1) SIC Round Robin Data Package training data sets. TWV: total water vapor. WS: wind speed. LWP: liquid water path. T2m: 2 m air temperature. Tsk: skin temperature. T_{emit} : emitting layer temperature.153

Figure 6-5: Scatter plot of *TB89 V* and *TB89 H* before (a) and after (b) correction over open water (red to yellow cluster) and consolidated ice (cyan to magenta cluster). Dashed lines show the ASI and ASI2 SIC isolines ranging from 0% to 100% with 20% interval. Arrow indicates increasing *PD*155

Figure 6-6: Histogram of ASI and ASI2 of the AMSR-E RRDV validation data set over 0% and 100% ice concentration.156

Figure 6-7: Scatter plot of *GR(23,18)* and *GR(36,18)* before and after correction for the RRDV validation data set over open water. Vertical and horizontal dashed lines show the default thresholds of *GR(36,18)* and *gr2318* used for ASI weather filter: 0.045 and 0.04 respectively.....157

Figure 6-8: Ice concentration retrievals of ASI and ASI2 and weather filters from 15 March, 2008. The top row is based on the original AMSR-E *TBs*, the bottom row is based on the atmospherically corrected *TBs*. From left to right column: SIC without any weather filter, *GR(23,18)*, *GR(36,18)*, SIC with external weather filter. The SIC maps are gridded to 6.25 km resolution, and the GR values to 25 km.....158

Figure 6-9: Scatter plot of *GR(23,18)* to PR18 (top panels) and *GR(36,18)* to PR18 (bottom panels) based on the original *TBs* (left panels) and corrected *TBs* (right panels) using AMSR-E L2A data in the Arctic from 20 Jan, 2008. The original threshold of weather filters used in *ASIWF* are marked by the blue horizontal lines, and the new threshold denoted by red line.159

Figure 6-10: Ice concentration retrieved by ASI and ASI2 overlaid on MODIS image of Fram Strait from 22. April, 2008. SIC of 15%, 30% and 90% are marked by green, yellow and red isolines, respectively.....160

Figure 6-11: *ASIWF* and *ASI2WF* SIC compared to Landsat image from 24 May 2005 near Davis Strait.161

Figure 6-12: Ice extent (a) and ice area (b) retrieved by various empirical SIC retrieval algorithms. ASI and ASI2 SIC are gridded to 6.25 km, and all the other algorithms use 25 km grid.....162

List of Tables

Table 2-1: Bias: the selected algorithms	18
Table 2-2: Standard deviation: the selected algorithms.....	18
Table 2-3: Average bias and standard deviation for the selected algorithms	19
Table 2-4: Tie-points for Northern Hemisphere used with non-atmospheric corrected TBs, NX columns are tie-points for the NORSEX algorithm.....	26
Table 2-5: Tie-points for Southern Hemisphere used with non-atmospheric corrected TBs, NX columns are tie-points for the NORSEX algorithm.....	26
Table 2-6: Tie-points for Northern Hemisphere used with non-atmospheric corrected TBs, NX columns are tie-points for the NORSEX algorithm. SMMR tie-points for FY and MY ice are set to AMSR tie-points since we do not have RRDP data for SMMR from 100% ice	27
Table 2-7: Tie-points for Southern Hemisphere used with non-atmospheric corrected TBs, NX columns are tie-points for the NORSEX algorithm. SMMR tie-points for FY and MY ice are set to AMSR tie-points since we do not have RRDP data for SMMR from 100% ice	27
Table 2-8: Tie-points for Northern Hemisphere used with non-atmospheric corrected TBs, NX columns are tie-points for the NORSEX algorithm. SMMR tie-points for FY and MY ice are set to AMSR tie-points since we do not have RRDP data for SMMR from 100% ice	28
Table 2-9: Tie-points for Southern Hemisphere used with non-atmospheric corrected TBs, NX columns are tie-points for the NORSEX algorithm. SMMR tie-points for FY and MY ice are set to AMSR tie-points since we do not have RRDP data for SMMR from 100% ice	28
Table 2-10: Mean difference per pixel for the coastline pixels of Figure 2-15. JAXA and UB denote the different geolocation procedures (Wiebe et al. 2008).....	42
Table 2-11: AMSR2 Geolocation errors in AMSR2 L1 data versions 1.1 and 2.0. EL: elevation direction, AZ: azimuth direction. After JAXA EORC (2015).....	42
Table 3-1: Open water, first-year and multiyear ice tie points for AMSR-E.....	51
Table 3-2: Open water, first-year and multiyear ice tie points for AMSR2	51
Table 3-3: List of possible channel combinations for the new snow depth algorithm. The numbers 1 and 2 refer to the regressions for sub-datasets 1 and 2, respectively. Note that RMSD 1 refers to the comparison with sub-dataset 2 and vice versa.....	58
Table 3-4: Slope, intercept, RMSD, correlation coefficient R and number of data pairs N, for both sub-datasets of the gradient ratios of the channels selected for the new snow depth retrieval algorithm. Note that for sub-dataset 1 RMSD refers to the comparison with sub-dataset 2 and vice versa.	59
Table 4-1: Regression results for multiyear ice (MYI) regions.	69
Table 4-2: Regression results for ice sheet region on top of Greenland.	70

Table 4-3: Average (October to April) FYI tie points for SSM/I and SSMIS TBs from DMSP spacecraft f11, f13, and f17 with ("with") and without ("without") inter-sensor calibration (see previous section).....	75
Table 4-4: Average (October to April) MYI tie points for SSM/I and SSMIS TBs from DMSP spacecraft f11, f13, and f17 with ("with") and without ("without") inter-sensor calibration (see previous section).....	76
Table 4-5: Average (October to April) open water tie points for SSM/I and SSMIS TBs from DMSP spacecraft f11, f13, and f17 with ("with") and without ("without") inter-sensor calibration (see previous section).....	77
Table 4-6: Left part: MYI area computed from SICCI MYI concentrations using a 30% threshold (column "SICCI30") in comparison to MYI area read from the publications of Comiso [2012] (column "Comiso") and Lindell and Long [2016] (column "LandL"). Each cell contains the value for November → April in 106 km ² . Right part: MYI area computed from SICCI MYI concentrations using indicated MYI concentration thresholds and months (column "SICCI**") in comparison to MYI area read from publications of Kwok [2004], Kwok et al. [2009], and Kwok and Cunningham [2015, KandC15]. These values are also all in 106 km ²	87
Table 5-1: Tie-points for Northern Hemisphere used with non-atmospheric corrected TBs, NX columns are tie-points for the NORSEX algorithm	95
Table 5-2: Tie-points for Southern Hemisphere used with non-atmospheric corrected TBs, NX columns are tie-points for the NORSEX algorithm	95
Table 5-3: Tie-points for Northern Hemisphere used with non-atmospheric corrected TBs, NX columns are tie-points for the NORSEX algorithm. SMMR tie-points for FY and MY ice are set to AMSR tie-points since we do not have RRDP data for SMMR from 100% ice	96
Table 5-4: Tie-points for Southern Hemisphere used with non-atmospheric corrected TBs, NX columns are tie-points for the NORSEX algorithm. SMMR tie-points for FY and MY ice are set to AMSR tie-points since we do not have RRDP data for SMMR from 100% ice	96
Table 5-5: Tie-points for Northern Hemisphere used with non-atmospheric corrected TBs, NX columns are tie-points for the NORSEX algorithm. SMMR tie-points for FY and MY ice are set to AMSR tie-points since we do not have RRDP data for SMMR from 100% ice	97
Table 5-6: Tie-points for Southern Hemisphere used with non-atmospheric corrected TBs, NX columns are tie-points for the NORSEX algorithm. SMMR tie-points for FY and MY ice are set to AMSR tie-points since we do not have RRDP data for SMMR from 100% ice	97
Table 5-7: Summer tie points and the corresponding standard deviation for the northern hemisphere. Melt pond fraction is below 0.15, cloud probability is below 0.05....	103
Table 5-8: Algorithms list. The P indicates that the algorithm is primarily using the polarisation for retrieving the ice concentration. G is indicating that the algorithm is primarily using the spectral gradient, and GP is using both.	105
Table 5-9: Composite algorithms.....	120
Table 5-10: Tie points for Northern Hemisphere for ASI_uncor, ASI_cor, Lin_uncor and Lin_cor for AMSR sensors.	125

Table 6-1: TIE POINTS OF ASI AND ASI2 USED IN THE VALIDATION OVER 0% AND 100% ICE CONCENTRATION, AND STANDARD TIE POINTS OF ASI_{WF} AND ASI2_{WF} USED IN THE APPLICATION TO AMSR-E SWATH DATA. P_0 IS THE TYPICAL P_D FOR OPEN WATER AT 89 GHZ, AND P_1 IS FOR CONSOLIDATED ICE. ASI_{WF} TIE POINTS ARE FROM [G. Spreen et. al], AND ERRORS ARE NOT GIVEN.....154

Table 6-2: BIAS AND STANDARD DEVIATION OF ASI AND ASI2 SIC OF THE VALIDATION RRDP DATA SET OVER 0% AND 100% ICE CONCENTRATION. SIC0 DATA IS FROM ALL MONTHS, AND SIC1 DATA IS FROM OCTOBER TO MAY. ASI AND ASI2 SIC: ALL WEATHER FILTERS TURN OFF, NO CAPPING AT 0% AND 100%. ASI_{WF} AND ASI2_{WF} : OPERATIONAL TIE POINTS, WEATHER FILTERS TURNED ON, CAPPING AT 0% AND 100%.156

Table 6-3: BIAS AND RMS ERRORS OF ASI_{WF} -LANDSAT AND ASI2_{WF} -LANDSAT ICE CONCENTRATION.....161

1 Introduction

1.1 Document Structure

This document describes in detail the Algorithm Theoretical Basis for the Sea Ice Essential Climate Variables products to be produced in ESA's Climate Change Initiative. In addition to the new developments, the document includes the ATBDv0, ATBDv1 and ATBDv2 contributions for the Sea Ice Concentration (SIC) aspects. Chapter 2 and 5 deal with Sea Ice Concentration, Chapter 3 describes Snow Algorithm, and Chapter 4 – Sea Ice Type.

1.2 Document Status

This is the first issue of the ATBD document for Phase 2 of the Sea Ice CCI project. The document describes all the algorithms used for the comparison, the chosen in RRDP exercise algorithms and the processing steps for obtaining the final sea ice concentration and sea ice thickness data sets. It also presents the new developments regarding the snow depth and sea ice type algorithms.

2 Sea Ice Concentration (SIC)

2.1 Overview

As a result of the RRDP exercise which was completed for 30 different sea ice concentration algorithms, the osisaf-4 algorithm was selected as the optimal algorithm for the sea ice concentration retrieval from satellite passive microwave data. The variability of the sea ice concentration calculated with each of the algorithms as a function of different noise sources was evaluated without weather filters and with the same set of tie-point for all algorithms. This evaluation is described in the PVASR with some additional comments below.

The osisaf-2 algorithm was adjusted to perform better for the thin sea ice conditions. We will relate to this revised osisaf-2 algorithm as SICCI algorithm. The algorithms used in it are the same as before: Bootstrap F and Bristol, but the weights of these two were adjusted as shown in Figure 2-1.

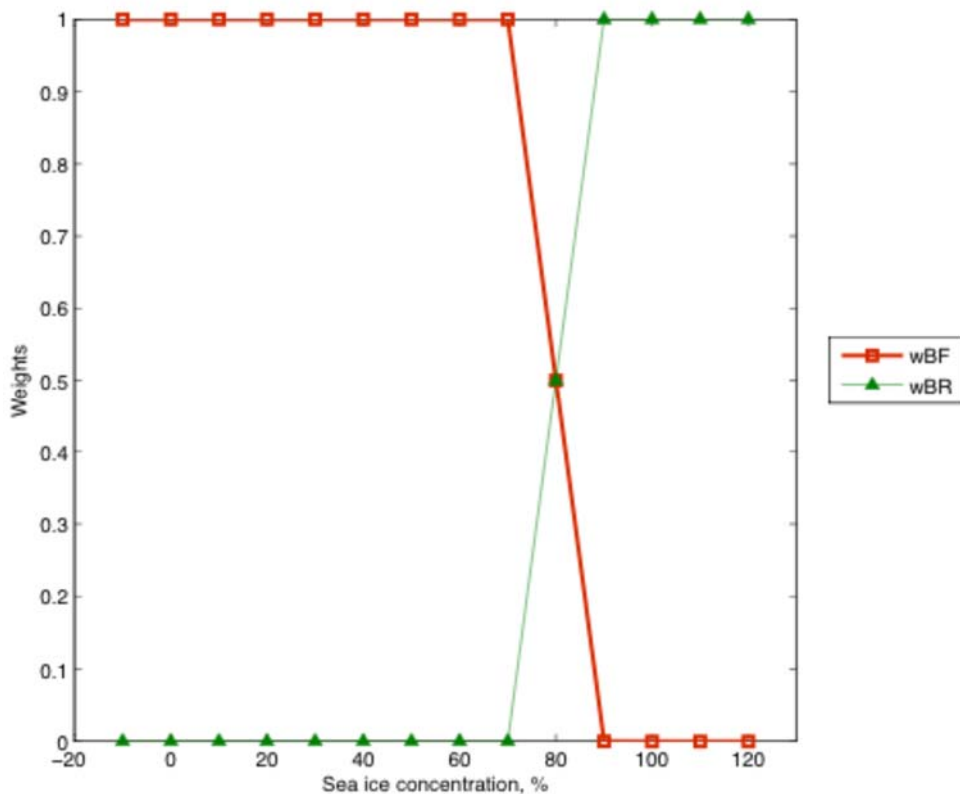


Figure 2-1: Weights of the SIC from Bootstrap F and Bristol algorithms in the SICCI algorithm scheme

The next five figures show the averages and standard deviations of the selected algorithms for the main data sets: SIC0, SIC1, thin ice. SIC 0 and SIC1 contain the concentrations obtained from RTM corrected brightness temperatures, and both runs are shown: 1) using standard RRDP tie-points and 2) using RTM-corrected tie-points.

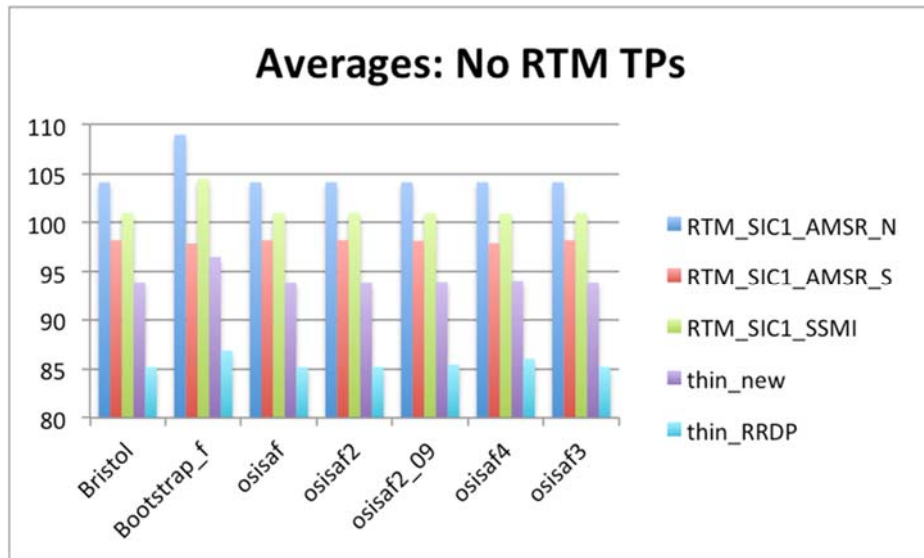


Figure 2-2: Average concentrations for datasets: SIC1 AMSR (Northern and Southern hemispheres separately) and SSM/I (both hemispheres) and thin ice (standard RRDP data set and new dataset). Standard RRDP tie-points are applied

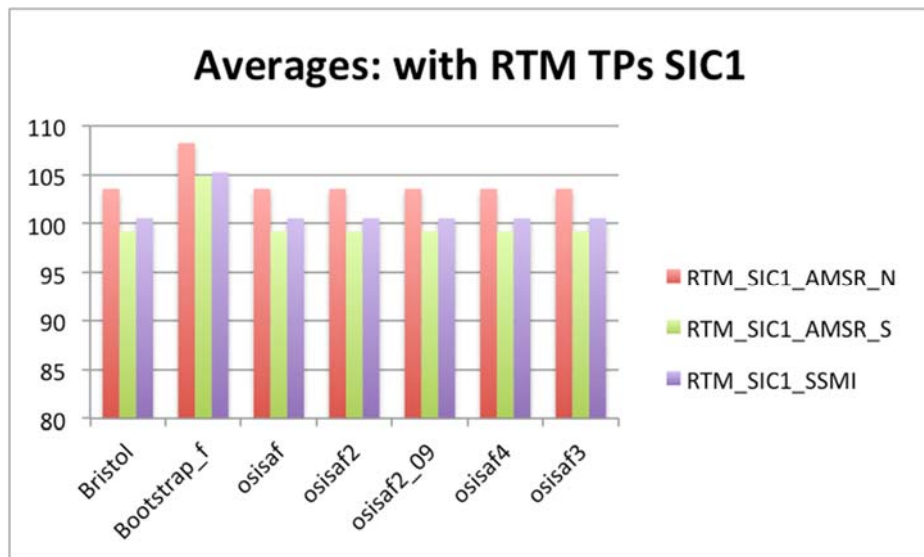


Figure 2-3: Average concentrations for datasets: SIC1 AMSR (Northern and Southern hemispheres separately) and SSM/I (both hemispheres). RTM-adjusted tie-points are applied

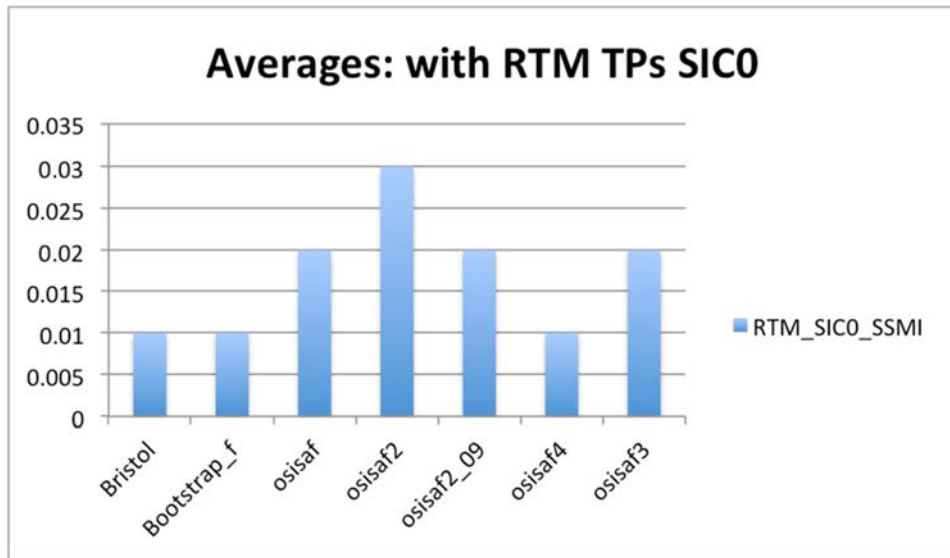


Figure 2-4: Average concentrations for dataset SIC0 SSM/I (both hemispheres). RTM-adjusted RRDP tie-points are applied

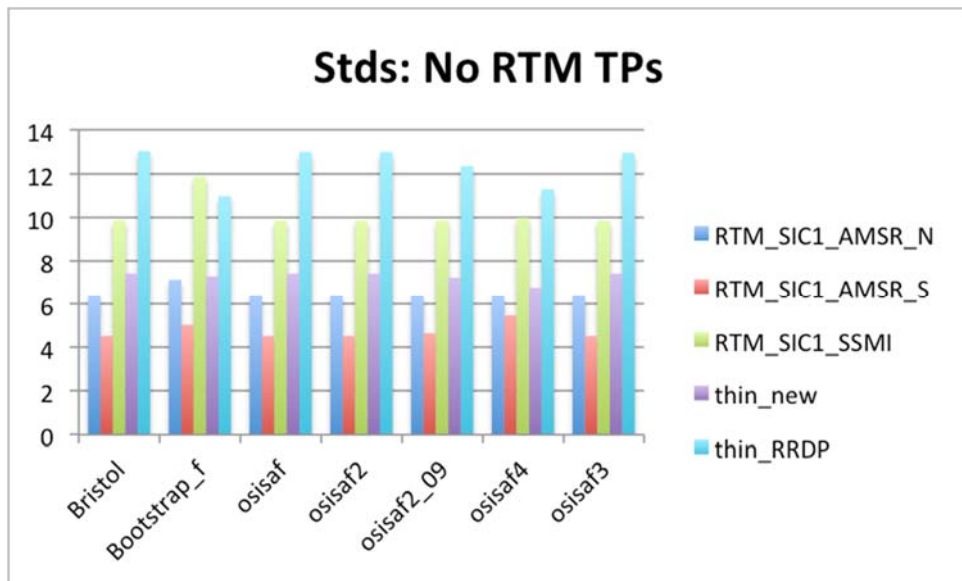


Figure 2-5: Standard deviations of concentrations for datasets: SIC1 AMSR (Northern and Southern hemispheres separately) and SSM/I (both hemispheres) and thin ice (standard RRDP data set and new dataset). Standard RRDP tie-points are applied

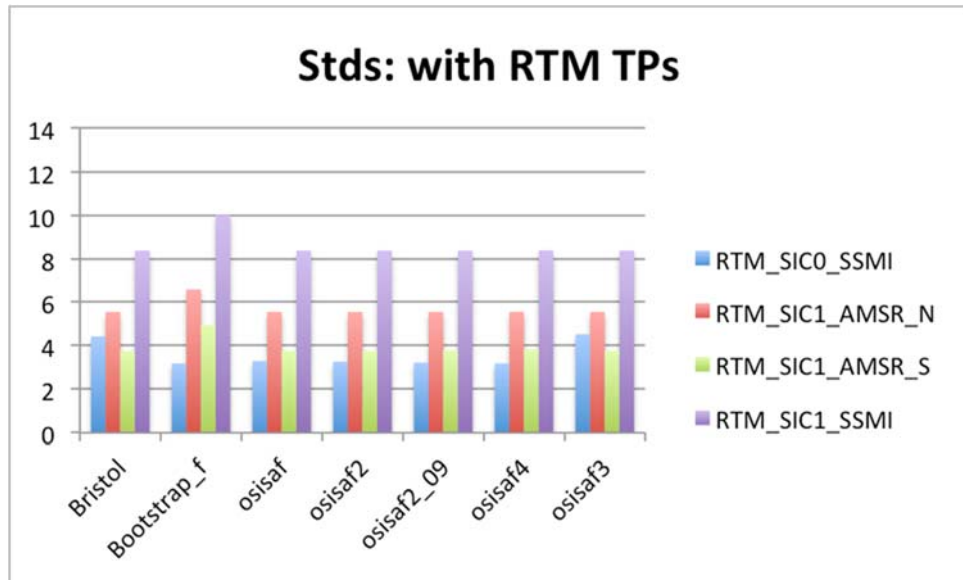


Figure 2-6: Standard deviations of concentrations for datasets: SIC0 SSM/I (both hemispheres), and SIC1 AMSR (Northern and Southern hemispheres separately) and SSM/I (both hemispheres). RTM-adjusted RRDP tie-points are applied

From the first 5 figures we see that the biases (see also the two next figures with actual biases, not averages) and stds are lower if we apply RTM-corrected tie-points for SIC1 as well as SIC0. Therefore we exclude the non- RTM corrected TPs from the analysis (except the thin ice cases, where the non-corrected data are supposed to be used). The performance for RRDP thin ice data set is less certain than for a new higher quality thin ice data set and we consider the new dataset as more accurate, therefore the RRDP thin ice is excluded as well.

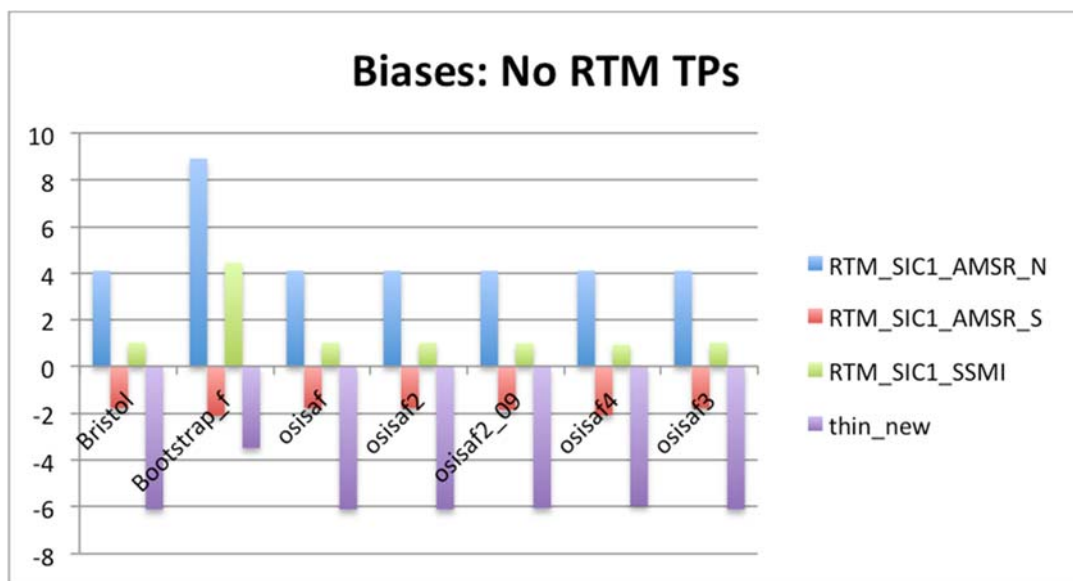


Figure 2-7: Concentration biases for datasets: SIC1 AMSR (Northern and Southern hemispheres separately) and SSM/I (both hemispheres) and thin ice (new dataset). Standard RRDP tie-points are applied

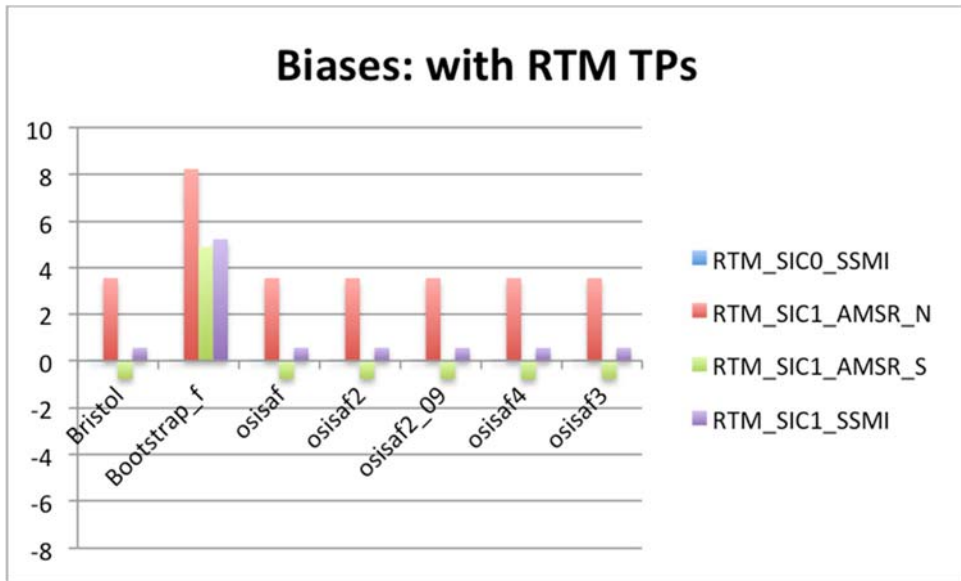


Figure 2-8: Concentration biases for datasets: SIC1 AMSR (Northern and Southern hemispheres separately) and SSM/I (both hemispheres) and thin ice (new dataset). RTM-adjusted RRDP tie-points are applied

This is what is now considered for the evaluation: the algorithms biases:

	Bristol	Bootstrap_f	osisaf	osisaf2	osisaf2_09	osisaf4	osisaf3
RTM_SICO_SSMI	0.01	0.01	0.02	0.03	0.02	0.01	0.02
RTM_SIC1_AMSR_N	3.57	8.25	3.57	3.57	3.57	3.57	3.57
RTM_SIC1_AMSR_S	-0.77	4.9	-0.77	-0.77	-0.77	-0.79	-0.77
RTM_SIC1_SSMI	0.56	5.24	0.56	0.56	0.55	0.55	0.56
thin_new_noRTMTPs	-6.11	-3.49	-6.11	-6.11	-6.06	-5.94	-6.11

Table 2-1: Bias: the selected algorithms

	Bristol	Bootstrap_f	osisaf	osisaf2	osisaf2_09	osisaf4	osisaf3
thin_new	7.43	7.3	7.43	7.43	7.24	6.78	7.43
RTM_SICO_S	4.42	3.18	3.29	3.26	3.22	3.18	4.52
RTM_SIC1_A	5.54	6.62	5.54	5.54	5.54	5.55	5.54
RTM_SIC1_A	3.74	4.93	3.74	3.74	3.76	3.82	3.74
RTM_SIC1_S	8.4	10.04	8.4	8.4	8.4	8.41	8.4

Table 2-2: Standard deviation: the selected algorithms

To avoid the subjective assessment giving the algorithms scores we take average bias (absolute value) and std.

The new osisaf4 is performing in total as the most optimal algorithm:

Average bias						
Bristol	Bootstr ap F	OSISAF	OSISAF2	OSISAF2(t=0.9)	SICCI	OSISAF3
2.204	4.378	2.206	2.208	2.194	2.172	2.206

Average bias						
Average standard deviation						
5.906	6.414	5.680	5.674	5.632	5.548	5.926

Table 2-3: Average bias and standard deviation for the selected algorithms

The Table 2-3 is illustrated in Figure 2-9, where the algorithms are sorted according their standard deviation values.

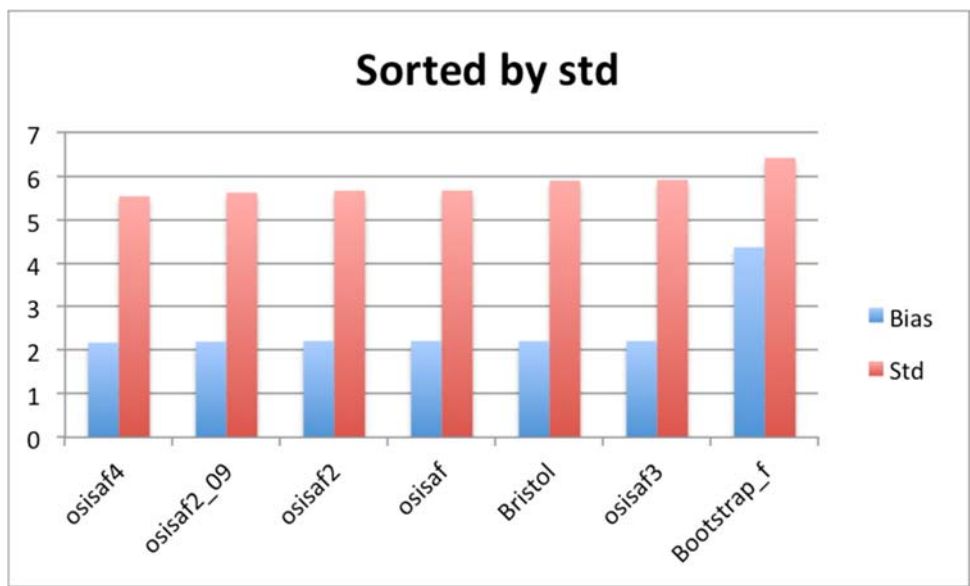


Figure 2-9: Algorithms ranking according to their mean biases and standard deviations

Algorithm biases will eventually be removed or at least substantially reduced by the dynamic tie-point procedure described later. We therefore do not put much emphasis on the bias results in the final algorithm selection except for the negative biases for the thin ice case that shows the underestimation, which will not disappear with dynamic TPs. We include the other bias results for completeness.

2.2 Physical background

2.2.1 Radiative transfer equation

The majority of the sea ice algorithms are based on the radiative transfer equation demonstrated schematically in Figure 2-1 (Svendsen et al., 1983).

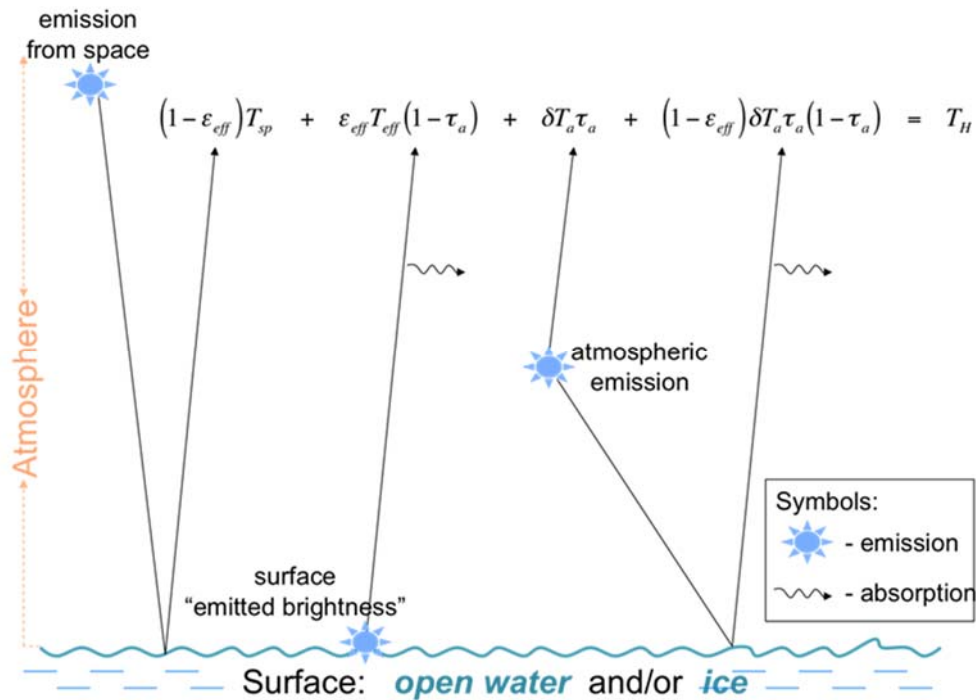


Figure 2-10: Radiative transfer model

In Figure 2-10 T_H is radiation sensed at satellite height which is composed of four terms: 1) radiation from space after reflection from the surface and two times passing the atmosphere, 2) emitted brightness from the surface seen through the atmosphere, 3) upwelling radiation from the atmosphere, and 4) downwelling atmospheric radiation reflected at the surface and transmitted back through the atmosphere. Here ϵ_{eff} is an “effective” (that is: average within field-of-view) emissivity of the surface, T_{eff} is an effective surface temperature, and product of these two gives emitted brightness, that is what a radiometer would detect immediately above the surface without radiation from above. T_{sp} is the temperature of free space (2.7 K), τ_a is total atmospheric opacity (optical depth), δT_a is the weighted average atmospheric temperature in the lower troposphere. Since τ_a is small, the approximation $e^{-\tau_a} = 1 - \tau_a$ is used, and a term $T_{sp} 2\tau_a$ is neglected.

The concentrations are defined as area fractions

$$1 = C_M + C_F + C_W \quad (3-1-1)$$

Measured brightness temperature is presented as sum of individual brightness temperatures for each surface type

$$TB = C_W TB_W + C_F TB_F + C_M TB_M \quad (3-1-2)$$

or

$$TB = (1 - C_{ice}) TB_W + C_{ice} TB_{ice} \quad (3-1-3)$$

in cases where only two surface types are resolved.

2.2.2 Passive microwave surface signatures

The algorithms use the emissivity dependency on frequency and polarization on order to distinguish different surface types. Emissivity, measured during the NORSEX campaign (Svendsen et al., 1983) is presented in Figure 2-11.

The NORSEX algorithm can serve as an example of using two channels to resolve different surface types. It uses 19 GHz V channel to distinguish water and ice, and 37 GHz V channel to distinguish first year ice and multiyear ice.

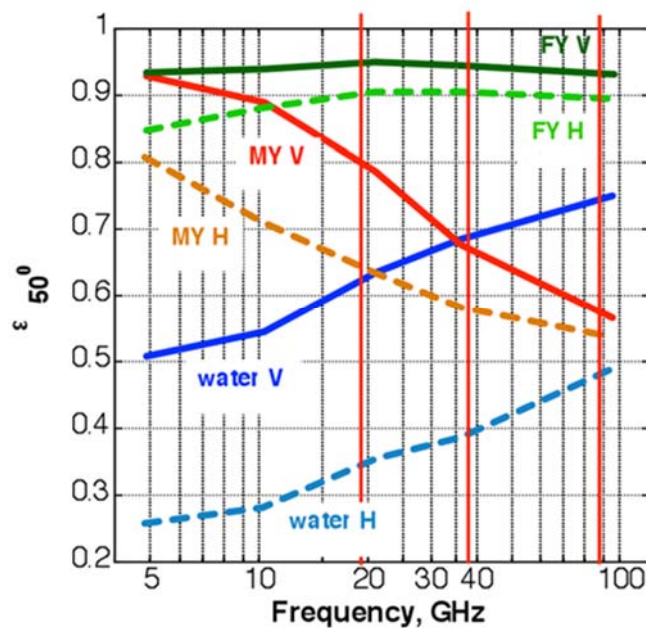


Figure 2-11: NORSEX radiometric signatures

Some of the algorithms use also polarization difference of the emissivity

$$P = TB(V) - TB(H), \tag{3-2-1}$$

or polarization ratio

$$\square \quad PR = \frac{TB(V) - TB(H)}{TB(V) + TB(H)} \tag{3-2-2}$$

in order to distinguish water from ice. Here TBs are brightness temperatures at vertical (V) and horizontal (H) polarizations. Polarization difference is known to be similar for all ice types and much smaller than for open water (Kern and Heygster, 2001; Kaleschke et al., 2001, Spreen et al. 2008).

2.3 Algorithm description

2.3.1 The SICCI2 merged algorithms

The SICCI algorithm is a combination of two other algorithms, one dynamically optimized for providing Best accuracy at 0% ice concentration cases (BOW), and one dynamically optimized for providing best accuracy at 100% ice concentration cases (BICE). These optimized algorithm are described below. The combination works as follows:

$$c = c_0 * w_0 + c_1 * w_1,$$

where c_0 and w_0 are SIC and weight for SIC from BOW dynamic algorithm, and c_1 , w_1 are SIC and weight for SIC from BICE dynamic algorithm.

if $c_0 < 0.7$:

$$w_0 = 1.0$$

if ($c_0 \geq 0.7$ and $c_0 < 0.9$):

$$w_0 = 1.0 - (c_0 - 0.7) / (0.9 - 0.7)$$

if $c_0 \geq 0.9$:

$$w_0 = 0.0$$

$$w_1 = 1.0 - w_0$$

In the algorithm used in the previous project phase, SICCI1, the same combination methodology was used (weights w_0 and w_1 above), but the two algorithms were not dynamically optimized, and were chosen so that BOW=ComisoF (Comiso, 1986), and BICE=Bristol (Smith and Barrett, 1994, Smith, 1996).

2.3.2 Dynamic SIC algorithms from triplet of Tbs

The concept of dynamic algorithm is first introduced in the SICCI2 project. In earlier efforts (OSISAF, SICCI1,...) the SIC algorithms (the way the brightness temperature channels are combined in algebraic equations, some coefficients of these questions, etc...) are "fixed", but the tie-points of the algorithms are derived dynamically. The dynamic tie-points approach is adopted to consistently achieve 0 bias at low and high concentration values. The dynamic tie-points also allow accommodating to calibration differences between instruments as well as sensor drift.

With the SICCI2 "dynamic algorithms", the very equation of the algorithms are tune to achieve least standard deviation of retrieved SIC, at the same time as to achieve 0 bias. The dynamic algorithm thus englobes the capabilities of the dynamic tie-points, but add the capability to reduce the retrieval noise.

The proposed new algorithm allows computing sea ice concentration as a linear combination of brightness temperatures T_b at three channels, e.g.:

$$ct = a \times T_{b_{18.7V}} + b \times T_{b_{36.5V}} + c \times T_{b_{36.5H}} + d \quad (\text{Eq. 1})$$

The 18.7 GHz and 36.5 GHz channels with vertical polarization and 36.5 GHz with horizontal polarization are acquired by the Advanced Microwave Scanning Radiometer (AMSR-E and AMSR2). These three channels - or their equivalent for the Special Sensor Microwave Imager (SSM/I) - have been used for many other published sea ice concentration algorithms.

Tuning of the algorithm involves finding an optimal plane in the three dimensional Tb space, on which any Tb triplet can be projected, and inside which the corresponding sea ice concentration can be computed. The algorithms are tuned against representative brightness temperature samples, one typical of 0% ice concentration cases (*ow*), and one typical of 100% ice concentration cases (*cice*). Each set holds hundreds or thousands of Tb triplets that are representative for these two extreme ice conditions. See section 2.5 for a description of how these samples are selected from satellite data.

The first step in the tuning of the algorithm is to perform a Principal Component Analysis (PCA) of the *cice* samples, with the three Tb channels as columns, and the samples are rows. This procedure returns the mean *cice* point, the three eigenvalues (sorted in decreasing order) and the corresponding three eigenvectors. The magnitude of the eigenvalues describes the variance of the *cice* samples along preferred directions (the eigenvectors) and around the mean *cice* point. At these channels, the largest variance is observed along the ice line that extends between the typical signature (aka tie-point) of First Year Ice (FYI) and Multi Year Ice (MYI) in the Arctic (Type-A and Type-B in the Antarctic). The first eigenvector (noted *u*) returned by the PCA of the *cice* sample defines the ice line in the three dimensions Tb space. That line goes through the mean *cice* point. In typical, winter conditions, the first eigenvalue is an order of magnitude larger than the two others. These define two directions in the Tb space with less (2nd) and least (3rd) variance in the *cice* sample. The *ow* sample does not enter a PCA, but is simply averaged to find the mean *ow* point, that is the typical signature of open water conditions (aka the open water tie-point).

A sea ice concentration in the form of Eq. 1 can be described as a coordinate transform, that map a point in the three dimensional (3D) Tb space into the one-dimensional (1D) axis of sea ice concentration. Such a coordinate transform is the composition of 4 steps : 1) a projection of a 3D point onto a 2D plane, 2) in that plane, a projection of the 2D point onto a 1D axis, 3) a scaling of the 1D axis, and 4) a shift of its origo :

$$ct_v(Tb_{18.7V}, Tb_{36.5V}, Tb_{36.5H}) = \alpha \times (v_x \times Tb_{18.7V} + v_y \times Tb_{36.5V} + v_z \times Tb_{36.5H}) + \beta$$

(Eq. 2)

By choosing $v = (v_x, v_y, v_z)$ to be a unit vector perpendicular to *u* in the 3D Tb space, we ensure that all points along the *cice* line correspond do the same sea ice concentration value. The constant α is computed so that the difference between $ct(cice)$ (the transformed mean *cice* point) and $ct(ow)$ (the transformed mean *ow* point) is 1, and the constant β is such that $ct(ow)=0$.

Solving the optimization problem is to find two vectors v_{bice} (resp. v_{bow}) that are both perpendicular to *u* in the 3D space, and that lead to smallest standard deviation of $ct(cice)$ (resp. $ct(ow)$). In practice, once *u* is computed from the Tb samples, a set of discretized rotation angles covering the range [-90:+90] is iterated upon. To each rotation angle, a new unit vector *v* is defined, that corresponds to a new algorithm (Eq. 2). The algorithm is applied on both the *cice* and *ow* samples, and the standard deviation of $ct(cice)$ and $ct(ow)$ are recorded. While iterating, the vectors v_{bice} and

v_{bow} are also kept. They correspond to a pair of algorithms ctBICE, and ctBOW that are optimized to the training *cice* and *ow* samples in terms of least standard deviation of retrieved ice concentration, and that have zero bias by construction. Thus, the coefficients to the algorithms are not only tuned dynamically to achieve zero biases, but also optimized to achieve least spread of retrieved ice concentrations.

The geometric descriptions above were all carried in a (18.7V, 36.5V, 36.5H) space. The same reasoning can however be carried within other 3D Tb spaces, as long as such space offer a clustering of the *cice* conditions along the ice line, and sufficient dynamic range between the *ow* signature, and the *cice* line. In this project, we introduce three new hybrid algorithms that all combine two optimized algorithms (each in the form of Eq. 2). The **SICCI2LF** operates in the (18.7V, 36.5V, 36.5H) space, **SICCI2HF** in (18.7V, 89.0V, 89.0H), and **SICCI2VLF** in (6V, 36.5V, 36.5H). All three spaces feature two « higher frequency » channels with same wavelength but alternate polarization, and a « lower frequency » channel. The role of the “higher” frequencies is to control the spread of *cice* samples along a line, and offer a good base for PCA. They also bring finer spatial resolution to the retrieved sea ice concentration. The addition of the “lower” frequency is to ensure sufficient dynamic range between *ow* and *cice* conditions, and thus aim at reducing retrieval noise. This is at the cost of bringing coarser spatial resolution into the algorithm, both in term of antenna footprint and spatial sampling.

The choice of channels also takes into account the long-term availability for generating climate data records of sea ice concentration. SICCI2LF can be applied to all passive microwave radiometers since the SMMR (October 1978) and all the way to present (on both AMSR-2 and SSMIS). SICCI2HF can be used from SSM/I F10 (January 1992) to present on both AMSR-2 and SSMIS, and SICCI2VLF can be applied on the whole period of AMSR-E and AMSR-2 instruments. Since all three algorithms are optimized on the instrument data itself, it will swiftly adapt to changes of frequencies, for example from 85.5 GHz on SSM/I, to 89.0 GHz on AMSR-E and AMSR-2, and 91.655 GHz for SSMIS.

2.3.3 NASA Team

The NASA Team algorithm is used in selection of dynamical tie-points for the SICCI algorithm (section 2.5). It is formulated as follows.

In the NASA Team algorithm (Cavalieri et al., 1984) radiative transfer equation is used in this form:

$$TB = T_s \varepsilon \quad (4-4-1)$$

The algorithm utilizes: 1) the polarization ratio

$$PR(f) = \frac{TB(f,V) - TB(f,H)}{TB(f,V) + TB(f,H)} \quad (4-4-2)$$

because it is small for all ice types compared to that of the ocean, and 2) the gradient ratio

$$GR(f_1, f_2, p) = \frac{TB(f_2, p) - TB(f_1, p)}{TB(f_2, p) + TB(f_1, p)} \quad (4-4-3)$$

Because the brightness temperature difference between the ice types increases with increasing frequency (see also the Figure 2-11. In these equations f is frequency and p is polarization (Andersen et al., 2006). Advantage of using the ratios is that they are almost independent of the physical temperature of the surface. NASA Team algorithm uses also a weather filter involving an additional channel 22V.

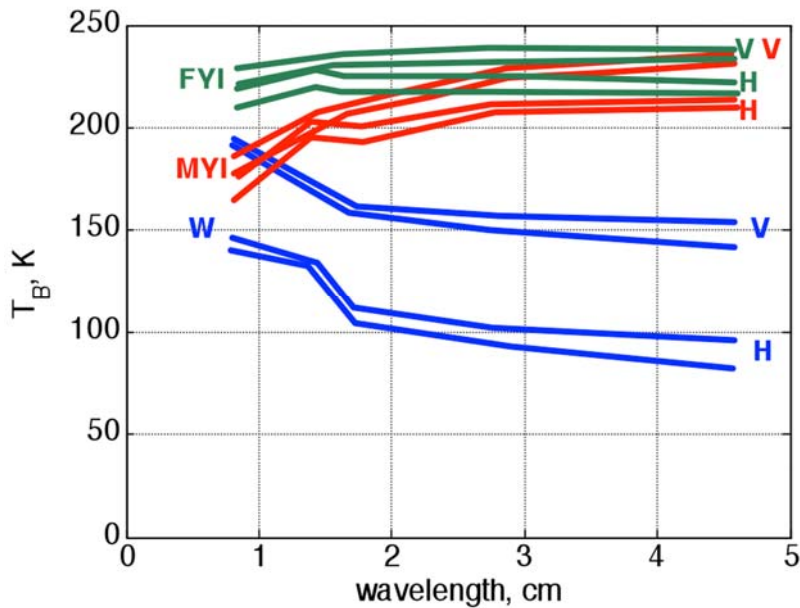


Figure 2-12: Usage of polarization and gradient ratios in NASA Team. Two curves for each case show limits of the value.

Assuming a mixture of open water, first-year ice and multiyear ice within the footprint of the satellite the partial concentrations may be inferred from the following expressions

$$C_{FY} = \frac{F_0 + F_1PR + F_2GR + F_3PR GR}{D}$$

$$C_{MY} = \frac{M_0 + M_1PR + M_2GR + M_3PR GR}{D} \quad (4-4-4)$$

$$D = D_0 + D_1PR + D_2GR + D_3PR GR$$

where PR=PR(19) and GR=GR(19,37,V). The coefficients F, M and D contain the tie point information (Andersen et al., 2006).

□
The tie points used for this algorithm are given in the next section.

2.3.4 Tie Points

Tie-points are typical brightness signatures of ice and water. The tie points are references either as brightness temperatures or emissivities for the channels (combinations of frequency and polarization) used in the algorithm. There is an individual tie point for each surface type: open water and different ice types. They vary from algorithm to algorithm and serve to ensure that algorithm gives 0% sea ice concentration for the areas of open water and 100 % concentration for areas of consolidated ice.

The tie points used in this work are presented in the following tables.

Open water:

NH	AMSR	NX	SSMI	NX	SMMR	NX
w06h	82.13		0		86.49	
w06v	161.35		0		153.79	
w10h	88.26		0		95.59	
w10v	167.34		0		161.81	
w18h	108.46		117.16		111.45	
w18v	183.72	170.01	185.04	171.56	176.99	162.61
w22h	128.23		0		135.98	
w22v	196.41		200.19		185.93	
w37h	145.29		149.39		147.67	
w37v	209.81	193.19	208.72	191.87	207.48	190.80
w85h	196.94		205.73		0	
w85v	243.20		243.67		0	

Table 2-4: Tie-points for Northern Hemisphere used with non-atmospheric corrected TBs, NX columns are tie-points for the NORSEX algorithm

SH	AMSR	NX	SSMI	NX	SMMR	NX
w06h	80.15		0.00		83.47	
w06v	159.69		0.00		148.60	
w10h	86.62		0.00		93.80	
w10v	166.31		0.00		159.12	
w18h	110.83		118.00		110.67	
w18v	185.34	171.86	185.02	171.52	175.39	160.77
w22h	137.19		0.00		129.63	
w22v	201.53		198.66		186.10	
w37h	149.07		152.24		149.60	
w37v	212.57	196.65	209.59	192.94	207.57	190.92
w85h	207.20		206.12		0.00	
w85v	247.59		242.41		0.00	

Table 2-5: Tie-points for Southern Hemisphere used with non-atmospheric corrected TBs, NX columns are tie-points for the NORSEX algorithm

First year Ice:

NH	AMSR	NX	SSMI	NX	SMMR	NX
fy06h	232.08				232.08	
fy06v	251.99				251.99	
fy10h	234.01				234.01	
fy10v	251.34				251.34	
fy18h	237.54		238.20		237.54	
fy18v	252.15	251.17	252.79	251.91	252.15	251.17
fy22h	236.72				236.72	
fy22v	250.87		250.46		250.87	
fy37h	235.01		233.25		235.01	
fy37v	247.13	244.47	244.68	241.53	247.13	244.47
fy85h	222.39		217.21			
fy85v	232.01		225.54			

Table 2-6: Tie-points for Northern Hemisphere used with non-atmospheric corrected TBs, NX columns are tie-points for the NORSEX algorithm. SMMR tie-points for FY and MY ice are set to AMSR tie-points since we do not have RRDP data for SMMR from 100% ice

SH	AMSR	NX	SSMI	NX	SMMR	NX
fy06h	236.52				236.52	
fy06v	257.04				257.04	
fy10h	238.50				238.50	
fy10v	257.23				257.23	
fy18h	242.80		244.57		242.80	
fy18v	258.58	258.41	259.92	259.93	258.58	258.41
fy22h	242.61				242.61	
fy22v	257.56		257.85		257.56	
fy37h	239.96		241.63		239.96	
fy37v	253.84	252.57	254.39	253.25	253.84	252.57
fy85h	232.40		235.76			
fy85v	242.81		244.84			

Table 2-7: Tie-points for Southern Hemisphere used with non-atmospheric corrected TBs, NX columns are tie-points for the NORSEX algorithm. SMMR tie-points for FY and MY ice are set to AMSR tie-points since we do not have RRDP data for SMMR from 100% ice

Multi-year ice:

NH	AMSR	NX	SSMI	NX	SMMR	NX
my06h	221.19				221.19	
my06v	246.04				246.04	
my10h	216.31				216.31	
my10v	239.61				239.61	
my18h	207.78		206.46		207.78	
my18v	226.26	222.11	223.64	219.20	226.26	222.11
my22h	199.60				199.60	
my22v	216.67		216.72		216.67	
my37h	184.94		179.68		184.94	
my37v	196.91	184.02	190.14	175.93	196.91	184.02
my85h	178.90		173.59			
my85v	187.60		180.55			

Table 2-8: Tie-points for Northern Hemisphere used with non-atmospheric corrected TBs, NX columns are tie-points for the NORSEX algorithm. SMMR tie-points for FY and MY ice are set to AMSR tie-points since we do not have RRDP data for SMMR from 100% ice

SH	AMSR	NX	SSMI	NX	SMMR	NX
my06h	225.37				225.37	
my06v	254.18				254.18	
my10h	221.47				221.47	
my10v	251.65				251.65	
my18h	217.65		221.95		217.65	
my18v	246.10	244.39	246.27	244.59	246.10	244.39
my22h	213.79				213.79	
my22v	240.65		242.01		240.65	
my37h	204.66		207.57		204.66	
my37v	226.51	219.62	226.46	219.59	226.51	219.62
my85h	197.78		200.88			
my85v	210.22		211.98			

Table 2-9: Tie-points for Southern Hemisphere used with non-atmospheric corrected TBs, NX columns are tie-points for the NORSEX algorithm. SMMR tie-points for FY and MY ice are set to AMSR tie-points since we do not have RRDP data for SMMR from 100% ice

2.3.5 Weather Filter

Weather filters are not directly used in the SICCI algorithm, since explicit correction of weather effects is performed using a Radiative Transfer Model and ERA-Interim data (section 2.4).

The Weather filter described below is however used in the selection of dynamical tie-points (Chapter 2.5).

Gloersen and Cavalieri (1986) filter is used for SMMR and Cavalieri et al. (1995) for SSM/I:

$$SMMR: C = 0 \text{ if } GR(37/18) > 0.07 \quad (4-5-1)$$

$$SSM/I: C = 0 \text{ if } GR(37/19) > 0.05 \text{ and/or } GR(22/19) > 0.045 \quad (4-5-2)$$

2.4 Atmospheric noise reduction using ERA Interim and RTM

Using an emission model, the brightness temperatures are corrected for the influence of water vapour in the atmosphere and open water surface roughness caused by wind shear. The emission model used for atmospheric noise reduction of the AMSR brightness temperatures, T_b , with ERA-Interim Numerical Weather Prediction (NWP) input is (Wentz, 1997; Wentz and Meissner, 2000):

$$T_b = f(T_s, U, V, L, T_a) \quad (5-1)$$

where T_s is the physical surface temperature, U is the sea surface wind speed, V is the integrated atmospheric water vapour column, L is the atmospheric liquid water column, and T_a is the surface (at 2 m) air temperature. Over areas with both ice and water the influence of open water roughness on the brightness temperatures and the ice emissivity is scaled linearly with the ice concentration. The emissivity of ice is given by standard tie-point emissivity. The correction procedure is described in details in Andersen et al. (2006). The NWP model grid points are co-located with the satellite swath data in time and space and a correction to the brightness temperatures using Eq. 5-1 is applied. Potential drift/biases in the NWP data fields are minimized by the dynamical tie-point adjustment later in the processing and eventually the residual error is included in the error estimate.

The representation of atmospheric liquid water column in the NWP data is not suitable to use for brightness temperature correction according to the PVASR. The satellite data are therefore not corrected for the influence of atmospheric liquid water. The other NWP variables are used directly.

2.5 Algorithm optimisation (dynamical algorithms)

During winter, in the consolidated pack ice well within the ice edge, the ice concentration is very near 100 %. This has been established using high resolution SAR data, ship observations and by comparing the estimates from different ice concentration algorithms (Andersen et al., 2007). The apparent fluctuations in the derived ice concentration in the near 100% ice regime are primarily attributed to snow/ice surface emissivity variability around the tie-point signature and only

secondarily to actual ice concentration fluctuations. In the marginal ice zone at intermediate ice concentrations and over open water the atmospheric attenuation/emission and wind shear and smearing dominates as error sources. The fluctuations due to atmospheric and surface emission are systematic. In fact, different algorithms with different sensitivity to atmospheric and surface emission compute quite different values for sea ice area and extent on seasonal and decadal time scales (Ivanova et al., 2013) and (Andersen et al., 2007). This means that not only does the estimated sea ice extent have a climatic trend also the atmospheric and surface constituents affecting the microwave emission are changing. In an attempt to compensate for the influence of such artificial trends the algorithms are tuned dynamically using a two weeks running window (± 7 days).

There is no additional attempt to compensate explicitly for sensor drift or inter-sensor calibration differences (the SSM/I data have been inter-calibrated but not with the SMMR dataset, the AMSR-E instrument does not have the same frequencies as the SSM/I) or possible biases in the NWP fields used for atmospheric noise reduction of the brightness temperatures. The dynamical tuning method is in principle compensating for these problems in a consistent manner.

2.5.1 The closed-ice samples

It is assumed that ice concentrations larger than 95 % from the NASA Team (NT>95) algorithm are in fact a representation of 100 % ice on average. The cloud of NT>95 samples are used for tuning of the algorithm (see 2.3.2). Additional tests ensure that samples are taken away from the coast regions, and inside a monthly climatology of ice.

2.5.2 The open water samples

The open water tie-point data are selected geographically along two belts on the northern and southern hemisphere respectively from the monthly maximum climatological ice extent +350-200 km further away. A land mask including the coastal zone and sea ice maximum extent climatology ensures open water data only and data points south of 50N in the northern hemisphere are not used. Total number of data points is limited to 5000 (selected randomly between available points). These open water samples are used for tuning of the algorithms (see 2.3.2).

2.5.3 Examples

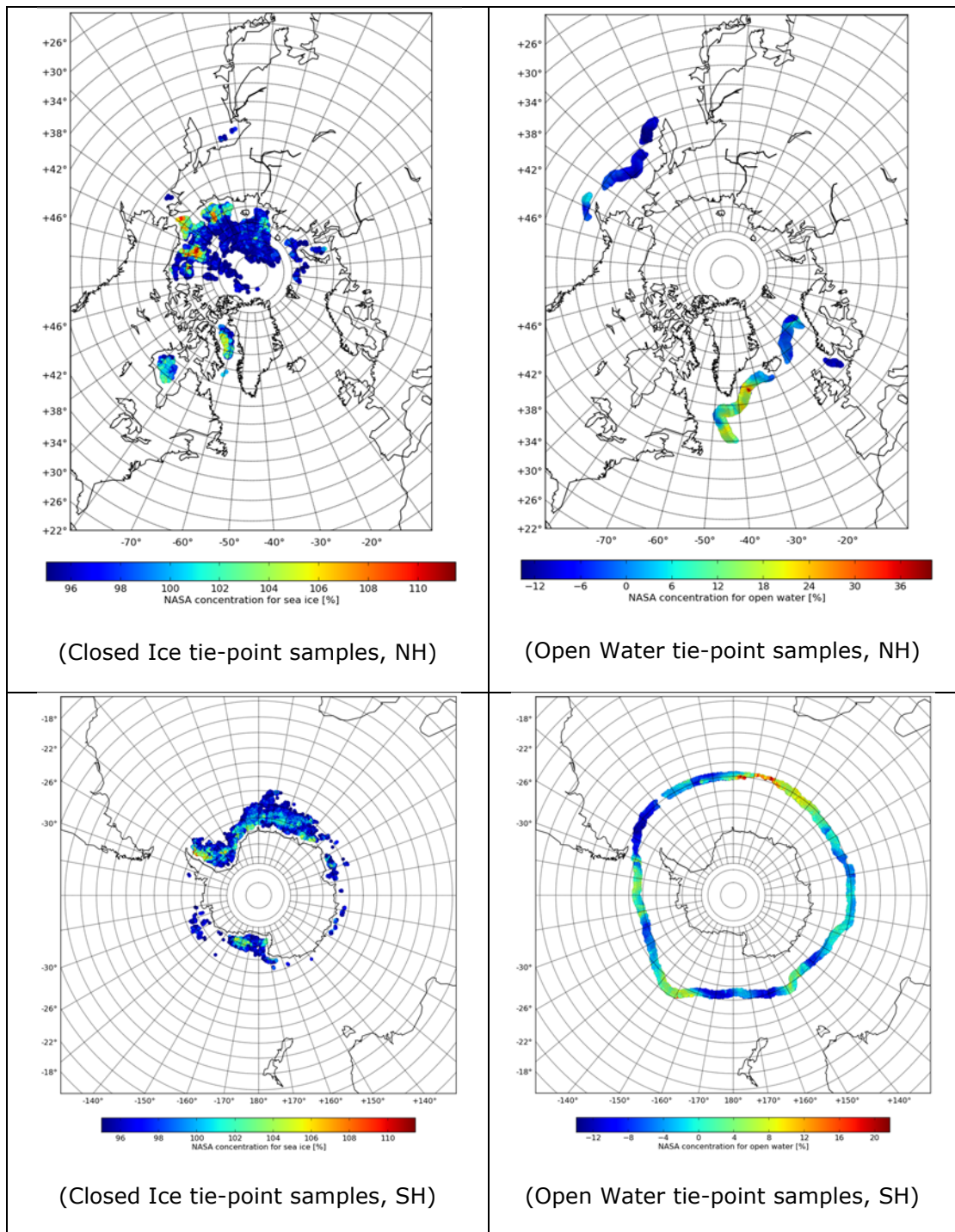


Figure 2-12: Example tie-point samples for Closed Ice (left) and Open Water (right), for NH (top) and SH (bottom). The colours scale with the NASA Team ice concentration.

2.6 Optimal estimation for sea ice concentration retrieval

The goal of retrieval or inversion techniques in general is to extract the geophysical information contained in a set of satellite measurements. Optimal estimation is one such statistical estimation technique that can be used for estimating a physical state vector using a set of (satellite) measurements. It is using a forward model describing the relationships between the physical state vector and the measurements, a first guess physical state vector (climatology, numerical modelling, or consistency) and covariance matrices for constraining the estimated parameters. Here, we describe the forward model and the optimal estimation process.

2.6.1 The forward model

The forward model is a combination of the Wentz and Meissner (2000) ocean and atmosphere model and a sea ice surface emission model. The T_b is a function of the following physical variables: the total column water vapour (in the atmosphere) [kg/m^2], V , the wind speed [m/s], W , the total column cloud liquid water [kg/m^2], L , the 2 m air temperature [K], T_a , the surface temperature either IST or SST [K], T_s (here this is synonymous with T_a), the effective temperature for each channel [K], $T_{i\text{amsrv}}$ and $T_{i\text{amsrh}}$ for vertical and horizontal polarisation (these are the same here), the sea ice concentration [0-1], C_{ice} , the sea ice emissivity for each channel [unitless], e_{icev} and e_{iceh} , i.e.

$$T_b = f(V, W, L, T_a, T_s, T_{i\text{amsrv}}, T_{i\text{amsrh}}, C_{ice}, e_{icev}, e_{iceh}) \quad (3.6.1)$$

The T_b model is used directly in the optimal estimation scheme for estimating the localised linear tangent model and for simulating the T_b 's given the estimated physical state for comparison with the measured T_b 's.

2.6.2 The sea ice surface emission

The sea ice surface T_b model which is part of the forward model is based on linear regression and the OIB March and April 2013 data from the RRDP (Pedersen and Saldo, 2016). The sea ice surface T_b 's are a function of the ice surface temperature [K], IST, the snow depth [m], SD , and the ice thickness [m], IT . In the optimal estimation scheme only the IST and the SD are free surface variables for sea ice. The IT is estimated directly from the T_b 's. The notation for the T_b is T for temperature, a number for the frequency in GHz and v or h for vertical and horizontal polarisation respectively.

$$T_{6v} = 151.98 + 0.40IST + 23.36SD - 3.03IT \quad (3.6.2)$$

$$T_{6h} = 55.26 + 0.69IST + 12.96SD - 1.66IT \quad (3.6.3)$$

$$T_{10v} = 145.89 + 0.44IST + 0.74SD - 4.20IT \quad (3.6.4)$$

$$T_{10h} = 45.11 + 0.75IST - 18.73SD - 3.49IT \quad (3.6.5)$$

$$T_{18v} = 138.07 + 0.48IST - 71.81SD - 5.57IT \quad (3.6.6)$$

$$T_{18h} = 78.42 + 0.64IST - 85.18SD - 5.34IT \quad (3.6.7)$$

$$T_{36v} = 123.10 + 0.53IST - 216.73SD - 4.04IT \quad (3.6.8)$$

$$T_{36h} = 131.86 + 0.43IST - 214.35SD - 3.04IT \quad (3.6.9)$$

$$T89v = 2.53 + 0.90IST - 180.43SD + 1.90IT \quad (3.6.10)$$

$$T89h = 31.12 + 0.74IST - 184.81SD + 3.20IT \quad (3.6.11)$$

2.6.3 The sea ice emissivity and the effective temperature

The effective temperature at different channels is correlated with the snow ice interface temperature. The snow ice interface temperature is a function of the snow depth among other things. The snow depth at near 100% ice cover is estimated using CRREL buoys from the RRD (Pedersen and Saldo, 2016) and linear regression. The three channels in the equation Tb6v, Tb19v and Tb37v were selected among all the AMSR channels using forward selection. Details are given in Kilic (2017).

First, the snow depth, SD_{sim} , is estimated (Kilic, 2017):

$$SD_{sim} = 1.77 + 0.017T6v - 0.028T19v + T37v \quad (3.6.12)$$

This snow depth is also used as a first guess in the optimal estimation scheme.

The snow ice interface temperature can be estimated using both the 6 GHz (Tsi6) and the 10 GHz (Tsi10) channels and the snow depth (Kilic, 2017). Using the estimates from both channels the two estimates are averaged (Tsi).

$$Tsi6 = 1.14T6v - \frac{0.82}{SD_{sim}} - 27.08 \quad (3.6.13)$$

$$Tsi10 = 1.10T10v - \frac{1.00}{SD_{sim}} - 14.28 \quad (3.6.14)$$

$$Tsi = \frac{Tsi6 + Tsi10}{2} \quad (3.6.15)$$

The effective temperature, T_{eff} , is found using linear regression and an emission model described in Tonboe et al. (2011). The equations for the effective temperature are derived by Kilic (2017). It is assumed that the effective temperature is identical for vertical and horizontal polarisation. However, these equations are derived for the vertical polarisation. The notation for the effective temperature is T_{eff} followed by the frequency in GHz.

$$T_{eff6} = 0.89Tsi + 30.25 \quad (3.6.16)$$

$$T_{eff10} = 0.90Tsi + 26.57 \quad (3.6.17)$$

$$T_{eff19} = 0.92Tsi + 21.54 \quad (3.6.18)$$

$$T_{eff23} = 0.93Tsi + 18.42 \quad (3.6.19)$$

$$T_{eff37} = 0.96Tsi + 10.90 \quad (3.6.20)$$

$$T_{eff89} = 1.06Tsi - 16.38 \quad (3.6.21)$$

The effective temperature is not a free variable in the optimal estimation scheme. It is estimated using the equations above before the optimal estimation iterations begin.

The emission model needs ice thickness (together with SD and IST) as input. The ice thickness, IT , could come as an auxiliary parameter from radar altimetry. However, here it is estimated using AMSR data in the following equation (eq. 3.6.22). The linear regression equation for ice thickness is based on OIB data from March and April 2013 in the RRDP (the database is described in Pedersen and Saldo, 2016).

$$IT = 4.82 - 47.39GR0610v - 52.83GR0618v + 49.96GR0618h + 33.40GR0636v + 0.14T6h - 0.12T19h - 0.039T37v \quad (3.6.22)$$

The spectral gradient, GR , at different frequencies is given by the following equations. The notation for the spectral gradient is GR followed by the two frequencies in GHz and the polarisation.

$$GR0610v = \frac{T_{10v} - T_{6v}}{T_{10v} + T_{6v}} \quad (3.6.23)$$

$$GR0618v = \frac{T_{19v} - T_{6v}}{T_{19v} + T_{6v}} \quad (3.6.24)$$

$$GR0619h = \frac{T_{19h} - T_{6h}}{T_{19h} + T_{6h}} \quad (3.6.25)$$

$$GR0636v = \frac{T_{37v} - T_{6v}}{T_{37v} + T_{6v}} \quad (3.6.26)$$

The spectral gradient between 6 and 10 GHz vertical polarisation is abbreviated $GR0610v$.

The emissivity [unitless], e , is the T_b [K] divided by the T_{eff} [K], here shown for the vertical polarisation for each of the frequencies. Similarly for the horizontal polarisation (not shown).

$$e_{6v} = \frac{T_{6v}}{T_{eff6}} \quad (3.6.27)$$

$$e_{10v} = \frac{T_{10v}}{T_{eff10}} \quad (3.6.28)$$

$$e_{19v} = \frac{T_{19v}}{T_{eff19}} \quad (3.6.29)$$

$$e_{37v} = \frac{T_{37v}}{T_{eff37}} \quad (3.6.30)$$

$$e_{89v} = \frac{T_{89v}}{T_{eff89}} \quad (3.6.31)$$

The emissivity is constrained to the interval [0,1].

2.6.4 The radiative transfer equation over open water and ice

The emissivity and the effective temperature are used in the radiative transfer equation which is also including the atmosphere. The atmospheric and open water emission is computed using Wentz and Meissner (2000) and details are given in their ATBD. The atmospheric component of this model is also used over ice. The radiative transfer equation is shown for 6 GHz vertical polarisation:

$$T_{6v} = TBU + \tau((1 + c_{ice})emissivity_v T_s + c_{ice}e_{icev}T_{i_{amsrv}} + (1 - c_{ice})(1 - emissivity_v)(T_{\Omega_{\text{megav}}} + \tau T_c) + c_{ice}(1 - e_{icev})(T_{BD} + \tau T_c)) \quad (3.6.32)$$

This model is valid for both ice and open water and at intermediate concentrations. The TBU is the direct upwelling temperature from the atmosphere [K], tau is the transmissivity of the atmosphere [unitless], C_{ice} is the sea ice concentration [0-1], emissivity_v is the open water emissivity [unitless], T_s is the surface temperature [K], e_{icev} is the sea ice emissivity [unitless], T_{iamsrv} is the sea ice effective temperature [K], $T_{\Omega av}$ is the atmospheric radiation scattered by the open water surface [K], T_c is the cosmic background radiation [K], here 2.7K, TBD is the down welling atmospheric temperature [K].

2.6.5 The sea ice concentration

The sea ice concentration is a free variable in the optimal estimation scheme. The first guess C_{ice} is provided by the bootstrap sea ice concentration algorithm in frequency mode using the T19v and the T37v brightness temperatures:

The tie-points are for: open water, T19v, $tw_{18v} = 179$ K, open water, T37v, $tw_{37v} = 202$ K, first-year ice, T19v, $tfy_{18v} = 253$ K, first year ice, T37v, $tfy_{37v} = 246$ K, multiyear ice, T19v, $tmy_{18v} = 218$ K, multiyear ice, T37v, $tmy_{37v} = 182$ K.

$$af = \frac{tfy_{37v} - tmy_{37v}}{tfy_{18v} - tmy_{18v}} \quad (3.6.32)$$

$$bf = tmy_{37v} - af * tmy_{18v} \quad (3.6.33)$$

$$qf = \frac{T_{37v} - tw_{37v}}{T_{19v} - tw_{18v}} \quad (3.6.34)$$

$$wf = tw_{37v} - qf * tw_{18v} \quad (3.6.35)$$

$$ti_{18vf} = \frac{bf - wf}{qf - af} \quad (3.6.36)$$

$$C_{ice} = \frac{T_{19v} - tw_{18v}}{ti_{18vf} - tw_{18v}} \quad (3.6.37)$$

The first guess C_{ice} is constrained to the interval [0,1].

2.6.6 The optimal estimation scheme

The optimal estimation scheme is using the derivative of the forward model, M , the difference between the measured and simulated Tb's ($T_b - T_a$), the estimated physical state vector, P , difference from first guess, P_0 , the state vector from last iteration, P_1 , and two co-variance matrices for constraining (S_e and S_p) to estimate a consistent set of physical variables that minimizes the difference between the measured and simulated Tb's:

$$P = P_1 + S(M^T S_e^{-1}(T_b - T_a) + S_p^{-1}(P_0 - P_1)) \quad (3.6.38)$$

P_1 is the physical state vector from the last iteration. S , where the diagonal is describing the P estimation uncertainty, is given by:

$$S = (S_p^{-1} + M^T S_e^{-1} M)^{-1} \quad (3.6.39)$$

Here the P state vector consists of the following variables:

- The surface temperature [K], T_s , over open water it is the SST and over ice it is the IST. The surface temperature is assumed equivalent to the 2 m air

- temperature which is a variable in the atmospheric model.
- Total column water vapour [kg/m^2], V , is the integrated column of water vapour in the atmosphere over both ice and open water.
- The 10m wind speed [m/s], W . The open water surface is getting rougher as a function of wind shear. This effect is only detectable over open water and there is no sensitivity to this parameter over ice.
- Total column cloud liquid water [kg/m^2], L , is the integrated column of liquid water in the atmosphere over both ice and open water.
- The sea ice concentration $[0,1]_{\text{cice}}$, is the fraction of the sea ice cover.
- The snow depth [m], SD , is snow depth on sea ice. There is no sensitivity to this parameter over open water (there is no snow on open water) and it is unlikely that it can be derived realistically at intermediate concentrations. Snow depth can be derived at near 100% ice concentrations.

2.6.6.1 The channels used in the optimal estimation

The following 12 channels are used in the optimal estimation scheme:

1. The 6.93 GHz brightness temperature vertical polarisation [K], T6v
2. The 6.93 GHz brightness temperature horizontal polarisation [K], T6h
3. The 10.65 GHz brightness temperature vertical polarisation [K], T10v
4. The 10.65 GHz brightness temperature horizontal polarisation [K], T10h
5. The 18.7 GHz brightness temperature vertical polarisation [K], T19v
6. The 18.7 GHz brightness temperature horizontal polarisation [K], T19h
7. The 23.8 GHz brightness temperature vertical polarisation [K], T23v
8. The 23.8 GHz brightness temperature horizontal polarisation [K], T23h
9. The 36.5 GHz brightness temperature vertical polarisation [K], T37v
10. The 36.5 GHz brightness temperature horizontal polarisation [K], T37h
11. The 89.0 GHz brightness temperature vertical polarisation [K], T89v
12. The 89.0 GHz brightness temperature horizontal polarisation [K], T89h

2.6.6.2 The estimation of the localized linear tangent, M

The emission model has 6 free physical variables as input for estimating the 12 T_b 's. i.e.

$$T_b = f(V, W, L, T_s, C_{ice}, SD) \quad (3.6.40)$$

For each estimated state vector P the T_b 's are simulated. Each of the variables in the state vector are perturbed sequentially by 1% of its value and then the difference between the T_b 's and the perturbed T_b 's are divided by the 1% variable perturbations sequentially, i.e.

$$M = \frac{\delta T_b}{\delta P} \quad (3.6.41)$$

This gives an $m \times n$ element matrix (here 6×12) with the T_b sensitivity to each of the state vector elements at a given point in state vector space. The dimensions of M are given by the length of the state vector (m) and the length of the measurement vector (n), i.e. the number of channels.

2.6.6.3 The covariance matrices

The S_e covariance matrix is an $n \times n$ matrix (here 12×12) where n is the number of measurement channels of independent measurements and where the diagonal is

describing the measurement variance (noise) and forward model variance. The S_p covariance matrix is an $m \times m$ matrix (here 6×6) where m is the number of free physical variables to be estimated. The diagonal is describing the physical variance for each of the free variables. The off-diagonal elements are describing the covariance between different physical variables, e.g. water vapour and surface temperature. These covariance matrices are used to constrain the estimate beyond first guess so that a small number gives an estimate close to first guess with a large weight on this parameter and a large number gives free constraints. A large number gives little weight in the estimation process. The iteration process stops after a certain number of iterations or when a cost function is satisfied.

2.7 Uncertainty model

The uncertainties described in the following sections are generally independent and the squared sum of the two estimated components of uncertainty is the total uncertainty squared. The tie-point uncertainty $\sigma_{\text{tie-point}}$, including residual atmospheric noise, sensor noise and ice surface emissivity variability, is derived from measurements as the first component of uncertainty. The representativeness error, σ_{smear} , is simulated using satellite imaging simulator. The imaging simulator is described in Tonboe et al. (2016).

$$\sigma_{\text{total}}^2 = \sigma_{\text{tie-point}}^2 + \sigma_{\text{smear}}^2 \quad (7-1)$$

2.7.1 Instrument noise, algorithm and tie-point uncertainties

Both the water surface and ice surface emissivity variability result in ice concentration uncertainties. Emission and scattering in the atmosphere also affects the Tb's and the computed ice concentrations. Different algorithms have different sensitivities to these surface and atmospheric parameters (Andersen et al., 2006B). Further, both the atmospheric and surface parameters affecting the ice concentration estimates have climatic trends (Andersen et al., 2007). To minimize the uncertainties due to these two parameters, the Tb's are corrected using NWP data for atmospheric humidity and open water roughness in the sea ice concentration processing. The dynamical tie-points minimize uncertainty due to the climatic trends in the atmosphere and on the ice surface on a hemispheric scale while regional biases may still exist.

Ice concentration can be interpreted as a superposition of water and ice:

$$\text{iceconc} = (1 - \alpha(\text{ic})) \cdot \text{water} + \alpha(\text{ic}) \cdot \text{ice} \quad (7-2)$$

where ic is the ice concentration calculated by the algorithm. The functional dependency between α and the calculated ice concentration ic is described by:

- $\text{ic} \leq 0$, $\alpha = 0$
- $0 < \text{ic} < 1$, $\alpha = \text{ic}$
- $\text{ic} \geq 1$, $\alpha = 1$

which can be written as

$$\alpha(\text{ic}) = \Pi_{0,1}(\text{ic})\text{ic} + H(\text{ic} - 1) \quad (7-3)$$

where $\Pi_{a,b}(x)$ is the Boxcar function and $H(x)$ the Heaviside step function. Using equation (7-2) and assuming the uncertainty for the ice and water part is independent, this leads to a total algorithmic uncertainty as

$$\sigma_{algo}(\alpha(ic)) = \sqrt{(1 - \alpha(ic))^2 \sigma_{water}^2 + \alpha^2(ic) \sigma_{ice}^2} \tag{7-4}$$

where $\sigma_{water} = \sigma(IC(P_{openwater}))$ and open water is determined by a monthly varying ocean mask, IC is the functional mapping of the ice concentration algorithm and P_c denotes the set of swath pixels for all swaths (used calculating the daily product) selected on the condition C.

$\sigma_{ice} = \sigma(IC(P_{ocean,nasateam>0.95}))$ e.g. the standard deviation of the calculated ice concentration of those pixels clear of the coast having a NASA Team concentration > 95%.

2.7.2 The SICCI2 algorithm uncertainty

2.7.2.1 combining the algorithm uncertainty of BOW and BICE.

The methodology above is applied to find both the BOW and the BICE algorithm uncertainties at both ends of the concentration range (thus 4 σ values in total). The algorithm uncertainty of the SICCI2 algorithm (that combines BOW and BICE linearly, see section 2.3.1) is thus computed as a linear combination of the variances. This is illustrated in the figure below:

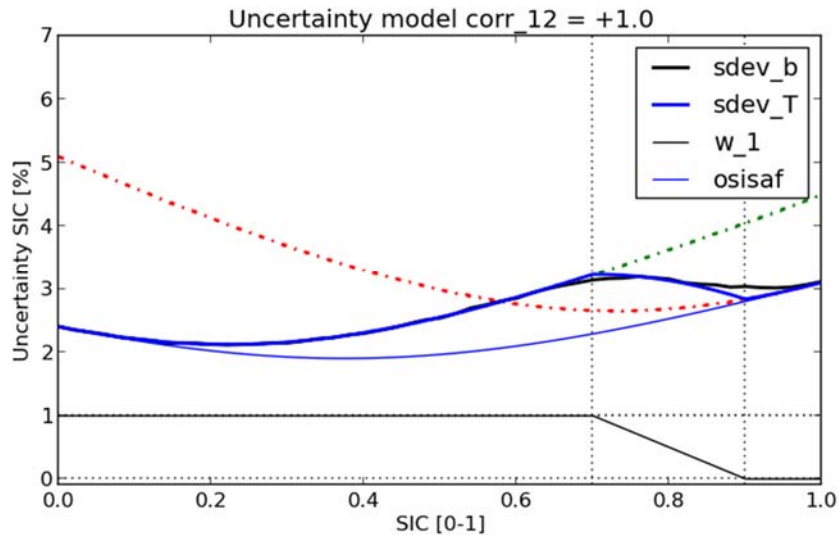


Figure 2-13: Illustration of the uncertainty merging of two algorithms (BOW in green, and BICE in red)

On the figure above, the thin blue line is the uncertainty merging equation that was used in SICCI1, the thick blue line is the new merging equation, that takes into account the merging weights (black solid line at the bottom). The black thick line is the result of Monte Carlo simulations assessing that the new uncertainty merging model is superior to the one used in SICCI1.

2.7.3 The geo-location error

The geo-location error occurs when the satellite is not exactly oriented. Simulations show that because of the large footprints compared to the typical geo-location errors (about $\pm 5\text{km}$) the ice concentration uncertainty due to geo-location errors is small and neglected here. Locally the geo-location errors may be significant but difficult to estimate.

The geolocation of AMSR-E was initially suboptimal and persisted for several years. Therefore, an own geolocation was developed at the University of Bremen (Wiebe et al. 2008). It consists of determining the sensor's nadir and scan angles (Figure 2-14). Attitude and position of the spacecraft itself is quite precisely known as can be seen from the MODIS images of resolution below 1 km taken from the same platform AQUA.

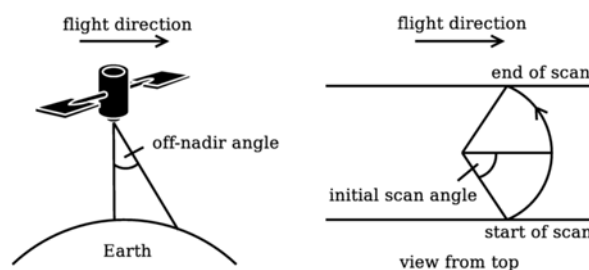


Figure 2-14: Viewing geometry of AMSR-E (Wiebe et al. 2008).

To check the geolocation, the brightness temperature difference between ascending and descending swaths of the same region and day is considered. In regions of sharp contrast like coastlines the difference will be high; in homogeneous regions it will be low. Figure 2-15(top) shows an example of the original JAXA geolocation for the 89 GHz v-polarization data. As at 89 GHz the resolution is highest, the geolocation error will be strongest at this frequency. Coastlines clearly stick out with their higher positive and negative brightness temperature differences. However, also other changes in the hours between the two overflights like cloud systems over ocean can be recognized. After correcting the geolocation, the contrasts near the coastlines have gone, only the geophysical contrasts remain (Figure 2-15(bottom)). The results of the optimization procedure was a correction of the nadir and scan angle leading to a repositioning of the boresight direction on earth between 6 km and

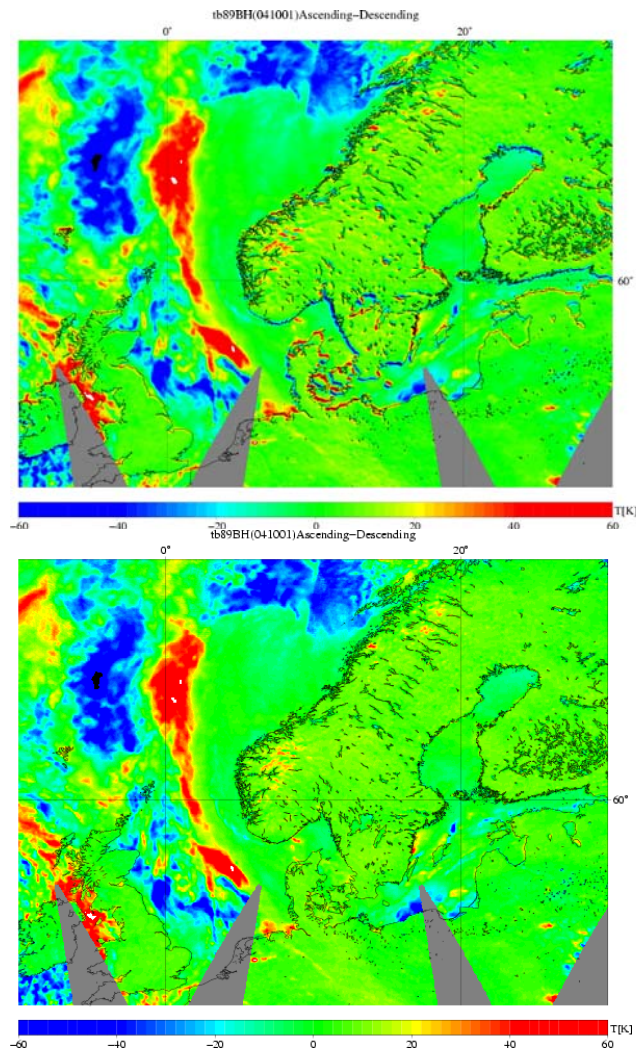


Figure 2-15: AMSR-E 89 GHz B-Scan ascending – descending brightness temperature differences. Left: original (JAXA) geolocation. Right: UB geolocation.

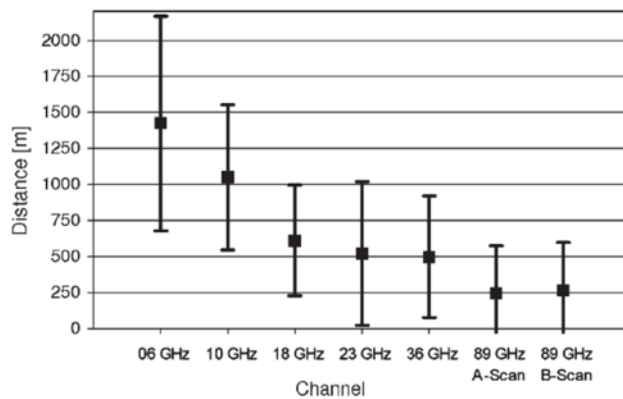


Figure 2-16: Residual, random geolocation error after geolocation correction (Wiebe et al. 2008).

7 km. The geolocation and repositioning needs to be done for each frequency separately as they use different feedhorns, but all feedhorns use the same antenna reflector. Also the residual, statistical geolocation error depends on frequency. It varies between 1400 m at 6 GHz and 250 m at 89 GHz (Figure 2-16).

The geolocation error in K is more difficult to assess as we do not have reference values. Moreover, average values over larger areas are of little help because the error only occurs in a small percentage of the pixels, namely those near edges. As an approximation, Wiebe et al. (2008) restricted the brightness temperature difference to pixels near the coastline. They show a similar step in brightness temperature as the ice edge does. As shown in Table I, the brightness temperature differences based on the optimized geolocation(column UB) increase monotonically with frequency from about 5 K (6 and 10 GHz) to 8 K (89 GHz). This statistical difference has several components:

- The geophysical changes (weather and surface temperature) in the hours between the two overflights
- The differences overlap of the fields of view (FOVs) resulting from the different boresight directions of the antenna beam during different overflights. This error cannot be avoided, even if considering ascending overflights only or descending overflights only.
- The difference from the non-overlapping parts of the fields of view (FOVs) of the ascending and descending overflights. The FOVs are elliptical and differently oriented during ascending and descending overflight so that they cannot overlap even with an ideal geolocation and identical boresight directions during the involved overflights.
- the residual, random geolocation error according Figure 2-16.

We cannot split between these four components. However, strong geophysical differences over open ocean occur only in a small percentage of the pixels (at least in Figure 2-15). Therefore we consider the error sum as given in Table I column UB as mainly caused by the remaining three components which we denote together as random errors. We take the difference values given above as reference for the best values which can be achieved with this method. As the brightness temperature contrast between open ocean and sea ice is similar, but somewhat lower than that between ocean and land, we can consider the values in the UB column of Table I as upper limits of the random influence. The result is that even with the achievable best geolocation, its influence of the unavoidable random errors near the ice edge amounts to several K and cannot be ignored. This random component in the brightness temperature will lead to an error contribution in SIC at intermediate ice concentrations. However, during the process of assessing the performance of different SIC retrieval algorithms, all error components can be avoided by using the SIC0 and SIC1 RRDP data sets.

Moreover, Table 2-10 shows that the average brightness temperature difference was reduced by about a factor of 2 by the new geolocation (compare columns JAXA and UB).

Frequency	JAXA [K]	UB [K]
6 GHz	8.75	4.94
10 GHz	9.52	4.94
18 GHz	15.13	5.76
23 GHz	12.50	5.38
36 GHz	15.74	6.53
89 GHz A	12.23	7.87
89 GHz B	12.55	7.81

Table 2-10: Mean difference per pixel for the coastline pixels of Figure 2-15. JAXA and UB denote the different geolocation procedures (Wiebe et al. 2008).

Also for AMSR2, the geolocation was tested (Figure 2-17) on the 89 GHz A-scan and based on the JAXA AMSR2 L1 data version 1.1. Along the coastlines not enhanced contrasts are visible which could pinpoint to a geolocation error. For the B-scan, similar results were found (not shown here). Therefore, we consider the geolocation to be sufficient in the sense of not introducing avoidable errors and refrain from additional investigations. Moreover, JAXA has performed an independent geolocation study for AMSR2 (JAXA-EORC 2015). The RMSE results are somewhat higher than those of Wiebe et al. (2008) in Figure 2-16, but still for each frequency clearly below the resolution.

Freq. [GHz]	Spatial res. [km]		Geoloc. Err. [km] (RMSE) V 1.1		Geoloc. Err. [km] (RMSE) V 2.0	
	EL	AZ	EL	AZ	EL	AZ
6.9	62	35	7.3	15.6	6.3	3.3
7.3	62	35	6.9	15.2	5.9	3.5
10	41	24	5.0	10.5	3.6	2.5
18	22	14	2.3	5.3	2.0	1.4
36	12	7	1.6	4.2	1.3	1.3
89	5	3	1.0	1.3	0.9	1.0

Table 2-11: AMSR2 Geolocation errors in AMSR2 L1 data versions 1.1 and 2.0. EL: elevation direction, AZ: azimuth direction. After JAXA EORC (2015).

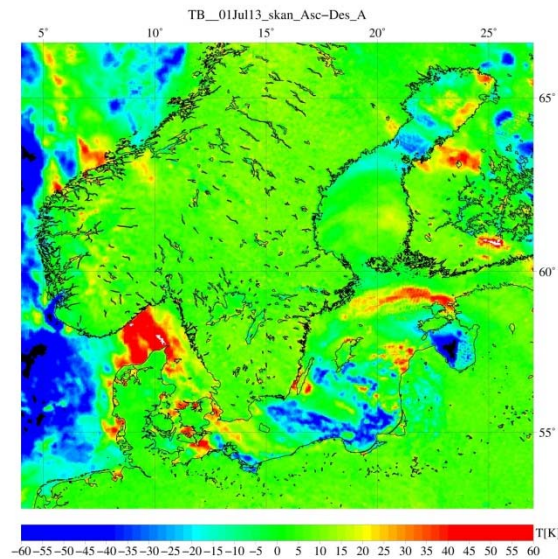


Figure 2-17: AMSR2 Brightness temperature difference ascending – descending on 1 July 2013, 89 GHz A-scan.

2.7.4 The representativeness error

Footprint sizes for the AMSR-2 channels used for ice concentration mapping range from about 50 km for the 6 GHz channels to about 10 km for the 36 GHz channels to less than 5 km for the 89 GHz channels. Footprints of uneven size are sometimes combined in the algorithms when computing the ice concentration. This is also the case for the two algorithms used in the SICCI project (SICCI2LF and SICCI2VLF). The footprint ice concentration is represented on a predefined grid. The ice concentration data are normally represented on a finer grid than the algorithm resolution. This uncertainty effect of this procedure is called smearing. However, in the SICCI CDR we have tried to match the grid resolution with the algorithm resolution (25 and 50 km) to minimize smearing. The smearing will not disappear completely because the different foot-prints have different resolution and because of the sea ice scale of variability is much higher than the resolution on any of the channels on the satellite i.e. the combination of footprints of uneven size in the ice concentration algorithm results in an additional smearing effect. This we call the footprint mismatch error. The smearing and the footprint mismatch error cannot be estimated separately. We have estimated the smearing error from simulations based on high-resolution satellite data.

The results from the imaging simulator are shown in Figure 2-18. The upper left panel is showing the sea ice situation at 1 km resolution, a MODIS scene 3000 x 2200 km from near the Ross Sea. The lower left panel is showing the sea ice concentration as seen with the SICCI2LF algorithm, i.e. simulated with the imaging simulator. The upper right panel is showing the 3 x 3 max-min proxy for the smearing at 25 km pixel resolution. The lower right panel is showing the difference SICCI2LF SIC at 25 km resolution and the MODIS reference at 25 km pixel resolution.

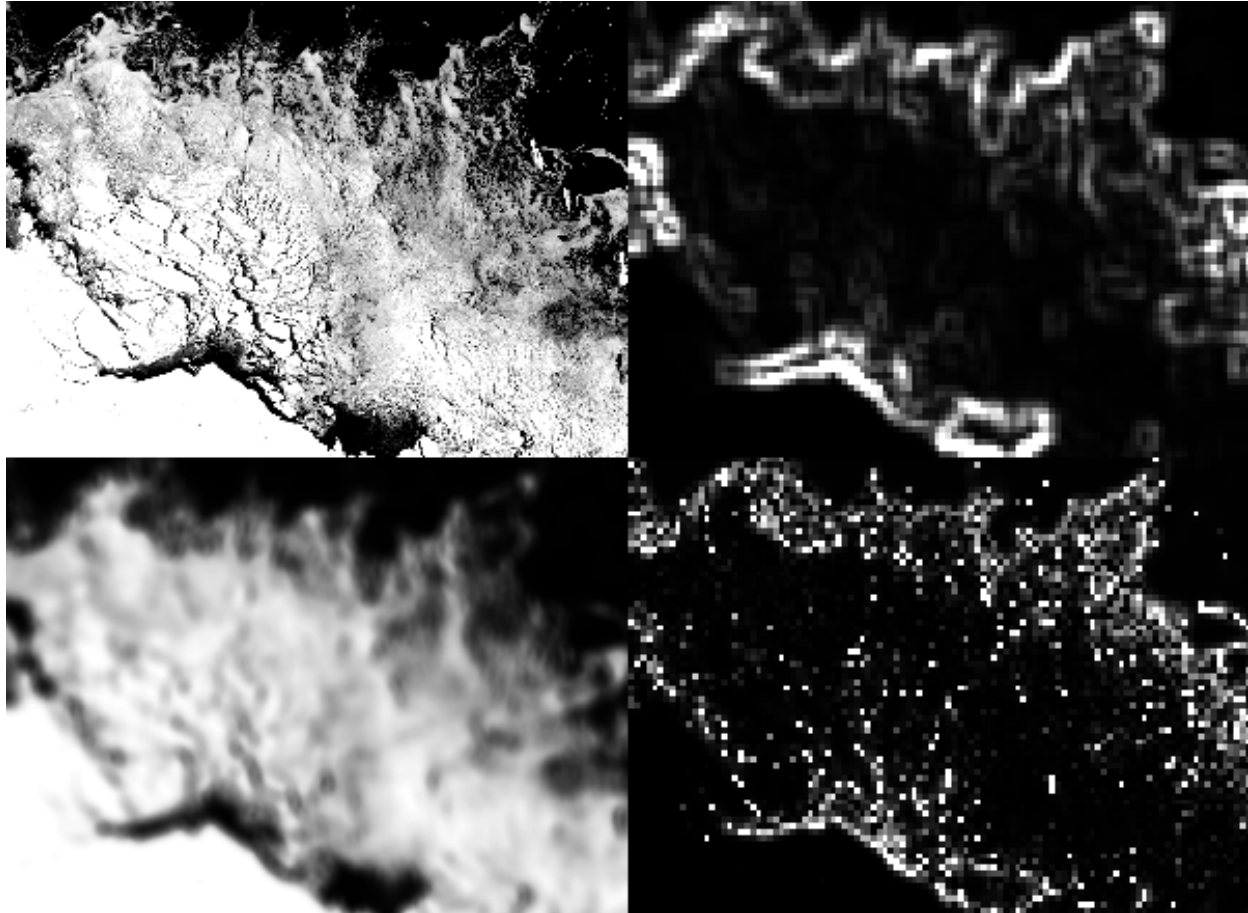


Figure 2-18: Upper left: MODIS reference at 1 km resolution [0-1] (3000 km x 2200 km), lower left: SICCI2LF SIC [0-1], upper right: the 3 x 3 max-min proxy [0-0.5], lower right: SICCI2LF at 25 km pixel resolution and MODIS reference at 25 km pixel resolution difference [0-0.5].

Figure 2-19 is showing the smearing error (simulated product and reference at 25 km resolution difference) for the low frequency (SICCI2LF) sea ice concentration algorithm vs. 3 proxies for estimating the smearing error: the 3 x 3 pixel standard deviation, the Laplacian, and the 3 x 3 pixel max-min difference. Other smearing proxies were tested as well but they are not shown. We have selected the 3 x 3 sea ice concentration max-min difference proxy as the proxy for estimating the smearing uncertainty component for both the low frequency (SICCI2LF) and the very low frequency (SICCI2VLF) algorithms. There is a 1:1 relationship between the proxy and the smearing uncertainty component for both algorithms. The uncertainty algorithm is described in more detail in the PVASR.

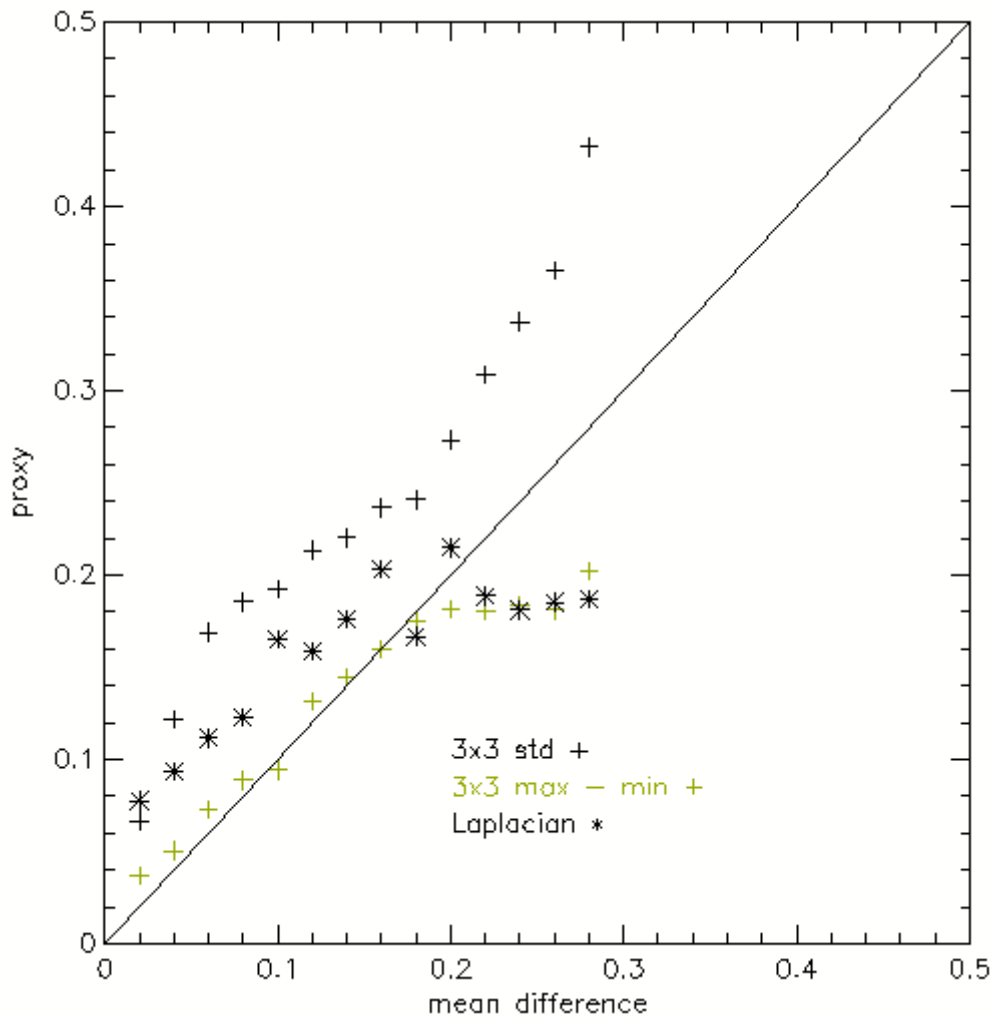


Figure 2-19: The smearing error component vs. three proxies for smearing for the SICCI2LF SIC algorithm at 25 km grid. Gridding and temporal compositing

The daily gridding searches for all satellite observation within 24 hours centered on 12:00 UTC, and grids these to the final output grid. The observations within one grid cell are averaged, using a decaying weight of the distance between the grid cell centre and the FoV centre. The function implemented is a Normal shape with standard deviation 4.2 km.

The aim of the gridding step is to localize swath-based information into the output grid, so that there is no grid cell with missing value, and that the gradients existing in swath projections are not utterly blurred with transferred to grid. We found it is not very important which weighting function is used, as long as it is rapidly decaying and tuned to the spacing of the target grid cells (25 km) and the spacing between the FoVs in swath (25 km).

The several swaths contributing to the daily time composite are equally weighted. The Level 2 algorithm uncertainty (section 2.7.1), and the observation time are averaged with the same formula.

In the averaging, observations from multiple satellite missions are available in overlapping periods. During overlaps in the SSM/I period, observations from different satellites are averaged.

2.8 Near-coast corrections

Due to the coarse resolution of the radiometers the data may be influenced by land up to 50 km from the coastline (for SSM/I and SSMIS) and up to 25km from the coastline for AMSR-E and AMSR2. The emissivity of land along the coastline is comparable to sea ice emissivity and much higher than water emissivity. This means that in the coastal zone if there is open water or intermediate concentrations the sea ice concentration will be overestimated. In earlier efforts (OSISAF, SICCI1), a statistical method similar to Cavalieri et al. (1999) was implemented **as a post-processing to the daily-gridded sea ice concentration maps**. Such a method showed limitation and the next versions of the SICCI2 (and OSISAF) datasets will rather correct the L1b brightness temperatures (thus at swath-level) from the contamination by land emissivity.

The correction algorithm is described in details in Maas and Kaleschke (2010). The basis principle is that, for each FoV in the swath file, one separates T_b into two components, T_{sea} and T_{land} ($T_b = (1 - \alpha) \times T_{sea} + \alpha \times T_{land}$), where α is a convolution of the antenna gain function and land fraction of the footprint. Local T_{land} is calculated by using land fraction from high-resolution shoreline data in a defined search area. Then T_{sea} is computed from formula above, and is the corrected brightness temperature to be used in the sea ice concentration algorithm.

The algorithm was fully re-implemented in more efficient python software code, and the following modifications were tuned and implemented:

- Computation of the fraction of land α in each FoV is no more computed on a projection plane, but in the view geometry of the instrument.
- The fraction of land α is computed from the same land mask as used otherwise in the SIC processing (e.g. for gridding and masking).
- The antenna pattern functions are approximated as Gaussian shapes indexed on the aperture angle from central view direction.

2.9 Gap filling by interpolation

For easing the use of the reprocessing data set, it was decided that some level of spatial interpolation should be performed for reducing the occurrence of gaps. Only missing data are interpolated. Interpolated data points are clearly marked in the product file so that users can choose to discard them and only ingest retrievals that rely on satellite signal.

Data gaps can occur in several forms, such as missing scan lines, missing orbits and polar observation hole. While spatial interpolation might be efficient in filling small gaps (e.g. one or two missing scan lines), it necessarily blurs the sea ice concentration features. This effect becomes overwhelming when large areas are missing. To overcome this issue, yet implementing a general approach for all cases, the ice concentration estimates from the previous and next daily products are used in the interpolation as well. In the case of SSM/I, it means that interpolation on a given date D uses pixels from 3 data files: $D-1$, D and $D+1$.

The interpolated value at grid cell (i,j) for day D is given by:

$$X_{i,j}^D = K \cdot \left(w_{i,j}^{D-1} \cdot X_{i,j}^{D-1} + w_{i,j}^{D+1} \cdot X_{i,j}^{D+1} + \sum_{k,l} W^D(k,l;i,j) X_{k,l}^D \right) \quad (10-1)$$

where X is the sea ice concentration value and K is a normalizing factor given by:

$$w_{i,j}^{D-1} + w_{i,j}^{D+1} + \sum_{k,l} W^D(k,l;i,j) = 1/K \quad (10-2)$$

From Eq. 10-1, it is clear that the *spatial* interpolation from neighbours of cell (i,j) only uses values from date D , while the *temporal* interpolation is only concerned with the value from the exact (i,j) cell but from dates $D-1$ and $D+1$. This strategy ensures that the interpolation will be efficient in the two following extreme scenarios. In a region where we never have satellite observations (e.g. the polar observation hole in the Northern Hemisphere), the spatial interpolation term will be the only contribution. Conversely, in the case of several missing swath on date D only (nominal coverage on $D-1$ and $D+1$), the interpolated values will be computed from the previous and next dates, taking advantage of the persistence of sea ice concentration over such a short period. The interpolation for intermediate cases (when both spatial and temporal neighbours exist) is a compromise of those extreme situations.

In Eq. 10-1, the weighting parameters are computed as follows:

$$w_{i,j}^D = 1/(\sigma_{i,j}^D)^2 \cdot (2N_{max} + 1) \quad (10-3)$$

$$W^D(k,l;i,j) = 1/(\sigma_{k,l}^D)^2 \times \exp\left(-0.5 \cdot \left(\frac{\Delta(k,l;i,j)}{R_{i,j}}\right)^2\right)$$

where σ is the standard deviation associated to each ice concentration estimate Δ is the distance between a given (k,l) neighbour and cell (i,j) and R is an auto-correlation radius. The spatial interpolation weight is thus based on an isotropic gaussian shape, and almost all (>99.9%) of the interpolation weight is concentrated inside a $[-3R;+3R] \times [-3R;+3R]$ km² area, which translates into a $[-N_{max};+N_{max}] \times [-N_{max};+N_{max}]$ grid cells square area. It was found that a spatially varying radius R was needed for optimal gap filling and the value $R = 1.5 \cdot \text{latitude of (i,j)}$ (in degrees) was chosen.

2.10 Conclusions (will be updated in final version)

The algorithm evaluation described in the associated PVASR1 document (ref) led to the recommendation that the best algorithm choice is an OSISAF like algorithm with dynamical tie-points and atmospheric correction. The selection of tie-points should be done with an algorithm which is sensitive to melt-ponds e.g. Bootstrap - F or NORSEX and it is not recommended to use cloud liquid water for atmospheric correction. However, other parameters (wind, water vapour and surface temperature) make a clear noise reduction.

This relatively simple setup deployed by EUMETSAT's Ocean and Sea Ice Satellite Application Facility (OSISAF) for their reprocessing and operational data streams performs among the best in the overall evaluation.

More advanced algorithms have shown some potential but also several drawbacks, so at this stage we can only recommend to continue work on self-correcting algorithms for future applications, but we must conclude that for a climate data record we still have to rely on a fairly simple and robust algorithm with well-described error properties.

Atmospheric correction of TBs before SIC calculation is our recommended way to reduce noise regionally from wind roughening of the ocean surface and attenuation of the surface radiation while propagating through the atmosphere.

It is of paramount importance that the tie-points to the ice concentration algorithms are tuned to the dataset of Brightness Temperatures that is targeted. It is a clear advantage to adapt tie-point to seasonal and inter-annual variations of the sea ice emissivity. The "dynamical tie-points" approach (adopted by the EUMETSAT OSISAF dataset) is a solution to both the issues above.

3 Snow algorithm

3.1 Overview

The snow depth algorithm consists of two components: A sea ice concentration algorithm and a snow depth algorithm. In the snow depth algorithm sea ice concentration is used to compensate the influence of open water on the observed brightness temperatures. Overall six different sea ice concentration algorithms were tested (Bristol [Smith and Barrett, 1994, Smith 1996], Nasa Team [Cavalieri, 1984, Anderson et al., 2006], Bootstrap p- and f-mode [Comiso, 1986, 1995], an experimental algorithm based on the 6.9 GHz channels suggested by L. T. Pedersen, hereafter called LEA (Leif's experimental algorithm), [2015, personal communication] and ASI [Kaleschke et al., 2001, Spreen et al., 2008]).

For the calculation of the sea ice concentration in all algorithms except for LEA, tie points for 100% ice cover and open water are needed. These tie points were calculated from the Round Robin Data Package (RRDP) for open water (SIC0) and 100% sea ice cover (SIC1) for AMSR-E and AMSR2 (see next section).

As data input for the new snow depth algorithm pre-allocated AMSR-E/AMSR2 brightness temperatures, surface roughness and Operation IceBridge (OIB) [Kurtz and Farrell, 2011] snow depth data with a resolution of 50 km from the NERSC AMSR-E /AMSR2 RRDP [Rinne and Mäkynen, 2013] were used. Ice Mass Buoy data were also tested. However, the snow depth averages showed a strong scatter. Since the ice mass buoys are fixed to the floe they are drifting with, they only represent one single sea ice sample within a 50 km pixel and thus may not be representative for the whole area covered by the AMSR-E and AMSR2 pixels. Therefore the ice mass buoy data were not considered any further.

To obtain a relationship between AMSR-E/AMSR2 brightness temperatures and OIB snow depth data two different approaches were used. In a first attempt a linear regression between brightness temperatures, polarisation ratio and gradient ratio for single and mixed polarisation and snow depth was performed. Here, the regression between gradient ratio and snow depth for a single polarisation showed the most promising results. For the vertically or horizontally polarised gradient ratios the difference in RMSD is usually smaller than 1 cm, and the correlation coefficient tends to be slightly lower than for the polarisation ratio, the brightness temperature and the mixed gradient ratio. Thus the single polarisation gradient ratio tends to be the best choice and will be used for the new algorithm.

In a second step multilinear regressions were performed. Overall the improvement was negligibly small (a few mm or less as quantified by the root mean square difference) and thus the additionally introduced uncertainty is most likely higher than the improvement in snow depth. For this reason a linear approach is used to set up the snow depth algorithm for the Arctic.

Overall in a comparison for both sensors the results are relatively similar for all six sea ice concentration algorithms. The root mean square deviation (RMSD) usually shows differences not exceeding 2 cm for one channel combination which is within the estimated uncertainty of the existing snow depth retrieval of approximately 5 cm [Markus and Cavalieri, 1998]. Similarly the RMSD results for one sea ice concentration algorithm for the two sensors usually do not differ by more than 2 cm. However, for which algorithm the obtained relationship shows the best agreement strongly depends on the choice of the tie points. From the small differences between the results for gradient ratios and brightness temperatures it is concluded that both approaches are similarly suitable.

To obtain a consistent data product for both sensors only one sea ice concentration algorithm was selected. Since AMSR-2 is still operational, it can be expected that more reference snow depth data will be available for the evaluation of AMSR2 snow

depth data than of AMSR-E snow depth data. Therefore, more weight was given to the regressions for AMSR2 than those for AMSR-E for the final decision.

Here, for AMSR2 the lowest correlation coefficient of -0.80 with a RMSD of 5.72 cm was found for LEA for the gradient ratio of the 10.7 and 7.3 GHz channels. In general the RMSD and also the correlation coefficient show that the regressions for the gradient ratios of the lower frequency channels tend to have a lower RMSD and a higher anti-correlation. The only exception is the gradient ratio of the 7.3 and 6.7 GHz channels.

Because for the lower frequency channels the differences between the sea ice concentration algorithms are very small, theoretically all sea ice concentration algorithms can be used to set up a new snow depth algorithm and the final choice will depend on a careful choice and evaluation of the open water and sea ice tie points.

To keep the results comparable to the existing NASA snow depth product [Cavalieri et al., 2014] for the Arctic, currently the NASA Team algorithm and the vertical polarisation will be used. However, one can also easily change to another sea ice concentration algorithm or polarisation. Overall there are several possibilities to set up a new snow depth algorithm; however, due to the strong water vapour absorption in the 23.8 GHz channels and weather influences on the 89 GHz channels, all channel combinations including these channels were excluded. An overview of all remaining combinations can be found in Section 3.4.

3.2 Calculation of Open Water, First-Year and Multiyear Ice Tie Points

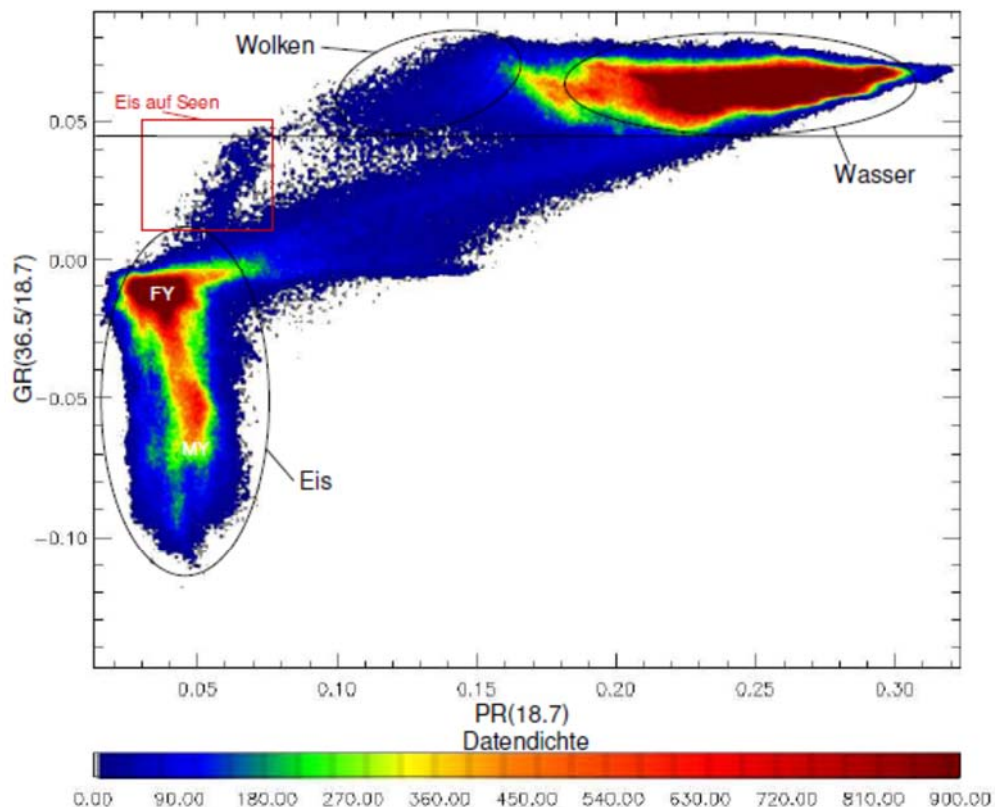


Figure 3-1: Scatterplot of the vertically polarised gradient ratio of the AMSR-E 18.7 and 36.5 GHz channels and the polarisation ratio of the 18.7

GHz channels. First-year ice, multiyear ice and open water areas are marked in the figure (Figure 3-3 in Spreen [2004]).

Table 3-1: Open water, first-year and multiyear ice tie points for AMSR-E

Frequency	Open Water		First-year Ice		Multiyear Ice	
	v-pol.	h-pol.	v-pol.	h-pol.	v-pol.	h-pol.
6.9 GHz	(160±2.1) K	(79±3.5) K	(252±6.3) K	(231±8.5) K	(249±5.0) K	(222±6.0) K
10.7 GHz	(166±2.3) K	(85±4.5) K	(251±6.8) K	(232±8.5) K	(243±6.0) K	(217±5.8) K
18.7 GHz	(185±3.6) K	(109±7.4) K	(251±7.4) K	(235±8.1) K	(230±8.1) K	(209±7.1) K
23.8 GHz	(202±7.4) K	(137±14) K	(250±7.6) K	(233±8.4) K	(221±9.2) K	(202±8.7) K
36.5 GHz	(212±4.5) K	(146±10) K	(245±8.1) K	(231±8.0) K	(202±9.4) K	(188±8.9) K
89.0 GHz	(249±7.1) K	(208±18) K	(230 ± 12) K	(219 ± 12) K	(194±10) K	(184 ± 10) K

Table 3-2: Open water, first-year and multiyear ice tie points for AMSR2

Frequency	Open Water		First-year Ice		Multiyear Ice	
	v-pol.	h-pol.	v-pol.	h-pol.	v-pol.	h-pol.
6.9 GHz	(162±2.1) K	(82±3.4) K	(259±3.7) K	(238±6.3) K	(252±2.5) K	(226±4.1) K
7.3 GHz	(163±2.1) K	(83±3.5) K	(260±3.8) K	(240±6.2) K	(252±2.6) K	(227±4.1) K
10.7 GHz	(171±2.3) K	(89±4.4) K	(260±3.9) K	(242±5.9) K	(248±3.3) K	(223±4.4) K
18.7 GHz	(190±3.7) K	(112±7.4) K	(260±4.5) K	(242±6.2) K	(234±5.3) K	(212±4.8) K
23.8 GHz	(206±7.3) K	(142±14) K	(259±5.1) K	(244±6.9) K	(225±6.5) K	(207±6.0) K
36.5 GHz	(215±4.6) K	(150±11) K	(254±6.3) K	(240±7.6) K	(206±6.8) K	(192±6.0) K
89.0 GHz	(249±7.1) K	(209±18) K	(239±14) K	(229±15) K	(203±11) K	(194±11) K

3.2.1 Open Water Tie Points

Open water tie points are calculated using Figure 3-1 (Figure 3-3in Spreen [2004]), a scatterplot between the gradient ratio of the 18.7 and 36.5 GHz channels and the polarisation ratio of the 18.7 GHz channels. Here, for the identification of open water areas only the polarisation ratio of the 18.7 GHz channels is used. According to the presented scatterplot, open water areas can be mainly found for polarisation ratios of 0.2 and higher. Thus this threshold is used to filter out possible cloud influences. Among the data points in the SIC0 dataset all brightness temperatures with associated polarisation ratio above (\geq) this threshold are used to determine the open water tie points. Furthermore, it was investigated how the tie points vary when the latitude boundary for the tie point calculation is increased. For this purpose the latitude above which (the border value is included in the calculation) the brightness temperatures are considered for the calculation of the open water tie points is increased in steps of 5° from 50°N to 75°N. For all tie points for which in the calculation values below 75°N are considered the calculated tie points show variations below 1 K, however, the tie points for the border value of 75°N can show variations of up to 5 K. Since for AMSR2 only a few hundred of over 10000 pixels remain it is questionable how representative these tie points are for open water. Because pixels further north are more likely to represent water close to the ice edge the boundary setting of 70°N was chosen to calculate the open water tie points. From the remaining data points the tie points and uncertainties are calculated by averaging the single values and calculating their standard deviation. Here, it has to be considered that the standard deviation rather represents variability instead of standard deviation. The tie points obtained for AMSR-E can be found in Table 3-1 and the tie points obtained for AMSR2 can be found in Table 3-2.

3.2.2 First-Year and Multiyear Ice Tie Points

Similar to the open water tie points the first-year and multiyear ice tie points are calculated using Figure 3-1 (Figure 3-3 in Spreen [2004]). First-year ice can be mainly found for gradient ratios between -0.02 and 0.00 with the polarizations ratio between 0.02 and 0.05. Similarly multiyear ice can be mainly found for gradient ratios between -0.075 and -0.05 with the polarization ratio between 0.045 and 0.055. Again from the data points in the SIC1 dataset all brightness temperatures with associated gradient and polarisation ratios within these borders are used for the calculation of the first-year and multiyear ice tie points. From these data points the tie points and uncertainties are then calculated by averaging the single values and calculating their standard deviation. Here, again, the standard deviation rather represents variability instead of standard deviation. The tie points obtained for AMSR-E can be found in Table 3-1 and the tie points obtained for AMSR2 can be found in Table 3-2.

3.3 Algorithm Description and Error Propagation

3.3.1 NASA Team Sea Ice Concentration Algorithm

The NASA Team algorithm is briefly described in Section 2.3.4. For the snow depth product an uncertainty estimate based on Gaussian error propagation will be provided. Here, the required framework is described.

In general the uncertainty following the Gaussian error propagation is given by

$$\sigma_f = \pm \sqrt{\sum_{i=1}^N \left(\frac{\partial f(\vec{x})}{\partial x_i} \sigma_{x_i} \right)^2}$$

where $f(\vec{x})$ is an arbitrary scalar function depending on the variables $\vec{x} = (x_1, \dots, x_i, \dots, x_N)$, σ_{x_i} is the statistical uncertainty of the variable x_i and N is the maximum number of variables occurring in $f(\vec{x})$.

In a first step in the NASA Team algorithm one defines twelve coefficients a_i, b_j with $i, j \in (0, 1, 2, 3, 4, 5)$:

$$a_0 = -T_{O18v} + T_{O18h}$$

$$a_1 = T_{O18v} + T_{O18h}$$

$$a_2 = T_{M18v} - T_{M18h} - T_{O18v} + T_{O18h}$$

$$a_3 = -T_{M18v} - T_{M18h} + T_{O18v} + T_{O18h}$$

$$a_4 = T_{F18v} - T_{F18h} - T_{O18v} + T_{O18h}$$

$$a_5 = -T_{F18v} - T_{F18h} + T_{O18v} + T_{O18h}$$

$$b_0 = -T_{O37v} + T_{O18v}$$

$$b_1 = T_{O37v} + T_{O18v}$$

$$b_2 = T_{M37v} - T_{M18v} - T_{O37v} + T_{O18v}$$

$$b_3 = -T_{M37v} - T_{M18v} + T_{O37v} + T_{O18v}$$

$$b_4 = T_{F37v} - T_{F18v} - T_{O37v} + T_{O18v}$$

$$b_5 = -T_{F37v} - T_{F18v} + T_{O37v} + T_{O18v}$$

Here, O stands for open water, M for multiyear ice and F for first-year ice, the numbers 18 and 37 stand for the AMSR-E/AMSR2 18.7 and 36.5 GHz channels, and v and h indicate vertical and horizontal polarisation, respectively.

If one now applies the Gaussian error propagation formula to these coefficients one obtains:

$$\sigma_{a_0} = \sigma_{a_1} = \pm \sqrt{\sigma_{T_{O18v}}^2 + \sigma_{T_{O18h}}^2}$$

$$\sigma_{a_2} = \sigma_{a_3} = \pm \sqrt{\sigma_{T_{M18v}}^2 + \sigma_{T_{M18h}}^2 + \sigma_{T_{O18v}}^2 + \sigma_{T_{O18h}}^2}$$

$$\sigma_{a_4} = \sigma_{a_5} = \pm \sqrt{\sigma_{T_{F18v}}^2 + \sigma_{T_{F18h}}^2 + \sigma_{T_{O18v}}^2 + \sigma_{T_{O18h}}^2}$$

$$\sigma_{b_0} = \sigma_{b_1} = \pm \sqrt{\sigma_{T_{O37v}}^2 + \sigma_{T_{O18v}}^2}$$

$$\sigma_{b_2} = \sigma_{b_3} = \pm \sqrt{\sigma_{T_{M37v}}^2 + \sigma_{T_{M18v}}^2 + \sigma_{T_{O37v}}^2 + \sigma_{T_{O18v}}^2}$$

$$\sigma_{b_4} = \sigma_{b_5} = \pm \sqrt{\sigma_{T_{F37v}}^2 + \sigma_{T_{F18v}}^2 + \sigma_{T_{O37v}}^2 + \sigma_{T_{O18v}}^2}$$

In the next step the polarization ratio of the 18.7 GHz channels and the gradient ratio of the vertically polarised channels at 18.7 and 36.5 GHz channels are calculated

$$GR = \frac{T_{37v} - T_{18v}}{T_{37v} + T_{18v}},$$

$$PR = \frac{T_{18v} - T_{18h}}{T_{18v} + T_{18h}}.$$

Applying the Gaussian error propagation gives:

$$\sigma_{GR} = \pm 2 \sqrt{\frac{T_{18v}^2 \sigma_{T_{37v}}^2 + T_{37v}^2 \sigma_{T_{18v}}^2}{(T_{37v} + T_{18v})^4}}$$

$$\sigma_{PR} = \pm 2 \sqrt{\frac{T_{18h}^2 \sigma_{T_{18v}}^2 + T_{18v}^2 \sigma_{T_{18h}}^2}{(T_{18v} + T_{18h})^4}}$$

In the next step from the twelve coefficients a_i , b_j twelve coefficients, four for open water (d_k), four for first-year ice (f_l) and four for multiyear ice (m_n) with $k, l, n \in (0,1,2,3)$, are derived:

$$d_0 = -a_2 b_4 + a_4 b_2$$

$$d_1 = -a_3b_4 + a_5b_2$$

$$d_2 = -a_2b_5 + a_4b_3$$

$$d_3 = -a_3b_5 + a_5b_3$$

$$f_0 = a_0b_2 - a_2b_0$$

$$f_1 = a_1b_2 - a_3b_0$$

$$f_2 = a_0b_3 - a_2b_1$$

$$f_3 = a_1b_3 - a_3b_1$$

$$m_0 = -a_0b_4 + a_4b_0$$

$$m_1 = -a_1b_4 + a_5b_0$$

$$m_2 = -a_0b_5 + a_4b_1$$

$$m_3 = -a_1b_5 + a_5b_1$$

The uncertainties of these coefficients are given by:

$$\sigma_{d_0} = \pm \sqrt{b_4^2 \sigma_{a_2}^2 + a_2^2 \sigma_{b_4}^2 + b_2^2 \sigma_{a_4}^2 + a_4^2 \sigma_{b_2}^2}$$

$$\sigma_{d_1} = \pm \sqrt{b_4^2 \sigma_{a_3}^2 + a_3^2 \sigma_{b_4}^2 + b_2^2 \sigma_{a_5}^2 + a_5^2 \sigma_{b_2}^2}$$

$$\sigma_{d_2} = \pm \sqrt{b_5^2 \sigma_{a_2}^2 + a_2^2 \sigma_{b_5}^2 + b_3^2 \sigma_{a_4}^2 + a_4^2 \sigma_{b_3}^2}$$

$$\sigma_{d_3} = \pm \sqrt{b_5^2 \sigma_{a_3}^2 + a_3^2 \sigma_{b_5}^2 + b_3^2 \sigma_{a_5}^2 + a_5^2 \sigma_{b_3}^2}$$

$$\sigma_{f_0} = \pm \sqrt{b_2^2 \sigma_{a_0}^2 + a_0^2 \sigma_{b_2}^2 + b_0^2 \sigma_{a_2}^2 + a_2^2 \sigma_{b_0}^2}$$

$$\sigma_{f_1} = \pm \sqrt{b_2^2 \sigma_{a_1}^2 + a_1^2 \sigma_{b_2}^2 + b_0^2 \sigma_{a_3}^2 + a_3^2 \sigma_{b_0}^2}$$

$$\sigma_{f_2} = \pm \sqrt{b_3^2 \sigma_{a_0}^2 + a_0^2 \sigma_{b_3}^2 + b_1^2 \sigma_{a_2}^2 + a_2^2 \sigma_{b_1}^2}$$

$$\sigma_{f_3} = \pm \sqrt{b_3^2 \sigma_{a_1}^2 + a_1^2 \sigma_{b_3}^2 + b_1^2 \sigma_{a_3}^2 + a_3^2 \sigma_{b_1}^2}$$

$$\sigma_{m_0} = \pm \sqrt{b_4^2 \sigma_{a_0}^2 + a_0^2 \sigma_{b_4}^2 + b_0^2 \sigma_{a_4}^2 + a_4^2 \sigma_{b_0}^2}$$

$$\sigma_{m_1} = \pm \sqrt{b_4^2 \sigma_{a_1}^2 + a_1^2 \sigma_{b_4}^2 + b_0^2 \sigma_{a_5}^2 + a_5^2 \sigma_{b_0}^2}$$

$$\sigma_{m_2} = \pm \sqrt{b_5^2 \sigma_{a_0}^2 + a_0^2 \sigma_{b_5}^2 + b_1^2 \sigma_{a_4}^2 + a_4^2 \sigma_{b_1}^2}$$

$$\sigma_{m_3} = \pm \sqrt{b_5^2 \sigma_{a_1}^2 + a_1^2 \sigma_{b_5}^2 + b_1^2 \sigma_{a_5}^2 + a_5^2 \sigma_{b_1}^2}$$

Furthermore, one obtains from the first four coefficients the quantity

$$d_d = d_0 + d_1 PR + d_2 GR + d_3 PRGR$$

and its uncertainty

$$\sigma_{d_d} = \pm \sqrt{\sigma_{d_0}^2 + PR^2 \sigma_{d_1}^2 + (d_1 + d_3 GR)^2 \sigma_{PR}^2 + GR^2 \sigma_{d_2}^2 + (d_2 + d_3 PR)^2 \sigma_{GR}^2 + GR^2 PR^2 \sigma_{d_3}^2}.$$

Now using the gradient ratio and the polarisation ratio from the first four coefficients, the first-year ice concentration and from the second four coefficients the multiyear ice concentration is derived:

$$c_f = \frac{f_0 + f_1 PR + f_2 GR + f_3 PRGR}{d_d}$$

$$c_m = \frac{m_0 + m_1 PR + m_2 GR + m_3 PRGR}{d_d}$$

The uncertainties of the first-year and multiyear ice concentration are then given by:

$$\sigma_{c_f} = \pm \sqrt{\frac{d_d^2 (\sigma_{f_0}^2 + PR^2 \sigma_{f_1}^2 + (f_1 + f_3 GR)^2 \sigma_{PR}^2 + GR^2 \sigma_{f_2}^2 + (f_2 + f_3 PR)^2 \sigma_{GR}^2 + PR^2 GR^2 \sigma_{f_3}^2) + (f_0 + f_1 PR + f_2 GR + f_3 PRGR)^2 \sigma_{d_d}^2}{d_d^4}}$$

$$\sigma_{c_m} = \pm \sqrt{\frac{d_d^2 (\sigma_{m_0}^2 + PR^2 \sigma_{m_1}^2 + (m_1 + m_3 GR)^2 \sigma_{PR}^2 + GR^2 \sigma_{m_2}^2 + (m_2 + m_3 PR)^2 \sigma_{GR}^2 + PR^2 GR^2 \sigma_{m_3}^2) + (m_0 + m_1 PR + m_2 GR + m_3 PRGR)^2 \sigma_{d_d}^2}{d_d^4}}$$

Finally from the first-year and the multiyear ice concentrations the total ice concentration and its uncertainty are derived:

$$c_t = c_f + c_m$$

$$\sigma_{c_t} = \pm \sqrt{\sigma_{c_f}^2 + \sigma_{c_m}^2}$$

3.3.2 Snow Depth Algorithm

3.3.2.1 Basic Algorithm

This section will shortly introduce the theoretical basics of the snow depth retrieval algorithm for AMSR-E and AMSR2. The algorithm itself is similar to the original algorithm of Markus and Cavalieri [1998]. It is based on a linear relationship between the open water corrected gradient ratio

$$GR_{p,ice} = \frac{T_B(\nu_1, p) - T_B(\nu_2, p) - k_1(1 - C_{ice})}{T_B(\nu_1, p) + T_B(\nu_2, p) - k_2(1 - C_{ice})}$$

and snow depth. Here $T_B(\nu_1, p)$ and $T_B(\nu_2, p)$ are the vertically polarised brightness temperatures at frequencies ν_1 and ν_2 ($\nu_1 > \nu_2$), respectively, C_{ice} is the sea ice concentration for the given grid cell (here from NASA Team), and k_1 and k_2 are

constants derived from the vertically polarised brightness temperatures of open water at frequencies ν_1 and ν_2 ($T_{B,OW}(\nu_1, p)$ and $T_{B,OW}(\nu_2, p)$):

$$k_1 = T_{B,OW}(\nu_1, p) - T_{B,OW}(\nu_2, p)$$

$$k_2 = T_{B,OW}(\nu_1, p) + T_{B,OW}(\nu_2, p)$$

Markus and Cavalieri [1998] used a linear regression between the calculated SSM/I gradient ratios and in-situ and ship-based snow depth observations to obtain an empirical relationship for the retrieval of snow depth on sea ice. Here also a multilinear approach was tested. This comparison showed that the improvement is only of the order of a few mm, which does not outweigh the additionally introduced uncertainty. Thus as for the original algorithm an empirical relation given by

$$S = a + bGR_{p,ice}$$

is used. Here a and b are constants derived from a linear regression.

3.3.2.2 Error Propagation

The error propagation of the gradient ratio and the snow depth is straight forward and, although the terms of the single components are quite complex, easy to derive. Since the uncertainties provided in Section 4.2 and 4.3.1 are all originating from some kind of statistical analysis, only the Gaussian error propagation will be derived here. Applying the error propagation to the analytic expression of the snow depth gives for the Gaussian error:

$$\sigma_S = \pm \sqrt{(\sigma_a)^2 + (GR_{V,ice}\sigma_b)^2 + (b\sigma_{GR_{ice}^V})^2}$$

Here, $\sigma_{GR_{V,ice}}$ is composed of five terms: $\sigma_{T_B(\nu_1,p)}$, $\sigma_{T_B(\nu_2,p)}$, $\sigma_{C_{ice}}$, σ_{k_1} , and σ_{k_2} as well as the variables themselves. Since σ_{k_1} and σ_{k_2} contain only additive terms and due to the square the minus in the derivative of k_1 can be neglected, they can both be calculated using the same equation:

$$\sigma_{k_1} = \sigma_{k_2} = \pm \sqrt{(\sigma_{T_B,OW}(\nu_1,p))^2 + (\sigma_{T_B,OW}(\nu_2,p))^2}$$

Thus the Gaussian error of $\sigma_{GR_{V,ice}}$ is given by:

$$\sigma_{GR_{ice}^V} = \pm \sqrt{(G1\sigma_{T_B(\nu_1,p)})^2 + (G2\sigma_{T_B(\nu_2,p)})^2 + (G3\sigma_{C_{ice}})^2 + (G4\sigma_{k_1})^2 + (G5\sigma_{k_2})^2}$$

where the terms G_i ($i = 1, 2, 3, 4, 5$) are given by

$$G1 = \frac{(k_1 + k_2)(1 - C_{ice}) - 2T_B(\nu_1, p)}{(T_B(\nu_1, p) + T_B(\nu_2, p) - k_2(1 - C_{ice}))^2}$$

$$G2 = \frac{(k_1 - k_2)(1 - C_{ice}) + 2T_B(\nu_2, p)}{(T_B(\nu_1, p) + T_B(\nu_2, p) - k_2(1 - C_{ice}))^2}$$

$$G3 = \frac{(k_1 - k_2)T_B(\nu_1, p) + (k_1 + k_2)T_B(\nu_2, p)}{(T_B(\nu_1, p) + T_B(\nu_2, p) - k_2(1 - C_{ice}))^2}$$

$$G4 = \frac{C_{ice} - 1}{T_B(v_1, p) + T_B(v_2, p) - k_2(1 - C_{ice})}$$

$$G5 = \frac{(T_B(v_1, p) - T_B(v_2, p) - k_1(1 - C_{ice}))(1 - C_{ice})}{(T_B(v_1, p) + T_B(v_2, p) - k_2(1 - C_{ice}))^2}$$

The uncertainty of the gradient ratio can then be used to derive the uncertainty of the retrieved snow depth.

3.3.2.3 Coefficients for the Arctic

Usually sea ice concentration has the strongest influence on the uncertainty of the retrieved snow depth. Thus to derive regression coefficients for the Arctic only pixels with sea ice concentrations $\geq 95\%$ were considered. Above this threshold the deviation from 100% retrieved sea ice concentration can also be caused by variations in sea ice emissivity. However, one cannot distinguish these two influences. Therefore, in the setup of the snow depth algorithm it is assumed that these variations are caused by variations of sea ice emissivity alone. Although this has the advantage of simplifying the calculation of the gradient ratio, it has the disadvantage that the uncertainty introduced in the gradient ratio by the variability of the emissivity and by the uncertainty of the retrieved sea ice concentration cannot be appropriately quantified. As a consequence in the setup of the snow depth algorithm uncertainties will not be considered. However, the uncertainties introduced by the emissivity and the sea ice concentration will have a strong influence on the reliability of the obtained snow depth algorithm.

In the following, AMSR-E and AMSR2 are considered separately although for both satellites the same procedure is used. As input for the setup of the new snow depth algorithm snow depth averages from Operation IceBridge (OIB) flights from the NERSC RRDp were used. The OIB flights in the Arctic are usually conducted in March and April each year. In this work data from flights between 2009 and 2011 are used for AMSR-E and data from flights between 2012 and 2014 are used for AMSR2.

Both datasets were split into two equally strong sub-datasets. The dataset was split such that the first sub-dataset contains the first and then every second data pair. The second sub-dataset contains all remaining data pairs. Here, the regression procedure was performed such that both sub-datasets were used as training dataset and as reference dataset by first using one sub-dataset as training dataset and the other as reference dataset and vice versa. Note that for each sub-dataset the RMSD was always calculated for the reference dataset. The regression results show that for AMSR2 all combinations of the channels ≤ 36.5 GHz can be used, while the choice of the single channels should be restricted to channels ≤ 18.7 GHz for AMSR-E. The only exception is the combination of the 7.3 and 6.7 GHz channels, which in comparison to all other combinations of the lower frequency channels has a higher RMSD and a lower anti-correlation. Furthermore, due to the strong influence of water vapour on the 23.8 GHz channels and weather effects on the 89 GHz channels, channel combinations including these channels are excluded as viable candidates.

Although the regression line usually shows the highest anti-correlation and lowest RMSD for the gradient ratio of the 6.9 (for AMSR2 also 7.3 GHz) and 10.7 GHz channels, the data pairs only show a small variation with changing gradient ratio. As a consequence even for high sea ice concentrations the uncertainty of the gradient ratio introduced by the variability of sea ice emissivity and the uncertainty of the sea ice covered area will likely result in an uncertainty of the gradient ratio that is larger than the range of values found for the gradient ratio. Therefore, this channel

combination is not used for the snow depth algorithm as well, so that only the combinations listed in Table 3-3 remain.

Table 3-3: List of possible channel combinations for the new snow depth algorithm. The numbers 1 and 2 refer to the regressions for sub-datasets 1 and 2, respectively. Note that RMSD 1 refers to the comparison with sub-dataset 2 and vice versa.

Satellite	Chan. Comb.	RMSD 1	R 1	RMSD 2	R 2
AMSR-E	18.7 GHz/6.9 GHz	6.97 cm	-0.62	6.12 cm	-0.57
AMSR-E	18.7 GHz/10.7 GHz	7.17 cm	-0.58	6.30 cm	-0.53
AMSR2	18.7 GHz/6.9 GHz	6.24 cm	-0.74	5.92 cm	-0.72
AMSR2	18.7 GHz/7.3 GHz	6.25 cm	-0.74	5.92 cm	-0.72
AMSR2	18.7 GHz/10.7 GHz	6.39 cm	-0.73	6.05 cm	-0.70
AMSR2	36.5 GHz/6.9 GHz	6.52 cm	-0.72	6.17 cm	-0.69
AMSR2	36.5 GHz/7.3 GHz	6.52 cm	-0.72	6.18 cm	-0.69
AMSR2	36.5 GHz/10.7 GHz	6.61 cm	-0.71	6.27 cm	-0.67
AMSR2	36.5 GHz/18.7 GHz	6.80 cm	-0.68	6.46 cm	-0.65

For AMSR-E for both channel combinations the correlation coefficients ($\Delta R \leq 0.05$) and the RMSD ($\Delta \text{RMSD} \leq 0.2$ cm) show only minimal differences for each sub-dataset so that in theory both channel combinations can be used. Here, the RMSD of the first sub-dataset is about 1 cm higher than the RMSD of the second sub-dataset. However, for the first sub-dataset also the correlation coefficient is lower than for the second sub-dataset. Since a lower correlation coefficient may indicate that besides an offset the overall agreement between retrieved snow depth and reference value is higher the correlation coefficient is given more weight for the decision which channel combination will be used. Since the correlation coefficient for the gradient ratio of the 18.7 and the 6.9 GHz channels from the first sub-dataset indicates a higher anti-correlation this gradient ratio is used to set up the new algorithm for AMSR-E.

Also for AMSR2 the correlation coefficients ($\Delta R \leq 0.07$) and the RMSD ($\Delta \text{RMSD} \leq 0.6$ cm) show only small differences for each sub-dataset so that again all these channel combinations may be used. Again the correlation coefficients for the gradient ratios of the first sub-dataset are lower while the RMSD is slightly higher. However, for AMSR2 the difference in RMSD is even smaller than for AMSR-E. Thus also here the gradient ratios from the first sub-dataset are used to set up the new snow depth algorithm for AMSR2. Since for AMSR-E the gradient ratio of the 6.9 and 18.7 GHz channels is used to set up a new snow depth retrieval algorithm this channel combination is also used for AMSR2 to assure consistency between both data products.

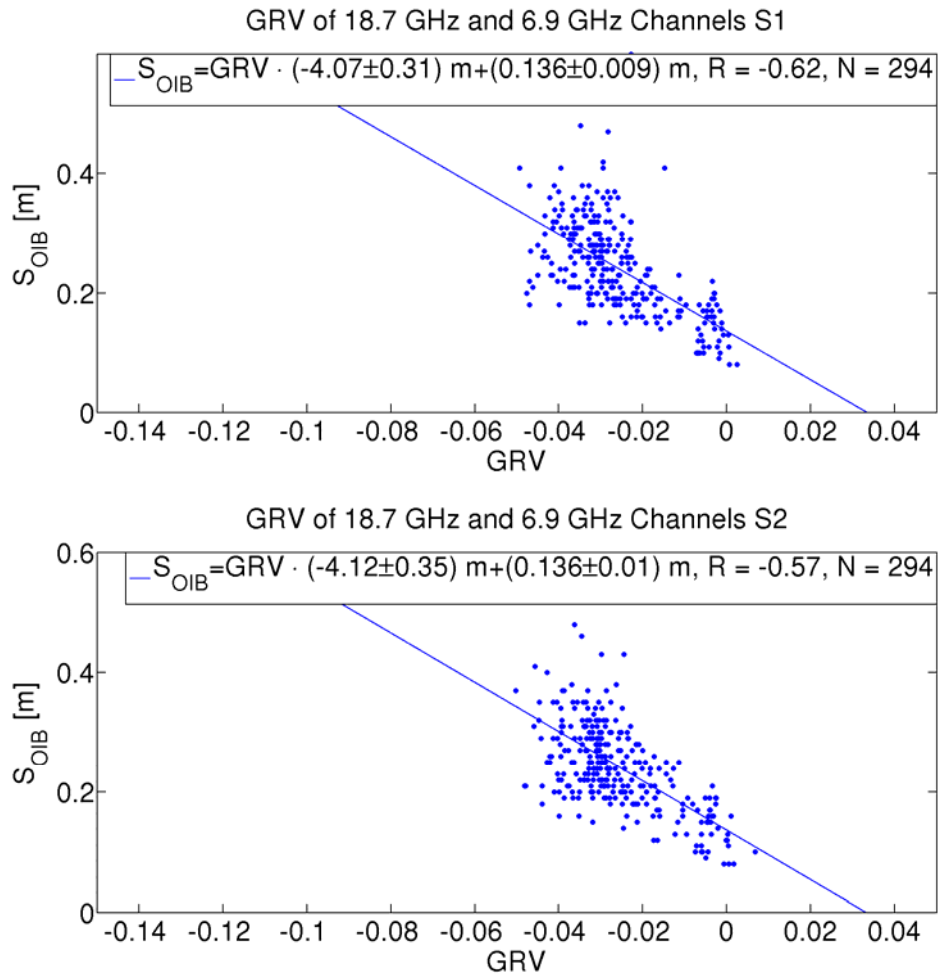


Figure 3-2: Linear regression between OIB snow depth and the gradient ratio of the vertically polarised brightness temperatures of AMSR-E 18.7 and 6.9 GHz channels. S1 and S2 indicate sub-dataset 1 and sub-dataset 2.

The relations between the selected gradient ratios are shown in Figure 3-2 and Figure 3-3 and the regression coefficients, the correlation coefficients, RMSDs as well as the number of data pairs included in every comparison are listed in Table 3-4.

Table 3-4: Slope, intercept, RMSD, correlation coefficient R and number of data pairs N, for both sub-datasets of the gradient ratios of the channels selected for the new snow depth retrieval algorithm. Note that for sub-dataset 1 RMSD refers to the comparison with sub-dataset 2 and vice versa.

Satellite	Chan. Comb.	Sub-dataset	Slope [m]	Intercept [m]	RMSD	R	N
AMSR-E	18.7/6.9	1	-4.07±0.31	0.136±0.009	6.97 cm	-0.62	294
ASMR-E	18.7/6.9	2	-4.12±0.35	0.136±0.010	6.12 cm	-0.57	294
AMSR2	18.7/6.9	1	-3.91±0.19	0.135±0.005	6.24 cm	-0.74	359
AMSR2	18.7/6.9	2	-3.82±0.20	0.139±0.005	5.92 cm	-0.72	358

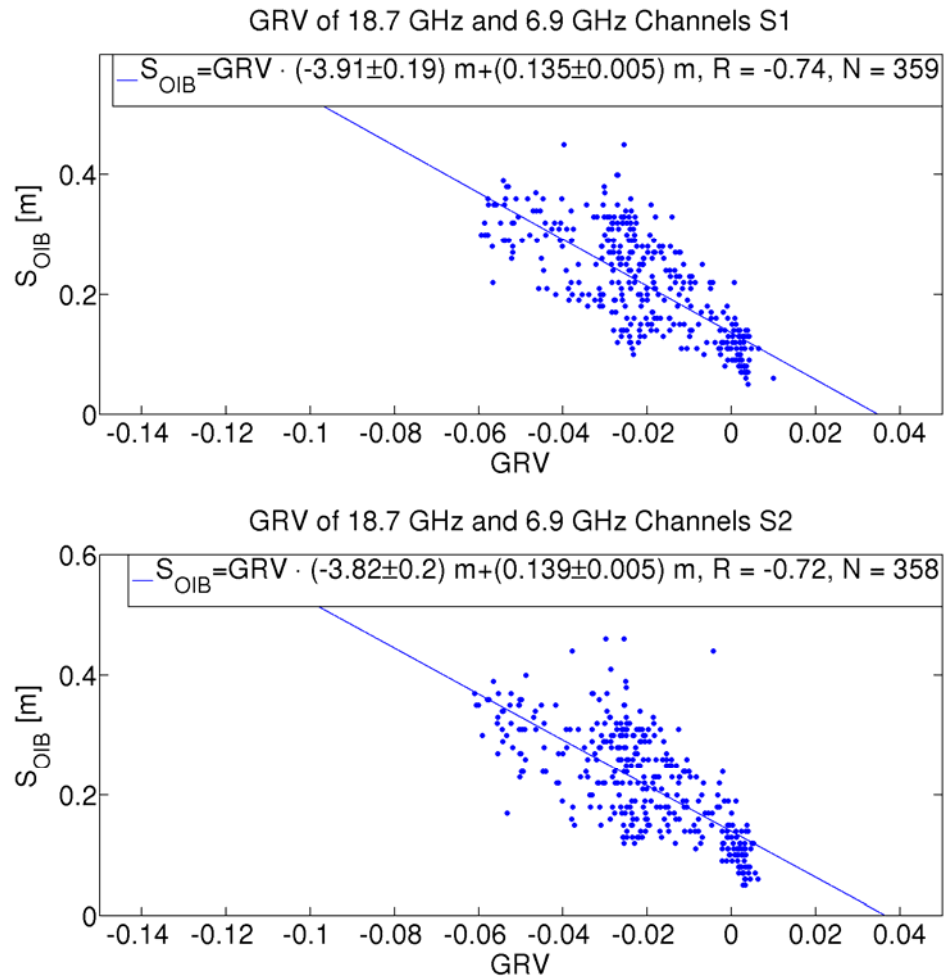


Figure 3-3: Linear regression between OIB snow depth and the gradient ratio of the vertically polarised brightness temperatures of AMSR2 18.7 and 6.9 GHz channels. S1 and S2 indicate sub-dataset 1 and sub-dataset 2.

3.4 Problems

Open water, first-year ice and multiyear ice tie points are difficult to determine and can have a strong influence on the retrieved snow depth. For the tie points currently used in the snow depth retrieval theoretically all six tested sea ice concentration algorithms and both polarisations could be used. To maintain comparability with the existing NASA snow depth product the NASA Team algorithm is used. However, the calculated tie points are just estimated based on information from one day [Spren, 2004] and thus for future snow depth algorithms a thorough tie point calculation with uncertainty estimation is needed.

GRV of 18.7 GHz and 6.9 GHz Channels

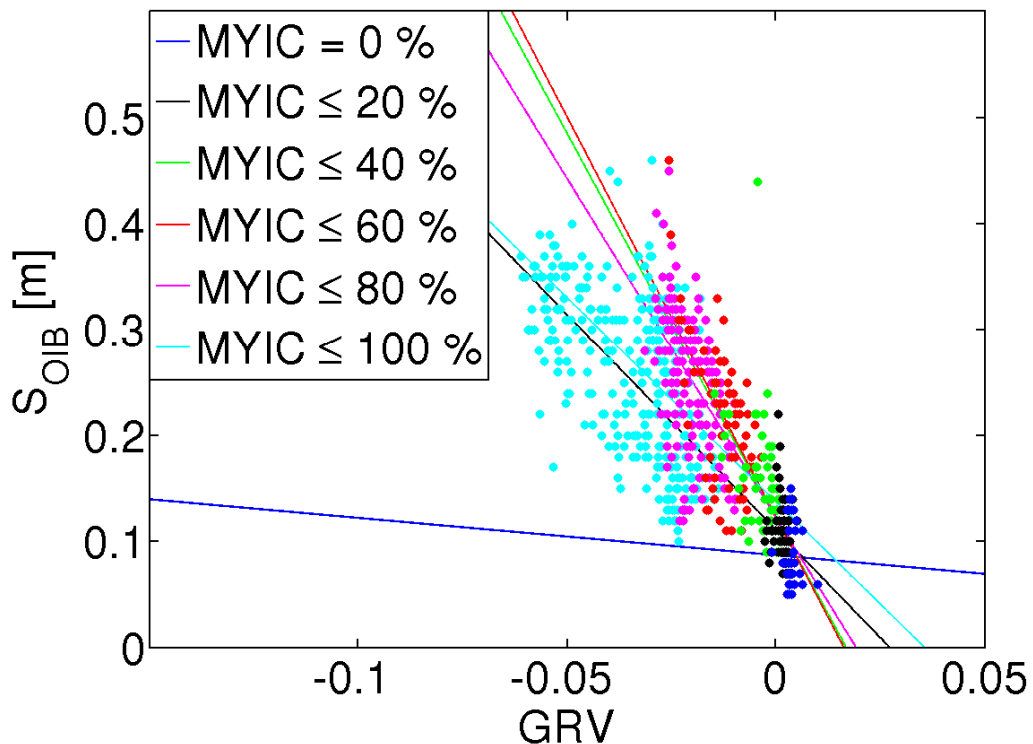


Figure 3-4: Linear regression between OIB snow depth and the gradient ratio of the vertically polarised brightness temperatures of AMSR2 18.7 and 6.9 GHz channels. The colours indicate the upper boundary of the determined NASA Team multiyear ice concentration.

Furthermore, it is known that with increasing snow depth the gradient ratio of the 36.5 and 18.7 GHz channels becomes similar to the gradient ratio of multiyear ice. Since contrary to the Antarctic in the Arctic larger areas are covered by multiyear ice, it was investigated, how the multiyear ice concentration changes for the calculated gradient ratio. For this purpose multiyear ice concentration was calculated using the NASA Team algorithm and added as additional information in the regression plots. An example for such a plot is shown in Figure 3-4 for the gradient ratio of the 18.7 and 6.9 GHz channels. In the plot the colours indicate all values below a certain multiyear ice concentration limit. In Figure 3-4 all data pairs with multiyear ice concentrations below the next lower limit are overlaid with dots with the corresponding colour. One can see that with decreasing gradient ratio the multiyear ice concentration increases.

To investigate if one can use surface roughness to distinguish multiyear and first-year ice the surface roughness from the NERSC RRDP dataset is plotted against the calculated gradient ratio. This is shown in Figure 3-5. The figure shows that surface roughness increases with decreasing gradient ratio and thus it cannot be used to distinguish snow on multiyear ice and snow on first-year ice. The reason is that thick snow on rough first-year ice radiometrically looks like multiyear ice. All three points mentioned above are open questions for further studies.

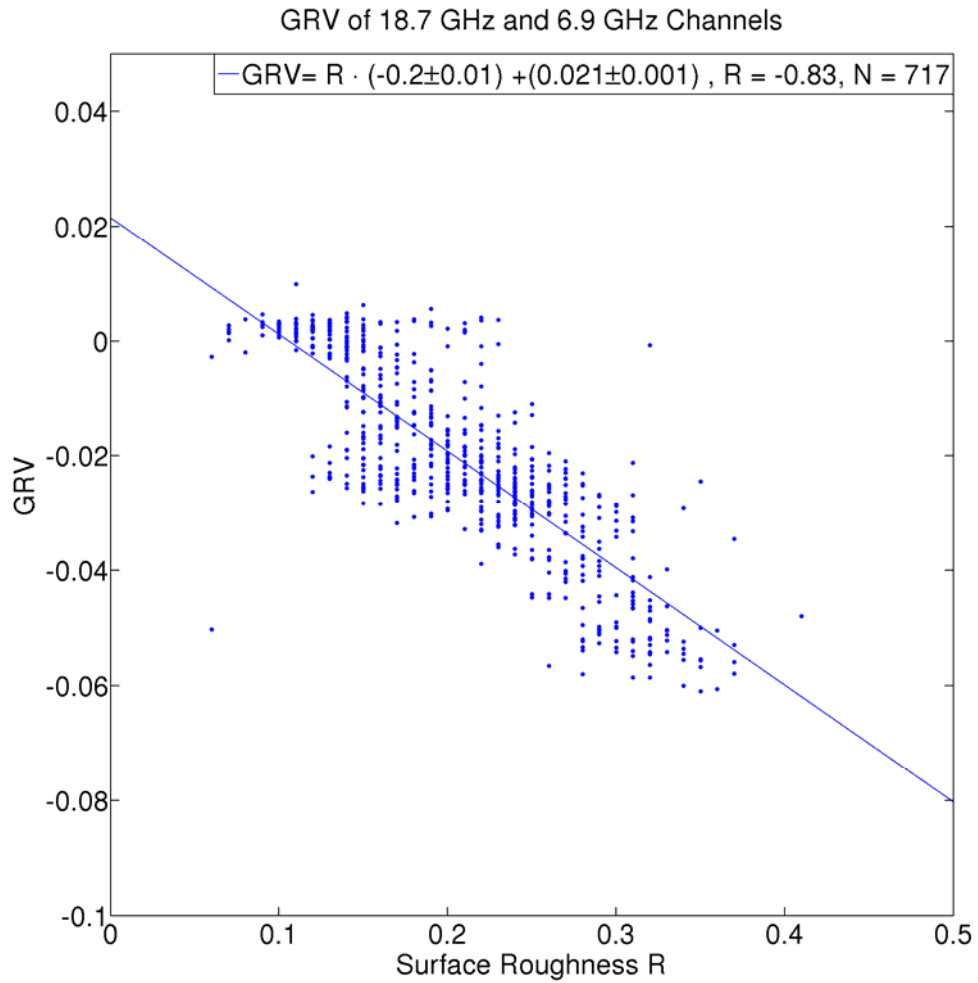


Figure 3-5: Linear regression between gradient ratio of the vertically polarised brightness temperatures of AMSR2 18.7 and 6.9 GHz channels and surface roughness from the SICCI NERSC RRDP dataset.

4 Sea Ice Type

4.1 Background

Within phase 1 of the ESA CCI sea ice ECV (ESA SICCI) project, multiyear ice (MYI) fraction was needed for the sea ice thickness (SIT) retrieval to use correct values of the sea ice density for the conversion of radar freeboard to SIT. One shortcoming of phase 1's work was that the currently available scatterometer data (QuikSCAT, OceanSAT-2, and ASCAT) do not provide a continuous, inter-sensor calibrated MYI fraction for the Arctic Ocean. Attempts to do so are under way with ESA SICCI phase 2, however.

In addition, a time series of MYI fraction derived from the above-mentioned satellites would start in 1999 and end today. For the years prior to 1999, i.e. the period 1993 to 1999 which is required to compute SIT from ERS1/2 radar altimetry, another scatterometer sensor, the one which was operated from aboard ERS1/2, would be needed which would add another source of inconsistency.

As an alternative solution one could derive the MYI SIC from passive microwave brightness temperature (TB) observations as, e.g., provided by SMMR, SSM/I and SSM/IS sensors. MYI SIC is part of the NASA-Team sea ice concentration algorithm. This algorithm employs the TB gradient ratio at 37 GHz and 19 GHz, both vertical polarization: GR3719; this ratio is sensitive to the MYI SIC.

This method has been used to derive MYI SIC and the resulting MYI SIC and MYI areas have been investigated [e.g. Johannessen and Miles, 2000]. One of the peculiarities arising when using fixed tie points to derive the MYI SIC is that MYI area in the Arctic Ocean seems to increase during the course of the freezing season – as can be seen in the above-mentioned paper. This seems to be unreasonable because per definition MYI is all the sea ice which has survived the summer melt season; accordingly, the sea ice cover around the minimum (September) sea ice area or extent is supposed to become the maximum MYI area for the following freezing season. No MYI is generated during the freezing season. Rather MYI is exported out of the Arctic Ocean into the Greenland Sea through Fram Strait and through other openings. Therefore one can rather expect the MYI area to decrease over time during the freezing season as is demonstrated e.g. in a recent paper where QuikSCAT and OceanSAT-2 scatterometer data are used to derive MYI area [Lindell and Long, 2016] and in a number of previous papers where the MYI area is retrieved from scatterometer data [e.g. Kwok, 2004; Swan and Long, 2012; Kwok and Cunningham, 2015].

Comiso [2012] published work about the temporal evolution of the Arctic MYI area based on passive microwave data for the period 1979 to 2011. In contrast to the results of Johannessen and Miles [2000] which are based on fixed MYI SIC tie points, Comiso [2012] used a set of monthly varying tie points to account for the intra-winter variation of the MYI TB signature. Consequently, the MYI area estimates shown in Comiso [2012] rarely exhibit an increase during winter but merely tend to have a decreasing trend. Comiso [2012] derived the MYI SIC tie points by taking the TB cluster describing 100% sea ice, plotting these as a frequency distribution and by using the TBs of 1/10 of the tail of the resulting histogram which ends on the MYI side to compute MYI tie points on monthly temporal scale.

Here we adopt a similar approach to the NASA-Team algorithm.

4.2 Data

We use daily gridded SSM/I – SSM/IS brightness temperatures (TB) provided by NSIDC as version 02 and version 04 data set [Maslanik and Stroeve, 2004, updated 2012 and 2015].

According to Walt Meier, GSFC, personal communication 28-10-2015, the following can be said about this data: "These TBs are from Remote Sensing Systems, Inc. (RSS, <http://www.remss.com>). The source swath TBs are inter-calibrated across sensors using a radiative transfer model to optimize consistency of ocean parameter retrievals. In other words, there is no baseline sensor - the model is the baseline. Details are here: <http://www.remss.com/measurements/brightness-temperature>.

There are also a couple peer-reviewed journal articles that describe the process. Note that this info describes Version 7. NSIDC has not yet updated all TBs to Version 7, though they are in the process of doing so."

And:

"The NSIDC TBs are gridded daily averages and are in the polar regions (RSS is optimized primarily for tropical and mid-latitude oceans), so further calibration has generally been done on the gridded fields, using simple linear regression for each channel. Here is the reference for the inter calibration between F17 SSMIS and F13 SSMI

Cavalieri, D. J., Parkinson, C. L., DiGirolamo, N. and A. Ivanoff. 2011. Intersensor Calibration between F13 SSMI and F17 SSMIS for Global Sea Ice Data Records. *IEEE Geoscience and Remote Sensing Letters*, 9(2), 233-236, doi: 10.1109/LGRS.2011.2166754.

This paper (I believe) discusses the inter-calibration of earlier sensors (primarily for the sea ice concentration product):

Cavalieri, D. J., C. I. Parkinson, P. Gloersen, J. C. Comiso, and H. J. Zwally. 1999. Deriving Long-term Time Series of Sea Ice Cover from Satellite Passive-Microwave Multisensor Data Sets. *Journal of Geophysical Research* 104(7): 15,803-15,814."

After asking back whether the inter-calibration mentioned in the recommended papers has been included in the TB data set I got the following answer (Walt Meier, GSFC, personal communication, 28-10-2015):

"Actually, no - the corrections in the Cavalieri/Parkinson paper are not in the TB fields. They are

applied within the NASA Team sea ice algorithm. The NSIDC approach has been to provide the TBs from RSS "as is" - just gridded - and allow users to apply any corrections they feel are needed."

Note that there is another paper [Meier et al., 2011] which deals with inter-sensor calibration between F13 and F17, however, here near-real-time data were used which presumably differ from those in the used TB data set.

The conclusion from this is that, if we wish to have a consistent MYI SIC and MYI area data set, we need to carry out an inter-sensor calibration by ourselves – which we will do as described below.

From the papers of Ivanova et al. [2014] and Ivanova et al. [2015] another issue needs to be taken into account. Those papers clearly revealed that it does make a difference from which data set the tie points which are used to compute the SIC are derived. The recommendation from these papers hence clearly is: derive the tie points from the same data set from which you are also computing any sea ice parameter with these tie points.

Consequently, we will derive tie points from the same TB data set used.

4.3 Methods

4.3.1 Inter-sensor calibration

The NSIDC TB data set is – for the period 1993-2014 which is used here – based on TB measured by SSM/I and SSM/IS on DMSP-F11, F13, and F17. TB data from F11 and F13 or F13 and F17 are read. Three regions covered predominantly by MYI (the main target of this study) are defined. Each of these regions covers 16 x 16 grid cells with 25 km grid cell size, i.e. an area of 400 km x 400 km. The daily gridded TB data of the overlap periods are extracted for each region. They are checked for quality and only those data are used where ASI sea ice concentration is above or equal to 95%.

Histograms and scatterplots of the TBs of both DMSP spacecraft are plotted for the channels relevant for the MYI SIC computation. Note that we shortened the overlap period between F13 and F17 to the same length (151 days) of the F11 to F13 overlap period to have a similar number of days for the inter-comparison of TBs from sensors of the different DMSP spacecraft. For each region and frequency a linear regression analysis is carried out once. From the resulting regression parameters the mean absolute difference between TB and the regression line and its standard deviation is computed. By excluding TB data pairs with a distance to the regression line above 3 times the standard deviation the linear regression analysis is repeated a second time. The resulting regression parameters (slope, intercept, correlation) are averaged for the three regions and saved; the total number of data pairs for each type is as well saved.

MYI regions were chosen because these are the main target of the study. The radiometric signal might however still be too variable to allow a proper inter-sensor calibration. Therefore, as an alternative, one region of the same size located on the summit of the Greenland Ice Sheet close to the NEEM site was selected – assuming that the presence of freezing conditions year round could provide a higher-quality set of coefficients for the inter-sensor calibration than the one obtained for MYI. The same analysis as described above was carried out – except that it is based on just one region and that there are no data discarded due to sea ice concentrations falling below a threshold. The location of the regions is shown in Figure 4-1.

Figures 2 to 7 show the TB of ASI SIC > 95% of the MYI-regions for the overlap periods used. TB at 19 GHz, 22 GHz and 37 GHz are shown in separate figures. The first three are for DMSP f11 to f13, the latter three are for DMSP f13 to f17. Note that even though these are MYI regions and hence supposed to show stable TB distribution, the fact that our overlap period covers the summer melt period (f11 to f13 is May to September) causes quite variable TB because we encounter melting conditions on the sea ice. Therefore TB at, e.g. 19 GHz, horizontal polarization, may have a substantial contribution of signatures arising from melt water on the sea ice (e.g. the red symbols and curves in Figure 4-2). It has been cross-checked whether this data is indeed associated with SIC > 95%. Yes, it is.

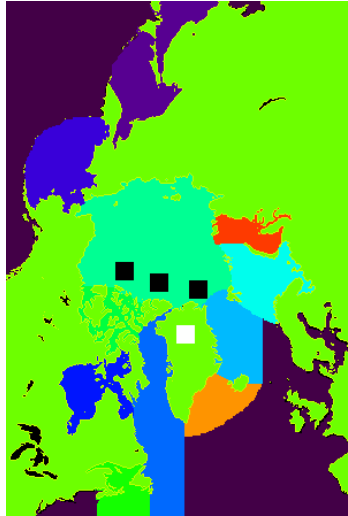


Figure 4-1: Map of the Arctic sectors used in this study. Turquoise are regions 8 and 9 used to derive the MYI area and the MYI tie points. Orange, medium, light and dark blue counted counterclockwise from the orange region are the sectors used to derive the open water tie points. Black boxes denote the locations of the MYI regions used for the inter-sensor calibration; the white box denotes the corresponding location on the Greenland ice sheet.

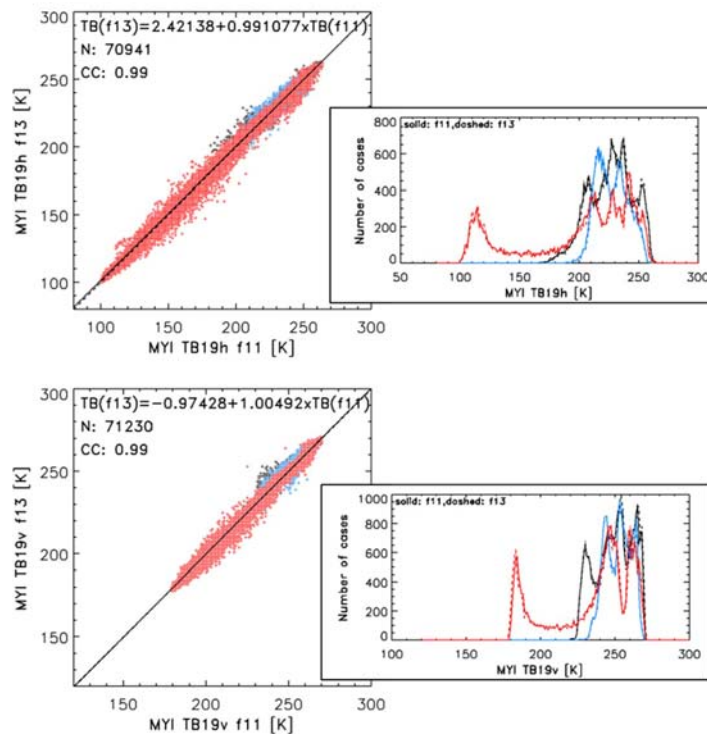


Figure 4-2: Inter-comparison of MYI-region TB from DMSP f11 and f13 for 19 GHz for horizontal (top) and vertical (bottom) polarization. Left: scatterplots, right histograms (binsize 1 K). Blue, red, and black symbols and lines denote the westernmost, easternmost and middle MYI region (see Figure 4-1).

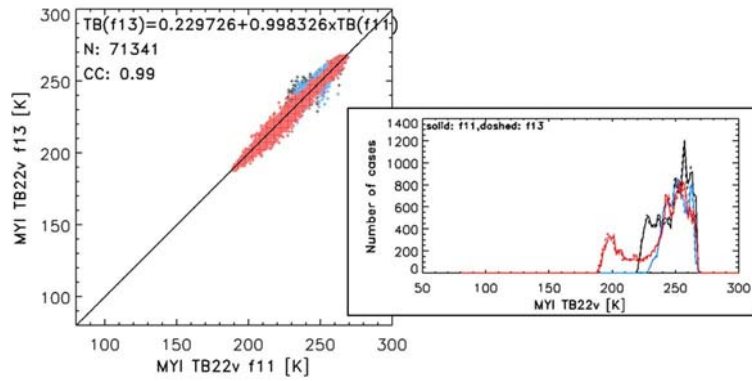


Figure 4-3: As Figure 4-2 but for TB at 22 GHz.

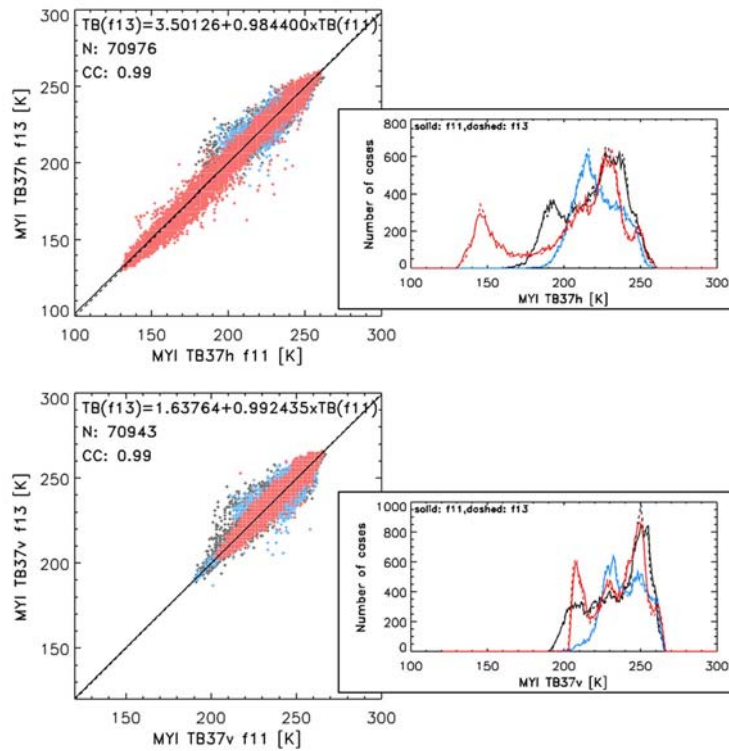


Figure 4-4: As Figure 4-2 but for TB at 37 GHz.

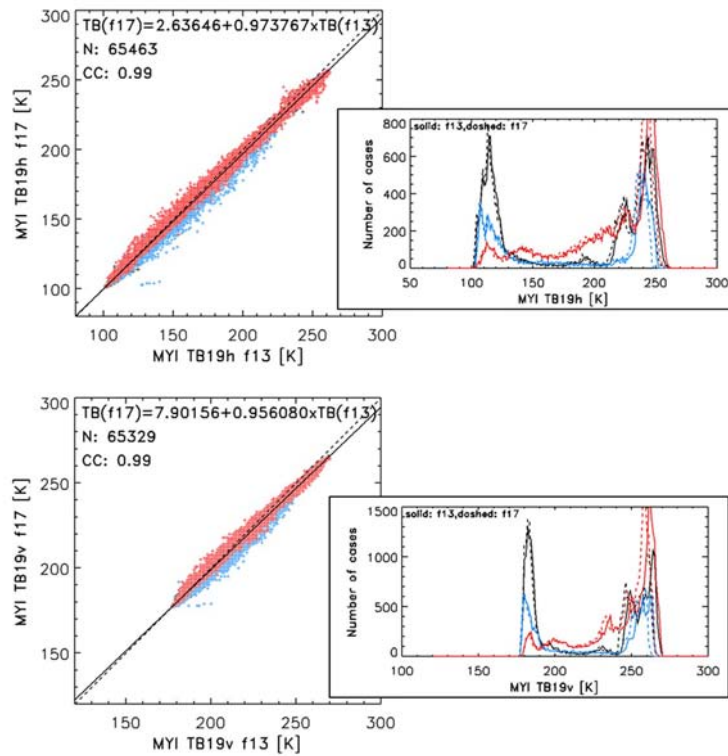


Figure 4-5: Inter-comparison of MYI-region TB from DMSP f13 and f17 for 19 GHz for horizontal (top) and vertical (bottom) polarization. Left: scatterplots, right histograms (binsize 1 K). Blue, red, and black symbols and lines denote the westernmost, easternmost and middle MYI region (see Figure 4-1).

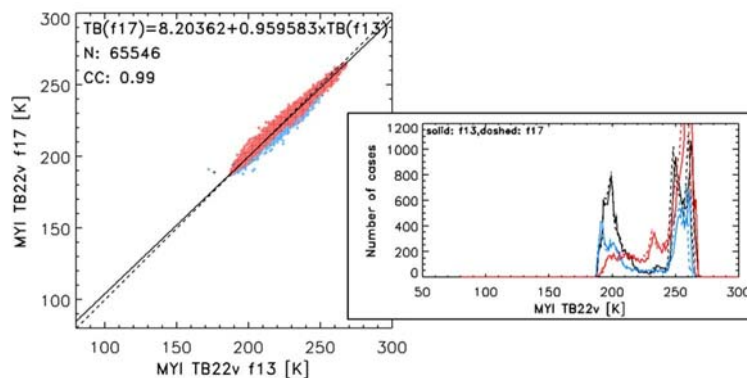


Figure 4-6: As Figure 4-5 but for TB at 22 GHz.

The regression coefficients for MYI regions are summarized in Table 1; those derived from the ice sheet region for comparison in Table 2. For MYI regions the correlation is better than 0.993 (0.998) for F11 to F13 (F13 to F17). Intercepts are similar for both sensor transitions for horizontally polarized TB but differ substantially for vertically polarized TB with intercepts close to zero for F11 to F13 and intercepts around 8 K for F13 to F17. The slopes are larger than 0.95 for all TB. A similar

observation can be made for the results of the ice sheet TBs (Table 2) which we take as a confirmation of the results obtained for the MYI regions.

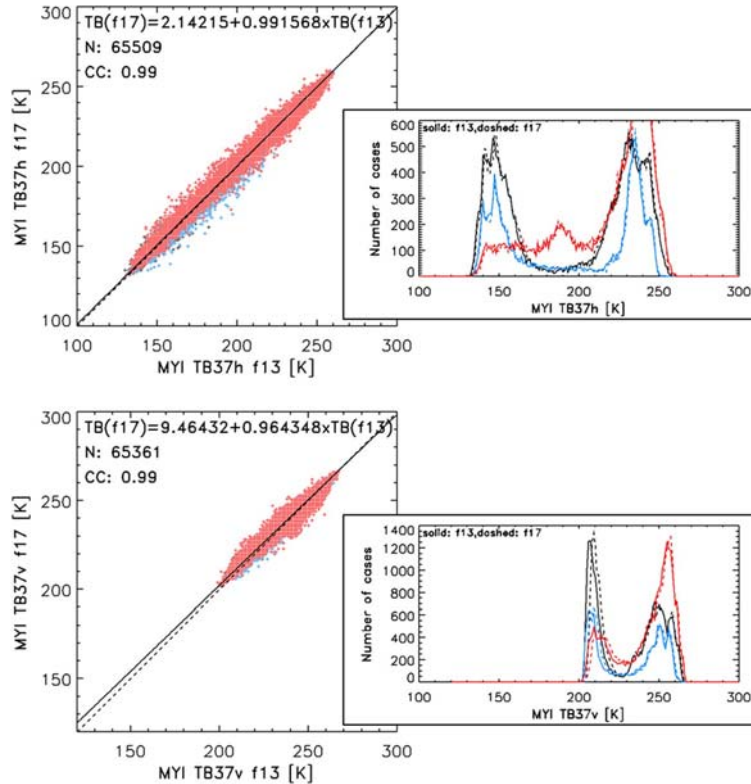


Figure 4-7: As Figure 4-5 but for TB at 37 GHz.

Table 4-1: Regression results for multiyear ice (MYI) regions.

Multiyear ice	Intercept [K]	slope	correlation	n
19H				
F11-to-F13	2.4214	0.991077	0.996637	70941
F13-to-F17	2.6365	0.973767	0.999600	65463
19V				
F11-to-F13	-0.9743	1.00492	0.996694	71230
F13-to-F17	7.9016	0.956080	0.999523	65329
22V				
F11-to-F13	0.2297	0.998326	0.996047	71341
F13-to-F17	8.2036	0.959583	0.999162	65546
37H				
F11-to-F13	3.5013	0.984400	0.993262	70976
F13-to-F17	2.1422	0.991568	0.998833	65509
37V				
F11-to-F13	1.6376	0.992435	0.993234	70943
F13-to-F17	9.4643	0.964348	0.998079	65361

In the following we use the coefficients derived for the MYI region to compute inter-sensor calibrated TB values. We carry out this computation with respect to F17, i.e. we correct F13 to the level of F17 and we correct F11 first to the level of F13 and then to the level of F17.

Note that we also inter-sensor corrected the 22 GHz TB because it is used for a weatherfilter. The inter-sensor correction is carried out before everything else is done, i.e. before tie points are selected (next subsection) and before MYI SIC and area are computed.

Table 4-2: Regression results for ice sheet region on top of Greenland.

Ice sheet	Intercept [K]	slope	correlation	n
19H				
F11-to-F13	1.2479	0.994922	0.997007	35353
F13-to-F17	3.8037	0.970532	0.998064	34562
19V				
F11-to-F13	-1.2032	1.00527	0.997130	35397
F13-to-F17	8.8370	0.953797	0.998150	34496
22V				
F11-to-F13	-0.9580	1.00278	0.995405	35440
F13-to-F17	10.1656	0.953355	0.996629	34495
37H				
F11-to-F13	1.9950	0.990209	0.993492	35531
F13-to-F17	3.18321	0.988134	0.995823	34596
37V				
F11-to-F13	0.5831	0.996832	0.993049	35497
F13-to-F17	8.7700	0.969254	0.994309	34858

4.4 Tie point selection

4.4.1 Sea Ice

Tie points are selected from areas where i) the Arctic Sectors (as can be obtained e.g. from the NSIDC) are "Arctic Ocean, sector no. 8" or "Canadian Archipelago, sector no. 9" (turquoise regions in Figure 1), and ii) the daily 5-day median filtered ASI-algorithm SIC (<http://icdc.zmaw.de>) is > 90% for months October to April of every winter. For these areas histograms of GR3719 are computed from TB37V and TB19V within the range 50K to 320K. These histograms have – in the simplest case – a bimodal distribution, one mode for FYI and one for MYI. However, in practice, these histograms turned out to exhibit one mode only, two modes, 3 modes or even 4 modes. In a first attempt we tried to follow the approach of Comiso [2012] more directly and used the TBs associated with the 5%, 10%, and 20% of the MYI tail of the histogram to compute the MYI tie points and correspondingly for the FYI tie point using the FYI tail of the histogram. MYI areas obtained with this approach did, however, not agree well enough with the results of Comiso [2012], Kwok [2004], Kwok and Cunningham [2015] and Lindell and Long [2016]; most often the MYI area obtained with our method was too small.

Therefore, we use a different way to compute the MYI and FYI tie points. We first estimate where the potential MYI-to-FYI transition occurs. For this we assumed that

basically the entire Arctic Ocean and Canadian Archipelago area (sectors 8 + 9) is ice covered during our period; this assumption is violated most in October and November. We then computed the ratio between this (constant) area and the minimum sea ice area of the preceding September taken from the same ASI SIC data set to obtain the fraction of MYI in our area of interest, i.e. sectors 8 + 9. The additional assumption made here is that MYI fractions in the Kara and Barents Seas can be neglected. The hypothesis is that this ratio can be used as a first guess to separate MYI from FYI in the histograms.

We compute the cumulative sum of the contributions to the GR3719 histogram, starting from the MYI side. Where this sum equals the product of the above-mentioned area ratio and the cumulative sum of the histogram as a whole we set the point where most likely the transition between contributions from MYI and contributions from FYI to the histogram occurs; this is our MYI-to-FYI transition GR3719. The histogram is now separated into a MYI part left and a FYI part right of the MYI-to-FYI transition GR3719 value. Subsequently, MYI and FYI GR3719 threshold values are selected from the GR3719 histograms by taking those GR3719 values which give 90% of the cumulative sums of the MYI part and 25% of the cumulative sum of the FYI parts of the histogram, respectively, starting from the MYI side and the FYI side, respectively. These thresholds are used further (see below).

The above procedure is repeated for every month between October and April. In order to account for the fact that the ratio between the original MYI area and the area of sectors 8 + 9 is changing due to MYI export out of the Arctic Ocean during winter the original ratio is reduced by a certain amount each month. This amount is kept constant for every month, except for October where it is just half the value of the other months, and for the entire period. This might be a weak point of the approach as we assume that MYI is exiting the Arctic Ocean at a constant rate no matter how large the actual MYI area is – which is however the parameter we wish to retrieve.

The percentages of the cumulative sums of the histograms (see above: 90% and 25%) and the so- called "ratio reduction" (see below) are the parameters which were now tuned such that inter- comparison of MYI area derived with our approach with the results of Kwok and Cunningham [2015] and Comiso [2012] yielded best agreement. We note that we did not take into account Lindell and Long [2016] because of an inconclusive description of whether their starting point is the September minimum sea ice extent or the minimum sea ice area. Also their estimates include the MYI area south of Fram Strait which we do not consider here and which is also difficult to quantify from the Lindell and Long [2016] paper and could only be estimated from Figure 11 of their paper to amount between 50 000 km² and 300 000 km².

Percentages were varied between 25% and 90%, trying 25, 50, 65, 75, and 90% for the MYI side and trying a percentage similar to the one used on the MYI side first before setting the percentage fixed to 25% to concentrate on the increasing flank of the main FYI lobe of the histogram. The percentage for the MYI side was more difficult to obtain and was optimized together with the "ratio reduction".

Different ratio reduction amounts were tested. Original ratios range between 0.38 and 0.81; we tested reduction amounts between 0.01 and 0.07 and figured out that with about 0.04 we obtain the most reasonable agreement between our estimates of the MYI area and those given in the above- mentioned publications.

Figure 4-8 illustrates how the GR3719 histograms may look over the course of a winter season. Usually there is a pronounced FYI mode (the maximum at the right)

and often there us a clear MYI mode (the maximum at the left), both being separated by a clear minimum. However, this is not always the case and the the MYI mode may be very broad and difficult to distinguish from the FYI mode or MYI might not even form an own mode. This can easily be explained by the variation of the radiometric signature of MYI as a function of ice age, snow cover and snow cover formation history, and snow cover property change during winter – as mentioned by Comiso [2012].

Another factor which comes into play and can be discovered in some of the histograms is that FYI similarly to MYI accumulates snow on top. The deeper the snow the more negative the GR3719 gets and the more similar the FYI signature gets to the MYI signature; this relationship has been exploited in fact to derive snow depth over FYI ice [Markus and Cavalieri, 1998].

It should be noted therefore that a substantial fraction of the MYI as detected by the NTA could be

FYI with a thick snow cover – particularly later in the winter season.

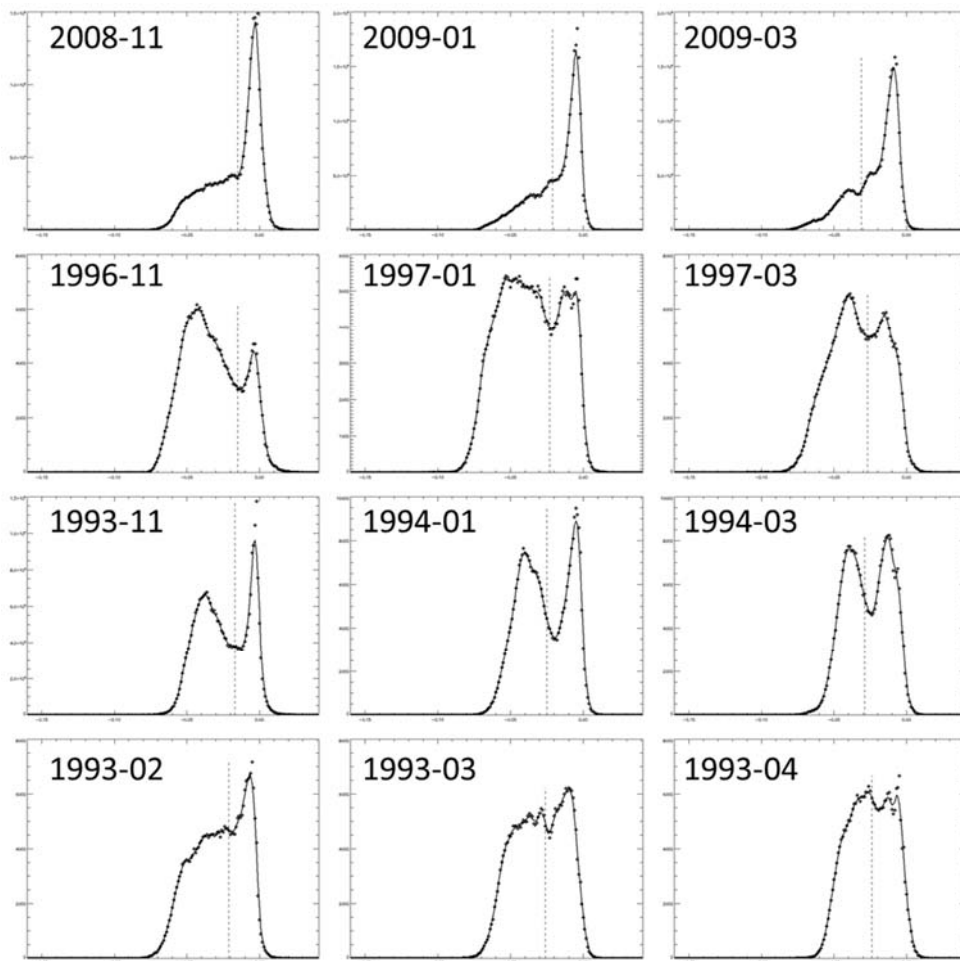


Figure 4-8: GR3719 histograms for selected years and months shown with the intention do demonstrate the variability of these histograms. Percentage is 50% and ratio reduction is 0.04.

Figure 4-9 is supposed to give one example of the impact of the choice of the percentage on the location of the MYI-to-FYI transition GR3719 value. While for 0.02 (top row) that transition value represented by the vertical dashed line is situated around -0.02 for 0.06 (bottom row) that transition values decreases from around -0.02 in November towards about -0.035 in March. Note that for 0.06 the dashed line is not in the distribution minimum anymore – in this example. The same applies for

0.04 – in this example. There are many other examples where the 0.04 MYI-to-FYI transition GR37 value is situated perfectly well in the minimum. With 0.02 one would include substantial parts of the FYI signature into the MYI part and hence the MYI tie point retrieval and with 0.06 one might miss the main mode of the MYI in the histogram. In order to account for most of the signature found for the MYI side of the histogram but to be on the same side about excluding spurious fraction from the FYI part of the histogram (in case the transition value is located on the FYI mode flank already) the value of 90% (see above) to compute the MYI tie point from the MYI part of the histogram seems to be a reasonable choice – in addition to the results of our inter-comparison with independent MYI area data sets.

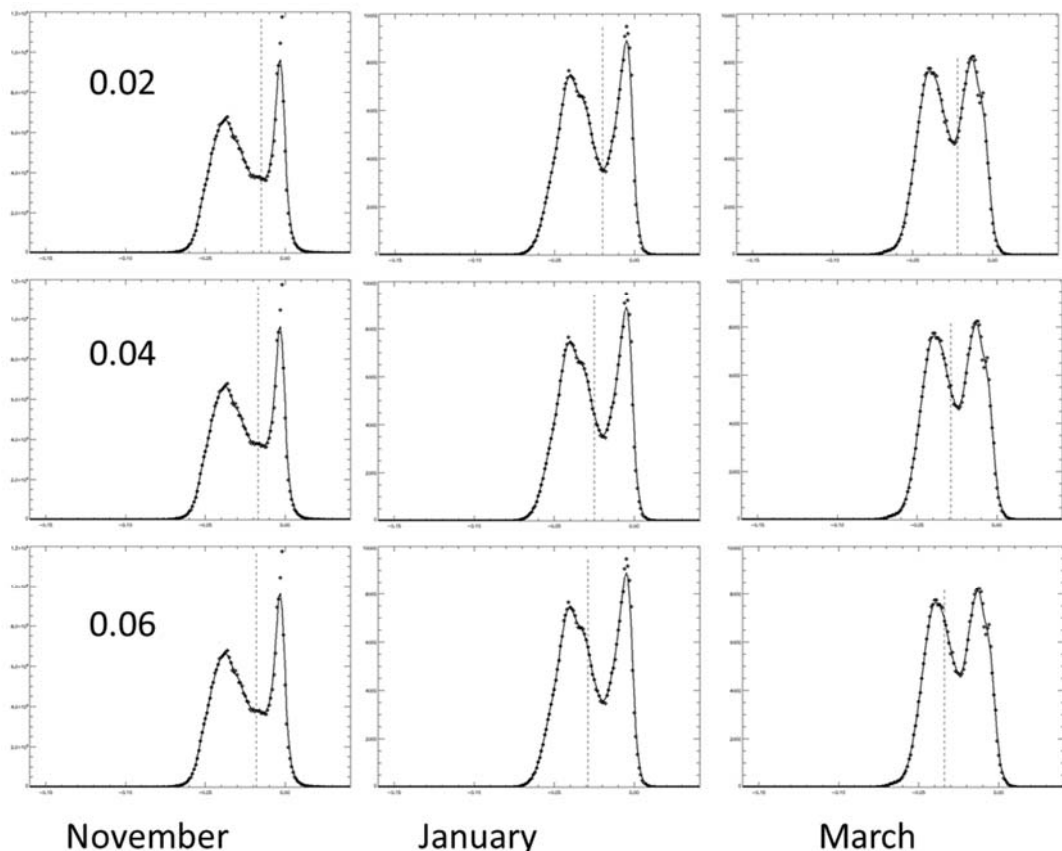


Figure 4-9: GR3719 histograms for selected months for winter 1993/94 shown with the intention to illustrate the shift of the MYI-to-FYI transition line (vertical dashed line) during the season with different values of the ratio reduction: 0.02, 0.04, and 0.06. Percentage is 50%.

The monthly MYI and FYI GR3719 thresholds values are subsequently used to compute the monthly MYI and FYI brightness temperature tie points. For this first the daily GR3719 is computed from the daily gridded TB values. Subsequently, MYI and FYI brightness temperature tie points are computed from values of all daily TB values of sectors 8 + 9 and with ASI SIC > 90% where the daily GR3719 values fall below (for the MYI tie points) or are larger than (for the FYI tie points) the MYI and FYI GR3719 threshold values, respectively. These monthly tie point values are saved and subsequently used to compute daily maps of NTA total, MYI and FYI sea ice concentration. Time series of the FYI and MYI tie points are shown in Figure 4-10 and Figure 4-11, respectively.

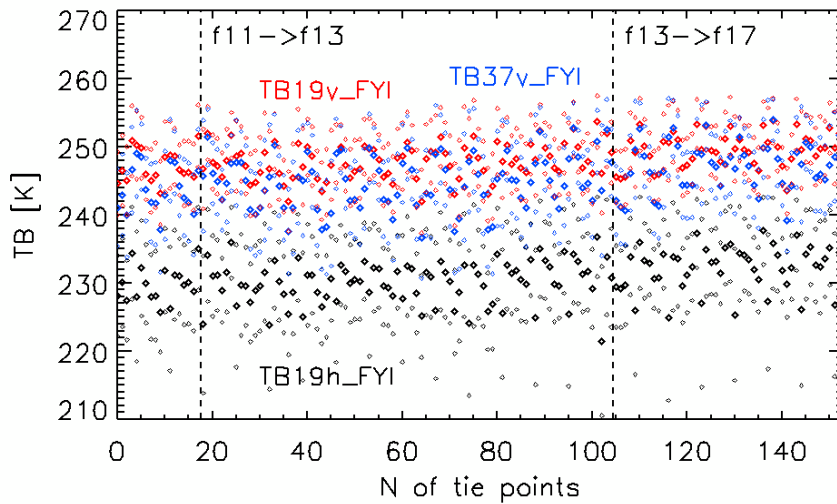


Figure 4-10: Monthly FYI tie points for the period January 1993 until December 2014. Shown are TB at 19 GHz, horizontal and vertical polarization, and TB at 37 GHz, vertical polarization. In total we have 154 tie points. Shown for every winter season – except 1992/93 and 2014/15 – are values for the months October to April. Small diamonds represent plus / minus one standard deviation.

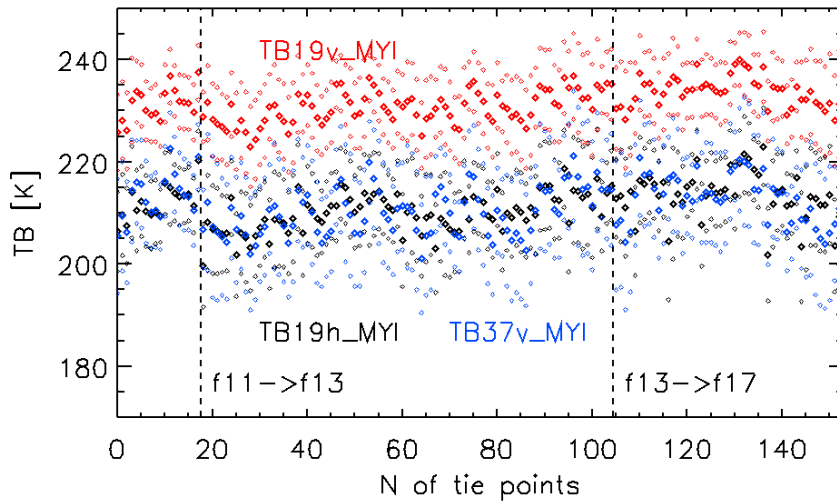


Figure 4-11: As Figure 10 but for monthly MYI tie points.

The average tie points for each DMSP sensor are given in Table 4-3 and Table 4-4.

Table 4-3: Average (October to April) FYI tie points for SSM/I and SSMIS TBs from DMSP spacecraft f11, f13, and f17 with (“with”) and without (“without”) inter-sensor calibration (see previous section).

	TB19H [K]		TB19V [K]		TB37V [K]		GR3719	
	With	without	with	without	with	without	with	without

f11	229.8	233.0	247.2	250.0	243.8	243.1	-0.0069	-0.0140
f13	230.1	233.6	247.9	251.0	244.8	244.0	-0.0063	-0.0141
f17	232.3	232.3	249.6	249.6	247.2	247.2	-0.0048	-0.0048

Table 4-4: Average (October to April) MYI tie points for SSM/I and SSMIS TBs from DMSP spacecraft f11, f13, and f17 with (“with”) and without (“without”) inter-sensor calibration (see previous section).

	TB19H [K]		TB19V [K]		TB37V [K]		GR3719	
	With	without	with	without	with	without	with	without
f11	212.1	214.5	231.2	233.3	213.3	211.2	-0.0403	-0.0497
f13	210.1	213.0	230.7	233.0	210.0	208.0	-0.0470	-0.0567
f17	213.5	213.5	233.8	233.8	212.7	212.7	-0.0473	-0.0473

Note that in addition to the TB values we also include the GR3719 values to illustrate potential differences in MYI to FYI distinction between inter-sensor calibrated and not inter-sensor calibrated data. For FYI, GR3719 increases from f11 to f17 from about -0.007 to -0.005. For MYI, GR3719 increases decreases from -0.040 to -0.047. In the uncalibrated case GR3719 also increases for FYI but more abruptly from -0.014 for f11 and f13 to -0.005 for f17; for MYI GR3719 first decreases and increases.

4.4.2 Open Water

Open water tie points are computed as follows. The gridded daily TB data of the required channels (19H, 19V, and 37V) are taken. Open water is defined as all grid cells which i) have an ASI SIC = 0% and which ii) are located in one of the Arctic sectors listed: Greenland Sea, Barents Sea, or Bering Sea (according to the NSIDC sectors, see Figure 1). TB data of one month are plotted as histograms. Starting at the calm, least influenced by the atmosphere open water tail of these histograms the lowest 2 percent of the TBs are taken and averaged to give a monthly open water tie point for each channel. Hence open water tie points change monthly as do the FYI and MYI tie points. The time series of open water tie points for the setting used to compute the SICCI MYI area data set is shown in Figure 4-12. The average tie point values for open water computed for each DMSP spacecraft involved are shown in Table 4-5 together with the corresponding values computed without inter-sensor calibration for 1993 to 2014.

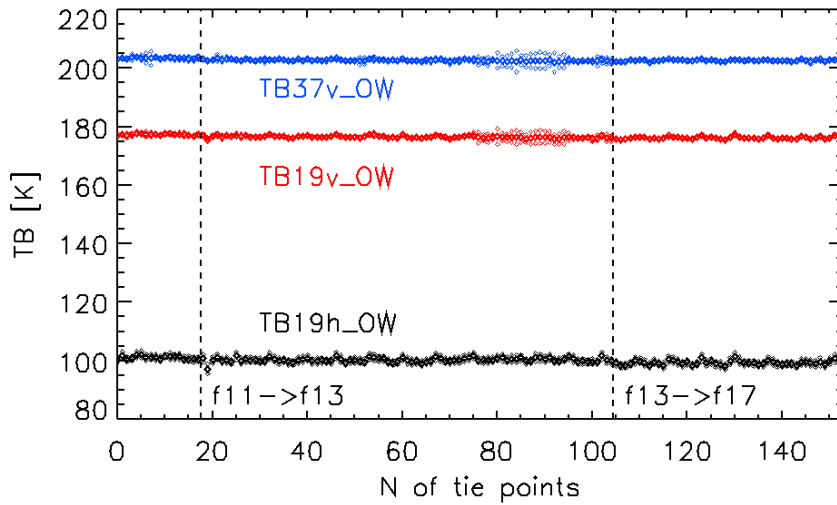


Figure 4-12: As Figure 10 but for monthly OW tie points.

Table 4-5: Average (October to April) open water tie points for SSM/I and SSMIS TBs from DMSP spacecraft f11, f13, and f17 with (“with”) and without (“without”) inter-sensor calibration (see previous section).

	TB19H [K]		TB19V [K]		TB37V [K]	
	With	without	with	without	with	without
f11	101.1	99.5	177.3	177.2	203.5	201.1
f13	100.3	100.3	176.5	176.4	202.7	200.5
f17	99.4	99.4	176.2	176.2	202.7	202.7

Note that the open water tie points do not differ much between with or without inter-sensor calibration – except for TB37V.

4.5 Computation of NASA-Team ice concentrations

The classical approach of the NASA-Team algorithm is followed using GR3719 and the polarization ratio at 19 GHz: PR19 as derived from our inter-sensor calibrated TB values and the tie points obtained from the same TB data set according to the description of the previous section. In Cavalieri et al. [1999] the open water, FYI and MYI tie points are combined in linear combinations to compute a set of coefficients a_i , $i = 0...5$ and b_i , $i = 0...5$. These are in turn used to compute another set of coefficients d_i , $i = 0...3$, f_i , $i = 0...3$, and m_i , $i = 0...3$. These are fed into the linear combination of PR19 and GR3719 to compute the concentration of FYI, the concentration of MYI and, as the sum of both, the total sea ice concentration.

Note that both, FYI concentration and MYI concentration might have (unphysical) negative values and/or values above 100% due to the nature of the retrieval algorithm. In the sea ice concentration product generated and used later-on to compute the MYI area we therefore include several sea ice concentration maps:

- Nominally computed FYI concentration
- Nominally computed MYI concentration

- Nominally computed total sea ice concentration
- Total sea ice concentration constrained to the range 0% to 100% by setting negative ($> 100\%$)
 - values to 0% (100%)
 - FYI concentration constrained to the range 0% to 100% as described above
 - MYI concentration constrained to the range 0% to 100% as described above
 - Total sea ice concentration computed from the constrained FYI and MYI concentrations and again additionally constrained to the range 0% to 100%.

In addition to these ice concentrations we provide a map of the weather flags; we include both flags separately (GR2219 and GR3719) and note where both or just one of them applies. Figures 13 to 16 display examples of the MYI coverage for selected winters. While Figures 13 to 15 focus on the high- end of the concentration side (colors: dark blue $< 30\%$, yellow 65%, red 80-90%, brown 100%) to demonstrate the main feature of the MYI distribution, Figure 16 focusses on the low end of the concentration side (white: 0%, red/yellow: $< 2\%$, bright green: $\sim 10\%$, green-into-blue: 20-30%, blue: $> 30\%$, violet: 100%); unfortunately color tables of these figure could not be exported from "ncview" which was used to create these maps.

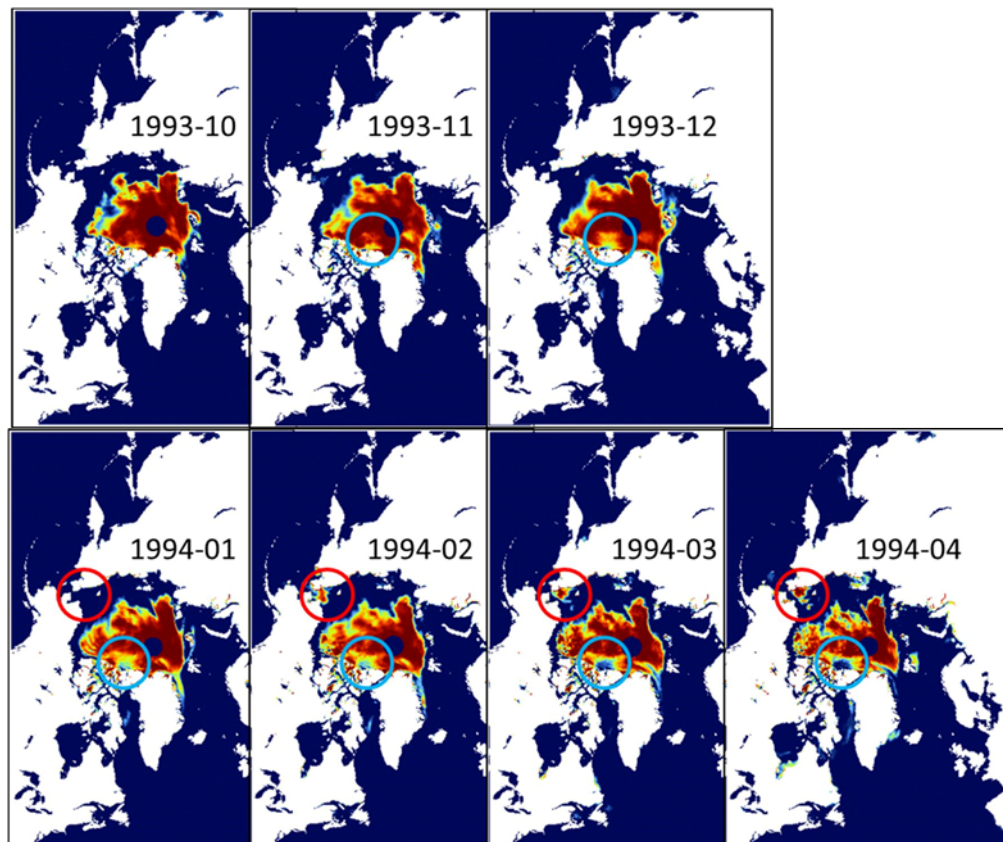


Figure 4-13: MYI sea ice concentration for the Arctic Ocean from October 1993 (top left) to April 1994 (bottom right); colors: dark blue: < 30%, yellow: 65%, orange: ~ 70%, red: 80-90%, brown: 100%. Red circles denote an area where a spurious MYI area occurs during the course of winter. Blue circles denote an area which is supposed to have 100% MYI concentration but where MYI concentration spuriously decreases over the course of winter.

The example shown in Figure 13 shows a plausible MYI distribution – at first glance. When browsing through the months one becomes aware of two areas with a spurious development in MYI coverage. One is located north of Bering Strait (red circles). During the winter until including January this area has MYI concentration < 30%. Starting in February, though, a patch with >70% MYI concentration appears out of nowhere north of Bering Strait. It is likely that this patch is associated with a substantial increase in the snow depth on FYI which is known to cause a change in GR3719 from FYI signature towards MYI signature. Note that dark blue areas are < 30% MYI concentration. Refer to Figures 15 and 16 for an inter-comparison of MYI concentration maps like the one shown in Figure 13 and MYI concentration maps giving details about the lower end of the MYI concentration. The second area with spurious MYI concentration development occurs just north of Ellesmere Island (blue circles). Here in an area of initially close to 100% or at least 90% MYI concentration in October a patch of seemingly monotonically decreasing MYI concentration is developing. MYI concentrations drop below 70% already in December and below 30% in March. Such a drop would not just require a substantial export of MYI out of the Arctic Ocean into the Canadian Archipelago – and here particularly into the channels between the Queen-Elisabeth Islands – but it would in addition require the replacement of the exported MYI by FYI. This could have grown locally but this is counteracting the idea of a large ice export event which should “fuel” more MYI of the surrounding region into that area. According to, e.g. Howell et al. [2008] such an export did not occur in winter 1993/94. Hence changes in the physical snow cover properties and in turn radiometric properties which developed slowly over the course of the winter are the most likely candidate to explain this spurious drop in MYI concentration.

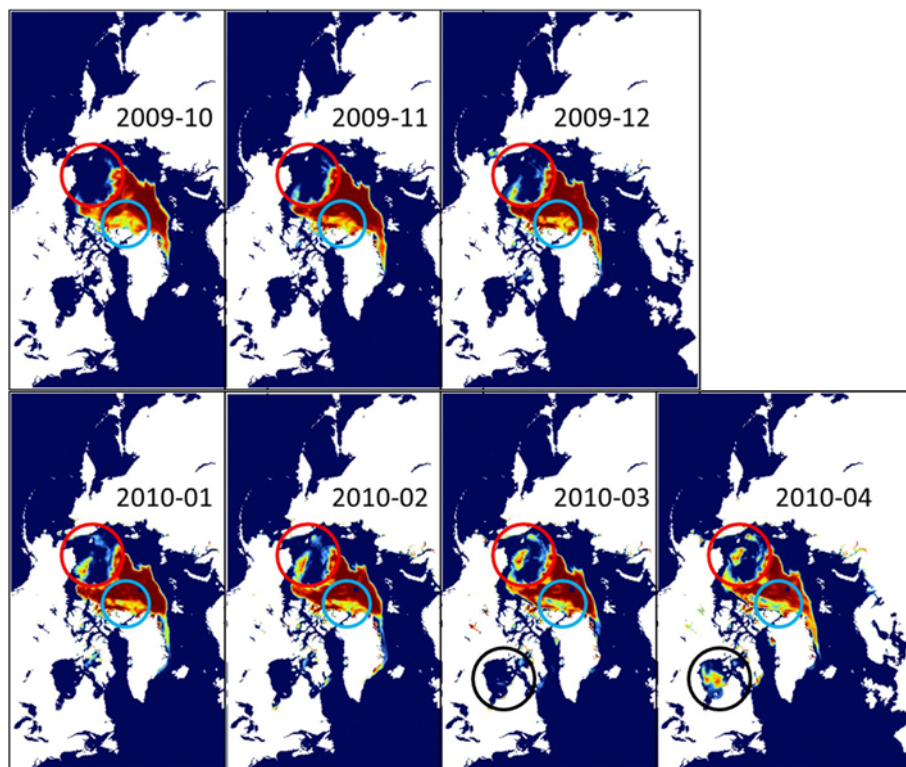


Figure 4-14: As Figure 5-13 but for October 2009 (top left) to April 2010 (bottom right); colors: dark blue: < 30%, yellow: 65%, orange: ~ 70%, red: 80-90%, brown: 100%. Black circles denote an area where a spurious MYI area occurs at the end of winter. Blue circles denote an area which is supposed to have 100% MYI concentration but where MYI concentrations seem to be spuriously low. Red circles denote an area where both real and spurious MYI co-exist.

The example shown in Figure 4-14 demonstrates the variability of the MYI coverage in the Beaufort / Chukchi Sea. While MYI is essentially confined to the Eastern Beaufort Sea in October a finger of MYI develops and stretches along the Alaskan coast towards the West – almost reaching Wrangel Island in March/April. While the pure movement / extent of this finger – or later – patch of MYI seems fine it is unphysical that there seems to be a slight increase in MYI concentration in this finger over time (red circles). At the same time there is a weaker finger of MYI with concentrations barely above 40% developing and extending from the North to West of Wrangel Island. Whether this is a real MYI feature or an area of FYI with thick snow cover remains to be proven. The MYI map for 2010, yearday 45 (i.e. 2010-02 in our case) shown in Figure 4-11 of Lindell and Long [2015] does not show this finger. However the Lindell and Long [2015] maps also lack the MYI finger north of Alaska – which we think is a realistic feature.

The blue circles again point to an area where one would expect MYI concentrations close to 100% but MYI concentrations drop below 70% or even below 60%. In contrast to Figure 13, however, this feature does not show a further substantial decrease of MYI concentration – a bit yes, but this seems more local – and it could hence be hypothesized that perhaps indeed this has been an area with quite an open sea ice cover at the end of summer 2009. ASI algorithm SIC maps of August and September 2009 do not support his hypothesis, though, so that we again can assume that the lower MYI concentration observed in the blue circles of Figure 14 is

caused by physical and hence radiometric snow properties which make the MYI look like FYI – at least partly.

Finally, the black circles denote an area in the Hudson Bay – a region free of MYI usually – where from March to April a large patch of MYI concentrations above 60% develops. This spurious MYI patch can most likely attributed to either thick snow on FYI or other surface conditions causing a MYI look-alike.

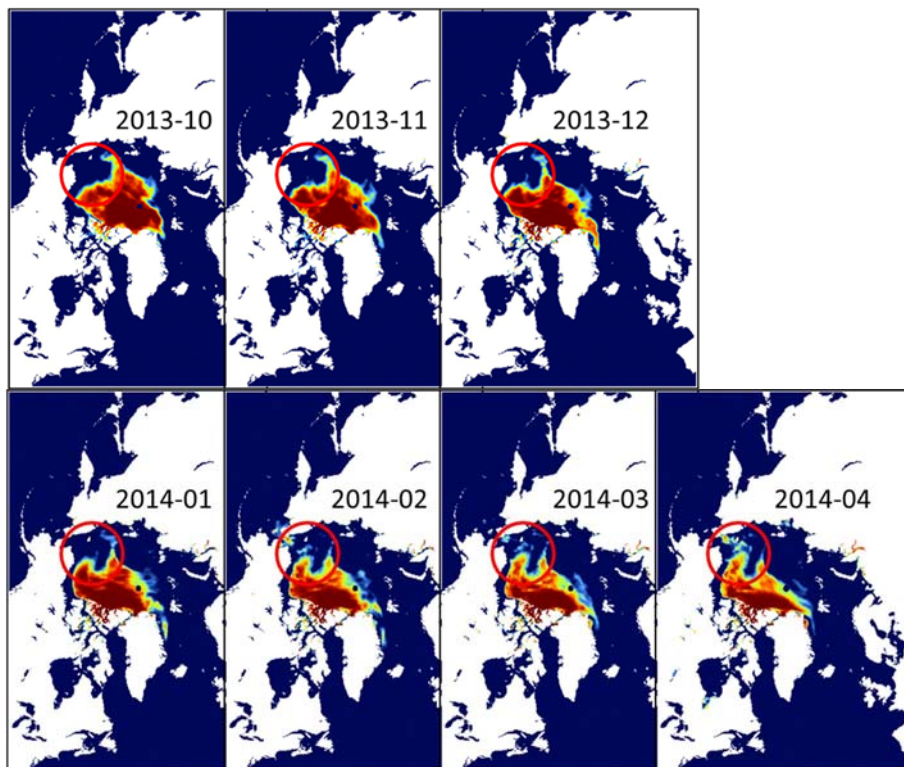


Figure 4-15: As Figure 5-14 but for October 2013 (top left) to April 2014 (bottom right); colors: dark blue: < 30%, yellow: 65%, orange: ~ 70%, red: 80-90%, brown: 100%. Red circles denote an area where both real and spurious MYI co-exist.

The series of MYI concentration maps shown in Figure 4-15 is finally a “good” example – at least in terms of the MYI coverage north of Greenland / the Canadian Archipelago. North of the Bering Strait again co-existence of a correctly identified MYI tongue developing during the course of winter and spurious MYI patches further West can be seen; the location of the latter is quite similar to those shown in Figure 4-13.

Figure 4-16 focusses on the MYI coverage for MYI concentration < 30% which is approximately given by the transition from bluish-green to solid blue. The majority of the sea ice cover exhibits non-zero MYI concentrations; the bulk of these is around 10%. There are several large areas, however, where MYI concentration is < 2%. These are given by the yellow – red – white patches. These develop and extent in coverage particularly after December and can be found, e.g. in the Laptev Sea and north of the Laptev Sea, in the Kara and Barents Seas, and in Baffin and Hudson Bay.

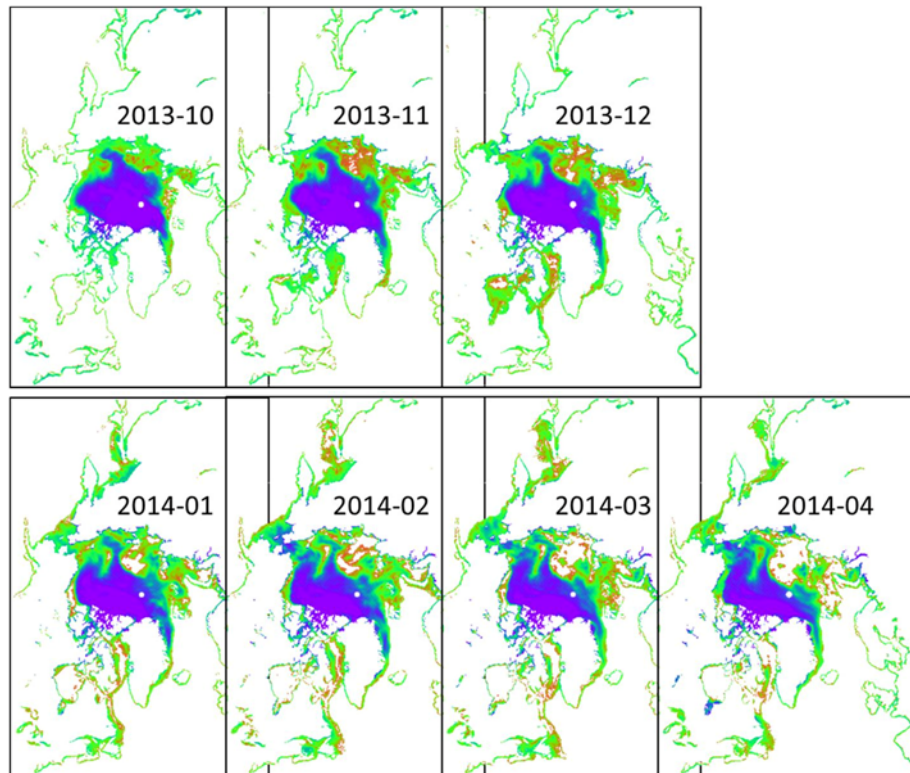


Figure 4-16: As Figure 5-15: but focusing on the low MYI concentration end. Colors: white: 0%, red-yellow: < 2%, bright green: ~ 10%, bluish-green: 20-30%, blue: > 30%.

The observations made in Figure 4-13 to Figure 4-16 with regard to spurious MYI concentrations in areas supposed to be covered by FYI and with regard to a substantial FYI region exhibiting about 10% MYI concentration lead to the recommendation that MYI concentration values below about 30% should not be considered as partly MYI covered regions. Instead FYI concentration should be set to 100% and MYI concentration to 0% here. Even though this creates a discontinuity at MYI concentration =

30% where then FYI concentration drops to 70% and MYI concentration jumps to 30%, it is likely that this will not have an influence on the usefulness of the data as proxy for a more correct choice of sea ice density values for freeboard to thickness conversion.

In the following the MYI area is computed and evaluated.

4.6 Computation of MYI area

In order to compute the MYI area first the daily FYI, MYI and total sea ice concentration maps are averaged to obtain monthly average ice concentrations. Averaged are the nominal, unconstrained ice concentrations (i.e. the first three of the bullet list above) and the constrained ice concentrations (the last three of the bullet list above). Here, for the monthly data, the weather filter is applied and only those grid cells from the daily ice concentrations are used where the daily weather filter indicates low weather influence. The monthly average ice concentration maps

are saved again in netCDF files. These contain 6 ice concentration fields (3 constrained and 3 unconstrained ones) and a layer with the number of days per month used to generate the respective average value; the minimum number of days per month required is 5.

Subsequently, the area of all grid cells with a total sea ice concentration above 40% and a MYI concentration above a) 30%, b) 50% and c) 70% are summed up for every winter month; winter is defined as October to April. The results are shown in Figure 17.

Note: because the pole hole extent changes from SSM/I to SSM/IS (compare Figure 4-13 with Figure 4-14) and because the MYI coverage is unknown for the area of the pole hole this area is excluded out of the MYI area computation. For SSM/IS years the pole hole of SSM/I is used.

In addition, to comply with Lindell and Long [2016] we only take into account cases where the total sea ice concentration is above 40%.

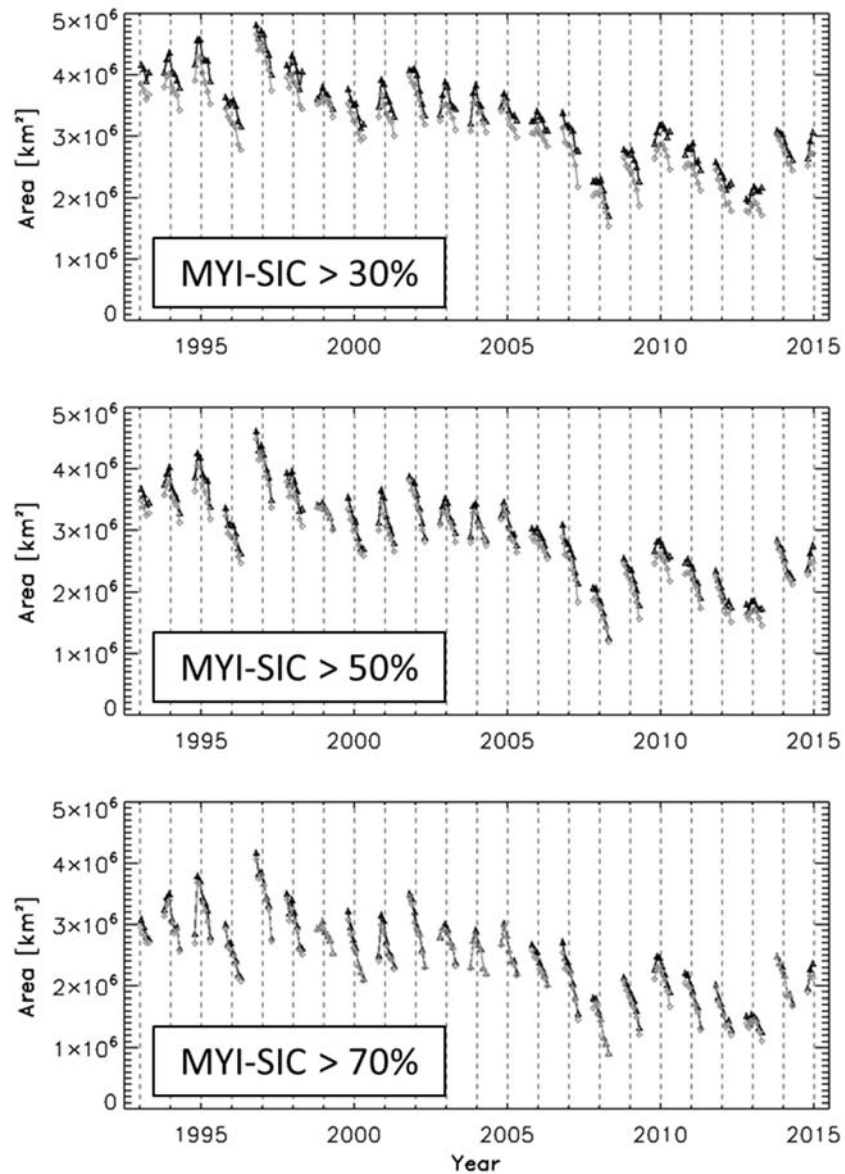


Figure 4-17: Time series of the monthly average MYI area for 1993-01 to 2014-12 computed from the monthly average MYI concentration using three different MYI concentration thresholds: 30%, 50%, and 70%. Shown are only months October to April. Black symbols: all Arctic sectors; grey symbols: only Arctic Ocean and Canadian Archipelago = sectors 8 & 9 (see Figure 4-1).

First results suggested to NOT compute the tie points for October but to instead use the apparently more stable tie points from November. This is to avoid an unphysical increase in MYI area from October to November which occurred in more than 50% of the winters investigated if the original October tie points were used (not shown). We note that taking the November tie points did not solve the problem completely as can be seen in Figure 4-17. Still for some winters an increase in MYI area from October to November can be observed: 1993/94, 1994/95, 2000/01, 2002/03, and 2003/04. Note that this increase is a function of the threshold used. As a consequence we recommend to not rely too much on October MYI concentrations and areas as computed from microwave radiometry.

Apart from this time series of MYI area shown in Figure 4-17 reveal the expected decrease in MYI area over the course of the winter, the known inter-annual variability, and the intra-seasonal variability. We note that the decrease in MYI area is more continuous (or monotonic) than in the results of Comiso [2012] for most of the winters shown. As expected MYI area is larger using a 30% MYI concentration cut-off compared to using a 50% or a 70% cut-off. Also, as expected, the black and the grey curves merge more and more when going from 30% to 70%, because high MYI concentrations are basically confined to sectors 8 and 9 (grey symbols) so that including the other sectors does not make a difference in the MYI area when using a 70% MYI concentration threshold. In contrast, using a 30% MYI concentration threshold provides MYI area which can be up to 500 000 km² larger.

The inter-comparison with independent studies is carried out for MYI area computed using the three different MYI concentration thresholds mentioned above. A threshold of 30% was used by Comiso [2012] to avoid contamination of his results by FYI with a MYI look-a-like radiometric signature and to exclude contributions from second-year ice – which motivates usage of this threshold in this study. Kwok and Cunningham [2015] showed estimates of the MYI area based on scatterometer data using a threshold of 70% - which motivates usage of this threshold. We chose to also include 50% to check for consistency. Note that in Lindell and Long [2016] no information about the MYI concentration threshold which is used to estimate the MYI area is given. This method purely relies on finding the minimum between the uni-modal (assumed) peak in Ku-Band radar backscatter for FYI on the one hand and MYI on the other hand.

Figure 4-18 compares MYI-concentration maps of the SICCI approach with the ice type maps provided by Lindell and Long [2016, their Figure 11]. Their results are based on QuikSCAT for 2000-2009 and on OSCAT for 2010-2014. The maps agree with each other reasonably well. Note that the ice type maps do not allow any conclusion about the AREA; these just provide information about the EXTENT – with unknown MYI concentration threshold to define what belongs to the MYI region and what not. The most obvious differences occur in the Greenland Sea where SICCI MYI concentration maps appear to provide much less MYI than the ice type maps based on scatterometer data. Note that Lindell and Long [2016] corrected their results for spurious MYI identification in areas or rough sea ice in the marginal ice zones. Apart from this there are a few less pronounced differences here and there. The largest one occurs in 2010 where SICCI appears to have identified much more MYI in the Beaufort / Chukchi Seas than Lindell and Long [2016] (pink circle in Figure 18). In contrast, 2001 is a year when conversely SICCI provided less MYI in the same region (Figure 4-18, yellow circle). Finally, in 2014 Lindell and Long [2016] identify a tongue of MYI extending into the East Siberian Sea which seems to be missed by SICCI (Figure 4-18, red circles). Actually SICCI simply has MYI concentrations in this region which are > 20% but < 30% and therefore this region does not show up in the MYI ice concentration map of 2014.

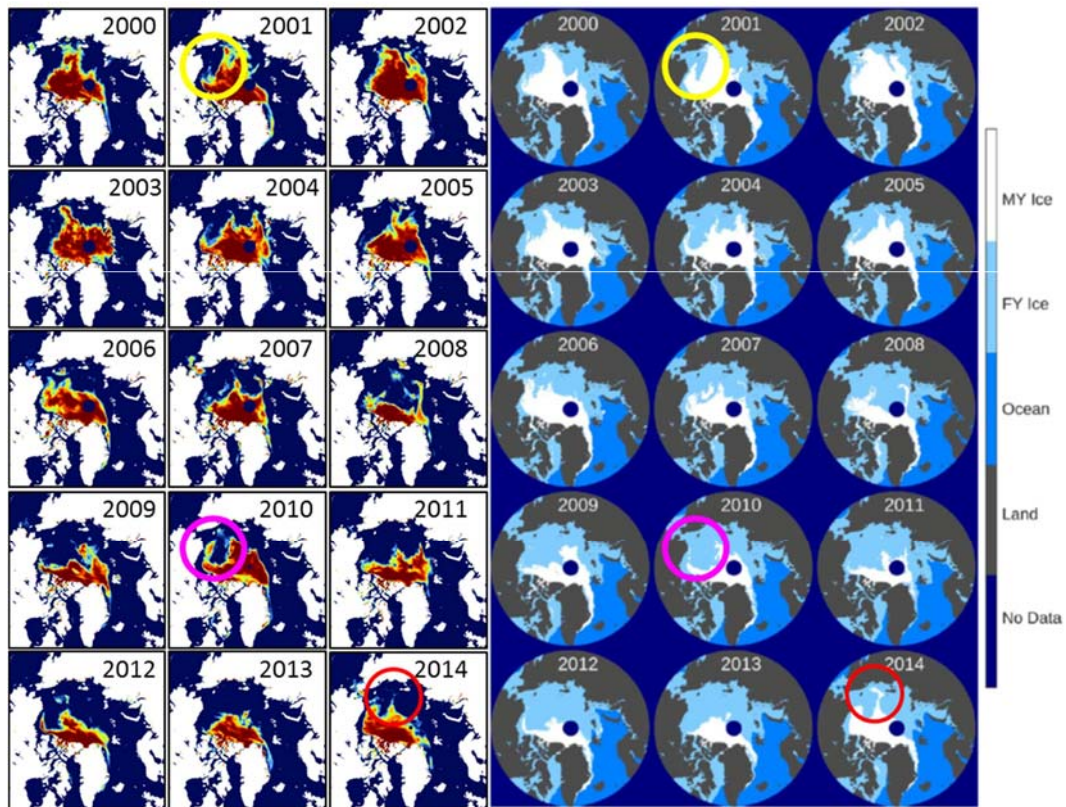


Figure 4-18: MYI concentration maps from SICCI (left) in comparison to ice type maps from Lindell and Long [2016] (right) for February 2000 to 2014. Colors in the maps on the left are: dark blue: < 30%, yellow: 65%, orange: 70%, red: 80-90%, brown: 100%. Circles denote a few areas of obvious differences.

Table 4-6 summarizes the results of our comparison to the above-mentioned data sets. Note the numbers given for Lindell and Long [2016, abbreviated as LandL in Table 6] include MYI of the entire Arctic region – including especially the Greenland Sea which may contain between 50 000 and 300000 km² of MYI (if not even more). The numbers of Kwok and Cunningham [2015, abbreviated as KandC15 in Table 6] are valid for the Arctic Ocean – i.e. only sector 8, the central Arctic Ocean sector (see Figure 1), while the numbers given for Comiso [2012] are also computed for the entire Arctic region but exclude the Greenland Sea. Kwok [2004] combined RADARSAT SAR and QuikSCAT data to derive the extent of what he calls a “perennial ice zone, PIZ” which includes MYI (also second-year ice) and embedded FYI and also to derive the MYI area based on this PIZ by – seemingly – summing up the area contributions from MYI fractions above about 0.3 (30%) [Kwok, 2004, Figure 1]. These numbers are also included in Table 6. Finally, Kwok et al. [2009] used QuikSCAT MYI fractions to derive Arctic sea ice volume. Here a MYI fraction of 0.5 (50%) [Kwok et al., 2009, Figure 5] was used to derive the MYI area.

For most winters SICCI MYI area, using a 30% MYI threshold, agrees with the MYI area of Comiso [2012]. The mean difference between the late fall MYI areas is 160 000 km²; the one between the spring MYI areas is 235 000 km². The larger value for the second difference is caused presumably by 1998/99, 2002/03, 2003/04, and 2009/10 where Comiso [2012] MYI area did not decrease over winter while it does in the SICCI data set. The average decrease in MYI area over winter is about 580000 km² for SICCI and 420 000 km² for Comiso [2012]. Note that export of

MYI ice into Kara and Barents Seas is counted as a reduction in MYI area for SICCI but is included in the MYI area of Comiso [2012].

Table 4-6: Left part: MYI area computed from SICCI MYI concentrations using a 30% threshold (column "SICCI30") in comparison to MYI area read from the publications of Comiso [2012] (column "Comiso") and Lindell and Long [2016] (column "LandL"). Each cell contains the value for November → April in 106 km². Right part: MYI area computed from SICCI MYI concentrations using indicated MYI concentration thresholds and months (column "SICCI") in comparison to MYI area read from publications of Kwok [2004], Kwok et al. [2009], and Kwok and Cunningham [2015, KandC15]. These values are also all in 106 km².**

Winter	SICCI30	Comiso	LandL	SICCI**		Kwok**	
1993/94	4.0 → 3.4	4.4 → 3.8	--	--	--	--	--
1994/95	4.3 → 3.5	4.6 → 4.0	--	--	--	--	--
1995/96	3.3 → 2.7	3.5 → 3.0	--	--	--	--	--
1996/97	4.5 → 3.7	4.4 → 4.0	--	--	--	--	--
1997/98	4.0 → 3.4	4.2 → 3.5	--	--	--	--	--
1998/99	3.6 → 3.3	3.5 → 3.6	--	--	--	--	--
1999/00	3.4 → 3.0	3.4 → 3.0	4.4 → 3.5	30%, Jan-Apr	3.3 → 3.0	3.8 → 3.3	Kwok 2004
2000/01	3.7 → 3.1	3.6 → 3.1	4.7 → 3.8	""	3.5 → 3.0	3.8 → 3.4	""
2001/02	4.0 → 3.2	4.0 → 3.4	5.0 → 4.2	""	3.8 → 3.2	4.4 → 4.0	""
2002/03	3.6 → 3.1	3.8 → 3.8	4.3 → 4.0	""	3.5 → 3.1	4.1 → 3.6	""
2003/04	3.6 → 3.1	3.5 → 3.4	4.3 → 3.4	50%, Nov-Feb/Mar	3.3 → 3.0	3.9 → 3.7	Kwok et al. 2009
2004/05	3.6 → 3.0	3.6 → 3.0	4.6 → 3.7	""	3.3 → 2.8	4.5 → 3.8	""
2005/06	3.2 → 2.8	3.0 → 2.9	4.0 → 3.0	""	2.9 → 2.7	3.8 → 3.4	""
2006/07	2.9 → 2.2	2.8 → 2.1	3.9 → 2.6	50%, Nov-Mar/Apr	2.8 → 2.1	3.8 → 3.0	""
2007/08	2.1 → 1.5	2.3 → 1.5	3.0 → 2.0	50%, Nov-Feb/Mar	1.9 → 1.5	3.1 → 2.2	""
2008/09	2.5 → 1.9	2.5 → 1.9	3.3 → 1.9	--	--	--	--
2009/10	2.9 → 2.4	3.2 → 3.1	3.0 → 2.4	--	--	--	--
2010/11	2.6 → 2.1	3.0	2.8 → 1.8	70%	2.1 → 1.3	2.2 → 1.5	KandC15
2011/12	2.4 → 1.8	--	2.6 → 1.4	""	2.0 → 1.2	2.0 → 1.2	""
2012/13	1.8 → 1.8	--	2.0 → 1.3	""	1.4 → 1.1	1.9 → 1.2	""
2013/14	3.0 → 2.4	--	3.1 → 2.7	""	2.4 → 1.7	2.5 → 1.9	""

MYI area read from Lindell and Long [2016] are generally larger than those obtained from SICCI; for the QuikSCAT period (1999/00 to 2008/09) the difference between the fall MYI area values is 890 000 km². For the OSCAT period (2009/10 to 2013/14) the difference is, however, only 160 000 km². For spring the respective differences are 520 000 km² and 180 000 km² for QuikSCAT and OSCAT, respectively; again Lindell and Long [2016] overestimates MYI area compared to SICCI. One reason for this discrepancy is certainly that Greenland Sea MYI area contributes to the LandL MYI area values. However, the Greenland Sea MYI area is smaller than 300 000 km² presumably and hence cannot explain the observed difference. It is not clear which MYI concentration the radar backscatter threshold used to discriminate between FYI and MYI corresponds to. Note that LandL MYI area exceeds the Comiso MYI area on average by 900 000 km² and by 400 000 km² for the QuikSCAT period for fall and spring, respectively. Note that the Lindell and Long [2016] is not entirely clear about the fact whether a MYI area or a MYI extent is shown. If the latter is the case, then the over-estimation of LandL versus SICCI and Comiso is not a surprise.

Comparison to the MYI area values that can be taken from papers from and with R. Kwok is a bit less straight-forward because apparently three different MYI fractions are used in those papers listed to estimate the MYI area. Best agreement

is achieved with the data from the Kwok and Cunningham [2015] paper where for 3 of the 4 winters SICCI and KandC MYI areas agree within about 100 000 km² for both fall and spring. For the earlier two papers, SICCI under-estimates the MYI area on average by 740 000 km² and 670 000 km² for fall and spring, respectively. This is at the lower end because SICCI includes the MYI area of the Canadian Archipelago while the two papers considered here do not. However, encouraging is that the winter-time decrease of the MYI area agrees within 80 000 km² with the one provided by these papers. The same applies to the SICCI MYI area data using 70% MYI concentration threshold.

4.7 Conclusion and Recommendations

Daily gridded brightness temperatures of three different DMSP spacecraft were inter-sensor calibrated to the level of DMSP-F17 using calibration coefficients derived from three, about 400 km x 400 km large, mainly MYI covered regions for the overlap periods May to September 1995 and 2007.

Following an approach which combines the classical NASA-Team algorithm [Cavalieri et al., 1999] and a modification of the Bootstrap algorithm [Comiso, 2012] a data set of the monthly average Arctic MYI concentration is computed – which comes together with FYI and total ice concentrations. The tie points required for this computation are derived from the inter-sensor calibrated brightness temperatures. The choice of parameters required for the tie point retrieval was optimized such that the obtained MYI area derived from the monthly MYI concentration maps agrees within reasonable bounds with the MYI area published by Comiso [2012] and Kwok and Cunningham [2015].

The monthly MYI concentration data set is provided to the SICCI SIT retrieval community.

MYI area is computed from the MYI concentration data using MYI concentration thresholds of 30, 50, and 70% to account for the diversity of such thresholds found in the literature. The evaluation of the MYI area with published values is (naturally) best for the results of Comiso [2012] and Kwok and Cunningham [2015]. Both SICCI and Comiso [2012] substantially under-estimate MYI area compared to a combined QuikSCAT – OSCAT data set [Lindell and Long, 2016]. This over-estimation could be explained with the difference in regions included in the MYI area estimate on the one hand. On the other hand the Lindell and Long [2016] lacks a couple of details which would be required to shed more light on the discrepancies observed – namely the MYI concentration value the radar backscatter value used would correspond to and more clear facts about whether MYI area or extent is shown. Inter-comparison with earlier work [Kwok, 2004; Kwok et al., 2009] again indicates a substantial under-estimation of the MYI area by SICCI (and hence Comiso) for both fall and spring but the seasonal decrease in MYI area from fall to spring matches well between SICCI and these two papers.

Spurious MYI areas can occur in regions usually dominated by FYI. These are presumably caused by thick snow on FYI and/or heavily deformed FYI which make FYI look-a-like MYI and is hence retrieved as MYI.

At least one example exists where in a region dominated by MYI the approach provided spuriously low MYI concentrations which even also further decreased over the course of the winter. This requires further attention.

It is recommended:

- To not use MYI concentration maps of October

- To carefully look for spurious MYI areas in regions supposed to be dominated by FYI – because thick snow on FYI, potentially paired with strong deformation, may cause FYI look like MYI.
- To carefully look for spuriously low MYI concentrations in areas dominated by MYI.
- To use a MYI concentration threshold of about 30% to delineate pure FYI covered regions from those which have a MYI fraction. In other words: Don't use the MYI concentration for values less than 30% but set these to zero (and the corresponding FYI concentration to the total ice concentration).

5 The SIC algorithm database

5.1 Overview

The sea ice concentration retrieval algorithms (17) for this project were either selected from the literature or constructed as combinations of existing algorithms or as linear functions of brightness temperature or polarisation parameters. The variability of the sea ice concentration calculated with each of the algorithms as a function of different noise sources is evaluated without weather filters and with the same tie-point set for all algorithms. This evaluation is described in the PVASR.

There are a number of studies dealing with sea ice concentration algorithm comparison. The Bootstrap and the NASA Team algorithms have been compared by Emery et al. (1994) for the year 1989 and by Comiso et al. (1997) for the year 1992 and showed the differences in Arctic sea ice concentrations of -8% to 10%, -7% to 37% respectively. Nine sea ice algorithms: NORSEX, NASA Team, Bootstrap, Near 90, Cal Val, Bristol, TUD and NASA Team 2 were inter-compared (Andersen et al., 2006) in terms of their sensitivity to atmospheric effects.

It was found that NORSEX, Bootstrap – F and Cal Val all belonging to the same family of algorithms showed lower sensitivity to noise over open water than those using the horizontally polarized channels or near 90 GHz channels. Algorithms using high frequencies such as Near 90, TUD and NASA Team 2 were highly sensitive to atmospheric water vapor and liquid water.

Seven algorithms: NASA Team, Bootstrap in each of its forms: polarization or frequency, Near 90, Bristol, TUD and NASA Team 2 (and its unconstrained version NT2U) were compared to a large set of ice - water classified SAR scenes (59 scenes) (Andersen et al., 2007) during winter (31 October – 31 March) of the years 2003-2004.

The focus of the Andersen et al. (2007) study was on the near 100% ice cover. Average sea ice concentration ranged from 96% to 100% depending on algorithm and tie-points. Also the sea ice area and the extent was evaluated for time series during the period from 1987 to 2004 covered by the SSM/I for the lower frequencies algorithms and from 1991 to 2004 for the high frequencies algorithms.

The analysis showed that because of different sensitivities to noise with climate trends the different algorithms are producing different estimates of the sea ice area and extent trends. For the first group the sea ice area negative trend amounted to 26300 – 32000 km²/yr and for the second 38100 – 45500 km²/yr. The problem of the differences in the algorithms and its importance in the projecting of the future of the Arctic sea ice is also discussed in Kattsov et al. (2010).

5.2 Physical Background

5.2.1 Radiative transfer equation

The majority of the sea ice algorithms are based on the radiative transfer equation demonstrated schematically in figure 1 (Svendsen et al., 1983).

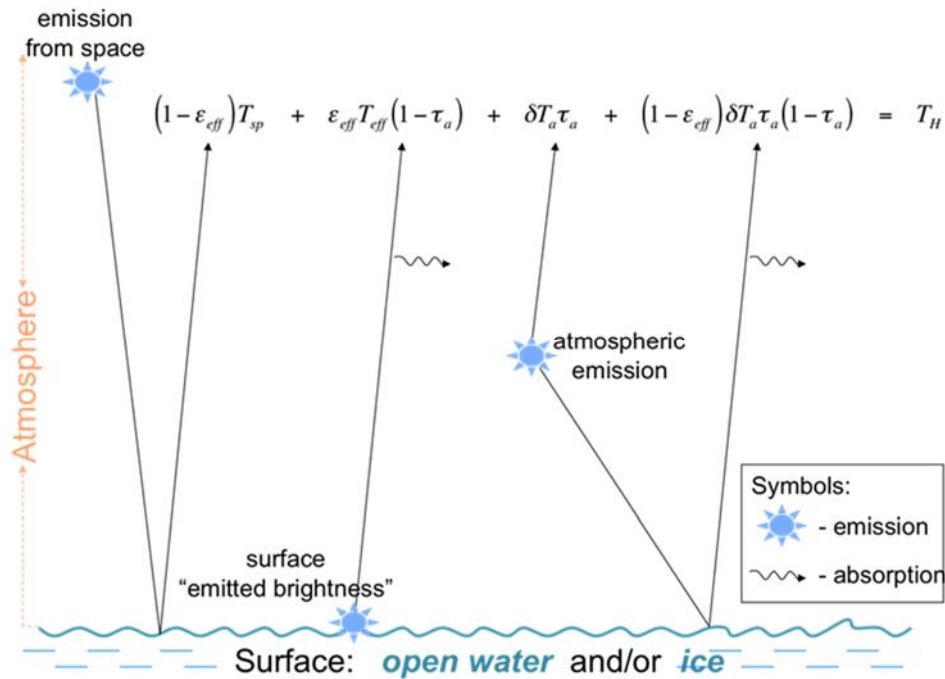


Figure 5-1: Radiative transfer model

In Figure 5-1: T_H is radiation sensed at satellite height which is composed of four terms: 1) radiation from space after reflection from the surface and two times passing the atmosphere, 2) emitted brightness from the surface seen through the atmosphere, 3) upwelling radiation from the atmosphere, and 4) downwelling atmospheric radiation reflected at the surface and transmitted back through the atmosphere. Here ϵ_{eff} is an “effective” (that is: average within field-of-view) emissivity of the surface, T_{eff} is an effective surface temperature, and the product of these two gives emitted brightness, that is what a radiometer would detect immediately above the surface without radiation from above.

T_{sp} is the temperature of free space (2.7 K), τ_a is total atmospheric opacity (optical depth), δT_a is the weighted average atmospheric temperature in the lower troposphere. Since τ_a is small, the approximation $e^{-\tau_a} = 1 - \tau_a$ is used, and a term $T_{sp} 2\tau_a$ is neglected.

The concentrations are defined as area fractions

$$1 = C_M + C_F + C_W \tag{6-1-1}$$

Measured brightness temperature is presented as sum of individual brightness temperatures for each surface type

$$TB = C_W TB_W + C_F TB_F + C_M TB_M \tag{6-1-2}$$

or

$$TB = (1 - C_{ice}) TB_W + C_{ice} TB_{ice} \tag{6-1-3}$$

in cases where only two surface types are resolved.

5.2.2 Passive microwave surface signatures

The algorithms use the emissivity dependency on frequency and polarization on order to distinguish different surface types. Emissivity, measured during the NORSEX campaign (Svendsen et al., 1983) is presented in Figure 5-2. The NORSEX algorithm can serve as an example of using two channels to resolve different surface types. It uses 19 GHz V channel to distinguish water and ice, and 37 GHz V channel to distinguish first year ice and multiyear ice.

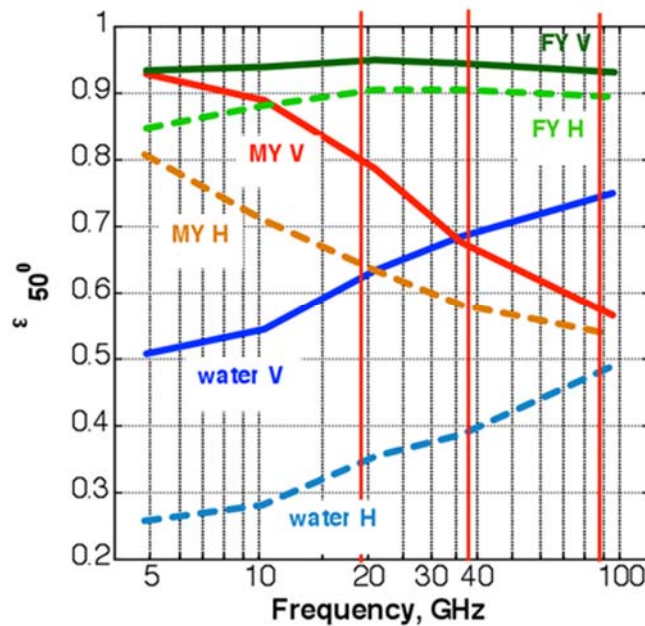


Figure 5-2: NORSEX radiometric signatures

Some of the algorithms use also polarization difference of the emissivity

$$P = TB(V) - TB(H), \quad (6-2-1)$$

or polarization ratio

$$\square \quad PR = \frac{TB(V) - TB(H)}{TB(V) + TB(H)} \quad (6-2-2)$$

in order to distinguish water from ice. Here TBs are brightness temperatures at vertical (V) and horizontal (H) polarizations. Polarization difference is known to be similar for all ice types and much smaller than for open water (Kern and Heygster, 2001; Kaleschke et al., 2001; Spreen et al. 2008).

5.2.3 Weather filters

To deal with weather effects many algorithms use weather filters or atmospheric correction in form of radiative transfer model with input from numerical weather

prediction models or standard atmosphere profiles. Six of these are described below.

1. Gloersen and Cavalieri (1986) filter for SMMR and Cavalieri et al. (1995) for SSM/I:

$$SMMR: C = 0 \text{ if } GR(37/18) > 0.07 \quad (6-2-3)$$

$$SSM/I: C = 0 \text{ if } GR(37/19) > 0.05 \text{ and/or } GR(22/19) > 0.045 \quad (6-2-4)$$

This filter was developed for the NASA Team algorithm and can be used with other algorithms (e.g. NRL, PR, Two-channel) that do not have weather filters originally.

2. In Comiso and Sullivan (1986) filter, the data points in the TB19V – TB22V scatter plot that are below the open-water filter line (see dotted line in figure 3) are set to 0 %. An additional mask is applied to deal with extreme atmospheric conditions. Data above a certain threshold for the difference of TB22V and TB19V is also set to 0 %. This filter is used in the Comiso Bootstrap algorithm.

3. Some algorithms use other algorithms as filters. For example ASI uses NASA Team (NT) as a weather filter:

$$C(ASI) = 0, \quad C(NT) \leq \text{threshold} \quad (6-2-5)$$

where the threshold is set to 30% (Kaleschke et al., 2001).

Some algorithms are hybrids of other algorithms (e.g. TUD) so they use the filters of the algorithms they are based on.

4. In some algorithms (like one-channel) atmospheric effects are dealt with through adjustment of tie-point signatures which allows incorporation of average atmospheric effects. For example the water tie-point is the apparent temperature of the water surface observed through an average atmosphere (Pedersen, 1991; Kaleschke et al., 2001).

5. ECICE correction of 85 GHz brightness temperature (Shokr et al., 2008). Influence of integrated water vapour (W) and cloud liquid water content (L) is subtracted from the original brightness temperature using

$$TB_{corrWL} = TB - \sum_{k=1}^n C_k \left(\sum_{i,j=0}^4 a_{ji} (\varepsilon(V)) W^i L^j \right)_k \quad (6-2-6)$$

where C_k is concentration of each ice type k , a_{ji} - coefficients that depend on the surface emissivity ε which in turn is a function of wind speed V . The term between the brackets in the right-hand side of the above equation is a fourth-order polynomial. Correction for the influence of wind speed over ocean surface is carried out using the following equation:

$$TB_{corrWLV} = TB_{corrWL} - C_{OW} \sum_{i=0}^4 b_i V^i \quad (6-2-7)$$

where the coefficients b_i are obtained using regression of results from the microwave radiative transfer model obtained at fixed of W, L, and V.

6. In the Kongoli algorithm (Kongoli et al., 2010) the weather is taken into account through obtaining of the geophysical parameters from the measured radiances inside the algorithm.

7. Other algorithms account for atmospheric influence by using more complete version of the radiative transfer equation. This is the case for NORSEX, Bristol, LTP-flex, LTP-nonlinear, NASA Team 2, Near 90GHz, UMass-AES, Walters.

5.2.4 Tie-points

Tie-points are typical brightness signatures of ice and water. The tie-points are references either as brightness temperatures or emissivities for the channels (combinations of frequency and polarization) used in the algorithm. There is an individual tie-point for each surface type: open water and different ice types. They vary from algorithm to algorithm and serve to ensure that algorithm gives 0% sea ice concentration for the areas of open water and 100 % concentration for areas of consolidated ice. Here are some examples of how the tie-points can be chosen.

Cavalieri et al. (1984) used average or minimum values from areas of known surface type during one week of the winter of 1979. The open water tie-point was found from an area in the Norwegian Sea. The first year ice signature was found from an area in the Baffin Bay known to have consolidated first year ice. The multi-year ice signature was found from an area in the Canadian Basin known to be almost totally covered by multiyear ice.

Svendsen et al. (1983) specifically constructed their algorithm so that it could use ground based measurements from field campaigns as tie-points.

Swift et al. (1985), Comiso (1986 and 1995) and Walters et al. (1987) used 2D scatter plots of the brightness temperatures to infer tie-points. Areas with similar characteristics to the ones listed above were used in order to ensure pure surface types (Pedersen 1991).

Another work on tie-points definition is presented in (Andersen 1998; Kern and Heygster, 2001) where the dynamical tie-points are considered. During the year there might occur deviations from chosen tie-points due to various factors such as for example melting processes or snow cover changes. This is why dynamical tie-points can be used instead of fixed to improve accuracy. For example, typical signatures for each month can be used.

The tie-points used in this work are presented in the following tables:

5.2.4.1 Open water

NH	AMSR	AMSR2	NX	SSMI	NX	SMMR	NX
w06h	82.13	82.76		0		86.49	
w06v	161.35	162.68		0		153.79	
w10h	88.26	90.29		0		95.59	
w10v	167.34	171.29		0		161.81	
w18h	108.46	114.08		117.16		111.45	
w18v	183.72	190.71	170.01	185.04	171.56	176.99	162.61
w22h	128.23	145.43		0		135.98	
w22v	196.41	207.78		200.19		185.93	
w37h	145.29	152.80		149.39		147.67	
w37v	209.81	215.71	193.19	208.72	191.87	207.48	190.80
w85h	196.94	210.55		205.73		0	
w85v	243.20	249.23		243.67		0	

Table 5-1: Tie-points for Northern Hemisphere used with non-atmospheric corrected TBs, NX columns are tie-points for the NORSEX algorithm

SH	AMSR	AMSR2	NX	SSMI	NX	SMMR	NX
w06h	80.15	83.08		0.00		83.47	
w06v	159.69	161.52		0.00		148.60	
w10h	86.62	91.06		0.00		93.80	
w10v	166.31	170.67		0.00		159.12	
w18h	110.83	114.11		118.00		110.67	
w18v	185.34	190.03	171.86	185.02	171.52	175.39	160.77
w22h	137.19	142.84		0.00		129.63	
w22v	201.53	205.70		198.66		186.10	
w37h	149.07	153.39		152.24		149.60	
w37v	212.57	215.23	196.65	209.59	192.94	207.57	190.92
w85h	207.20	207.92		206.12		0.00	
w85v	247.59	246.66		242.41		0.00	

Table 5-2: Tie-points for Southern Hemisphere used with non-atmospheric corrected TBs, NX columns are tie-points for the NORSEX algorithm

5.2.4.2 First year Ice

NH	AMSR	AMSR2	NX	SSMI	NX	SMMR	NX
fy06h	232.08	240.67				232.08	
fy06v	251.99	259.51				251.99	
fy10h	234.01	244.00				234.01	
fy10v	251.34	261.26				251.34	
fy18h	237.54	244.51		238.20		237.54	
fy18v	252.15	260.96	251.17	252.79	251.91	252.15	251.17
fy22h	236.72	246.14				236.72	
fy22v	250.87	260.24		250.46		250.87	
fy37h	235.01	241.81		233.25		235.01	
fy37v	247.13	254.91	244.47	244.68	241.53	247.13	244.47
fy85h	222.39	228.58		217.21			
fy85v	232.01	238.09		225.54			

Table 5-3: Tie-points for Northern Hemisphere used with non-atmospheric corrected TBs, NX columns are tie-points for the NORSEX algorithm. SMMR tie-points for FY and MY ice are set to AMSR tie-points since we do not have RRD data for SMMR from 100% ice

SH	AMSR	AMSR2	NX	SSMI	NX	SMMR	NX
fy06h	236.52	238.20				236.52	
fy06v	257.04	260.58				257.04	
fy10h	238.50	241.31				238.50	
fy10v	257.23	262.38				257.23	
fy18h	242.80	239.19		244.57		242.80	
fy18v	258.58	260.73	258.41	259.92	259.93	258.58	258.41
fy22h	242.61	239.51				242.61	
fy22v	257.56	259.00		257.85		257.56	
fy37h	239.96	232.68		241.63		239.96	
fy37v	253.84	251.23	252.57	254.39	253.25	253.84	252.57
fy85h	232.40	229.20		235.76			
fy85v	242.81	241.11		244.84			

Table 5-4: Tie-points for Southern Hemisphere used with non-atmospheric corrected TBs, NX columns are tie-points for the NORSEX algorithm. SMMR tie-points for FY and MY ice are set to AMSR tie-points since we do not have RRD data for SMMR from 100% ice

5.2.4.3 Multi-year ice

NH	AMSR	AMSR2	NX	SSMI	NX	SMMR	NX
my06h	221.19	224.60				221.19	
my06v	246.04	250.07				246.04	
my10h	216.31	219.95				216.31	
my10v	239.61	245.54				239.61	
my18h	207.78	204.34		206.46		207.78	
my18v	226.26	227.11	222.11	223.64	219.20	226.26	222.11
my22h	199.60	195.45				199.60	
my22v	216.67	213.99		216.72		216.67	
my37h	184.94	178.15		179.68		184.94	
my37v	196.91	191.70	184.02	190.14	175.93	196.91	184.02
my85h	178.90	180.97		173.59			
my85v	187.60	191.37		180.55			

Table 5-5: Tie-points for Northern Hemisphere used with non-atmospheric corrected TBs, NX columns are tie-points for the NORSEX algorithm. SMMR tie-points for FY and MY ice are set to AMSR tie-points since we do not have RRDP data for SMMR from 100% ice

SH	AMSR	AMSR2	NX	SSMI	NX	SMMR	NX
my06h	225.37	225.74				225.37	
my06v	254.18	256.38				254.18	
my10h	221.47	223.55				221.47	
my10v	251.65	254.78				251.65	
my18h	217.65	212.37		221.95		217.65	
my18v	246.10	244.08	244.39	246.27	244.59	246.10	244.39
my22h	213.79	208.80				213.79	
my22v	240.65	236.81		242.01		240.65	
my37h	204.66	197.66		207.57		204.66	
my37v	226.51	219.68	219.62	226.46	219.59	226.51	219.62
my85h	197.78	200.12		200.88			
my85v	210.22	211.59		211.98			

Table 5-6: Tie-points for Southern Hemisphere used with non-atmospheric corrected TBs, NX columns are tie-points for the NORSEX algorithm. SMMR tie-points for FY and MY ice are set to AMSR tie-points since we do not have RRDP data for SMMR from 100% ice

5.2.5 Summer Tie-points

During the Arctic summer, up to 80% of sea ice may be contaminated by melt ponds (Grenfell and Lohanick, 1985) as a result of the higher air temperature. The

radiometric signature of melt ponds cannot be distinguished from leads and cracks due to the limit in penetration depths at AMSR frequencies. This may greatly undermine the summer sea ice concentration estimation. Other than that, the ice emissivity is more variable during summer especially at near 90 GHz determined by several factors: wet snow that increases the ice emissivity, snow grain size that induces more volume scattering and thus decreases ice emissivity, surface melting which decreases the emissivity, etc. In addition, the characteristics of multi-year ice and first-year ice become less distinguishable during summer which complicates ice type analysis. Therefore, summer ice retrieval is less straight forward and requires special treatments.

In this part of the study, we attempt to determine the typical ice Tbs in the melting season excluding the impact of melt ponds. To compute such summer tie points, we need to identify the consolidated ice pixels with the lowest possible melt pond contamination. The RRD P SIC1 data set already includes the brightness temperatures of pixels with near 100% ice concentration, but it does not provide any information about the melt pond fraction (MPF). To make up for that, the Melt Pond Detection (MPD) retrieval scheme described in Istomina et al., 2015 is adopted. The MPD algorithm is based on the observation of optical properties of the ice surface. It utilizes a physical model of sea ice and melt ponds with no a priori assumptions on the surface albedo. Clouds in the satellite scene must be screened out as preparation for the melt ponds retrieval to avoid cloud contamination in the satellite data and the final melt pond results. The cloud screening scheme used in this study is designed explicitly for the Medium Resolution Imaging Spectrometer (MERIS) for which data for the years 2010 and 2011 are available. However, melt ponds are not the only factor that influences the ice emissivity. The other factors such as wet snow and snow grain size are not considered here. The variability induced by those factors is reflected by the standard deviation of the tie points.

The summer tie points are thus identified in the following steps. The RRD P SIC1 data points during the summer months (June to September) from 2010 and 2011 with the highest 20% Tbs are first selected as candidates for tie points determination. The high Tbs of each frequency channel occur roughly in the same region, yet differ slightly in geolocation and time. The ideal approach would be to obtain the intersection of those data points at each frequency. But it yields too few data points. To get a reasonable number of candidates for tie points determination, instead of intersection, we obtained the union of the data points with high Tbs at all frequencies. This results in 468 data points mainly located in the East Siberian Sea and Canadian Basin. All MERIS observations within 24 km radius of these selected pixels are then collocated spatially and temporally for cloud screening. Finally, the MPD is applied on the collocated MERIS footprints with cloud coverage below a certain threshold. Note that more than one MERIS overflight might be collocated with one selected AMSR-E pixel, whereas each overflight has thousands of footprints within the search radius due to the fine resolution of MERIS of 1 km over ocean. For each selected AMSR-E pixel, the average value and the standard deviation of the melt pond fraction based on the collocated footprints from each overflight are computed. In order to get a reasonable number of AMSR observations with low cloud and melt pond contamination, the choice of threshold in each step is of most importance. Figure 5-3 shows the distribution of mean melt pond fraction at varying cloud probability below 0.5. With low cloud probability (below 0.05), the mean value of melt pond fraction ranges from 5% to 45%. As the cloud probability increases, most melt pond fraction results fall in the range below 20%. The optical property of cloud is similar to that of 20% melt pond fraction. The generally even distribution of melt pond fraction over varying cloud probability proves that no cloud is mistaken as melt pond in these results. To balance between melt pond retrieval quality and

quantity, cloud probability of 0.05 is chosen as the upper threshold. The further research on summer tie points is then based on these MPD results.

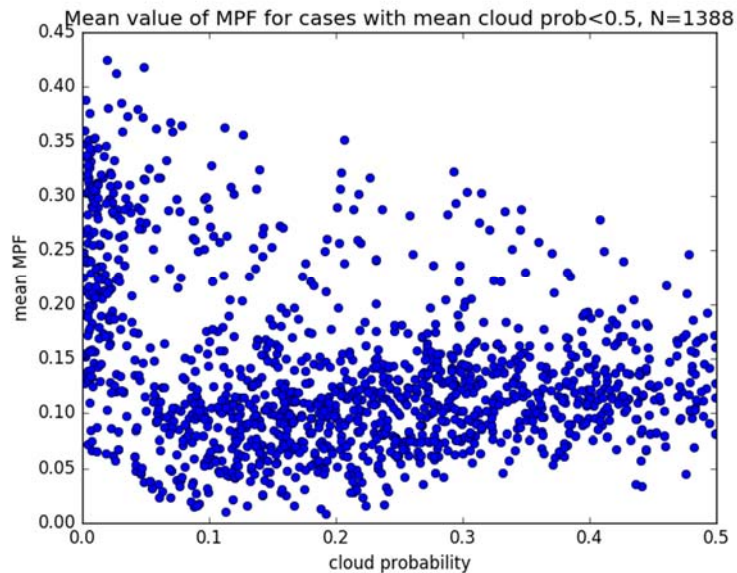


Figure 5-3: Scatter plot the the mean melt pond fraction and cloud probability of all SIC1 pixels from June to September in 2010 and 2011 with high Tbs and cloud probability below 0.5.

Due to the extensive melting and ponding events in summer, the radiometric properties of first-year and multi-year ice become more difficult to distinguish. However, the histograms of the brightness temperatures at AMSR-E frequencies clearly display two peaks (Figure 5-4), especially at frequencies lower than 36-GHz. Could the two peaks represent two ice types? Or are they merely caused by temporal variation of Tbs throughout the melting season? To answer that, the geolocation and air temperature records of the high and low peak are investigated, and shown in Figure 5-5. The corresponding air temperature of high peak Tbs are generally lower than that of low peak Tbs, indicating higher consolidated ice fraction. Most higher Tb pixels are located in June, when the melt events begin. As the air temperature rises, more melt ponds are formed, and the number of data points with lower Tbs increase from June to September as a result. Meanwhile the number of high Tbs pixels decreases with time. Although the 2m air temperature falls below freezing point in September, most data points are still covered by melt ponds and have relatively low Tbs, since refreezing does not take place immediately. In conclusion, the two peaks of Tbs do not represent different ice types. They are caused by the variation of surface Tbs under different stages of melt events.

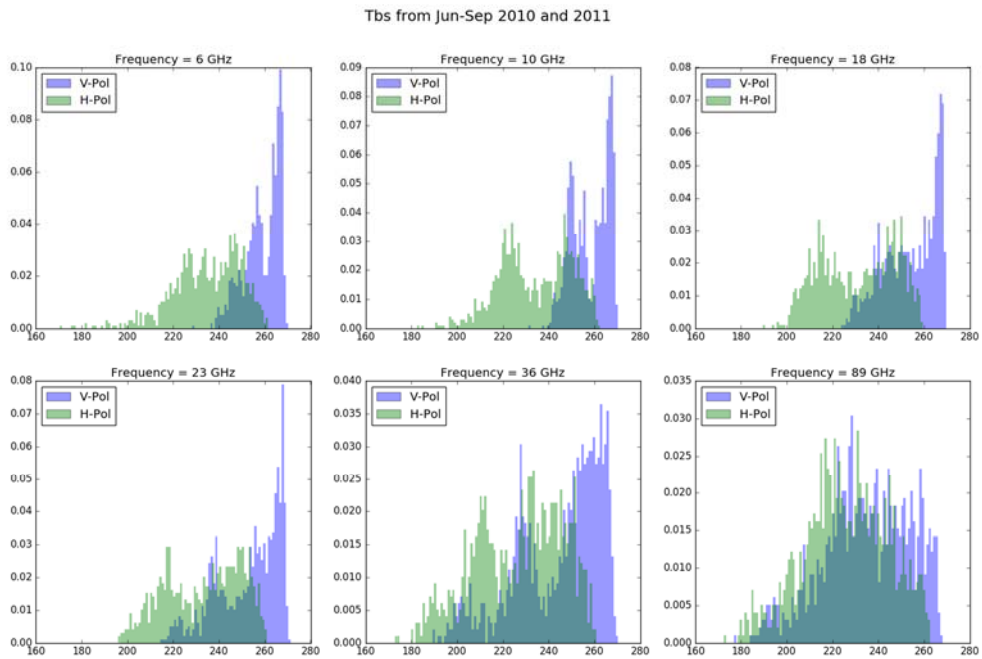


Figure 5-4: Histogram of the Tbs of RRD SIC1 data from June to September in 2010 and 2011.

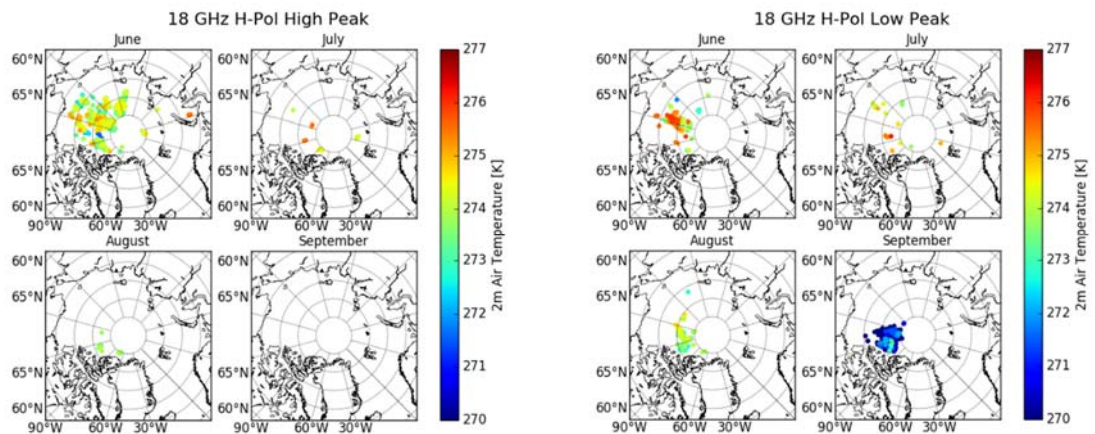


Figure 5-5: Air temperature of data points within high peak and low peak of Tb 18H from each month.

As mentioned in the previous paragraphs, more than one overflight of MERIS might be collocated with each selected SIC1 data point, and each overflight contains thousands of collocated foot prints. This results in non-unique melt pond

fraction results for the selected SIC1 data points. To decide which melt pond results to be used in the following study, two criteria are adopted: one chooses the result with the least standard deviation of melt pond fraction, and the other criteria selects the result with largest number of collocated foot prints. Each yields 185 data points at unique geolocation and time with near 100% ice concentration and low cloud coverage. The histogram of the resulting melt pond fraction based on these two criteria are shown in Figure 5-6. The distributions of MPF based on these two criteria are very similar: both show two peaks at around 0.1 and 0.3. The low MPF peak is easily understood since only data points of high Tbs are selected. Whereas for the high MPF peak, or in other words, the low occurrences of MPF around 0.2, the cause remains unclear. Our first guess is the impact of clouds. As explained before, the optical property of clouds is very similar to that of 0.2 melt pond fraction. Melt pond fraction around this value might be mistaken as cloud and thus being filtered out. But this couldn't be the cause here, since only data points with cloud probability below 0.05 are considered. Such low cloud

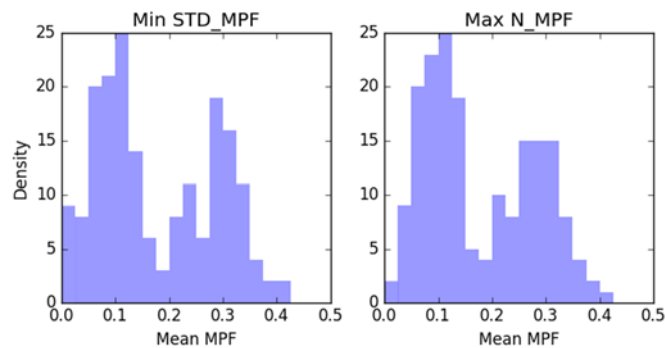


Figure 5-6: Histogram of the retrieved melt pond fraction based on two criteria: minimum standard deviation of melt pond on the left, and maximum number of collocated footprints on the right.

fraction wouldn't have such big impact on the resulted MPF distribution.

The question becomes even more interesting once the corresponding brightness temperatures are brought into consideration. The variation of Tbs corresponds to increasing MPF display a strong frequency dependency. The left panel of Figure 5-7 shows the average and standard deviation of surface emissivity at all AMSR-E frequencies with varying melt pond fractions: the blue lines represent cases with low melt pond fraction (MPF<0.15), MPF above 0.2 (the boundary of the two peaks) is shown by the green lines, and MPF above 0.3 is shown by the red lines. The surface emissivity is computed by dividing the Tbs by the skin temperature taken from ECMWF Era Interim data. To compare with the current knowledge of surface emissivity, the right panel of Figure 5-7 is appended, showing the emissivity of ice and water at AMSR-E frequencies. With melt pond fraction below 0.15, the frequency dependence of surface emissivity is quite similar to that of late summer ice or first year ice, except for at 89 GHz, where the melt pond fraction causes lower emissivity. As the melt pond fraction increases, the surface emissivity at lower frequencies decreases accordingly, displaying a mixed signature of open water and consolidated ice as expected. However, at 89 GHz, the surface emissivity rises with the melt pond fraction. According to the surface emissivity shown in the right plot of Figure 5-7, this can only be caused by larger ice fraction, which contradicts with the melt pond fraction results, unless the ice fraction mainly consists of very thin ice. In that scenario, the emitting layer of lower frequencies might be below the thin ice layer due to their larger penetration

depth, resulting in lower brightness temperatures, whereas for 89 GHz, the penetration depth is below 1cm (Mathew 2009). As a result, the emission comes from the ice layer, hence higher T_b s. This hypothesis is only valid if the air temperature is below freezing point. According to the collocated Era Interim atmospheric profiles, the air temperatures of the high MPF data points are all around 275 K, above the freezing point of saline water. To verify the probability of refreezing events at these data pixels, the air temperature records from the previous week are necessary as well, possibly together with other auxiliary data. However, the detailed explanation to the abnormal frequency dependence of surface emissivity is beyond the scope of the summer tie points study. A further investigation is still ongoing, and the results will be discussed in the study of high resolution ice concentration retrieval algorithm in summer. We include these preliminary findings here to illustrate the challenges of summer sea ice retrieval.

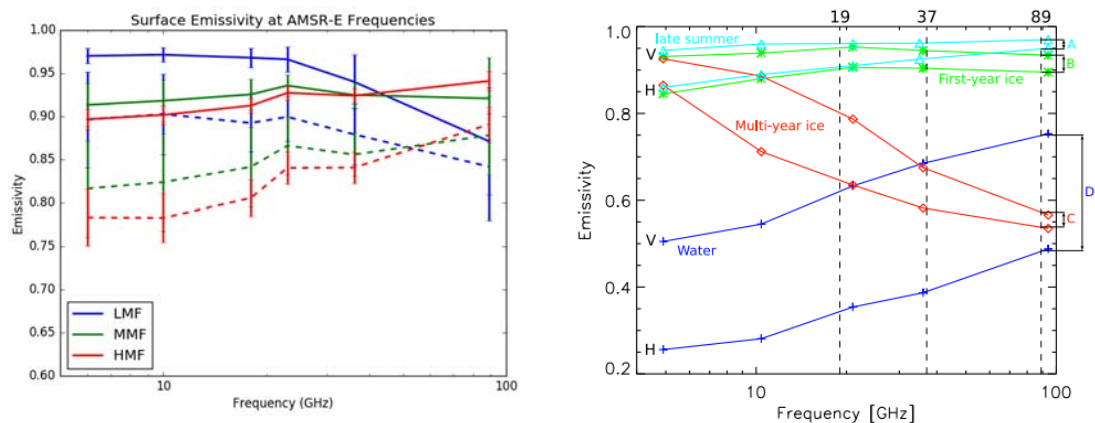


Figure 5-7: Left panel: surface emissivity at AMSR-E frequencies with varying melt pond fraction. LMF denotes melt pond fraction below 0.15. MMF represents MPF above 0.2. HMF means MPF above 0.3. The solid lines show emissivity at vertical polarization, whereas the dashed lines are for horizontal polarization. The error bars stand for the standard deviation of emissivity. Right panel: typical surface emissivity at AMSR-E frequencies (Spren 2008).

Throughout the study, each choice of threshold, each selection of sub data set, would influence the uncertainty of the final tie points. On the other hand, stricter cloud and melt pond filter would result in less representative tie points. Choosing 0.15 as the threshold for melt pond fraction, a total number of 97 data points are selected as consolidated ice data points with low melt ponds contamination. The resulting summer tie points are displayed in Table 5-7. The horizontally polarized T_b s have much higher standard deviation compared to the vertical polarization. This might be introduced by the higher sensitivity of T_b -H to the variation in snow grain size, wetness of snow, etc.

NH	Summer (June-Sep)	
Tie points	Average (K)	Std (K)
H6	245.91	15.30
V6	266.18	2.51
H10	247.68	12.93
V10	266.54	2.37
H18	244.84	9.25
V18	265.60	3.22
H23	246.79	7.65
V23	265.09	4.07
H36	241.23	9.60
V36	257.95	8.65
H89	230.95	16.92
V89	239.04	17.07

Table 5-7: Summer tie points and the corresponding standard deviation for the northern hemisphere. Melt pond fraction is below 0.15, cloud probability is below 0.05.

5.3 Algorithms description

The algorithms retrieving Arctic sea ice concentration from satellite passive microwave data are listed in Table 5-8 with their channels (frequency and polarization: vertical - V and horizontal - H). The algorithms are categorised into polarization and gradient dominated types, they are marked with letters P and G respectively in the table. PG means that both are used. Because of the different channels used here these algorithms can only be applied to certain kind of sensors. Most work for all: SMMR, SSM/I and AMSR-E, but others work only for SMMR and AMSR-E (One channel, Two channels 10GHz), or only for AMSR-E and a limited SSM/I period (ASI, NASA Team 2, Near 90GHz, TUD). A brief description of each algorithm is following in this chapter while the Python codes are presented on the projects web page.

	Algorithm	Reference	Channels
1	ASI	Kaleschke et al. 2001	85V, 85H <i>P</i>
2	Bootstrap	Comiso, 1986	19V, 37V, 37H <i>PG</i>
3	Bristol	Smith, 1996	19V, 37V, 37H <i>PG</i>
4	CalVal	Ramseier, 1991	19V, 37V <i>G</i>
5	ECICE	Shokr et al., 2008	19V, 19H, 37V, 37H <i>P</i>
6	Kongoli	Kongoli et al., 2010	AMSU: 23,31,50; MHS: 89,157

	Algorithm	Reference	Channels
7	NASA Team	Cavalieri et al., 1984	19V, 19H, 37V PG
8	NASA Team 2	Markus and Cavalieri, 2000	19V, 19H, 37V, 85V, 85H PG
9	Near 90 GHz	Svendsen et al., 1987	85V, 85H P
10	NORSEX	Svendsen et al., 1983	19V, 37V G
11	NRL	Lo, 1983	37V, 37H P
12	One channel	Pedersen, 1991	6H
13	OSISAF	Eastwood (ed.) 2012	19V, 37V, 37H PG
14	P10	This report	10V, 10H P
15	P18	This report	18V, 18H P
16	P37	This report	37V, 37H P
17	P90	This report	85V, 85H P
18	PR algorithm	Pedersen, 1991	19V, 19H, 37V, 37H P
19	TUD	Pedersen, 1998	19V, 37V, 37H, 85V, 85H PG
20	Two channels	Pedersen, 1991	(10V, 10H)/(19V, 19H)/(22V, 22H)/(37V, 37H) P
21	UMass-AES	Swift et al., 1985	19V, 37V G
22	Walters	Walters et al., 1987	19V, 19H, 22V, 22H, 37V, 37H P
23	(NT + BF)/2	This report	19V, 19H, 37V PG
24	(NT + BF + N90lin dyn)/3	This report	19V, 19H, 37V, 85V, 85H PG
25	(P37 + N90lin dyn)/2	This report	37V, 37H, 85V, 85H P
26	(P37 + N90lin dyn + BF)/3	This report	19V, 37V, 37H, 85V, 85H PG
27	(BF + (BF ²)* N90lin dyn)/(1+ BF ²)	This report	19V, 37V, 85V, 85H PG
28	(BF + (BF ³)* N90lin dyn)/(1+ BF ³)	This report	19V, 37V, 85V, 85H PG
29	(BF + N90lin dyn)/2	This report	19V, 37V, 85V, 85H PG
30	(BF + BF * N90lin dyn)/(1+ BF)	This report	19V, 37V, 85V, 85H PG
31	VASIA	Tikhonov et al., 2015	19V, 37V, 37H, 85V, 85H
32	ASI1		
33	ASI2		
34	LIN1		
35	LIN2		
36	Optimal Estimation		

Table 5-8: Algorithms list. The P indicates that the algorithm is primarily using the polarisation for retrieving the ice concentration. G is indicating that the algorithm is primarily using the spectral gradient, and GP is using both.

The abbreviations used in the Table 5-8: NT – NASA Team, BF – Bootstrap frequency mode.

5.3.1 ASI

The ASI algorithm (Kaleschke et al., 2001, Spreen et al., 2008) was developed as a hybrid of Near 90 GHz (see section 5.3.9) and NASA Team (see section 5.3.7) algorithms in order to benefit from high-resolution data and, at the same time, avoid the atmospheric influence they are subject to. The approach uses the coarser but less weather-affected NASA Team algorithm to find the open water pixels and sets high-resolution concentration to zero in such points (Kaleschke et al., 2001). Water and ice are distinguished by polarization difference.

$$P = T_B^V - T_B^H$$

The basic equations for the algorithm are based on the Near 90GHz algorithm that will be presented below in the relevant section:

$$\begin{aligned} P &= c(aC + b), \\ a &= \Delta e_{ice} T_{ice} - \Delta e_{water} T_{water}, \\ b &= \Delta e_{water} T_{water}, \\ c &= (1.1e^{-\tau} - 0.11)e^{-\tau}, \end{aligned} \quad (6-3-1)$$

where C is the total sea ice concentration, P is polarization ratio for 85 GHz channel, Δe is the difference in surface emissivity between vertical and horizontal polarization for the ice or water surface fraction, τ is the total atmospheric optical depth. Inserting tie-points $C(P_0) = 0$ (ice free) and $C(P_1) = 1$ (ice-covered) in the equation leads to

$$\left. \frac{\partial C(P)}{\partial P} \right|_{C=0} = \frac{b}{aP_0} \quad (6-3-2)$$

$$\left. \frac{\partial C(P)}{\partial P} \right|_{C=100} = \frac{1+b/a}{P_1} \quad (6-3-3)$$

The third order polynomial function

$$C(P) = d_3 P^3 + d_2 P^2 + d_1 P + d_0 \quad (6-3-4)$$

is then used to obtain concentration, where the coefficients d_i can be derived from prescribing C(P) with $C(P_0) = 0$ and $C(P_1) = 1$ (Kaleschke et al. 2001). The algorithm uses fixed coefficients:

$$d_3 = 0.971, d_2 = 0.0192, d_1 = -0.0016, d_0 = 0.0000164.$$

This makes it impossible to apply the atmospheric corrected tie-points as it is done for some other algorithms, which makes this algorithm perform worse for the corrected input brightness temperatures.

5.3.2 Bootstrap

The Bootstrap algorithm (Comiso, 1986) is based on cluster analysis of the emissivity scatter plots for three channels. The algorithm works in two modes: polarization mode for consolidated ice and frequency mode for discriminating of atmosphere and ocean (roughness) effects on the open water from low-concentration ice as well as for discriminating of the emissivity variations because of changes in snow cover and other surface effects in consolidated ice areas from actual variations in concentration.

The algorithm is presented schematically in Figure 5-8 (Comiso, 1995).

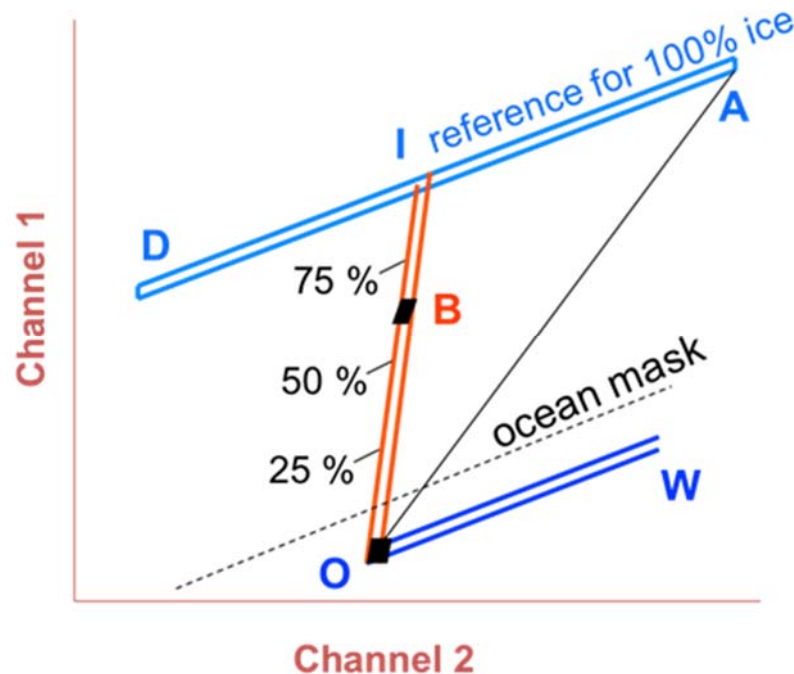


Figure 5-8: Bootstrap algorithm scheme

Sea ice concentration is obtained as

$$C_T = \frac{T_B - T_B^W}{T_B^I + T_B^W} \quad (6-3-5)$$

where W signifies the open water tie-point, and I signifies the value at the intersection of the ice cluster line and the line from the open water tie-point to the observed brightness temperature. Using either 37 GHz measurements in two polarizations (polarization mode) or 37 and 19 GHz in vertical polarization (frequency mode) this equation can be solved (Andersen et al., 2006).

In this work we consider the two modes separately:

5.3.2.1 Frequency mode

$$\begin{aligned}
 af &= \frac{TBfy37V - TBmy37V}{TBfy18V - TBmy18V} \\
 bf &= TBmy37V - af * TBmy18V \\
 qf &= \frac{TB37V - TBow37V}{TB18V - TBow18V} \\
 wf &= TBow37V - qf * TBow18V \\
 ti18vf &= \frac{bf - wf}{qf - af} \\
 C &= \frac{TB18V - TBow18V}{ti18vf - TBow18V}
 \end{aligned} \tag{6-3-6}$$

5.3.2.2 Polarisation mode

$$\begin{aligned}
 ap &= \frac{TBfy37V - TBmy37V}{TBfy37H - TBmy37H} \\
 bp &= TBmy37V - ap * TBmy37H \\
 qp &= \frac{TB37V - TBow37V}{TB37H - TBow37H} \\
 wp &= TBow37V - qp * TBow37H \\
 ti37hp &= \frac{bp - wp}{qp - ap} \\
 ti37vp &= ap * ti37hp + bp \\
 C &= \frac{TB37V - TBow37V}{ti37vp - TBow37V}
 \end{aligned} \tag{6-3-7}$$

5.3.3 Bristol

The Bristol algorithm (Smith and Barrett, 1994, Smith, 1996) has been developed to overcome the problems of NASA Team and Bootstrap connected with the horizontal channels sensitivity to layering in the snow and discontinuous concentrations obtained by Bootstrap when it switches its modes. Similarly to Bootstrap, Bristol uses the three-dimensional scatter plots, but it combines polarization and frequency schemes in one by introducing transformed coordinates (Smith, 1996):

$$\begin{aligned}
 x &= TB37V + 1.045TB37H + 0.525TB19V \\
 y &= 0.9164TB19V - TB37V + 0.4965TB37H
 \end{aligned} \tag{6-3-8}$$

5.3.4 CalVal

The CalVal algorithm (Ramseier, 1991) is a simplified modification of AES-York (Ramseier et al., 1988). It obtains sea ice concentration presented as linear combination of 19V and 37V channels brightness temperatures

$$C_T = C_1 TB_{37V} + C_2 TB_{19V} + C_3 \tag{6-3-9}$$

with coefficients C_i presented by two sets depending on season (Andersen et al., 2006). These coefficients are functions of the ice and water emissivities, brightness temperatures and atmospheric effects (Steffen et al., 1992).

5.3.5 ECICE □

Algorithm ECICE (Shokr et al., 2008), a mathematical optimization technique, using polarization ratio was developed to estimate total sea ice concentration and distinguish three ice types: new ice, young ice and first-year ice. The best estimate of sea ice concentration is obtained by minimizing the sum of squared difference between observed and estimated radiometric values based on a linear radiometric model for each ice type. The standard concept of tie-point is replaced by probability density distribution of the radiometric values for each ice type.

A flowchart of the algorithm is presented in Figure 5-9.

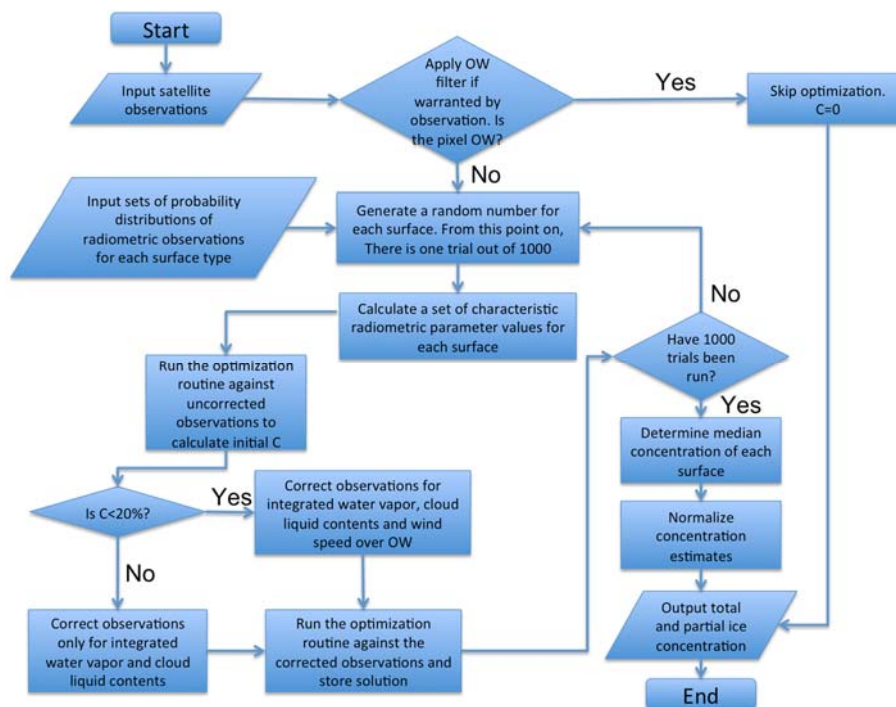


Figure 5-9: Flowchart of the ECICE algorithm

5.3.6 Kongoli (not used)

The Kongoli algorithm (Kongoli et al., 2010) is a two-step technique that retrieves surface emissivities from microwave remote sensing observations, followed by the retrieval of sea ice concentration from the emissivities. Surface emissivity spectra are interpreted for determining sea ice fraction by comparison with a catalogue of sea ice emissivities to find the closest match. The catalogue was pre-computed from known ocean, first year and multiyear sea ice reference emissivities for a range of fractions.

The surface emissivities are retrieved using comprehensive physical algorithm called the Microwave Integrated Retrieval System (MIRS). Data flow in MIRS is shown in Figure 5-10 where TPW stands for total precipitable water, CLW – cloud liquid water, RWP – rain water path, and IWP – ice water path.

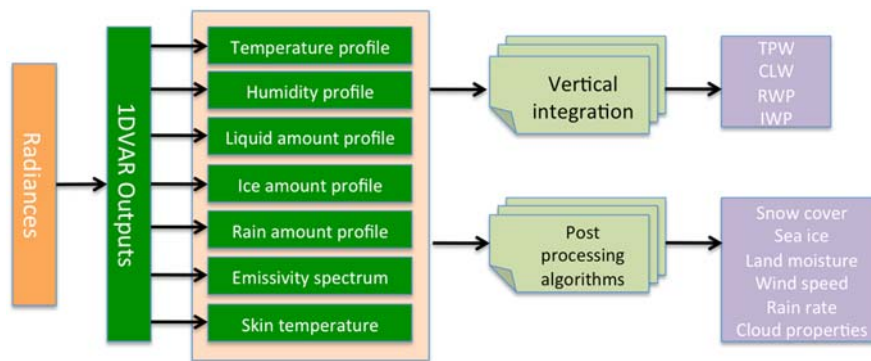


Figure 5-10: MIRS data processing concept.

Measured radiances are used to retrieve geophysical parameters and radiometric parameters from 1-DVAR method. Then, new geophysical parameters are computed from the post-processing of the 1-DVAR-retrieved parameters (based on retrieved emissivity spectrum and surface temperature).

The MIRS sea ice algorithm diagram is shown in Figure 5-11.

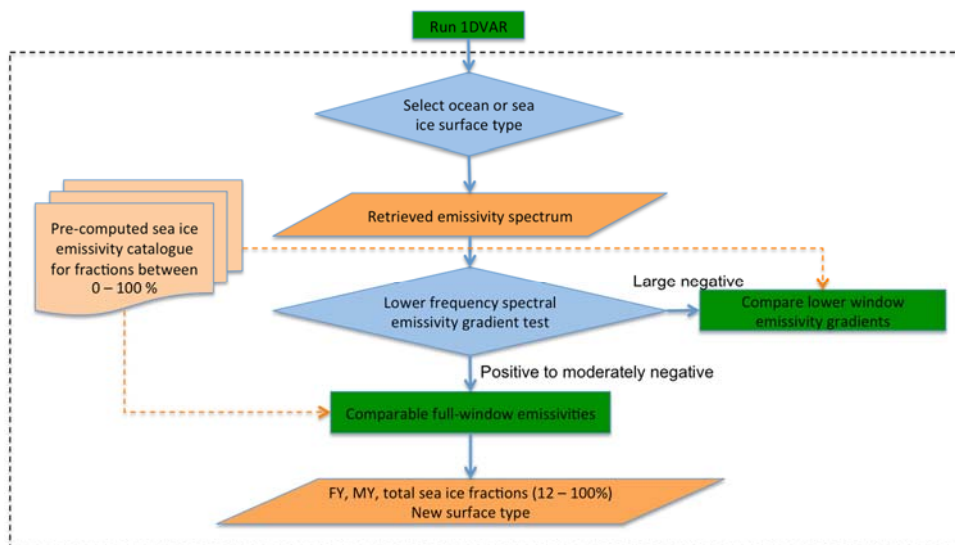


Figure 5-11: Diagram depicting the MIRS sea ice algorithm.

5.3.7 NASA Team

In the NASA Team algorithm (Cavalieri et al., 1984) radiative transfer equation is used in this form:

$$TB = T_s \varepsilon \tag{6-3-10}$$

The algorithm utilizes: 1) the polarization ratio

$$PR(f) = \frac{TB(f,V) - TB(f,H)}{TB(f,V) + TB(f,H)} \tag{6-3-11}$$

because it is small for all ice types compared to that of the ocean, and 2) the gradient ratio

$$GR(f_1, f_2, p) = \frac{TB(f_2, p) - TB(f_1, p)}{TB(f_2, p) + TB(f_1, p)} \tag{6-3-12}$$

because the brightness temperature difference between the ice types increases with increasing frequency (see also the Figure 5-12). In these equations f is frequency and p is polarization (Andersen et al., 2006). Advantage of using the ratios is that they are almost independent of the physical temperature of the surface. NASA Team algorithm uses also a weather filter involving an additional channel 22V.

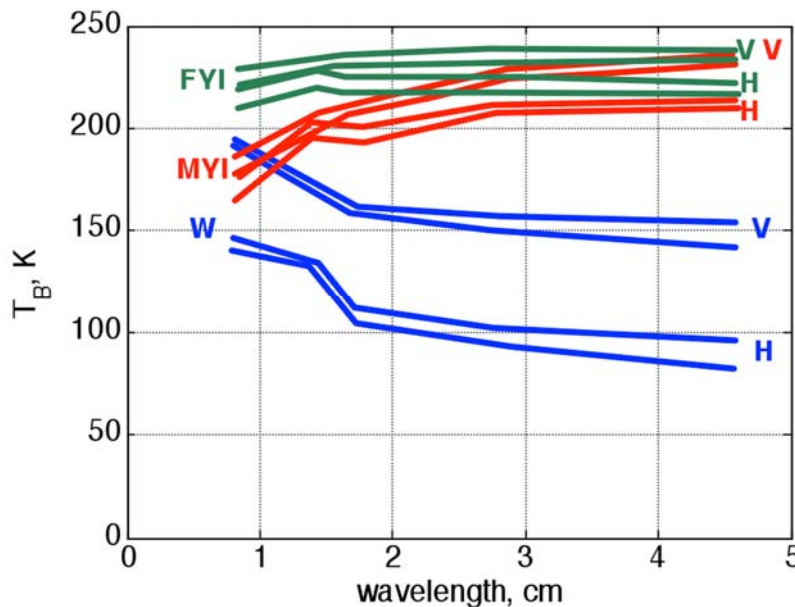


Figure 5-12: Usage of polarization and gradient ratios in NASA Team. Two curves for each case show limits of the value.

Assuming a mixture of open water, first-year ice and multiyear ice within the footprint of the satellite the partial concentrations may be inferred from the following expressions

$$\begin{aligned}
C_{FY} &= \frac{F_0 + F_1 PR + F_2 GR + F_3 PR GR}{D} \\
C_{MY} &= \frac{M_0 + M_1 PR + M_2 GR + M_3 PR GR}{D} \\
D &= D_0 + D_1 PR + D_2 GR + D_3 PR GR
\end{aligned} \tag{6-3-13}$$

where PR=PR(19) and GR=GR(19,37,V). The coefficients F, M and D contain the tie-point information (Andersen et al., 2006).

5.3.8 NASA Team 2

The new enhanced version of the NASA Team algorithm – NASA Team 2 – was produced by Markus and Cavalieri (2000) in order to overcome the problem of low ice concentrations resulting from surface snow effects particularly in the Antarctic (Comiso et al., 1997). The new algorithm uses, in addition to its standard channels (19 and 37 GHz), the high frequency ones (85 GHz) and is based on new polarizations obtained by rotation of the certain domains (see below). To reduce the atmosphere influence on the high frequency channels a look-up table generated by running the radiative transfer model with all combinations of ice concentrations and various atmospheric conditions was used.

By applying rotations (by angles ϕ_i) to the (PR(19), GR(19,37,V)) and (PR(85), GR(19,37,V)) domains ice type dependencies are eliminated and three new parameters in all are thus defined:

$$\begin{aligned}
\Delta GR &= GR(19,85,H) - GR(19,85,V) \\
PR_R(19) &= -GR(19,37,V) \sin \phi_{19} + PR(19) \cos \phi_{19} \\
PR_R(85) &= -GR(19,37,V) \sin \phi_{85} + PR(85) \cos \phi_{85}
\end{aligned} \tag{6-3-14}$$

(Andersen et al., 2006)

In this work we use the unconstrained version of this algorithm, which allows concentrations below 0% and above 100%. This is achieved by the extending of the SIC range when creating the look-up tables.

5.3.9 Near 90 GHz

The algorithm Near 90 GHz (Svendsen et al., 1987) was developed for the total sea ice concentration retrieval from only high-frequency channels data. It was based on the variation of the polarization difference for 85 GHz channels. The algorithm was made self-adjusting in order to compensate large effects on the high-frequency signal from varying atmospheric conditions and ice radiation properties. The radiative transfer equation is used in this form:

$$TB = (1 - \varepsilon) T_{sp} e^{-2\tau_\infty} + (1 - \varepsilon) T_a (1 - e^{-2\tau_\infty}) + T_s \varepsilon e^{-\tau_\infty} + T_a (1 - e^{-\tau_\infty}) \tag{6-3-15}$$

Concentrations for 100% sea ice and 0% (open water) cases are interpolated by a smooth function:

$$\begin{aligned}
 C_T &= \left(1 + \frac{b}{a}\right) \frac{P}{P_1} - \frac{b}{a}, \quad C_T \rightarrow 1 \\
 C_T &= \left(\frac{b}{a}\right) \frac{P}{P_0} - \frac{b}{a}, \quad C_T \rightarrow 0
 \end{aligned}
 \tag{6-3-16}$$

The constants a and b depend on the sea ice and open water tie-points. P_1 and P_0 are observed polarisation differences over sea ice and open water to be estimated from the current orbit (Andersen et al., 2006).

$$P = T_B^V - T_B^H$$

To take into account areas of intermediate concentrations it is assumed that the variation in atmospheric effects is a smooth function of C_T and we interpolate between the equations with the third order polynomial

$$C_T = d_3 P^3 + d_2 P^2 + d_1 P + d_0 \tag{6-3-17}$$

This allows us to ensure continuity in both C_T and its derivative and results in the following matrix equation

$$\begin{bmatrix} P_1^3 & P_1^2 & P_1 & 1 \\ P_0^3 & P_0^2 & P_0 & 1 \\ 3P_1^3 & 2P_1^2 & P_1 & 0 \\ 3P_0^3 & 2P_0^2 & P_0 & 0 \end{bmatrix} = \begin{bmatrix} 1 \\ 0 \\ -0.14 \\ -1.14 \end{bmatrix} \tag{6-3-18}$$

where typical values of the sea ice signatures have been used $b/a = \Delta\epsilon_w 272 / (\Delta\epsilon_{ice} T_{ice} - \Delta\epsilon_w 272) = -1.14$. Inserting the values of d_0, d_1, d_2 and d_3 found from equation (6-3-18) into equation (6-3-17) together with the measured polarizations, C_T is found (Svendsen et al., 1987).

Figure 5-13 shows an example of the algorithm behaviour for two tie-point sets: a standard one and one with atmospheric correction (marked by RTM). Figure 5-14 is the same but for a larger range of P .

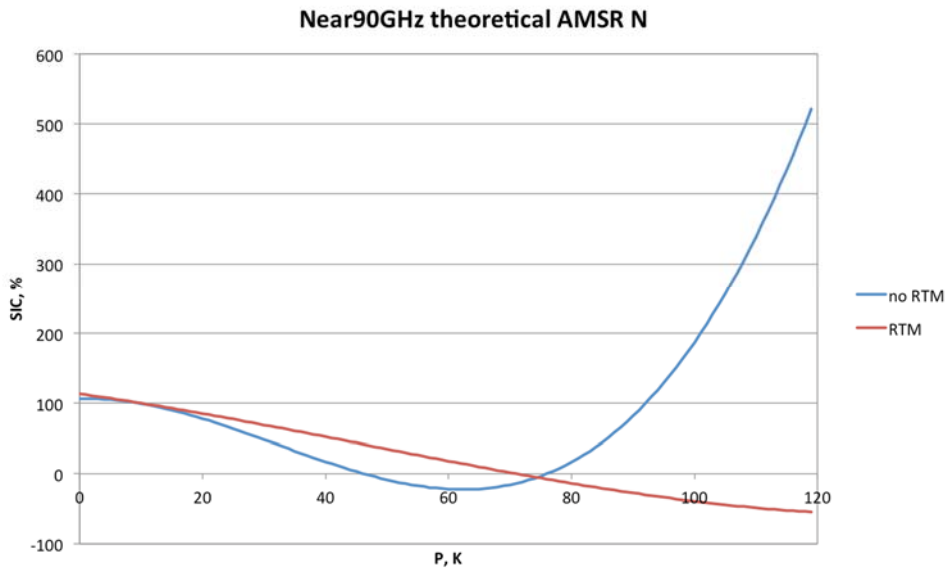


Figure 5-13: Theoretical SIC(P) for Near90GHz for two tie-points sets: standard and with atmospheric correction

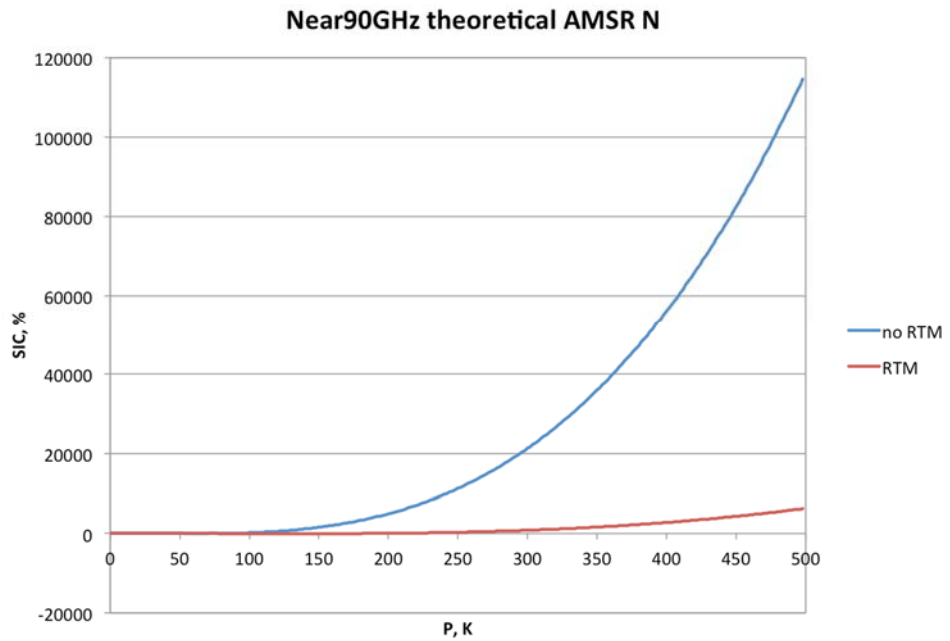


Figure 5-14: Same as Figure 5-13, but for larger range of P

5.3.10 Near 90 Linear

We also use a modification of this algorithm – Near 90 GHz linear with dynamic tie-points. First, using tie-points, polarizations are calculated for first-year ice (PFY), multi-year ice (PMY) and open water (PW):

$$\begin{aligned}
 PFY &= TB_{fy85V} - TB_{fy85h} \\
 PMY &= TB_{my85V} - TB_{my85h} \\
 PW &= TB_{w85V} - TB_{w85h}
 \end{aligned}
 \tag{6-3-20}$$

Then ice polarization (PI) is defined as:

$$PI = \frac{PFY + PMY}{2} \tag{6-3-21}$$

And the sea ice concentration:

$$C = \frac{P - PW}{PI - PW} \tag{6-3-22}$$

5.3.11 NORSEX

The NORSEX algorithm (Svendsen et al, 1983) is based on radiative transfer equation taking into account atmospheric effects. The radiative transfer equation is used in this form, see figure 1:

$$TB = (1 - \varepsilon)T_{sp} + (1 - \varepsilon)T_a(1 - \tau_\infty) + T_s\varepsilon(1 - \tau_\infty) + T_a \tag{6-3-23}$$

Sea ice concentration can be obtained from (3-32) together with equations

$$1 = C_M + C_F + C_W \tag{6-3-24}$$

$$T_E = \varepsilon_{eff}T_{eff} = C_M\varepsilon_M T_{ice} + C_F\varepsilon_F T_{ice} + C_W\varepsilon_W 272 \tag{6-3-25}$$

$$T_{ice} = \alpha T_a + (1 - \alpha)272 \tag{6-3-26}$$

by correct choice of two passive microwave channels and knowledge of the surface air temperature T_a . This temperature is input based on climatology.

37V channel was chosen because of the large difference in the emissivity spectra between FY and MY ice in this channel. The difference between open water and ice is more pronounced in 19V channel, so it was used to distinguish these two surfaces. The horizontal channels were excluded though because of the layering effect in the snow and ice (Svendsen et al., 1983). A further development of the algorithm is presented in (Bjoergo et al., 1997) where a SMMR – SSM/I match-up is suggested.

In this work we use a special set of tie-points for NORSEX because this algorithm requires tie-points that are referred to the surface (atmospherically corrected TBs). More details are given in PVASR.

5.3.12 NRL (Replaced by P37 which allows dynamic tie-points (6.3.17))

The NRL algorithm (Lo, 1983) is based on the idea that the difference between horizontally and vertically polarized brightness temperatures is very small for

different ice types, whereas it is large for open water. This is most pronounced at 37 GHz, see Figure 5-2.

$$C = A_0 - A_1(TB_{37V} - TB_{37H}), \quad (6-3-24)$$

where A_0 and A_1 contain tie-points information (Pedersen, 1991).

5.3.13 One channel (6H)

By the One channel it is possible to distinguish two surface types, ice and water, under the assumption that only those two types are present. Neglecting all atmospheric effects and considering only one ice type the radiative transfer equation can be rewritten as

$$TB = C TB_{ice} + (1 - C) TB_{water} \quad (6-3-25)$$

$$C = \frac{TB - TB_{water}}{TB_{ice} - TB_{water}} \quad (6-3-26)$$

where TB_{water} and TB_{ice} are tie-points (Pedersen, 1991).

5.3.14 OSISAF

This algorithm (Eastwood (ed.) 2012) combines Bootstrap frequency mode (B_f) and Bristol (BR):

$$Wc = \frac{abs(t - B_f) + t - B_f}{2 * t}$$

$$C = BR * (1 - Wc) + Wc * B_f \quad (6-3-27)$$

if $B_f < 0$, then $C = B_f$

where $t=0.4$.

This algorithms is named OSISAF-2.

We use also two modifications of these algorithms (called here OSISAF), where we skip this condition: if $B_f < 0$, then $C = B_f$, and OSISAF-3:

$$Wc = \frac{abs(t - B_f) + t - B_f}{2 * t}$$

$$c3 = 2 * B_f - BR \quad (6-3-28)$$

$$C = BR * (1 - Wc) + Wc * c3$$

5.3.15 P10

This is a 10GHz polarization algorithm

$$P = T_B^V - T_B^H$$

Using tie-points, polarizations are calculated for first-year ice (PFY), multi-year ice (PMY) and open water (PW):

$$\begin{aligned} PFY &= TB_{fy10V} - TB_{fy10h} \\ PMY &= TB_{my10V} - TB_{my10h} \\ PW &= TB_{w10V} - TB_{w10h} \end{aligned} \quad (6-3-29)$$

Then ice polarization (PI) is defined as:

$$PI = \frac{PFY + PMY}{2} \quad (6-3-30)$$

And the sea ice concentration:

$$C = \frac{P - PW}{PI - PW} \quad (6-3-31)$$

5.3.16 P18

Similar to P10, a 18GHz polarization algorithm ($P=TB_{18V}-TB_{18H}$) is defined as:

$$\begin{aligned} PFY &= TB_{fy18V} - TB_{fy18h} \\ PMY &= TB_{my18V} - TB_{my18h} \\ PW &= TB_{w18V} - TB_{w18h} \end{aligned} \quad (6-3-32)$$

Then ice polarization (PI) is defined as:

$$PI = \frac{PFY + PMY}{2} \quad (6-3-33)$$

And the sea ice concentration:

$$C = \frac{P - PW}{PI - PW} \quad (6-3-34)$$

5.3.17 P37

Similar to P10, a 37GHz polarization algorithm ($P=TB_{37V}-TB_{37H}$) is defined as:

$$\begin{aligned} PFY &= TB_{fy37V} - TB_{fy37h} \\ PMY &= TB_{my37V} - TB_{my37h} \\ PW &= TB_{w37V} - TB_{w37h} \end{aligned} \quad (6-3-35)$$

Then ice polarization (PI) is defined as:

$$PI = \frac{PFY + PMY}{2} \quad (6-3-36)$$

And the sea ice concentration:

$$C = \frac{P - PW}{PI - PW} \quad (6-3-37)$$

5.3.18 P90

This algorithm is a modification of ASI, where first the polarization is modified as

$$P1 = \frac{(P - 2.63)}{0.752} \quad (6-3-38)$$

and then the same equation is solved as in ASI:

$$C1 = d_3 * P1^3 + d_2 * P1^2 + d_1 * P1 + d_0, \quad (6-3-39)$$

where $d_0 = 0.971$, $d_1 = 0.0192$, $d_2 = -0.0016$, $d_3 = 0.0000164$.

To adjust C near 0:

$$C = C1 + \frac{(P1 - 8)}{700} \quad (6-3-40)$$

To prevent large P giving ice and low P losing ice, following constraint is applied:

$$\begin{aligned} \text{if } P1 > 48, \text{ then } C &= -0.026 \\ \text{if } P1 < 8.5, \text{ then } C &= 1.03 \end{aligned} \quad (6-3-41)$$

5.3.19 PR algorithm

The Polarization Ratio (PR) algorithm is designed in (Pedersen, 1991). Inserting of (3-3) into (3-4) and solving for C yields a complicated expression for concentration as a nonlinear combination of the measured PR and the tie-point radiances:

$$C = \frac{TBV_w(1 - PR) - TBH_w(1 + PR)}{PR(TBV_{ice} + TBH_{ice} - TBV_w - TBH_w) - (TBV_{ice} - TBH_{ice} - TBV_w + TBH_w)}$$

(6-3-42)

The resulting ice concentration is the average of the one obtained by 19 and 37 GHz channels, respectively. The found ice concentration is corrected by the empirically fitted curve

$$C_{new} = \frac{1 - (1 - C)}{1 + (1 - C)} = \frac{C_{old}}{2 - C_{old}} \quad (6-3-43)$$

in order to correct for nonlinearity.

5.3.20 TUD

The TUD algorithm (Pedersen, 1998) represents the Bootstrap algorithm (see section 2.3.2) with improved resolution. The polarization difference of high frequency channels is used to split the coarse resolution pixels up into four cells:

$$C = \left(C_{Bootstrap} \left[1.35 - (TB85V - TB85H)/40 \right] \right)^{0.5} - 0.03 \quad (6-3-44)$$

5.3.21 Two channels (not used, replaced by 3.3.14-17)

In the Two-channel algorithm (Pedersen, 1991), equations (2-1-1) and (2-1-2) are used. Measurements from two channels, TBH and TBV, are used to solve the two linear equations of two unknowns. The solution is

$$C_F = \frac{(TBH - TBH_W)(TBV_M - TBV_W) - (TBV - TBV_W)(TBH_M - TBH_W)}{(TBH_F - TBH_W)(TBV_M - TBV_W) - (TBV_F - TBV_W)(TBH_M - TBH_W)} \quad (6-3-45)$$

$$C_M = \frac{(TB - TB_W) - C_F(TB_F - TB_W)}{TB_M - TB_W} \quad (6-3-46)$$

where either H or V polarizations can be used.

The atmospheric contribution is considered constant in this algorithm.

5.3.22 UMass-AES

To achieve rapid machine processing, the simple but accurate algorithm UMass-AES (Swift et al., 1985) was developed. It is based on the same version of the radiative transfer equation as NORSEX (see section 5.3.11) but with different atmospheric opacity values (liquid water component is not included) and air temperature estimation approach. By assigning numerical values to some terms the equations are reduced to

$$\begin{aligned} TB19 - 13 &= \varepsilon 19(T_s - 12) \\ TB37 - 26 &= \varepsilon 37(T_s - 26) \end{aligned} \quad (6-3-47)$$

Area fractions are then determined by solving the simultaneous set of equations:

$$\begin{aligned} \epsilon_{19} &= \epsilon_{19_{FY}} - f_w(\epsilon_{19_{FY}} - \epsilon_{19_w}) - f_{MY}(\epsilon_{19_{FY}} - \epsilon_{19_{MY}}) \\ \epsilon_{37} &= \epsilon_{37_{FY}} - f_w(\epsilon_{37_{FY}} - \epsilon_{37_w}) - f_{MY}(\epsilon_{37_{FY}} - \epsilon_{37_{MY}}) \end{aligned} \quad (6-3-48)$$

5.3.23 Walters (not used)

In the Walters algorithm, the UMass-AES algorithm has been improved to a new level by (Walters et al., 1987). The radiative transfer equation is used in form

$$TB = (1 - \epsilon)T_{sp}\tau_\infty^2 + (1 - \epsilon)T_a(1 - \tau_\infty)\tau_\infty + T_s\epsilon\tau_\infty + T_a(1 - \tau_\infty) \quad (3-22-1)$$

Solving of (3.17.1) for ϵ gives

$$\epsilon = \frac{(T_a - TB) - (T_{sp} - T_a)\tau_\infty^2}{(T_a - T_s) + (T_{sp} - T_a)\tau_\infty^2} \quad (3-22-2)$$

Emissivity at the surface is given as

$$\epsilon = \epsilon_w C_w + \epsilon_F C_F + \epsilon_M C_M \quad (3-22-3)$$

where ϵ_w now is a function of surface temperature and wind speed at the surface.

Using 3 frequencies and 2 polarizations, the following 6×6 matrix equation is obtained

$$\mathbf{E}\mathbf{f} = \mathbf{e} + \Delta \quad (3-22-4)$$

where \mathbf{E} is the matrix of tie-point emissivities at the three frequencies and two polarizations, \mathbf{f} is the vector of surface types, \mathbf{e} is the vector of “measured” emissivities and Δ is the error term to be minimized by adjusting \mathbf{f} and the variable part of \mathbf{E} alternated by adjusting \mathbf{e} by changing atmospheric parameters (Pedersen, 1991).

5.3.24 Algorithm combinations

The short names of the composite algorithms will be used in the documentation for convenience.

Short name	Description
Combo1	(NASA Team + Bootstrap_F)/2
Combo2	(NASA Team + Bootstrap_F + Near90GHz lin dyn)/3
Combo3	(P37 + Near 90GHz lin dyn)/2
Combo4	(P37 + Near 90GHz lin dyn + Bootstrap_F)/3
Combo5	(Bootstrap_F + (Bootstrap_F ²)* Near 90GHz lin dyn)/(1+ Bootstrap_F ²)
Combo6	(Bootstrap_F + (Bootstrap_F ³)* Near 90GHz lin dyn)/(1+ Bootstrap_F ³)
Combo7	(Bootstrap_F + Near 90GHz lin dyn)/2
Combo8	(Bootstrap_F + Bootstrap_F * Near 90GHz lin dyn)/(1+ Bootstrap_F)

Table 5-9: Composite algorithms

5.3.25	Comiso_ucorr
5.3.26	OSISAF_w_RTM Original OSISAF algorithm using fixed TPs and atmospheric correction of input TBs.
5.3.27	The "SICCI1" algorithms The SICCI1 algorithm uses the same linear weighting as described in 2.3.1 but with BOW=ComisoF and BICE=Bristol. The "ucorr" refers to applying the algorithm on original brightness temperature, and "w_RTM" refers to applying the algorithm on brightness temperatures with atmospheric correction (see 2.4).
5.3.28	The "N90lin" algorithms These algorithms use the same principle and formulas as the ComisoF algorithm (5.3.2.1) but with channels Tb89V and Tb89H instead of Tb37V and Tb19V. This "N90lin" is a generalization of the "Near 90 Linear" algorithm (5.3.10) but where the <i>cice</i> line is allow to deviate from the 1-to-1 line. The "ucorr" refers to applying the algorithm on original brightness temperature, and "w_RTM" refers to applying the algorithm on brightness temperatures with atmospheric correction (see 2.4).
5.3.29	Comiso_w_RTM
5.3.30	The "SICCI2" algorithms. The SICCI2 algorithms are the combined dynamic algorithms as described in 2.3.2. The SICCI2LF operates in the (18.7V, 36.5V, 36.5H) space, SICCIHF in (18.7V, 89.0V, 89.0H), and SICCI2VLF in (6V, 36.5V, 36.5H). The "ucorr" refers to applying the algorithm on original brightness temperature, and "w_RTM" refers to applying the algorithm on brightness temperatures with atmospheric correction (see 2.4).
5.3.31	VASIA_combo A new algorithm VASIA (Tikhonov et al., 2015) is implemented and included to the algorithm inter-comparison study for the first time. It contains an emission model of the system ocean – sea ice – snow – atmosphere. The algorithm is designed to identify melting in addition to standard sea ice concentration retrieval. The algorithms works as follows: 1. Satellite tangents are calculated from the Tbs:

$$t_{85-37}^h = \frac{Tb85H - Tb37H}{85.5 - 37}$$

$$t_{85-19}^v = \frac{Tb85V - Tb19V}{85.5 - 19.35}$$

$$t_{37-19}^v = \frac{Tb37V - Tb19V}{37 - 19.35}$$

2. Calculate theoretical tangents for sea ice concentration expressed in 10ths, I , in a range from 0 to 10 (but extended to the range from -1.5 to 2.5 to allow sea ice concentrations below 0% and above 100% for this study):

$$f_{85-37}^h(I) = -0.085 \times I + 0.908$$

$$f_{85-19}^v(I) = -0.086 \times I + 0.55$$

and the criterion coefficient:

$$F_1 = \frac{1}{2} \left[\frac{(f_{85-37}^h(I) - t_{85-37}^h)^2}{(t_{85-37}^h)^2} + \frac{(f_{85-19}^v(I) - t_{85-19}^v)^2}{(t_{85-19}^v)^2} \right]$$

3. Criterion function F_1 is calculated for ice concentration (expressed in 10ths) from 0 to 10 (from -1.5 to 2.5 in this study) with a step equal to 0.1.

4. The minimum value of criterion function F_1 determines the ice concentration I_1 without error correction related to melting effects. Here we call this part of the algorithm VASIA1.

5. The lower boundary for the function of t_{37-19}^v of sea ice concentration is calculated:

$$\delta_{37-19}^v(I_1) = -0.187 \times I_1 + 1.1$$

and compared to the satellite tangent t_{37-19}^v .

5. If $\delta_{37-19}^v(I_1) < t_{37-19}^v$, I_combo = I1 (VASIA1).

6. If $\delta_{37-19}^v(I_1) \geq t_{37-19}^v$, I_combo = I2 (VASIA2). The criterion function F_2 is calculated:

$$F_2 = \frac{1}{2} \left[\frac{(\phi_{85-37}^h(I) - t_{85-37}^h)^2}{(t_{85-37}^h)^2} + \frac{(\phi_{85-19}^v(I) - t_{85-19}^v)^2}{(t_{85-19}^v)^2} \right],$$

where

$$\phi_{85-37}^h(I) = -0.039 \times I + 1.19$$

$$\phi_{85-19}^v(I) = -0.04 \times I + 0.7$$

7. The minimum of the function F_2 is calculated and the respective sea ice concentration I_2 determines the final value.

For more details please see the original paper of Tikhonov et al. (2015). It presents the VASIA_combo algorithm, which we implement here with an extended SIC range. We also add the two alternatives VASIA1 and VASIA2 as separate algorithms to study their skills independently. The difference between the two is expected to be a measure of melting (Tikhonov et al., 2015).

5.3.32 VASIA1

Please see 5.3.31

5.3.33 VASIA2

Please see 5.3.31

5.3.34 NT2_corr

The NASA Team 2 algorithm (NT2, Markus and Cavalieri, 2000) is modified to allow sea ice concentration values below 0% and above 100% to allow full variability of sea ice concentration around 0% and 100%. This was done by extending the range of the sea ice concentration lookup table retrieved by the algorithm for each of the modelled atmospheres (12). The algorithm's tie points are corrected to be consistent with the RRDP2. First a correction factor is calculated for open water (ow), first year ice (fy) and multi-year ice (my):

$$\Delta_{ow} = Tb_{ow}(atm\ 8) - Tb_{ow}(RRDP)$$

$$\Delta_{fy} = Tb_{fy}(atm\ 1) - Tb_{fy}(RRDP)$$

$$\Delta_{my} = Tb_{my}(atm\ 1) - Tb_{my}(RRDP)$$

Here $Tb(atm)$ refers to original tie points of NT2 at given atmosphere number and $Tb(RRDP)$ refers to the tie points from the RRDP2. Then this correction factor is subtracted from the original NT2 tie points at all atmospheres. The atmospheres number 1 and 8 (Table II in Markus and Cavalieri, 2000) were chosen for the tie point correction as the ones most often selected by the algorithm for consolidated ice and open water RRDP2 datasets respectively.

5.3.35 Alg6GHz

This algorithm takes 6 GHz V and 37 GHz V TBs as input as well as wind speed and skin temperature from ERA Interim. The algorithm uses a set of initial tie-points that are subsequently modified:

$$\begin{aligned} TB6V_{Ice} &= 255.2 \\ TB6V_W &= 162.67 \\ TB37V_W &= 215.71 \end{aligned}$$

It linearly interpolates between the 6V ice and water TPs to find a first guess SIC

$$SIC_0 = 1 - (TB6V_{Ice} - TB6V) / (TB6V_{Ice} - TB6V_W)$$

This first guess SIC is subsequently used to perform ocean surface correction of the input TBs (for the ocean fraction of the TB)

```
c      Quadratic wind correction
      TB6Vc = TB6V-(1-SIC0)*(0.0199*ws*ws-0.0039*ws)
```

Subsequently the 6 GHz TB can be converted to an estimated emissivity using the skin temperature from ERA Interim to compute the effective temperature according to results in the PVASR

```
c      Effective temperature for 6V
      SKT0 = 0.45*skt + 271.46*0.55
      e6V = TB6Vc/SKT0
```

Now the ice signature (emissivity) is computed using the 37V input to incorporate some ice type (MY vs FY) information

```
c      6V emissivity of ice from TB37V
      e6VI = 0.9645
      if(SIC0.gt.0.2) then
          TB37I = (TB37V-(1-SIC0)*TB37VW)/SIC0
          e6VI = 0.000244*TB37I + 0.9089
          e6VI = SIC0*e6VI + (1-SIC0)*0.9645
      endif
```

Finally the ice concentration (SIC) can be computed by linearly interpolating between the ocean surface emissivity and the ice emissivity

$$SIC = 100 - 100 * (e6VI - e6V) / (e6VI - 0.585)$$

Where 0.585 is the ocean surface emissivity at 6 GHz V polarisation and calm winds.

5.3.36 ASI_uncor

ASI_uncor is a modified version of the ASI algorithm (Spreen et al., 2008). ASI_uncor utilizes the polarisation difference in brightness temperatures at near 90 GHz (85 GHz for SSM/I, 89 GHz for AMSR-E and AMSR-2) to benefit from its higher spatial resolution. Different from the standard ASI algorithm, ASI_uncor uses modified tie points, and does not adopt any weather filter.

At near 90 GHz, the polarisation difference in the emissivity is similar for both first-year and multi-year ice, and is much lower than that of open ocean. Hence no ice type based tie points are needed. Based on the radiative transfer equation of microwave radiation presented by Svendsen (1987), the polarisation difference measured by satellite can be expressed as:

$$P = [CP_{ic} + (1-C)P_{ow}]a \quad (3-43-1)$$

$$P = [CP_{ic} + (1-C)P_{ow}]a \quad (3-43-2)$$

$$a = e^{-\tau} (1.1e^{-\tau} - 0.11) \quad (3-43-3)$$

where C is the total ice concentration, P_{ow} and P_{ic} are the typical polarisation difference of open water and consolidated ice at the surface, a is the atmospheric impact, and τ is the total opacity of the atmosphere.

By rearranging the equations (3-43-1) and (3-43-2), we get the total ice concentration as a function of measured polarisation:

$$C = (P/a - P_{ow}) / (P_{ic} - P_{ow}) \quad (3-43-4)$$

$$P_0 = aP_{ow} \quad (3-43-5)$$

$$P_1 = aP_{ic} \quad (3-43-6)$$

Applying Taylor expansion to the equation (3-43-3) around $C=0$ and $C=1$, neglecting all higher terms, we get:

$$C = \left(\frac{P}{P_0} - 1 \right) \left(\frac{P_{ow}}{P_{ic} - P_{ow}} \right) \quad \text{for } C \rightarrow 0 \quad (3-43-7)$$

$$C = \frac{P}{P_1} + \left(\frac{P}{P_1} - 1 \right) \left(\frac{P_{ow}}{P_{ic} - P_{ow}} \right) \quad \text{for } C \rightarrow 1 \quad (3-43-8)$$

For sea ice signature under Arctic conditions, $P_{ow}/(P_{ic} - P_{ow}) = -1.14$ is a typical value (Svendsen, 1987). To retrieve intermediate SIC, we interpolate between the above two equations with the third order polynomial:

$$C = d_3 P^3 + d_2 P^2 + d_1 P + d_0 \quad (3-43-9)$$

where the unknown coefficients d_i can be determined by the linear equation system:

$$\begin{bmatrix} P_0^3 & P_0^2 & P_0 & 1 \\ P_1^3 & P_1^2 & P_1 & 1 \\ 3P_0^3 & 2P_0^2 & P_0 & 0 \\ 3P_1^3 & 2P_1^2 & P_1 & 0 \end{bmatrix} \begin{bmatrix} d_3 \\ d_2 \\ d_1 \\ d_0 \end{bmatrix} = \begin{bmatrix} 0 \\ 1 \\ -1.14 \\ -0.14 \end{bmatrix} \quad (3-43-10)$$

The typical polarisation difference of open water (P_0) and closed ice (P_1) is essential for determining the coefficients of the third order polynomial to correctly retrieve the total ice concentration.

In nature, P_0 and P_1 are variable due to changes in the atmospheric influence and the radiometric property of water and ice. Such variability is especially pronounced during summer when melting and flooding events occur. Therefore, a careful choice of tie points is essential for determining the coefficients d_i of the

third order polynomial, and thus for correctly retrieving the total ice concentration.

Here we assume that the microwave signature of consolidated ice has little variation during winter, and thus using fixed tie points in the ice concentration retrieval. Instead of the standard tie points described in Spreen (2008), the tie points used here are chosen based on the average polarisation difference at near 90 GHz of the RRDP SIC1 and SIC0 data for AMSR-E and AMSR-2 as shown in Table 5-10: Tie points for Northern Hemisphere for ASI_uncor, ASI_cor, Lin_uncor and Lin_cor for AMSR sensors..

Algorithm	ASI_uncor & Lin_uncor		ASI_cor & Lin_cor	
Sensor Name	AMSR-E	AMSR-2	AMSR-E	AMSR-2
P0 (K)	39	39	70.5	70.9
P1 (K)	9.7	9.3	12.2	11.5

Table 5-10: Tie points for Northern Hemisphere for ASI_uncor, ASI_cor, Lin_uncor and Lin_cor for AMSR sensors.

Although AMSR-E and AMSR-2 have almost identical frequency channels, their calibrations are different resulting in inconsistency in the T_b measurements. To overcome this problem, we adopt the inter-calibration scheme provided by Okuyama and Imaoka (2015) to convert AMSR-2 observations L1B version 2, to equivalent AMSR-E T_b s L2A version 12, before inserting the values to the ice algorithm.

Weather influence such as atmospheric water vapour and cloud liquid water may cause false detection of sea ice over open water. The standard ASI algorithm uses two individual parameters, GR23 and GR36, to screen out such weather impacts. All pixels with GR23 higher than 0.04 or GR36 higher than 0.045 will be determined as false ice detection and their ice concentration would be set to zero. Other than that, an additional lower frequency ice algorithm (Bootstrap) is combined to filter out ice concentration lower than 5%. For a better inter-comparison with the other algorithms, ASI_uncor does not use any weather filter.

5.3.37 ASI_cor

This algorithm is similar to ASI-uncor, but has a retrieval curve closer to linear, due to the reduced atmospheric influence (Figure 5-10).

Traditional ice concentration algorithms often adopt external threshold-based filters to screen out weather impact over open water which causes false detection of ice. At higher microwave frequencies, the atmospheric influence is even more pronounced. However, such weather filters only work over the open ocean, and may exclude regions of low ice concentration. In this study, we take another approach to correct the weather influence by simulating changes in T_b s caused by the atmospheric water absorption/emission and wind roughened ocean surface scattering. The difference between T_b s simulated by a radiative transfer model (Wentz and Meissner, 2000) using clear atmosphere and collocated ECMWF Era-Interim atmosphere profile is interpreted as the T_b differences induced by weather effect, and is then subtended from the observed T_b s. New tie points are computed based on the average polarisation difference of the corrected T_b s of RRDP SIC0 and SIC1 data, which leads to new coefficients d_i for the linear equation system

(3-43-10). The corrected Tbs are then input to the new retrieval polynomial. This new algorithm is named as ASI_cor.

A first guess of surface classification and emissivity tie points are necessary for the radiative transfer model. Here we use the NasaTeam algorithm to retrieve the total ice concentration and multi-year ice fraction during the winter months, and utilize the monthly ice emissivity values provided in Mathew et al. (2009) as input to the forward model. Due to melting events during summer, the radiometric signature of first-year ice may appear similar to multi-year ice, which complicates ice type distinguishing. Also the atmospheric water content is often higher during summer, causing higher occurrence of false ice concentration detection over the ocean. In addition to that, the monthly first-year ice emissivities presented in Mathew et al. (2009) are problematic due to the melting events. Therefore, a different weather correction scheme is needed for summer, and new tie points as well. Details about summer tie points are described in Chapter 5.2.5. The summer correction scheme is still under investigation, and only the winter results are presented here. The plot below shows the retrieval curve of ASI_uncor and ASI_cor using AMSR-E and AMSR-2 tie points. Notice that after weather correction, the retrieval curve of ASI_cor is closer to a linear function. Since the non-linearity of the ASI algorithm is caused by the atmospheric absorption and emission, with those effects corrected from the Tbs, ideally the relationship between SIC and polarisation difference should be linear.

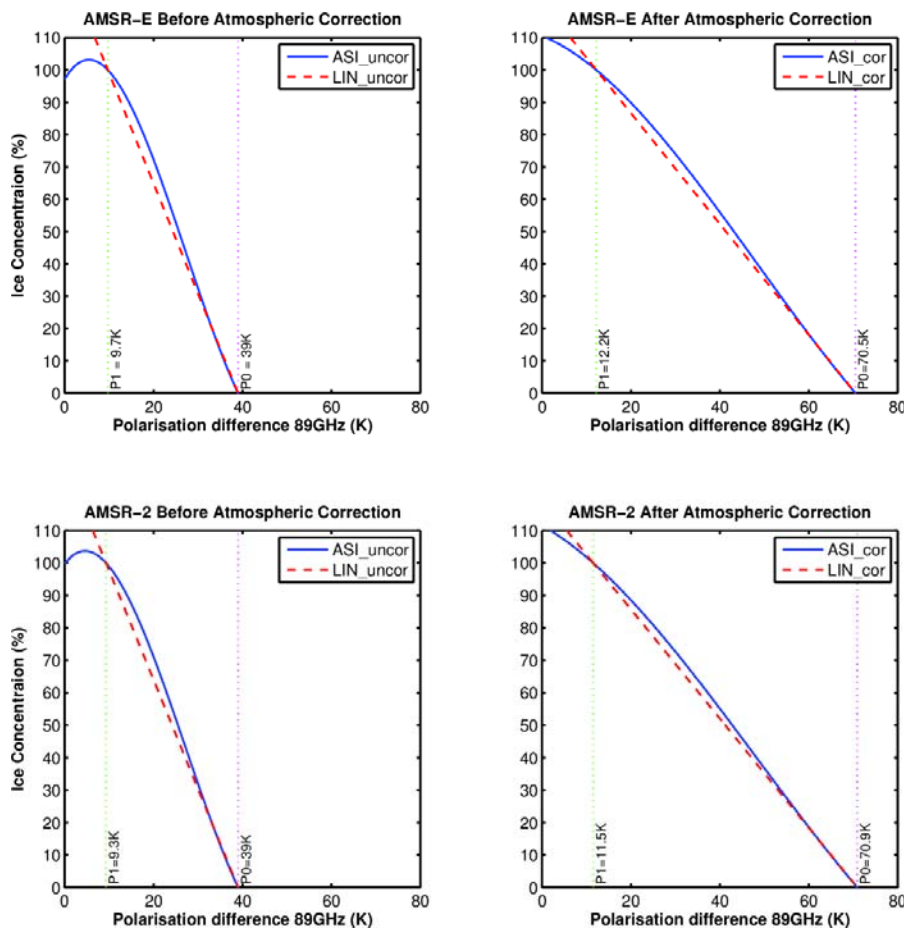


Figure 5-15: Total ice concentration as function of the polarisation difference at 89 GHz before (left panel) and after (right panel) weather correction using ASI (blue solid curves) and Lin90 (red dashed lines) algorithms. The top panel are the retrieval curves for AMSR-E, and the lower panel for AMSR-2.

5.3.38 LIN1

Lin90_uncor is a simplified version of ASI algorithm. Instead of a non-linear function, it assumes a linear relationship between the polarisation difference in Tbs at near 90 GHz with the total ice concentration. The core function of

$$\text{Lin_uncor is: } \frac{P-P_0}{P_1-P_0}$$

where P0 and P1 are typical polarisation difference in Tbs at near 90 GHz, C is the total ice concentration and P is the satellite measured polarisation difference. The tie points are the same as ASI_uncor and are shown in Table 5-10. The retrieval curves are shown as dashed red lines in the left panel of Figure 5-10.

5.3.39 LIN2

Lin90_cor is a modified version of Lin90_uncor using the same principal and different tie points. Instead of using the satellite measured Tbs as input to the ice retrieval algorithm, the Tbs are first corrected for weather influence using the method described in Chapter 5.3.37. The corrected Tbs are then input to the retrieval equation shown as dashed red lines in the right panel of Figure 5-10.

5.3.40 Optimal Estimation algorithm

5.4 Algorithm database computer code

5.4.1 Python code

```
import math
import numpy as np
import os
import glob
import datetime

def asi(tb85v, tb85h):
    # ASI
    P0 = 47.0 #The coefficients are checked with Christian Melsheimer (see e-mail from him to Leif Friday,
    # May 24, 2013 17:50). Same values are used for N and S. And for AMSR and SSM/I.
    P1 = 11.7
    A=np.matrix([[P1**3.0, P1**2.0, P1, 1.0],\
                 [P0**3.0, P0**2.0, P0, 1.0],\
                 [3.0*P1**3.0, 2.0*P1**2.0, P1, 0.0],\
                 [3.0*P0**3.0, 2.0*P0**2.0, P0, 0.0]])
    b=np.matrix([1.0, 0.0, -0.14, -1.14])

    d=A.I * b.T
    # d[0]=1.64/100000.0 d[1]=-0.0016 d[2]=0.0192 d[3]=0.971

    P = tb85v - tb85h
    C = d[0] * P**3 + d[1] * P**2 + d[2] * P + d[3]

    return C

def bootstrap_f(tb18v, tb37v, tiepts):
    tw18v = tiepts[6]
    tw37v = tiepts[0]
    tfy18v = tiepts[8]
    tfy37v = tiepts[2]
    tmy18v = tiepts[7]
```

```

tmy37v = tiepts[1]

if (tb18v-tw18v)==0: #open water
    cf=0.0
else:
    af = (tfy37v - tmy37v)/(tfy18v - tmy18v)
    bf = (tmy37v - af*tmy18v)
    qf = (tb37v - tw37v)/(tb18v - tw18v)
    wf = (tw37v - qf*tw18v)
    til8vf = (bf - wf)/(qf - af)
    cf = (tb18v - tw18v)/(til8vf - tw18v)
return cf

def bootstrap_p(tb37v, tb37h, tiepts):

    tw37h = tiepts[3]
    tw37v = tiepts[0]
    tfy37h = tiepts[5]
    tfy37v = tiepts[2]
    tmy37h = tiepts[4]
    tmy37v = tiepts[1]

    if (tb37h-tw37h)==0: #open water
        cp=0.0
    else:
        ap = (tfy37v - tmy37v) / (tfy37h - tmy37h)
        bp = (tmy37v - ap * tmy37h)
        qp = (tb37v - tw37v) / (tb37h - tw37h)
        wp = (tw37v - qp * tw37h)
        if (qp - ap)==0:
            cp=-9.98
        else:
            ti37hp = (bp - wp) / (qp - ap)
            ti37vp = ap * ti37hp + bp
            if (ti37vp - tw37v)==0:
                cp=-9.98
            else:
                cp = (tb37v - tw37v) / (ti37vp - tw37v)
    return cp

def bristol(tb18v, tb37v, tb37h, tiepts):
    #Bristol ice concentration algorithm

    tw18v = tiepts[6]
    tw37h = tiepts[3]
    tw37v = tiepts[0]
    tfy18v = tiepts[8]
    tfy37h = tiepts[5]
    tfy37v = tiepts[2]
    tmy18v = tiepts[7]
    tmy37h = tiepts[4]
    tmy37v = tiepts[1]

    xa = tmy37v + (1.045*tmy37h) + (0.525*tmy18v)
    xd = tfy37v + (1.045*tfy37h) + (0.525*tfy18v)
    xh = tw37v + (1.045*tw37h) + (0.525*tw18v)
    xt = tb37v + (1.045*tb37h) + (0.525*tb18v)

    ya = (0.9164*tmy18v) - tmy37v + (0.4965*tmy37h)
    yd = (0.9164*tfy18v) - tfy37v + (0.4965*tfy37h)
    yh = (0.9164*tw18v) - tw37v + (0.4965*tw37h)
    yt = (0.9164*tb18v) - tb37v + (0.4965*tb37h)

    a_ht = (yt - yh)/(xt - xh)
    b_ht = yh - (a_ht*xh)
    a_da = (ya - yd)/(xa - xd)
    b_da = yd - (a_da*xd)

    xi = (b_da - b_ht)/(a_ht - a_da)
    cf = (xt - xh)/(xi - xh)
    c = cf
    return c

def calval(tb37v, tb18v, tiepts):

    tw18v = tiepts[6]
    tw37v = tiepts[0]
    tfy18v = tiepts[8]
    tfy37v = tiepts[2]
    tmy18v = tiepts[7]

```

```

tmy37v = tiepts[1]

A=np.matrix([[tw37v, tw18v, 1.0],\
             [tfy37v, tfy18v, 1.0],\
             [tmy37v, tmy18v, 1.0]])

b=np.matrix([0.0, 1.0, 1.0])

d=A.I * b.T
C=d[0]*tb37v+d[1]*tb18v+d[2]

return C

def nasa(tb18v, tb18h, tb37v, tiepts):
    #NASA-Team ice concentration algorithm

    ow18v = tiepts[6]
    ow18h = tiepts[9]
    ow37v = tiepts[0]
    fy18v = tiepts[8]
    fy18h = tiepts[11]
    fy37v = tiepts[2]
    my18v = tiepts[7]
    my18h = tiepts[10]
    my37v = tiepts[1]

    a0 = - ow18v + ow18h
    a1 = ow18v + ow18h
    a2 = my18v - my18h - ow18v + ow18h
    a3 = - my18v - my18h + ow18v + ow18h
    a4 = fy18v - fy18h - ow18v + ow18h
    a5 = - fy18v - fy18h + ow18v + ow18h

    b0 = - ow37v + ow18v
    b1 = ow37v + ow18v
    b2 = my37v - my18v - ow37v + ow18v
    b3 = - my37v - my18v + ow37v + ow18v
    b4 = fy37v - fy18v - ow37v + ow18v
    b5 = - fy37v - fy18v + ow37v + ow18v

    gr = (tb37v - tb18v)/(tb37v + tb18v)
    pr = (tb18v - tb18h)/(tb18v + tb18h)

    d0 = (-a2*b4) + (a4*b2)
    d1 = (-a3*b4) + (a5*b2)
    d2 = (-a2*b5) + (a4*b3)
    d3 = (-a3*b5) + (a5*b3)

    dd = d0 + d1*pr + d2*gr + d3*pr*gr

    f0 = (a0*b2) - (a2*b0)
    f1 = (a1*b2) - (a3*b0)
    f2 = (a0*b3) - (a2*b1)
    f3 = (a1*b3) - (a3*b1)
    m0 = (-a0*b4) + (a4*b0)
    m1 = (-a1*b4) + (a5*b0)
    m2 = (-a0*b5) + (a4*b1)
    m3 = (-a1*b5) + (a5*b1)

    cf = (f0 + f1*pr + f2*gr + f3*pr*gr)/dd
    cm = (m0 + m1*pr + m2*gr + m3*pr*gr)/dd

    ct = cm + cf
    return ct, cm

def near90(tb85v, tb85h, tiepts):
    #tmy85v = tiepts[30]
    tfy85v = tiepts[31]
    #tmy85h = tiepts[32]
    tfy85h = tiepts[33]
    tw85v = tiepts[34]
    tw85h = tiepts[35]

    P = tb85v - tb85h
    P0 = tw85v - tw85h
    P1 = tfy85v - tfy85h

```

```

A=np.matrix([[P1**3.0, P1**2.0, P1, 1.0],\
             [P0**3.0, P0**2.0, P0, 1.0],\
             [3.0*P1**3.0, 2.0*P1**2.0, P1, 0.0],\
             [3.0*P0**3.0, 2.0*P0**2.0, P0, 0.0]])
b=np.matrix([1.0, 0.0, -0.14, -1.14])

d=A.I * b.T

#d=np.linalg.solve(A,b.T)
C = d[0] * P**3 + d[1] * P**2 + d[2] * P + d[3]
return np.float(C)

def near90_linear_dyn(tb85v, tb85h, tiepts):
    tmy85v = tiepts[30]
    tfy85v = tiepts[31]
    tmy85h = tiepts[32]
    tfy85h = tiepts[33]
    tw85v = tiepts[34]
    tw85h = tiepts[35]

    PFY = tfy85v - tfy85h
    PMY = tmy85v - tmy85h
    PW = tw85v - tw85h

    PI = (PFY + PMY)/2
    P = tb85v - tb85h

    c = (P - PW) / (PI-PW)

    return c

def norsex(tb18v, tb37v, sensor_name, lat):
    SAT = 260.0
    T_sa = 270.0
    T_a = 250.0
    To = 272.0

    tau_sa19v = 0.0610
    tau_sa37v = 0.1000
    tau_a19v = 0.0440
    tau_a37v = 0.0700
    TB_w_19v, TB_w_37v, TB_fy_19v, TB_fy_37v, TB_my_19v, TB_my_37v = norsex_TPs(sensor_name, lat)
    t_atm_surf=SAT #Initialize atmospheric surface temperature

    for i in range(0,2):

        #interpolate opacity between arctic and subarctic values:
        tau19v = tau_a19v + (t_atm_surf - T_a) * (tau_sa19v - tau_a19v) / (T_sa - T_a)
        tau37v = tau_a37v + (t_atm_surf - T_a) * (tau_sa37v - tau_a37v) / (T_sa - T_a)

        #Constants to be used in computing ice concentrations:
        a11 = TB_fy_19v - TB_w_19v
        a21 = TB_fy_37v - TB_w_37v
        a12 = TB_my_19v - TB_w_19v
        a22 = TB_my_37v - TB_w_37v
        d_coef = a11 * a22 - a12 * a21

        #find emitted brightness temperature at the surface by correcting for
        #atmospheric disturbances:
        TB_surf_19v = (tb18v - t_atm_surf * (2.0 * tau19v - tau19v**2.0 + 0.01)) / (1.0 - 2.0 * tau19v +
        tau19v**2.0 - 0.01)
        TB_surf_37v = (tb37v - t_atm_surf * (2.0 * tau37v - tau37v**2.0 + 0.01)) / (1.0 - 2.0 * tau37v +
        tau37v**2.0 - 0.01)

        #Find new atmospheric surface brightness temperature and mean surface
        #emissions by solving for first year and multi-year ice concentrations.
        c1 = TB_surf_19v - TB_w_19v
        c2 = TB_surf_37v - TB_w_37v
        Cmy = (a11 * c2 - a21 * c1) / d_coef
        Cfy = (a22 * c1 - a12 * c2) / d_coef
        CT = Cfy + Cmy

        t_atm_surf = To + (SAT - To) * CT

    return CT

def P37(tb37v, tb37h, tiepts):
    # instead of NRL
    tw37h = tiepts[3]
    tw37v = tiepts[0]

```

```

tfy37h = tiepts[5]
tfy37v = tiepts[2]
tmy37h = tiepts[4]
tmy37v = tiepts[1]

PFY = tfy37v - tfy37h
PMY = tmy37v - tmy37h
PW = tw37v - tw37h

PI = (PFY + PMY)/2
P = tb37v - tb37h

c = (P - PW) / (PI-PW)

return c

def onechannel(tb6h, tiepts):
    #Simple 1 channel algorithm

    fy6h = tiepts[17]
    my6h = tiepts[16]

    ow6h = 82.3
    i6h = (fy6h+my6h)/2.0

    ct = (tb6h - ow6h)/(i6h - ow6h)
    return ct

def osisaf(c0,c1,t):

    wc = (abs(t - c0) + t - c0) / (2.0 * t)
    c = c1 * (1.0 - wc) + wc * c0
    if c0 < 0:
        c = c0

    return c

def sicci(c0,c1):

    if c0<0.7:
        wCF=1.0

    if (c0 >= 0.7 and c0 < 0.9):
        wCF=1.0-(c0-0.7)/(0.9-0.7)

    if c0 >= 0.9:
        wCF=0.0

    wBR = 1.0-wCF

    c = c0 * wCF + c1 * wBR

    return c

def P90(tb85v, tb85h):
    X=(tb85v-tb85h)
    P=(X-2.63)/0.752

    d3=1.64/100000.0
    d2=-0.0016
    d1=0.0192
    d0=0.971

    c1 = d3 * P**3.0 + d2 * P**2.0 + d1 * P + d0

    c = c1+(P-8)/700 #to adjust near SIC0
    if (P>48):
        c=-0.026 #to prevent large P85 giving ice
    if (P<8.5):
        c=1.03 #to prevent low P85 losing ice

    return c

def pr(tb18v, tb18h, tb37v, tb37h, tiepts):
    #Simple polarization ratio algorithm

    ow18v = tiepts[6]
    ow18h = tiepts[9]
    ow37v = tiepts[0]
    ow37h = tiepts[3]
    fyl8v = tiepts[8]

```

```

fy18h = tiepts[11]
fy37v = tiepts[2]
fy37h = tiepts[5]
my18v = tiepts[7]
my18h = tiepts[10]
my37v = tiepts[1]
my37h = tiepts[4]

i18v = (fy18v+my18v)/2
i18h = (fy18h+my18h)/2
i37v = (fy37v+my37v)/2
i37h = (fy37h+my37h)/2

PR18 = (tb18v - tb18h)/(tb18v + tb18h)
PR37 = (tb37v - tb37h)/(tb37v + tb37h)

c18 = (ow18v*(1 - PR18) - ow18h*(1 + PR18))/(PR18*(i18v + i18h - ow18v - ow18h) - (i18v - i18h - ow18v
+ ow18h))
c37 = (ow37v*(1 - PR37) - ow37h*(1 + PR37))/(PR37*(i37v + i37h - ow37v - ow37h) - (i37v - i37h - ow37v
+ ow37h))
c_old = (c18 + c37)/2
c = c_old/(2-c_old)

return c, PR18, PR37

def tud(c85, cf):
    #TUD ice concentration algorithm

    if ((c85>0) & (cf>10)):
        c = np.sqrt(cf*c85)
    else:
        c = cf

    return c

def P10(tb10v, tb10h, tiepts):
    #Simple 2 channel algorithm 10 GHz

    tw10h = tiepts[21]
    tw10v = tiepts[18]
    tfy10h = tiepts[23]
    tfy10v = tiepts[20]
    tmy10h = tiepts[22]
    tmy10v = tiepts[19]

    PFY = tfy10v - tfy10h
    PMY = tmy10v - tmy10h
    PW = tw10v - tw10h

    PI = (PFY + PMY)/2
    P = tb10v - tb10h

    c = (P - PW) / (PI-PW)

    return c

def P18(tb18v, tb18h, tiepts):

    tw18v = tiepts[6]
    tw18h = tiepts[9]
    tfy18v = tiepts[8]
    tfy18h = tiepts[11]
    tmy18v = tiepts[7]
    tmy18h = tiepts[10]

    PFY = tfy18v - tfy18h
    PMY = tmy18v - tmy18h
    PW = tw18v - tw18h

    PI = (PFY + PMY)/2
    P = tb18v - tb18h

    c = (P - PW) / (PI-PW)

    return c

def UMass(tb18v, tb37v, tiepts):
    #The code is based on C. T. Swift, L. S. Fedor, and R. O. Ramseier, ?An Algorithm
    #to Measure Sea Ice Concentration With Microwave Radiometers,? Journal of Geophysical
    #Research, vol. 90, no. C1, pages 1087 - 1099, 1985.

    tw19v = tiepts[6]
    tw37v = tiepts[0]

```

```

tfy19v = tiepts[8]
tfy37v = tiepts[2]
tmy19v = tiepts[7]
tmy37v = tiepts[1]

#solution of the equations (11)-(12) in Swift et al 1985
#here we use brightness temperatures instead!! (Rasmus 2012)
#e19v=(TB19v-13)/(Ts-12);
#e37v=(TB37v-26)/(Ts-26);

a1 = (tfy19v - tb18v) / (tfy19v - tw19v)
a2 = (tfy19v - tmy19v) / (tfy19v - tw19v)
a3 = (tfy37v - tb37v) / (tfy37v - tmy37v)
a4 = (tfy37v - tw37v) / (tfy37v - tmy37v)
fw = (a1 - a2 * a3) / (1.0 - a2 * a4)

Cmy = a3 - fw * a4
Cfy = 1.0 - fw - Cmy
CT = Cmy + Cfy
return CT

def norsex_TPs(sensor_name,lat):
# values produced by Leif, described in PVASR
if lat >= 0:
# Northern hemisphere:
if (sensor_name == 'AMSRE' or sensor_name == 'AMSR2'):
TB_w_19v = 170.01
TB_w_37v = 193.19
TB_fy_19v = 251.17
TB_fy_37v = 244.47
TB_my_19v = 222.11
TB_my_37v = 184.02
elif sensor_name == 'SSM/I':
TB_w_19v = 171.56
TB_w_37v = 191.87
TB_fy_19v = 251.91
TB_fy_37v = 241.53
TB_my_19v = 219.20
TB_my_37v = 175.93
elif sensor_name == 'SMMR':
TB_w_19v = 162.61
TB_w_37v = 190.80
TB_fy_19v = 251.17
TB_fy_37v = 244.47
TB_my_19v = 222.11
TB_my_37v = 184.02

elif lat < 0:
# Southern hemisphere:
if (sensor_name == 'AMSRE' or sensor_name == 'AMSR2'):
TB_w_19v = 171.86
TB_w_37v = 196.65
TB_fy_19v = 258.41
TB_fy_37v = 252.57
TB_my_19v = 244.39
TB_my_37v = 219.62
elif sensor_name == 'SSM/I':
TB_w_19v = 171.52
TB_w_37v = 192.94
TB_fy_19v = 259.93
TB_fy_37v = 253.25
TB_my_19v = 244.59
TB_my_37v = 219.59
elif sensor_name == 'SMMR':
TB_w_19v = 160.77
TB_w_37v = 190.92
TB_fy_19v = 258.41
TB_fy_37v = 252.57
TB_my_19v = 244.39
TB_my_37v = 219.62

return TB_w_19v, TB_w_37v, TB_fy_19v, TB_fy_37v, TB_my_19v, TB_my_37v

# TL (14.01.2013) separate algorithms from main function to allow reuse
# of the algs by importing the ic_algs.py file from elsewhere
if __name__ == '__main__':
#sensor_name = 'AMSRE'
sensor_name = 'AMSR2'
filelist = glob.glob(os.path.join('/media/sf_Work/ESA_CCI/RRDP2/ASCAT-vs-AMSRx-vs-ERA-vs-
allfiles_0.93/' + sensor_name + '/*.text'))
now = datetime.datetime.now()

```

```

for filename in filelist:
    #open input RRDp file
    f1 = open(filename)
    lines = f1.readlines()
    f1.close()
    print filename
    if sensor_name == 'AMSRE':
        filename_o = os.path.join('RRDP2_SIC/' + sensor_name + '/' + filename[74:112] + '-SIC-' +
now.strftime("%Y-%m-%d") + '.txt')
    if sensor_name == 'AMSR2':
        filename_o = os.path.join('RRDP2_SIC/' + sensor_name + '/' + filename[74:113] + '-SIC-' +
now.strftime("%Y-%m-%d") + '.txt')

    f2 = open(filename_o, 'wt')

    k=0
    for line in lines:

        if k > 1:
            line = line.replace('noval0', '-999')
            line = line.replace('noval1', '-999')
            line = line.replace('noval2', '-999')
            line = line.replace('noval3', '-999')
            line = line.replace('noval4', '-999')
            line = line.replace('noval5', '-999')
            line = line.replace('noval6', '-999')
            line = line.replace('noval', '-999')
            line = line.replace('-inf', '-999')

        l = line.strip()
        #f2.write(l)
        k=k+1
        if k == 1:
            f2.write(l)
            f2.write('\n')

        l2 = l.split(',')
        try:
            v1 = float(l2[0])
        except:

            if k==2:
                f2.write(l)
                f2.write('%s\n' %
('Near90_lin_dyn,Near90GHz,ASI,P90,P37,Bootstrap_p,P18,Bristol,PR,NASA_Team,NORSEX,Bootstrap_f,CalVal,UMas
s_AES,P10,One_channel,TUD,bf_nt,bf_nt_n90ld,p37_n90ld,p37_n90ld_bf,bf2_n90ld,bf3_n90ld,bf_n90ld,bf_bfn90ld,
osisaf,SICCI'))
            #else:
            #f2.write('\n')
        else:

            tb6v = float(l2[37])
            tb6h = float(l2[36])
            tb10v = float(l2[41])
            tb10h = float(l2[40])
            tb18v = float(l2[43])
            tb18h = float(l2[42])
            tb22v = float(l2[45])
            tb22h = float(l2[44])
            tb37v = float(l2[47])
            tb37h = float(l2[46])
            tb85v = float(l2[49])
            tb85h = float(l2[48])

            if (k==3 and float(l2[0]) >= 0):
                print 'Northern hemisphere'
            if (k==3 and float(l2[0]) < 0):
                print 'Southern hemisphere'

            #tiepts: w37v my37v fy37v w37h my37h fy37h
            # w18v my18v fy18v w18h my18h fy18h
            # w6v my6v fy6v w6h my6h fy6h
            # w10v my10v fy10v w10h my10h fy10h
            # w22v my22v fy22v w22h my22h fy22h
            # my85v fy85v my85h fy85h w85v w85h

            if sensor_name == 'AMSRE':
                # Northern Hemisphere tie-points:
                if float(l2[0]) >= 0:
                    #print 'Northern hemisphere'
                    #AMSR: #water from Tiepoints_20130117.xls e-mail from Leif Jan 17,20130 at 14:41,
Ice hard copy 8 Apr, 2013: 2007-2011. MY: 15% lowest 37H months 1-4+10-12. FY: 15% highest 37H months1-

```

```

4+10-12
    tiepts = [209.81, 196.91, 247.13, 145.29, 184.94, 235.01, 183.72, 226.26, 252.15,
108.46, 207.78, 237.54, 161.35, 246.04, 251.99, 82.13, 221.19, 232.08, 167.34, 239.61, 251.34, 88.26,
216.31, 234.01, 196.41, 216.67, 250.87, 128.23, 199.6, 236.72, 187.6, 232.01, 178.9, 222.39, 243.2, 196.94]
    elif float(l2[0]) < 0:
        #print 'Southern hemisphere'
        # Southern Hemisphere tie-points:
        #AMSR: #water from Tiepoints_latest_S.xlsx e-mail from Leif Jan 31,2013 at 21:51,
Ice hard copy 8 Apr, 2013: 2007-2011. MY: 15% lowest 37H months 5-11. FY: 15% highest 37H months 5-11
        tiepts = [212.57, 226.51, 253.84, 149.07, 204.66, 239.96, 185.34, 246.1, 258.58,
110.83, 217.65, 242.8, 159.69, 254.18, 257.04, 80.15, 225.37, 236.52, 166.31, 251.65, 257.23, 86.62,
221.47, 238.5, 201.53, 240.65, 257.56, 137.19, 213.79, 242.61, 210.22, 242.81, 197.78, 232.4, 247.59,
207.2]
    else:
        print('hemisphere not defined')

    if sensor_name == 'AMSR2': #.xls files in the e-mail from Leif 16 Oct 2015 21:54:15 CEST,
Subject: RE: AMSR2 TPs for RRD2_v0.9
        if float(l2[0]) >= 0:
            #print 'Northern hemisphere'
            tiepts = [215.71, 191.70, 254.91, 152.80, 178.15, 241.86, 190.71, 227.11, 260.96,
114.08, 204.34, 244.51, 162.68, 250.07, 259.51, 82.76, 224.60, 240.67, 171.29, 245.54, 261.26, 90.29,
219.95, 244.00, 207.78, 213.99, 260.24, 145.43, 195.45, 246.14, 191.37, 238.09, 180.97, 228.58, 249.23,
210.55]
            elif float(l2[0]) < 0:
                #print 'Southern hemisphere'
                tiepts = [215.23, 219.68, 251.23, 153.39, 197.66, 232.68, 190.03, 244.08, 260.73,
114.11, 212.37, 239.19, 161.52, 256.38, 260.58, 83.08, 225.74, 238.20, 170.67, 254.78, 262.38, 91.06,
223.55, 241.31, 205.70, 236.81, 259.00, 142.84, 208.80, 239.51, 211.59, 241.11, 200.12, 229.20, 246.66,
207.92]
            else:
                print('hemisphere not defined')

    if ((float(l2[4]) == 0.0 and float(l2[1]) != -45.0) or float(l2[4]) == 1.0):
        CT_bootstrap_f = bootstrap_f(tb18v, tb37v, tiepts)
        CT_bootstrap_p = bootstrap_p(tb37v, tb37h, tiepts)
        CT_bristol = bristol(tb18v, tb37v, tb37h, tiepts)
        CT_calval = calval(tb37v, tb18v, tiepts)
        CT_nasa, CMY = nasa(tb18v, tb18h, tb37v, tiepts)
        CT_norsex = norsex(tb18v, tb37v, sensor_name, float(l2[0]))
        CT_P37 = P37(tb37v, tb37h, tiepts)
        CT_P18 = P18(tb18v, tb18h, tiepts)
        CT_pr, PR18, PR37 = pr(tb18v, tb18h, tb37v, tb37h, tiepts)
        CT_UMass = UMass(tb18v, tb37v, tiepts)

        CT_bf_nt = (CT_bootstrap_f + CT_nasa)/2.0
        CT_osisaf = osisaf(CT_bootstrap_f, CT_bristol, 0.4)
        CT_sicci = sicci(CT_bootstrap_f, CT_bristol)
        CT_asi = asi(tb85v, tb85h)
        CT_near90 = near90(tb85v, tb85h, tiepts)
        CT_near90_linear_dyn = near90_linear_dyn(tb85v, tb85h, tiepts)
        CT_P90 = P90(tb85v, tb85h)
        CT_tud = tud(CT_near90_linear_dyn, CT_bootstrap_f)

        CT_bf_nt_n90ld = (CT_bootstrap_f + CT_nasa + CT_near90_linear_dyn)/3.0
        CT_p37_n90ld = (CT_P37 + CT_near90_linear_dyn)/2.0
        CT_p37_n90ld_bf = (CT_P37 + CT_near90_linear_dyn + CT_bootstrap_f)/3.0
        CT_bf2_n90ld =
(CT_bootstrap_f+(CT_bootstrap_f**2.0)*CT_near90_linear_dyn)/(1.0+CT_bootstrap_f**2.0)
        CT_bf3_n90ld =
(CT_bootstrap_f+(CT_bootstrap_f**3.0)*CT_near90_linear_dyn)/(1.0+CT_bootstrap_f**3.0)
        CT_bf_n90ld = (CT_bootstrap_f+CT_near90_linear_dyn)/2.0
        CT_bf_bfn90ld =
(CT_bootstrap_f+CT_bootstrap_f*CT_near90_linear_dyn)/(1.0+CT_bootstrap_f)
        CT_onechannel = onechannel(tb6h, tiepts)
        CT_P10 = P10(tb10v, tb10h, tiepts)

        if (tb18v < -900 or tb37v < -900 or tb37h < -900 or tb18h < -900 or tb85v < -900 or
tb85h < -900 or tb6h < -900 or tb10v < -900 or tb10h < -900 or tb6v < -900):
            CT_bootstrap_f = -9.99
            CT_bootstrap_p = -9.99
            CT_bristol = -9.99
            CT_calval = -9.99
            CT_nasa = -9.99
            CT_norsex = -9.99
            CT_P37 = -9.99
            CT_P18 = -9.99
            CT_pr = -9.99
            CT_UMass = -9.99

            CT_bf_nt = -9.99
            CT_osisaf = -9.99

```

```

CT_sicci = -9.99
CT_asi = -9.99
CT_near90 = -9.99
CT_near90_linear_dyn = -9.99
CT_P90 = -9.99
CT_tud = -9.99

CT_bf_nt_n90ld = -9.99
CT_p37_n90ld = -9.99
CT_p37_n90ld_bf = -9.99
CT_bf2_n90ld = -9.99
CT_bf3_n90ld = -9.99
CT_bf_n90ld = -9.99
CT_bf_bfn90ld = -9.99
CT_onechannel = -9.99
CT_P10 = -9.99

f2.write(1)

f2.write('%s%.6f%s%.6f%s%.6f%s%.6f%s%.6f%s%.6f%s%.6f%s%.6f%s%.6f%s%.6f%s%.6f%s%.6f%s%.6f%s%.6f\n' %
(' ',CT_near90_linear_dyn*100,' ',CT_near90*100,' ', CT_asi*100,' ', CT_P90*100,' ', CT_P37*100,' ',
CT_bootstrap_p*100,' ', CT_P18*100,' ', CT_bristol*100,' ', CT_pr*100,' ', CT_nasa*100,' ',
CT_norsex*100,' ', CT_bootstrap_f*100,' ', CT_calval*100,' ', CT_UMass*100,' ', CT_P10*100,' ',
CT_onechannel*100,' ', CT_tud*100,' ', CT_bf_nt*100,' ', CT_bf_nt_n90ld*100,' ', CT_p37_n90ld*100,' ',
CT_p37_n90ld_bf*100,' ', CT_bf2_n90ld*100,' ', CT_bf3_n90ld*100,' ', CT_bf_n90ld*100,' ',
CT_bf_bfn90ld*100,' ', CT_osisaf*100,' ', CT_sicci*100))

f2.close()

```

5.4.2 Additional algorithms in IDL and MatLab

5.4.2.1 NASA Team2 – corr (MatLab)

```

% load original tie points: tbmcc, tbmow, tbmfy, tbmthin
% tbmcc: ice type c (ice having significant surface effects)

% Brightness temperatures: v19i, h19i, TB22v, TB37v, v85i, h85i

% RRDP2 tie points:
ow_rrdp = [ow18h ow18v ow22v ow37h ow37v ow89h ow89v];
fy_rrdp = [fy18h fy18v fy22v fy37h fy37v fy89h fy89v];
my_rrdp = [my18h my18v my22v my37h my37v my89h my89v];

% correct tie points of NT2:
ow_corr = tbmow(9,:) - ow_rrdp;
fy_corr = tbmfy(2,:) - fy_rrdp;
my_corr = tbmcc(2,:) - my_rrdp;

tbmow = tbmow - repmat(ow_corr,12,1);
tbmfy = tbmfy - repmat(fy_corr,12,1);
tbmcc = tbmcc - repmat(my_corr,12,1);

% The NT2 algorithm:
GR1=(TB37v-v19i)./(TB37v+v19i);
GR2=(TB22v-v19i)./(TB22v+v19i);

n_atm=12; % number of atmospheres (models of atmosphere)
%Rotation:
phi19=-0.18; % angle in radians between GR-axis and A-B line (FY-MY line) for the PR(19)-GR(37V19V)
domain, Arctic;
phi85=-0.06; % same for the PR(85)-GR(37V19V)

% Create lookup table (extended SIC range)
for ca=-20:150
    for cb=-20:(150-ca)
        caf=ca/100;
        cbf=cb/100;
        for k=1:n_atm
            tb19h=(1-caf-cbf)*tbmow(k,1)+caf*tbmfy(k,1)+cbf*tbmcc(k,1);
            tb19v=(1-caf-cbf)*tbmow(k,2)+caf*tbmfy(k,2)+cbf*tbmcc(k,2);
            tb37v=(1-caf-cbf)*tbmow(k,5)+caf*tbmfy(k,5)+cbf*tbmcc(k,5);
            tb85h=(1-caf-cbf)*tbmow(k,6)+caf*tbmfy(k,6)+cbf*tbmcc(k,6);
            tb85v=(1-caf-cbf)*tbmow(k,7)+caf*tbmfy(k,7)+cbf*tbmcc(k,7);

            tb19ht=(1-caf-cbf)*tbmow(k,1)+caf*tbmfy(k,1)+cbf*tbmthin(k,1);

```



```

        ca=ca+imin;
        cc=cc+jmin;
    end
    camina(k)=ca-21;
    ccmina(k)=cc-21;
    dmina(k)=dmin;
end

bestk=20;
dmin=1000;
for k=1:n_atm
    if dmina(k) < dmin
        dmin=dmina(k);
        bestk=k;
    end
end
atm_num(x) = bestk;
dmin2(x) = dmin;
icecon(x)=camina(bestk)+ccmina(bestk);
else
    icecon(x)=-999;
    atm_num(x) = -999;
    dmin2(x) = -999;
end
end
end

```

5.4.2.2 VASIA (MatLab)

```

% 1. Calculate the tangents 85-37h, 85-19v and 37-19v:
t85_37h = (tb85h - tb37h) ./ (85.5 - 37);
t85_19v = (tb85v - tb18v) ./ (85.5 - 19.35);
t37_19v = (tb37v - tb18v) ./ (37 - 19.35);

% 2&3 Criterion function F1
%I = 0:0.1:10; original algorithm
I = -15:0.1:25; % extended SIC range
f85_37h = -0.085.*I + 0.908;
f85_19v = -0.086.*I + 0.55;

for i=1:length(t85_37h)

    %VASIA1:
    F1 = 0.5.*(((f85_37h - t85_37h(i)).^2) ./ (t85_37h(i)^2) + ((f85_19v - t85_19v(i)).^2) ./
(t85_19v(i)^2));
    [min_value,min_index] = min(F1);
    I1 = I(min_index);
    clear min_value min_index

    %VASIA2:
    phi85_37h = -0.039.*I + 1.19;
    phi85_19v = -0.04.*I + 0.7;
    F2 = 0.5.*(((phi85_37h - t85_37h(i)).^2) ./ (t85_37h(i)^2) + ((phi85_19v - t85_19v(i)).^2) ./
(t85_19v(i)^2));
    [min_value,min_index] = min(F2);
    I2 = I(min_index);

    % 5&6 VASIA or VASIA2
    delta37_19v = -0.187.*I1 + 1.1;

    if delta37_19v < t37_19v(i)
        I3 = I1;
    else
        I3 = I2;
    end

    vasia1(i) = 100*I1/10;
    vasia2(i) = 100*I2/10;
    vasia_combo(i) = 100*I3/10;

end
end

```

5.4.2.3 IDL code for ASI and LIN algorithms

```

;*****
FUNCTION range01,img
; Cut off CT<0% and CT>100%

```

```

ind=where(img gt 1.0,count)
if count ne 0 then img(ind)=1.0
ind=where(img lt 0.0,count)
if count ne 0 then img(ind)=0.0
return,img
END ; range01
; ice = lin90(polarisation89, p0, p1, /nocutoff)
;
p0 = double(p0)
p1 = double(p1)
a = [[p1,1],[p0,1]]
b = [1,0]
; condition of matrix a;
;*****

FUNCTION lin90, polarisation89, p0, p1, nocutoff=nocutoff
; #NAME
;   lin90
; #PURPOSE:
;   retrieve Cis using polarisation difference at 89 GHz.
; #Keyword:
;   nocutoff: SIC can be outside the range [0,1]
; #USAGE:
cond=COND(a,/DOUBLE)
; Solving the equation system using Cramer's rule
solvc=CRAMER(a,b,/DOUBLE)
; Solving the equation system using the routine lubksb described in section 2.3 of Numerical
Recipes
in C: The Art of Scientific Computing (Second Edition)
LUDC,a,ind
solvlu=LUSOL(a,ind,b)
d=solvc
test = TOTAL(FLOAT(solvc) EQ FLOAT(solvlu))
IF test NE 2 THEN BEGIN
PRINT, 'Function lin90 : An error ocured solving the equation system.'
STOP
ENDIF
lin_ct = d[0]*polarisation89 + d[1]
if keyword_set(nocutoff) then c = lin_ct else begin
; set sic = 0 where p89>p0
; set sic = 1 where p89<p1
p11=WHERE(polarisation89 LT p1)
; help,p11
if p11[0] NE -1 then lin_ct[p11]=1.
pg0=WHERE(polarisation89 GT p0)
IF pg0[0] NE -1 THEN lin_ct[pg0]=0.
; Cut off CT<0% and CT>100%
Error: Reference source not found
Ref. Error: Reference source not found
c=range01(lin_ct)
endelse
return,c
end ; lin90
;*****
;*****
;*****

FUNCTION asi_bootstrap, polarization89, p0, p1, bootstrap_ct=bootstrap_ct, thresh=thresh,
nocutoff=nocutoff
;+
;NAME:
; asi_bootstrap
;PURPOSE:
;This is the core function, the ARTIST Sea Ice algorithm: It
;translates the given near-90GHz polarisation difference into ice
;concentration, given the two "tie points", i.e. pol. difference for
;open water and sea ice, and the bootstrap ice concentration which is
;used as a kind of weather filter,i.e. ice concentration is considered
;0 where bootstrap ice concentration is below a threshold value.
;USAGE:
;ice = asi_bootstrap(polarization89, p0, p1, bootstrap_ct, thresh)
;INPUT PARAMETERS:
;polarisation89: near-90GHz polarisation difference, i.e. TbV - TbH [array]
;   p0,p1: pol. difference for open water and sea ice,
;           respectively [float]
;   bootstrap_ct: Bootstrap ice concentration [array], must be of same
;                 dimensions as polarisation89
;   thresh: Threshold value for bootstrap: where bootstrap ice
;           conc. is below the threshold, resulting ice conc. is set to 0.
;-

```

```

; Calculate coefficients (third order polynomial approximation)
d=svendsen(p0,p1)
; Total ice concentration CT (Equation (11), Svendsen 87)
asi_ct=(d[0]*polarization89^3.0+d[1]*polarization89^2.0+d[2]*polarization89+d[3])
if keyword_set(nocutoff) then asi_ct = asi_ct else begin
; help,p11
;Set all ice for polarizations <p1 =1 and all >p0 = 0
p11=WHERE(polarization89 LT p1)
if p11[0] NE -1 then asi_ct[p11]=1.
pg0=WHERE(polarization89 GT p0)
IF pg0[0] NE -1 THEN asi_ct[pg0]=0.
; Cut off CT<0% and CT>100%
asi_ct=range01(asi_ct)
endelse

if keyword_set(bootstrap_ct) then begin
; Open water mask from bootstrap algorithm
cloudmask=WHERE(bootstrap_ct LT thresh,count)
IF count NE 0 THEN asi_ct(cloudmask)=0
; Bad values
indwrong=WHERE(FINITE(bootstrap_ct) NE 1,count)
IF count NE 0 THEN asi_ct(indwrong)!=values.f_nan
endif ;; end if bootstrap_ct set

Error: Reference source not found
Ref. Error: Reference source not found
Version / 13 May 2014
RETURN,asi_ct
END ;asi_bootstrap
;*****
;*****
;*****

FUNCTION svendsen,p0,p1
;+
;NAME:
;svendsen
;
;PURPOSE:
;Svendsen sea ice concentration algorithm:
;Inversion of the matrix given in:
; Svendsen, E, Maetzler, C. and Grenfell, T. C,
; A model for retrieving total sea ice concentration from a
; spaceborne dual-polarized passive microwave instrument operating
; near 90 GHz"
; IJRS, volume=8, year=1987, pages={1479--1487}
;
; (Direct solution of the equation system, Lars uses
; approx_svendsen.pro)
;
; To check if the matrix inversion is stable, two IDL methods are used
; (CRAMER and LUSOL, see documentation of IDL) and the results compared.
;
;The resulting coefficients are needed for the ASI
;algorithm.
;
;USAGE:
;result = svendsen(p0,p1)
;INPUT:
; p0, p1: 89 GHz (near-90GHz) polarisation difference for open water and sea ice
; respectively
;OUTPUT:
;result is a 4-element array containing the 4 coefficients
;
;HISTORY: Jan 2004, Gunnar Spreen
;-
;f=b/a

f=-1.14
p0=DOUBLE(p0)
p1=DOUBLE(p1)
; equation system
a=[[p1^3, p1^2, p1, 1],[p0^3,p0^2,p0,1],[3*p1^3,2*p1^2,p1,0],[3*p0^3,2*p0^2,p0,0]]
b=[1.,0.,1+f,f]
; condition of matrix a

```

```

cond=COND(a,/DOUBLE)
; Solving the equation system using Cramer's rule
solvc=CRAMER(a,b,/DOUBLE)
; Solving the equation system using the routine lubksb described in section 2.3 of Numerical
Recipes
in C: The Art of Scientific Computing (Second Edition)
LUDC,a,ind
solvlu=LUSOL(a,ind,b)
d=solvc
test = TOTAL(FLOAT(solvc) EQ FLOAT(solvlu))
IF test NE 4 THEN BEGIN
Error: Reference source not found
Ref. Error: Reference source not found
Version / 13 May 2014
PRINT, 'Function svendsen : An error ocured solving the equation system.'
STOP
ENDIF
RETURN,d
END ;svendsen
;*****

```

5.4.2.4 FORTRAN code for 6GHz alg

```

subroutine alg6V(TB6V,TB37V,ws,skt,SIC)
c
c Subroutine to compute SIC from 6V and 37V TBs
c
c Tie points
TB6Vice= 255.2
TB6VW = 162.67
TB37VW = 215.71

SIC0 = 1-(TB6Vice-TB6V)/(TB6Vice-TB6VW)

c Quadratic wind correction
TB6Vc = TB6V-(1-SIC0)*(0.0199*ws*ws-0.0039*ws)
c Effective temperature for 6V
SKT0 = 0.45*skt + 271.46*0.55
e6V = TB6Vc/SKT0

c 6V emissivity of ice from TB37V
e6VI = 0.9645
if(SIC0.gt.0.2) then
TB37I = (TB37V-(1-SIC0)*TB37VW)/SIC0
e6VI = 0.000244*TB37I + 0.9089
e6VI = SIC0*e6VI + (1-SIC0)*0.9645
endif
SIC = 100-100*(e6VI-e6V)/(e6VI-0.585)

return
end

```

6 High frequency SIC algorithm with atmospheric correction

6.1 Abstract

An improved sea ice concentration (SIC) retrieval algorithm named ASI2 that uses weather corrected polarization difference (PD) in brightness temperatures (TBs) at 89 GHz measured by AMSR-E/2 is developed. Effects of wind, total water vapor, liquid water path and surface temperature on the measured brightness temperatures at 89 GHz are evaluated through a radiative transfer model. TBs of Open Ocean yield higher sensitivity to the atmospheric water due to its low emissivity, whereas that of sea ice is more influenced by the surface conditions such as temperature and ice type. The weather effects are corrected by simulating changes in TBs caused by the atmospheric water absorption/emission and wind roughened ocean surface scattering using numerical weather prediction reanalysis data fields as atmospheric profiles. ASI2 is validated on a collection of AMSR-E observations over open water and 100% SIC. The correction significantly reduces the standard deviation and bias of SIC over open water, yet yields little change over 100% SIC. Combined with an improved weather filter based on the corrected TBs at lower frequencies, ASI2 allows retrieval of low ice concentration and resolves a more realistic ice concentration gradient across the ice edge compared to the original ASI algorithm.

6.2 Introduction

Sea ice plays an important role in the global climate system. An accurate knowledge of the spatial and temporal distribution of sea ice is thus essential to understand and predict weather and climate. Observations by passive microwave radiometers on satellites are able to deliver such information, because they are available under all light conditions, and are less dependent on cloud cover.

The Arctic Radiation and Turbulence Interaction Study (ARTIST) Sea Ice (ASI) algorithm utilizes the polarisation difference in brightness temperatures (TBs) at near 90 GHz. Granted by the high spatial resolution (4×6 km²) of the 89 GHz channels of the Advanced

Microwave Scanning Radiometer - Earth Observing System (AMSR-E), ASI SIC improves the horizontal resolution by a factor of four compared to the widely used 18 GHz and 37 GHz based algorithms such as Bootstrap, NASA Team or Bristol, and thus reveals fine structures of ice, such as leads and ice conditions near the ice edge. Despite its advantage in resolution, the accuracy of ASI retrievals in regions with low SIC are reduced by the more pronounced atmospheric attenuation at 89 GHz. Changes in the observed TBs induced by atmospheric absorption and emission generally increase the retrieved SIC, and often lead to detection of spurious ice over open ocean. Several weather filters based on the gradient ratio of TBs at lower frequencies have been developed to eliminate spurious ice, on a statistical basis. But such threshold based weather filters often falsely remove low concentration sea ice near the ice edge, and limit the retrieval of smaller SIC. In marginal ice zone, comparisons of ASI SIC to SAR and optical images show rms error up to 26.2%. The standard deviation of ASI SIC may reach up to 25% in low ice concentration regions.

Another approach is to correct the atmospheric influences on the TBs explicitly. The enhanced NASA Team algorithm (NASA Team 2) reduces the atmospheric

impact by constructing a lookup table containing all combinations of SIC and 12 classes of atmospheric conditions using a radiative transfer model, and minimizing the difference between the modelled and measured gradient and polarisation ratios of TBs. The SEALion algorithm corrects the weather influences by iteratively reducing difference between the observed and simulated PD using MicroWave MODel (MWMOD). Here parameters such as total water vapor, liquid water path and wind speed are acquired externally from microwave observations and numerical weather prediction (NWP) model data. [S. Andersen et al.] attempted to correct the weather influence on TBs up to 37 GHz by simulating TBs using the MWMOD and a fast radiative transfer model. Atmospheric parameters are acquired from High Resolution Limited Area Model (HIRLAM) system data.

In this study, we follow the approach of correcting AMSR-E and AMSR-2 TBs using NWP model data. We apply a detailed atmospheric correction including the specific geophysical states of the individual grid cell to the AMSR-E measured TBs up to 89 GHz, and develop an improved.

ASI algorithm based on the weather corrected TBs. At 89 GHz, the TB measurements are more prone to atmospheric influence compared to the lower frequencies. The considered geophysical parameters for the correction are: water vapor (TWV), liquid water path (LWP), wind speed (WS) and surface temperature (Ts). The effect of the correction mainly depends on three factors: (i) the quality of the geophysical data, (ii) the agreement of the chosen geophysical data in time and geo-location to the exact AMSR-E observation, and (iii) the geophysical parameters included in the correction. The geophysical states are acquired from the European Re-Analysis (ERA) Interim data. ERA Interim was chosen for its consistency with independent observations and its wide data coverage. ERA Interim data does not fully qualify factor (ii) because it has coarser spatial resolution (0.75°) compared to 89 GHz TBs and may have a maximum 1.5 hours difference in time to the AMSR-E observation. Nevertheless, factor (ii) is less critical for parameters with low spatial and temporal variability like water vapor and surface temperature, and the ERA Interim data already provide good estimation of the actual atmospheric condition. To determine the best combination of geophysical parameters input to the correction, we first evaluate the sensitivity of TBs at 89 GHz to single geophysical parameter through a radiative transfer model as described in Section 6.4, then test the correction using all possible parameter combinations on 0% and 100% ice concentration cites as described in Section 6.5. The correction using the best parameter combination is integrated into the ASI algorithm. A new ASI retrieval equation is derived from the weather corrected signatures of open water and consolidated ice. The weather corrected TBs at 89 GHz is then ingested to the new retrieval equation to compute ice concentration. With the weather corrected TBs at 18V and 36V, the weather filter is improved as well and causes less misclassification in marginal ice zone (Section 6.7). Henceforth, this version of ASI algorithm based on weather corrected surface signatures and corrected TBs at 89 GHz is called ASI2, and that with improved weather filter is called ASI2WF . In Section 6.6, the ASI2 ice concentration is validated in regions of 0% and 100% ice concentration. Although the main challenge of atmospheric correction is in regions of intermediate and low ice concentration, training and validating the method in such regions require a large set of intermediate ice concentration at the exact time and footprint of AMSR-E observation, which is difficult to obtain. As a compromise, we choose regions of 0% and 100% ice concentration for the validation of the ASI2 ice concentration. ASI2WF retrievals near the ice edge are qualitatively evaluated with optical satellite images, and quantitatively compared to Landsat ice concentration data in Section 6.7. In addition, ASI2WF daily ice extent and area are compared to other passive microwave algorithms (Sec. 6.7). Finally, conclusion and discussion follow in Section 6.8.

6.3 Methodology

6.3.1 Data Set

The main satellite data used in this study is AMSR-E Level 2A Version 3 data. AMSR-E measures at two polarisations and at six different frequencies ranging from 6.9 to 89 GHz at the incident angle 55°. The Level 2A dataset contains brightness temperatures of the six frequency channels at different resampled resolutions. For the atmospheric correction we use TBs of the higher frequency channels at the 18 GHz resolution, i.e., 21 km to make sure that the measurements describe the identical regions. As the successor of AMSR-E, AMSR-2 onboard the GCOM-W1 satellite measures at similar frequencies and provides a spatially resampled dataset (Level 1R Version 2) as well. AMSR-2 L1R Version 2 data is also used to evaluate the atmospheric correction.

For the correction scheme presented here the needed geophysical parameters are acquired from Era-Interim 3 hourly/0.75° forecast data. The following ERA-Interim numerical weather prediction (NWP) parameters are evaluated as input to the correction: total water vapor (TWV), liquid water path (LWP), wind speed (WS), 2 m air temperature (T2m) and skin temperature (Tskin). Tskin is the temperature of the interface of atmosphere and surface. Over open ocean, Tskin is equivalent to sea surface temperature, whereas over sea ice, it is the temperature of the top of the snow on the sea ice if present. In previous weather correction studies (see Section 6.2), T2m is often used as a proxy of surface temperature. In this study, both Tskin and T2m are tested as surface temperature in the correction, and their performance is discussed in Section 6.5. All ERA-Interim parameters are collocated in space and time (within 1.5 hours difference) with the AMSR-E/-2 observations.

A data set of AMSR-E and AMSR-2 TBs measured over areas of 0% and 100% ice concentration called the Round Robin Data Package (RRDP), produced in the context of the European Space Agency's Sea Ice Climate Change Initiative 2 project (ESA SICCI2), is used to train and validate the atmospheric correction. This data set is available from the Integrated Climate Data Center (ICDC, <http://icdc.zmaw.de/1/projekte/esa-cci-sea-ice-ecv0.html>). RRDP consists of AMSR-E Level 2 A Version 3 data from 2007 to 2011, and AMSR-2 L1R Version 2 data from 2013 to 2014 in the Arctic. The influence of the weather correction is the strongest in regions of low ice concentrations. However, ground truth of intermediate ice concentration is difficult to obtain. A thorough investigation in low yet not 0% ice concentration areas would require high resolution ice concentration observations with little time difference and exact geo-referencing to AMSR-E observation. These two requirements are already difficult to fulfil, and we would need a large set of such validation scenes to not introduce biases due to the peculiarity of single scenes. Therefore, we choose 0% and 100% ice concentration from RRDP, where the surface type is known for a large number of cases and seasons, for training and validating the correction. High resolution ice concentration data derived from Landsat images are used for small-scale validation.

For RRDP the open water (SIC0) and consolidated ice (SIC1) surfaces are identified based on data from various satellites. Open water areas at high latitude are identified from ice charts, climatology and satellite images. Regions of 100% SICs are determined by the ice drift data set from Environmental Satellite (ENVISAT) Advanced Synthetic Aperture Radar (ASAR) in areas of high SIC. It is assumed that in near 100% ice area, after one day's convergence, the small water fraction of the area is either frozen up or closed by ridging. However, this

assumption is less reliable in summer due to surface melting, therefore only SIC1 data from winter months (October to May) is used here. The RRDP data from 2008 is used for training the correction and is henceforth referred to as RRDP training data set. The rest of RRDP data set (2007-2011 AMSR-E except 2008 and 2013-2014 AMSR-2) is used for validating the weather corrected SIC, and is referred to as RRDP validation data set.

6.3.2 ARTIST Sea Ice Algorithm

The ARTIST Sea Ice algorithm, ASI in short, is the core ice retrieval algorithm of this study. It is an enhancement of the Svendsen sea ice algorithm for near 90 GHz frequencies, and has been developed to benefit from the high spatial resolution of the near 90 GHz channels of the AMSR-E sensors. The total SIC is calculated from the polarisation difference of the TBs at 89 GHz: $PD = TB_V - TB_H$, where V denotes vertical polarisation, and H denotes horizontal polarisation. The total SIC is expressed as a third order polynomial of PD , whose coefficients are determined by the typical values of PD over water (P_0) and consolidated ice (P_1), so called tie points. The standard ASI AMSR-E/2 tie points used for the dataset available at www.seaice.uni-bremen.de are $P_1 = 11.7$ K, $P_0 = 47$ K, which also include the average atmospheric influence. Constant tie points are used here to achieve a large continuous global.

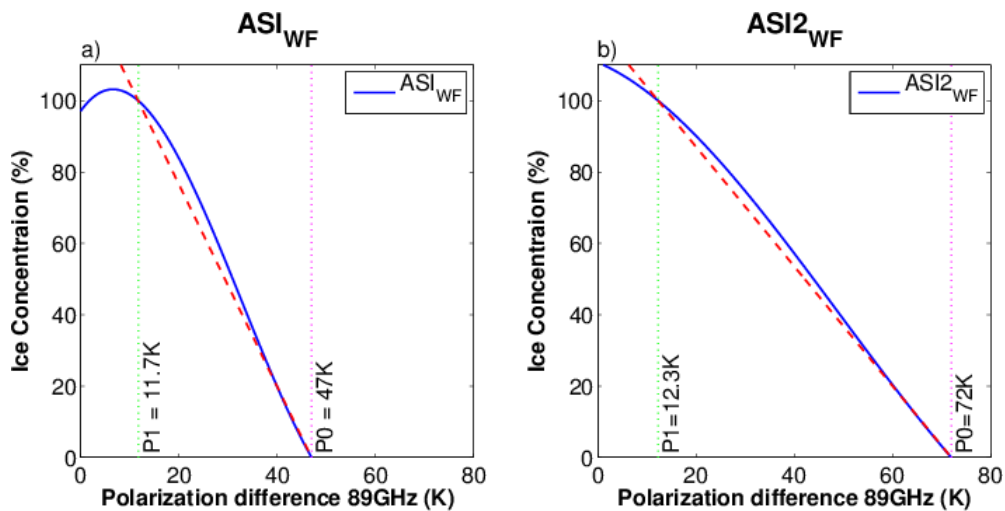


Figure 6-1: Ice concentration C as a function of PD of ASI_{WF} (a) and $ASI2_{WF}$ (b). Tie points are marked by the vertical lines. Tie points of (a): $P_1 = 11.7$ K, $P_0 = 47$ K; of (b): $P_1 = 12.3$ K, $P_0 = 72$ K.

SIC time series. From the tie points and boundary conditions on the derivatives, the third order polynomial is determined:

$$C_{ASI} = 1.64 \cdot 10^{-5} PD^3 - 0.0016 PD^2 + 0.0192 PD + 0.9710. \quad (1)$$

For all PD greater than P_0 or less than P_1 , the corresponding SIC is 0% or 100%, respectively. Figure 6-1a illustrates the relationship between C_{ASI} and PD . The blue polynomial displays the C_{ASI} as a function of PD . The red dashed line shows the SIC as a linear function of PD determined by the tie points P_1 and P_0 marked by the vertical lines. For these tie points at SIC lower than 30%, the relationship between C_{ASI} and PD is close to linear. Near 100% SIC, the non-linearity of ASI retrieval curve is more pronounced.

Two external weather filters are adopted to screen out pixels contaminated by high atmospheric water content of the open ocean. The gradient ratio (GR) of the 36 and 18 GHz channels is used for identifying high liquid water path cases:

$$GR(36, 18) = \frac{TB(36V) - TB(18V)}{TB(36V) + TB(18V)}. \quad (2)$$

For $GR(36,18) \geq 0.045$, $C(ASI) = 0$ [3]. High water vapor cases are screened out by gradient ratio $GR(23,18)$. For $GR(23,18) \geq 0.04$, $C(ASI) = 0$. For the case the two weather filters do not screen out all anomalies, the Bootstrap algorithm is used in addition to assure 0% SIC:

$$C(Bootstrap) = 0 \Rightarrow C(ASI) = 0. \quad (3)$$

Henceforth, we call this version of ASI that include two weather filters and the Bootstrap filter as ASIWF algorithm. All three weather filters are supposed to only filter out spurious ice in the open ocean. For low ice concentration, however, they already might get triggered under strong atmospheric influence situations. For such cases, low ice concentrations would be falsely removed and the ice margins would change.

6.3.3 Radiative Transfer Model

To account for the atmospheric influence on the measured TBs , a radiative transfer model is used in the correction. We apply the Wentz forward model, which is a linearized radiative transfer model at AMSR-E frequencies and incidence angle without atmospheric scattering. It consists of three main components. The core is a radiative transfer equation that determines how much of the surface thermal emission and scattered down-welling sky radiation is transferred to the satellite antenna. The other two components are the atmosphere absorption model and the sea-surface emission and scattering model.

The radiative transfer equation can be expressed as

$$TB = TB_U(\nu, \theta) + s(\nu, \theta)T_s \exp^{-\tau(\nu, \theta) \sec \theta} + [1 - s(\nu)]TB_D(\nu) \exp^{-\tau(\nu) \sec \theta}, \quad (4)$$

where TB is the observed brightness temperature, TB_U and TB_D are the up-welling and down-welling radiation of the atmosphere respectively, s is surface emissivity, T_s is the physical temperature of the emitting layer, τ is the total atmospheric opacity, ν and θ denote the observing frequency and angle respectively.

The key component of the atmosphere model is the total atmospheric opacity τ determined by the vertically integrated absorption coefficients of oxygen, water vapor and liquid water path. The oxygen absorption is nearly constant globally, with a dependence on the air temperature, which is small at the atmospheric window frequencies of AMSR-E. The water vapor absorption is a linear function of the water vapor paths with a small second order term, and the final component liquid water absorption is approximated to be linear to the product of average cloud temperature and liquid water path.

The surface emissivity is the weighted sum of ocean, first-year ice (FYI) and multiyear ice (MYI) emissivities. The ocean emissivity is simulated by the ocean-surface model depending on the water temperature, salinity, and wind speed. Three scales of waves responsible for the variation of ocean emissivity are simulated: the sea foam, long wave compared to the radiation wavelength, and small wave. Emissivities of FYI and MYI are taken from. To account for the background seasonal variability of sea ice signature, we adopt the monthly ice emissivities.

The average MYI emissivity is 0.774 ± 0.049 at V-polarisation and 0.731 ± 0.044 at H-polarisation. The average FYI emissivity is 0.872 ± 0.043 at V and 0.805 ± 0.049 at H. The fraction of each surface type is derived from the NASA Team algorithm. Although the derived MYI fraction may not be accurate, the average polarisation difference in emissivity of both ice types are similar (0.043 and 0.067), and are much lower than that of open water (0.26). Therefore, uncertainties in MYI retrieval will only have marginal influence on the procedure proposed here.

6.3.4 Weather Correction and ASI2 Algorithm

The atmospheric correction is carried out by simulating changes in TBs caused by the atmospheric water absorption/emission and wind roughened ocean surface scattering using Era-Interim data fields as atmospheric profiles. Firstly, we simulate the TBs under a clear and dry atmosphere (TB_{M0}), assuming the surface temperature to be 271.15 K for ocean and 250 K for sea ice. Secondly, the NWP data collocated both in time and space is input to the Wentz forward model to simulate the TBs under actual atmospheric condition (TB_{MA}). To prevent a potential systematic bias, we subtract the difference between TB_{MA} and TB_{M0} from the measured TBs instead of directly using the TB_{MA} . The corrected TBs are expressed as:

$$TB_C = TB_{sat} - (TB_{MA} - TB_{M0}). \quad (5)$$

To determine which geophysical parameters should be included in the correction, all single parameters and possible parameter combinations are tested, and the corrected TBs at 89 GHz are evaluated on the RRDP training data set. For ideally constant atmosphere and ice conditions, the TBs of ice and water should remain constant under clear atmosphere. In reality, the observed TBs have fluctuations due to variations in atmospheric opacity and surface emissivity. For the usually snow-covered sea ice during winter, the Weddell Sea experiments show a standard deviation of

2.5 K of the brightness temperature if observed near the surface. In melting season, the snow metamorphism and melt ponds further increase the variability of emissivities of sea ice. For ocean surface, such fluctuation on top of the atmosphere TBs is more pronounced due to the higher atmospheric water content and wind roughening effect. By testing the correction on a training data set over pure surface types in winter where the sea ice condition is more stable, we are able to separate the variability of the observed TBs induced by the atmosphere and by the surface. Once the atmospheric influence is corrected, we expect a narrower distribution of the TBs , e.g., lower standard deviation in our RRDP SIC0 and SIC1 data sets. The atmospheric parameter combination that leads to the lowest standard deviation is thus determined as the best input for the correction.

The correction based on the best parameter combination is then combined with the ASI algorithm. In order to derive a modified algorithm, new tie points free of weather contamination are identified as the modal values of corrected PD at 89 GHz over open water and consolidated ice sites of the training data set. A new ASI retrieval polynomial is derived from these weather corrected tie points. The corrected PD s at 89 GHz are ingested to the new polynomial to compute total ice concentration. This version of ASI algorithm derived from weather corrected tie points and PD is thus called ASI2.

The ASI2 SIC is validated using the RRDP validation data set over 0% and 100% ice concentrations. Bias and standard deviation of ASI and ASI2 relative to the reference SIC are compared in Section 6.6. As described in Section 6.3.2, the gradient ratios of $GR(23,18)$ and $GR(36,18)$ are used by the standard ASI algorithm for screening out pixels contaminated by high TWV and LWP over open water, respectively. As an additional evaluation of the correction using the RRDP validation data set, new GR values based on the weather corrected TBs at 18 V, 23 V and 36 V are computed, and their correlation to weather contamination is discussed in the same section. We expect a lower correlation between $GR(23,18)$ and TWV after an effective TWV correction.

While the atmospheric correction considerably reduces the weather contamination on SIC retrieval, it cannot eliminate it completely. This is mainly caused by the poor representation of clouds in the NWP model at the exact time and location of the satellite footprint. The remaining weather contamination over the open ocean and for low ice concentration areas is eliminated in 6.7 with a new weather filter with adapted threshold based on the atmospherically corrected TBs at 36 V and 18 V. We call the ASI2 algorithm with improved $GR(36,18)$ filter ASI2_{WF}.

The ASI2_{WF} algorithm is then applied to AMSR-E L2A swath data. The ASI2_{WF} tie points

are adjusted to better represent the weather corrected open water and sea ice signals for the application on large scale swath data. Two case studies are conducted comparing ASI_{WF} and ASI2_{WF} SIC to i) MODIS image (Sec. 6.7.2), and ii) Landsat images (Sec. 6.7.3). Daily ice extent and ice area from 2008 are compared to NASA Team 2 and SICCI algorithm (Sec. 6.7.4).

6.4 SENSITIVITY OF SIMULATED BRIGHTNESS TEMPERATURES TO ATMOSPHERIC PARAMETERS

The atmospheric influence on the observed TBs at 89 GHz and the ASI SIC are assessed by simulating TBs and SIC with atmospheric parameters varying in typical ranges for Arctic conditions using the Wentz forward model. The effects of TWV , LWP , WS and T_s are evaluated over three surface types: open water (OW), first-year ice (FYI) and multiyear ice (MYI).

Figure 6-2 shows the influences of the chosen atmospheric parameters on the top of atmosphere TBs over OW, FYI and MYI. The corresponding PD s are shown in Figure 6-3. In general, over all three surface types, the variability of the TBs with most parameters is nearly linear in the considered range, except for LWP . PD decreases with all increasing parameters except for the surface temperature. TBs of open water are more sensitive to all considered parameters than consolidated ice due to its lower surface emissivity and shows stronger sensitivity for horizontal than vertical polarisation. FYI and MYI show similar PD sensitivity to atmospheric influence.

6.4.1 Sensitivity to Wind Speed

Over open water, wind roughens the sea surface and results in higher emissivity and higher TBs . However, as shown by the red lines in Figure 6-2a, the vertically polarized TBs decrease slightly with stronger wind. This is caused by the mixing of polarisations: the wind roughened surface is less polarized in the vertical direction despite the overall higher surface emissivity.

6.4.2 Sensitivity to Total Water Vapor

The Arctic troposphere often has low humidity, especially over consolidated ice. Over 80% of the training data set have total water vapor below 15 kg/m^2 . Over all three surface types, the simulated TBs increase with TWV as expected at both 89-H and 89-V, shown by the blue lines in Figure 6-2. The increase in TBs at horizontal polarisation is larger than that at vertical polarisation, especially for open water. This leads to a strong drop in PD from approximately 80 K (at $TWV = 0 \text{ kg/m}^2$) to 50 K (at $TWV = 20 \text{ kg/m}^2$) over open water (Figure 6-3). At vertical polarisation, the sensitivity to water vapor is similar over both ice and water, whereas at horizontal polarisation, the sensitivity over water is higher due to the low horizontally polarized emissivity of the sea surface.

6.4.3 Sensitivity to Liquid Water Path

A range of LWP wider than typical in the Arctic (up to 0.3 kg/m^2) is chosen in the sensitivity study to present the non-linear influence of clouds on the simulated TBs and PDs . Over open ocean, high liquid water path is one of the major causes of spurious ice in SIC retrieval. The PD drops strongly from around 80 K at $LWP = 0 \text{ kg/m}^2$, to 45 K at $LWP = 0.25 \text{ kg/m}^2$ (green curve in Figure 6-3a). Over closed ice, liquid water changes the polarisation ratio (PR) and spectral gradient ratio (GR) of TBs at 18 GHz and 36 V, and thus causes a shift of the radiometric signature from multiyear ice to first-year ice. Such shift in retrieved ice type may indirectly influence the atmospheric correction. In the correction process, the fraction of each ice type is identified by the NASA Team algorithm and input to the Wentz forward model for surface emission simulation. Due to the lower TB sensitivity of FYI to LWP and TWV than MYI (Figure 6-2b and c), an over-estimation of FYI induced by LWP lowers the difference between TB_{MA} and TB_{MO} . As a result, the corrected TBs are higher at both polarisations (Equation 5). However, the resulting SIC is determined by PD . Both ice types show similar PD sensitivity to atmospheric influences (Figure 6-3b and c). Therefore, the ice type shift induced by LWP does not influence the retrieved SIC after correction.

6.4.4 Sensitivity to Surface Temperature

Over consolidated ice, the simulated TBs increase with the surface temperature at both polarisations since the FYI and MYI emissivities used in the simulation are constant. Yet over open water, the TBs decrease with surface temperature. Since TB is the product of emissivity and physical temperature, the drop of TB must be caused by decreasing emissivity. [T. Meissner and F. J. Wentz] showed that ocean emissivity at 89 GHz decreases with sea surface temperature, confirming our hypothesis. The simulated PDs on the other hand increase with surface temperature over both ocean and sea ice. As a result, when ice surface temperature gets higher yet still stays below the melting point of sea ice, the AS_{IWF} will underestimate SIC. However, the error is below 2% SIC if the ice temperature increases from 250 to 270 K.

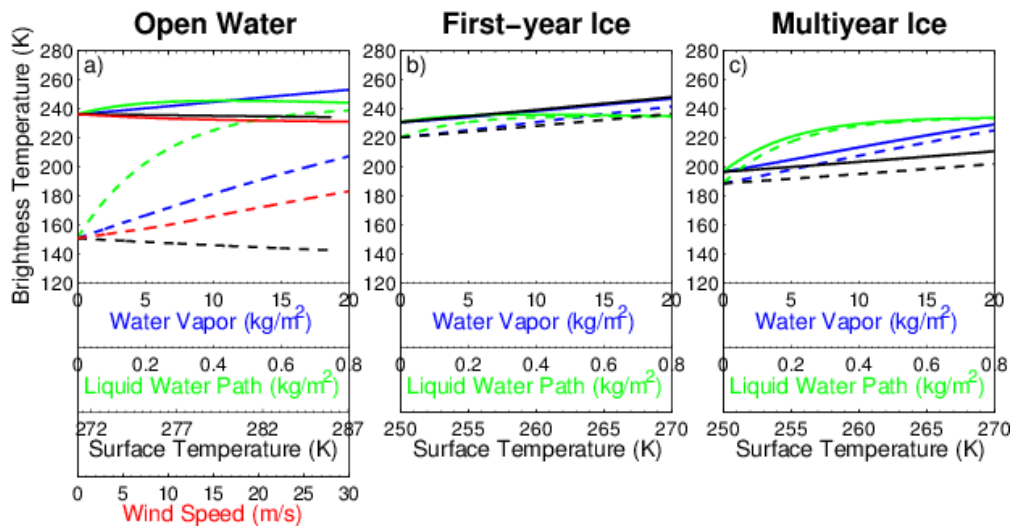


Figure 6-2: Simulated brightness temperatures at 55° incidence angle with varying atmospheric parameters over (a) open water, (b) first-year ice, and (c) multiyear ice. Each color represents one varying parameter. The solid curves: vertically polarized TBs, the dashed curves: horizontally polarized TBs

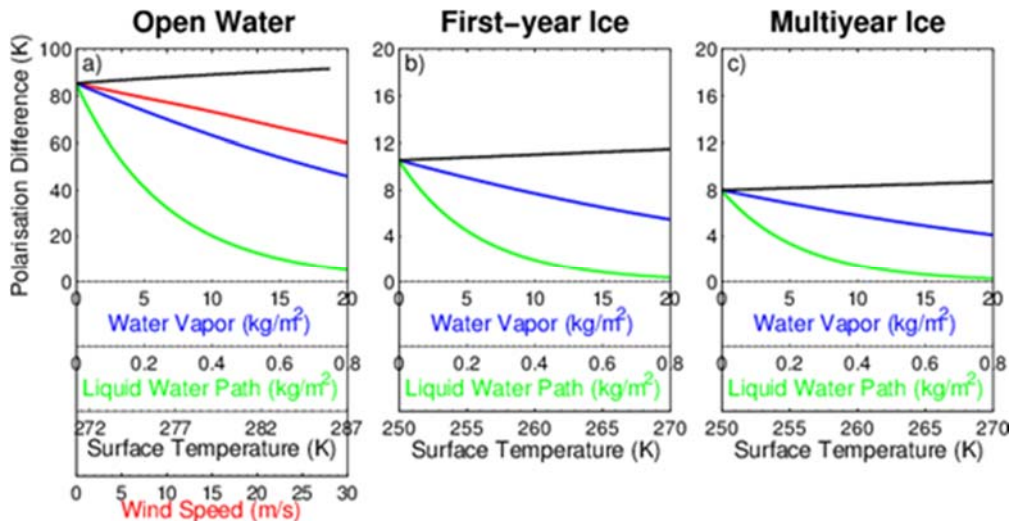


Figure 6-3: Simulated PD to atmospheric influences over (a) open water, (b) first-year ice, and (c) multiyear ice. Each color represents one varying parameter

Here we only consider the impact of each atmospheric parameter separately. In reality, parameters are correlated and often vary simultaneously. For instance, a rise in surface temperature often means higher *TWV* and *LWP*. Therefore, the atmospheric influence on retrieved SIC is indeed mixed. To examine such mixed effect under realistic atmospheric condition, we adopt the RRDP data set that consists of satellite measurements and collocated atmospheric profiles. The results are discussed in Section 6.5.

6.5 SELECTING ATMOSPHERIC PARAMETERS FOR BRIGHTNESS TEMPERATURE CORRECTION

To achieve the best atmospheric correction effect, we first need to determine which geophysical parameters are included in the correction. All single parameters and possible combinations are evaluated on the RRDP training data sets of 0% and

100% ice concentration. The ERA-Interim geophysical parameters TWV , LWP , WS , T_{2m} and T_{skin} are tested. Both T_{2m} and T_{skin} are tested as surface temperature in the correction. For consolidated ice, the penetration depth of the microwave radiation varies with ice type and frequency. At 89 GHz, the penetration depth is less than 1 cm for first-year ice and about 4 cm for multiyear ice. Therefore the surface temperature products taken from ERA-Interim might be a few Kelvin different from the temperature of the emitting layer (T_{emit}). [N. Mathew et. al] found that T_{emit} is linearly related to the lowest level air temperature (T_{2m}) at AMSR-E frequencies. At 89 GHz during Arctic winter (December to March), $T_{emit} = 0.37 \times T_{2m} - 4.2$. In spring (April to May) and autumn (August to November), $T_{emit} = 0.37 \times T_{2m} - 2.8$. Here we use their method to compute the T_{emit} , and include it in the TB correction study.

Figure 6-4 shows the standard deviation of TBs at 89 GHz before (horizontal lines) and after (vertical bars) correction over open water (upper panel) and consolidated ice (lower panel) of the RRDP training data set. Generally, with the weather correction, the standard deviation reduces more over ocean than over sea ice for most parameter combinations.

Over open water among all single parameter corrections, water vapor correction decreases the standard deviation of TBs the most, from 19.4K to 13.8K at H-Pol and from 7.4K to

4.6 K at V-Pol, agreeing with the TB sensitivity study in 6.4. The wind speed correction alone has little impact on the TBs standard deviation of ocean surface possibly due to the mixing of polarisations (6.4). The standard deviation of TB_V decreases by less than 1 K, whereas that of TB_H remains almost unchanged. Yet once combined with water vapor, the correction lowers the standard deviation of TBs further than water vapor alone. Despite the high sensitivity (Figure 6-2), the liquid water path correction decreases the standard deviation by less than 5 K over ocean, and by less than 1 K over ice, less than the influence of the water vapor correction. This can be explained by the high spatial and temporal variability of clouds at the time and place of the satellite overpass. It is challenging for NWP model to represent clouds correctly and the NWP data is only available every 3 hours, i.e., up to 1.5 hours separated from the satellite acquisition time. This will cause discrepancy in the geolocation and time between the ERA-Interim LWP data fields and the clouds in AMSR-E footprints. Water vapor on the other hand, is much less variable, therefore the probability of a good match between the ERA-Interim and AMSR-E measurement is higher. Both tested surface temperature parameters, T_{skin} and T_{2m} , increase the standard deviation over open water by about 2 K instead of reducing it.

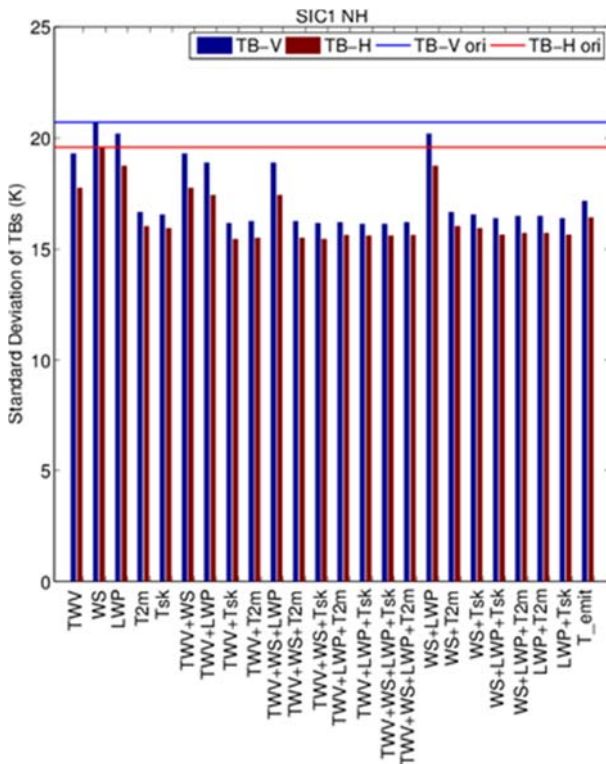
However, once combined with TWV which is strongly correlated with the surface temperature, the correction reduces the standard deviation of TBs slightly more than TWV correction alone. Over sea ice, correction in surface temperature reduces the standard deviation the most among all single parameter corrections, because surface properties are dominant for the ice emission observed from space. The similar performance of T_{skin} and T_{emit} corrections (Figure 6-4) shows that the T_{skin} product of ERA-Interim data is representative for the emitting temperature at 89 GHz of ice. To simplify the correction procedure, we use T_{skin} as the sea ice temperature. Combined corrections with one of the surface temperature parameters outperform the single temperature corrections.

Over open water, the most effective correction is the combination of TWV , WS and T_{skin} , which reduces the standard deviation by 6.2 K at H-Pol, and by 3.0 K at V-

Pol. Over consolidated ice, the most effective correction is the combination of TWV , LWP and T_{skin} for TB_V , and the same combination without liquid water path for TB_H . The difference in TB_V standard deviation with and without liquid water path correction is only about 0.1 K, much lower than the error margin of AMSR-E TBs (1.2 K at 89 GHz) and is thus negligible. Since the wind speed has no effect over sea ice, to allow a consistent correction routine for both open water and ice, we select the combination of TWV , WS and T_{skin} for the brightness temperature correction.

6.6 ASI2 VALIDATION OVER 0% AND 100% ICE CONCENTRATIONS

The ASI2 algorithm integrated with weather correction is developed as described in 6.3.4. ASI2 tie points are chosen as the modal value of the corrected polarisation difference at 89 GHz of the RRDP training data set. A new set of ASI tie points is derived in the same way to evaluate ASI SIC retrievals on the RRDP validation data set. Table 6-1 shows the tie points of ASI and ASI2 used in the validation over 0% and 100%. The AMSR-2 TBs are converted to equivalent AMSR-E TBs based on the inter-calibration study by [A. Okuyama et. al]. The tie points of AMSR-2 are almost identical to AMSR-E, proving the positive effect of the calibration, and providing a potential to expand ASI2 to AMSR-2 measurements. In this study, our focus is on the AMSR-E measurements. Comparing the tie points before and after the correction, P_0 increases drastically by 27 K, whereas P_1 only increases by around 2 K, agreeing with the conclusion that open water is more sensitive to atmospheric influences (Section 6.4).



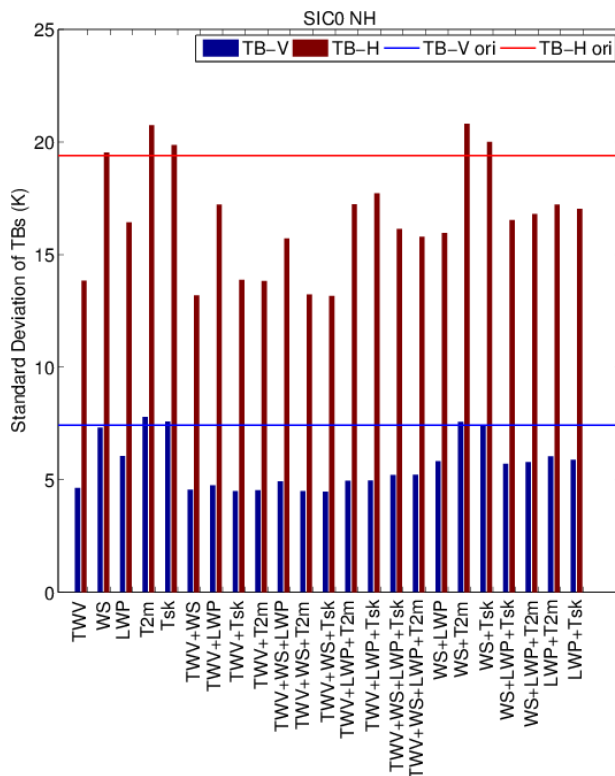


Figure 6-4: Standard deviation of TBs at 89 GHz before (horizontal lines) and after correction (vertical bars) using different parameters and their combinations. Blue denotes vertical polarisation, and red denotes horizontal. Based on the pure 0% (top, SIC0) and 100% (bottom SIC1) SIC Round Robin Data Package training data sets. TWV: total water vapor. WS: wind speed. LWP: liquid water path. T2m: 2 m air temperature. Tsk: skin temperature. T_{emit} : emitting layer temperature.

Figure 5-5 shows the density plot of TB_V and TB_H of the RRDP validation data set before (a) and after (b) the weather correction. Each subplot contains two clusters, representing the TBs of open water and sea ice. ASI and ASI2 SIC isolines based on the tie points shown in Table 6-1 ranging from 0% to 100% with 20% interval are marked by the dashed lines. The axis perpendicular to the SIC isolines represent the PD at 89 GHz. Before the atmospheric correction, TB_V of 100% ice concentration spans from 160 K to 260 K, and TB_H from about 150 K to 250 K. After the correction, the range of TBs at V-pol and H-pol decreases by 20 K and 10 K respectively. However, the ice cluster becomes wider along the PD axis after the correction, indicating a more variable sea ice signal. Over open water, the reduction in distribution is even more pronounced especially at H polarisation, due to its high sensitivity to the atmosphere. More importantly, the water and ice clusters overlap at high TBs before the correction. These open water pixels with high TBs are contaminated by high atmospheric water content, and would cause retrieval of spurious ice. Before the correction the OW cluster covers the complete 0% to 100% ice concentration range (dashed lines). After the correction, the two clusters are farther apart, leaving fewer open water pixels close to the ice cluster. The ice concentration range for the open water cluster is reduced to 0% to 80% and the point density has a much clearer maximum at 0% ice concentration compared to before the correction. With the tie points based on the atmosphere corrected TBs the adjacent SIC isolines are further apart, showing a wider dynamic PD range of the ice concentration signal at 89 GHz. Water and ice are thus easier to distinguish after the correction, lowering the chance of erroneous ice detection. The remaining ambiguous water pixels are probably

contaminated by liquid cloud water which is not included in the weather correction.

The bias and standard deviation of ASI and ASI2 SIC over the RRD validation data set are shown in Table 6-2. These statistics are based on ASI and ASI2 using the tie points given in Table 6-1, all weather filters turned off and no capping at 0% and 100% SIC. As additional information, the statistical results of ASI_{WF} and ASI2_{WF} using the standard tie points and corresponding weather filters are included in the lower part of Table 6-2, showing the performance of the standard ASI/-2 algorithms at 0% and 100% SIC. Over open water, the standard deviation of SIC decreases by approximately 12% after the atmospheric correction. The bias drops too, from 21.6% to 15.2%, showing a clear improvement yet still far from the ideal value 0%. Over consolidated ice, changes in bias of SIC induced by weather correction are in the order of 0.1%, and are thus negligible. Also the improvement in standard deviation is with 0.4% small but at least indicates the ASI2 can provide slightly more stable ice concentrations also at 100% ice cover. For intermediate ice concentrations this improvement should be more enhanced.

As an additional analysis, the histograms of ASI (blue) and ASI2 (red) SIC over the RRD validation data set are shown in Figure 5-6. Over open water, the majority of the ASI SIC falls in the range between -20% and -10%, followed by a long tail of positive SIC up to 100%. The wide range of positive SIC is caused by weather contamination: *PD* of open water decreases to the level of ice covered surface (Figure 6-5). With the weather correction, ASI2 SIC has a narrower distribution that peaks around the 0% and retrieves less extreme high SIC. Over consolidated ice, the distributions of ASI and ASI2 SIC are similar. In conclusion, the atmospheric correction mainly improves SIC retrievals in regions of low ice concentration, and causes little change to near 100% sea ice.

The remaining bias and standard deviation of ASI2 SIC over open water indicates that the atmospheric contamination is not completely corrected. Ideally the bias would be zero after correction, while the standard deviation will always reflect the radiometer noise. As discussed in Section 6.4, the dominant atmospheric influences over ocean are *TWV* and *LWP*. [D. J. Cavalieri et. al] found that *GR*(23,18) is sensitive to *TWV*, and *GR*(36,18) to *LWP*. The *GR*(23,18) based on the corrected *TBs* should no longer be correlated to *TWV* if the correction is successful. In that case, the remaining bias of ASI2 is caused by *LWP*. To examine this hypothesis, *GR*(23,18) and *GR*(36,18) are computed using the uncorrected and corrected *TBs* of the RRD validation data set over open water (Figure 6-7). The colors represent the corresponding Era Interim *TWV* values. The thresholds of *GR*(23,18) and *GR*(36,18) used by ASI_{WF} are marked by the dashed lines (0.04 and 0.045 respectively). Before the weather correction, *GR*(23,18) increases nearly monotonically with *TWV* up to 30 kg/m². The default threshold filters out pixels with *TWV* above 12 kg/m². After applying weather correction on *TBs* at 18 V and 23 V, the new *GR*(23,18) values are not sensitive to *TWV* anymore, and its range is narrower. Only 60 out of 4896 data points have *GR*(23,18) above the default threshold 0.04 used for the ASI weather filter. On the other hand, *GR*(36,18) keeps its distribution after the correction, only with increased values, confirming our hypothesis.

Table 6-1: TIE POINTS OF ASI AND ASI2 USED IN THE VALIDATION OVER 0% AND 100% ICE CONCENTRATION, AND STANDARD TIE POINTS OF ASI_{WF} AND ASI2_{WF} USED IN THE APPLICATION TO AMSR-E SWATH DATA. *P0* IS THE TYPICAL *PD* FOR OPEN WATER AT 89 GHZ, AND *P1* IS FOR CONSOLIDATED ICE. ASI_{WF} TIE POINTS ARE FROM [G. Spreen et. al], AND ERRORS ARE NOT GIVEN THERE.

Tie Points (K)	AMSR-E		AMSR-2	
	ASI	ASI2	ASI	ASI2
P_0	45 ± 13.6	72 ± 13.5	45 ± 13.1	72 ± 12.2
P_1	9.7 ± 2.5	11.6 ± 3.18	9.3 ± 2.3	11.2 ± 2.7

	ASI_{WF}	$ASI2_{WF}$	ASI_{WF}	$ASI2_{WF}$
	P_0	47	72 ± 13.5	47
P_1	11.7	12.3 ± 3.18	11.7	12.3 ± 3.18

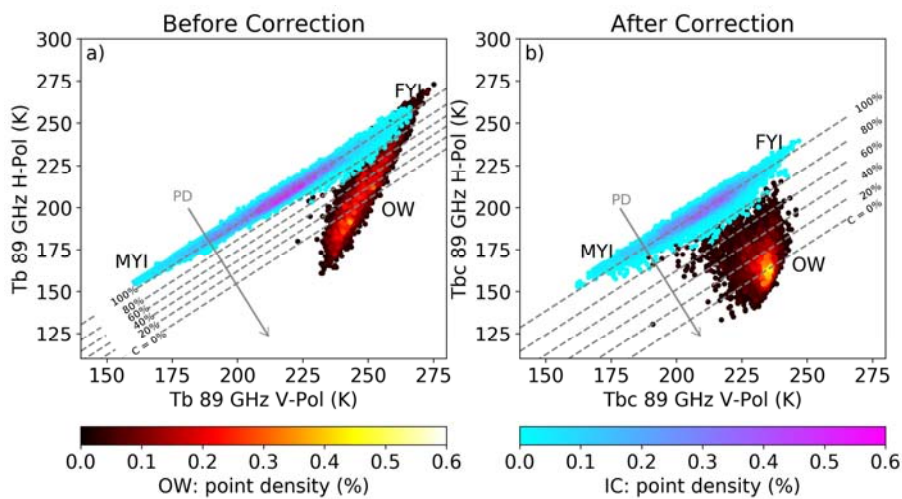


Figure 6-5: Scatter plot of $TB89 V$ and $TB89 H$ before (a) and after (b) correction over open water (red to yellow cluster) and consolidated ice (cyan to magenta cluster). Dashed lines show the ASI and ASI2 SIC isolines ranging from 0% to 100% with 20% interval. Arrow indicates increasing PD

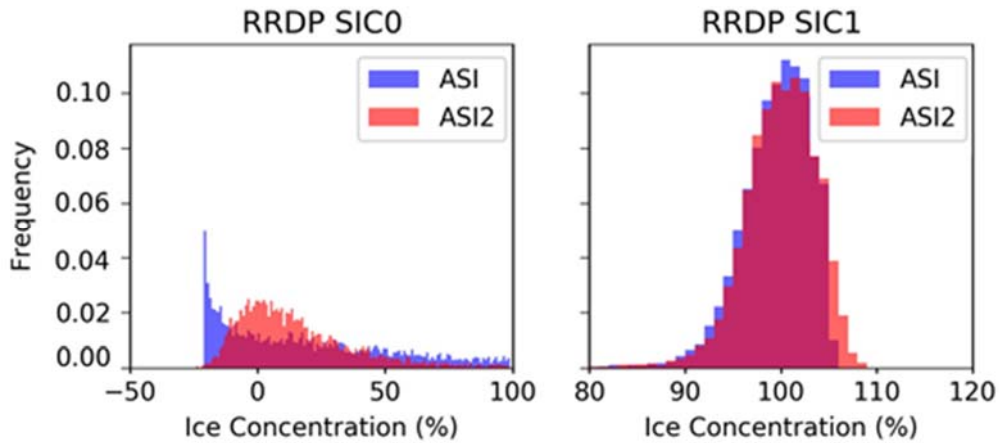


Figure 6-6: Histogram of ASI and ASI2 of the AMSR-E RRD validation data set over 0% and 100% ice concentration.

Table 6-2: BIAS AND STANDARD DEVIATION OF ASI AND ASI2 SIC OF THE VALIDATION RRD DATA SET OVER 0% AND 100% ICE CONCENTRATION. SIC0 DATA IS FROM ALL MONTHS, AND SIC1 DATA IS FROM OCTOBER TO MAY. ASI AND ASI2 SIC: ALL WEATHER FILTERS TURN OFF, NO CAPPING AT 0% AND 100%. ASI_{WF} AND ASI2_{WF}: OPERATIONAL TIE POINTS, WEATHER FILTERS TURNED ON, CAPPING AT 0% AND 100%.

SIC (%)		AMSR-E		AMSR-2	
		ASI	ASI2	ASI	ASI2
SIC0	Bias	21.6	15.2	21.3	14.2
	Std	35.4	22.9	34.3	20.7
SIC1	Bias	-0.6	-0.2	-0.4	0.2
	Std	3.9	4.0	3.6	3.4
		ASI _{WF}	ASI2 _{WF}	ASI _{WF}	ASI2 _{WF}
SIC0	Bias	4.7	0.04	3.5	0.5
	Std	14.3	1.5	11.5	3.6
SIC1	Bias	-0.5	-1.1	-0.3	-0.6
	Std	1.7	2.4	1.3	1.7

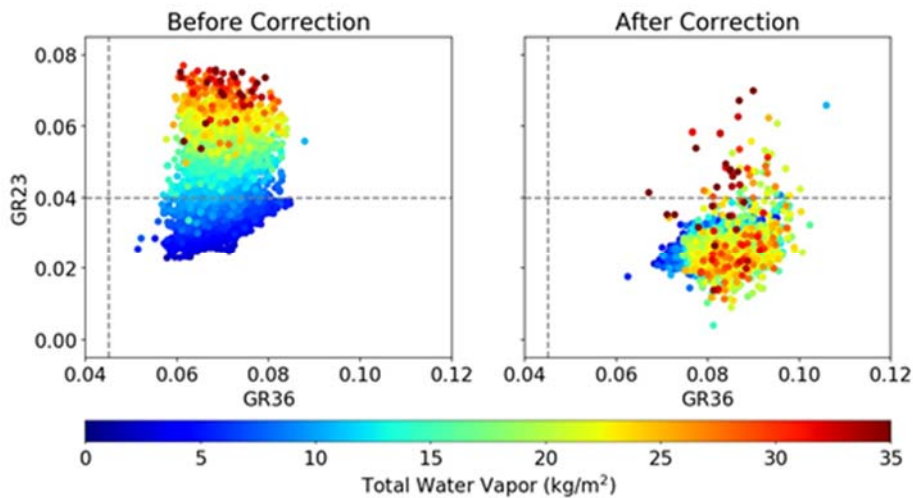


Figure 6-7: Scatter plot of $GR(23,18)$ and $GR(36,18)$ before and after correction for the RRDp validation data set over open water. Vertical and horizontal dashed lines show the default thresholds of $GR(36,18)$ and $gr2318$ used for ASI weather filter: 0.045 and 0.04 respectively.

6.7 ASI2 APPLICATION TO AMSR-E L2A BRIGHTNESS TEMPERATURES

The weather correction is applied to AMSR-E L2A swath measurements. ASI_{WF} and $ASI2_{WF}$ SIC retrievals are based on the tie points given in Table 6-1. Instead of using the ASI2 tie points derived from the RRDp training data set, the sea ice tie point (P_1) is increased within its standard deviation to better represent the sea ice signatures. Figure 6-1b shows the operational ASI2 retrieval curve. Figure 6-8 shows example maps of ice concentration, $GR(23,18)$ and $GR(36,18)$ derived from the uncorrected (upper panels) and corrected (lower panels) TBs from 15 March 2008. The retrieved ice concentration is resampled with 6.25 km grid spacing. The GR values are gridded to 25 km resolution. From left to right, the first column shows the SIC maps based on ASI and ASI2 algorithms without any weather filter. Abundant spurious ice are observed in the Greenland Sea, Barents Sea and Bering Sea. After the correction, the intensity of spurious ice is reduced by up to 30%, yet still persists. The structure of the spurious ice can be associated with cloud patterns and therefore high liquid water in the atmosphere, which is not accounted for in the correction. To achieve a reasonable daily ice concentration retrieval, the external weather filter $GR(36,18)$ sensitive to LWP is still needed for ASI2. The second and third columns display the $GR(23,18)$ and $GR(36,18)$ maps with the default thresholds (0.04 and 0.045 respectively) marked on the color bar. The uncorrected $GR(23,18)$ is above the threshold near the ice edge east of Greenland, Davis Strait and Bering Sea. Retrieval of low ice concentration in these regions is thus compromised by the $GR(23,18)$ weather filter. After the weather correction, the corrected $GR(23,18)$ is in general below the default threshold. Clusters of $GR(23,18)$ higher than 0.03 are found in the same location as the extreme high spurious ice in Bering Sea and Greenland, but are far away from the ice edge and therefore filtering them out will not influence the ice concentration retrieval.

From the uncorrected $GR(36,18)$ map (Figure 6-8c), clusters of $GR(36,18)$ above 0.07 are observed in similar locations as the spurious ice in Figure 6-8a. Along the sea ice edge east of Greenland, a sharp gradient of $GR(36,18)$ (from -0.02 to 0.06) is observed between the ice pack and open water. Sea ice might be present within this feature of high $GR(36,18)$ within the marginal ice zone. This showcases

the difficulty of selecting a $GR(36,18)$ threshold that would screen out weather contamination and at the same time preserve the precise ice edge. After the correction, $GR(36,18)$ values of open water increase, showing better contrast to the ice covered area. High $GR(36,18)$ values (above 0.08) agree in location and shape with the spurious ice. It is thus possible to select a corrected $GR(36,18)$ threshold that efficiently clears the weather effects and preserves low SIC domain.

6.7.1 New Weather Filter

To determine new thresholds for the weather corrected $GR(23,18)$ and $GR(36,18)$ values, a number of scatter plots of GR values to $PR18$ from January and March 2008 in the northern hemisphere are examined together with the GR maps.

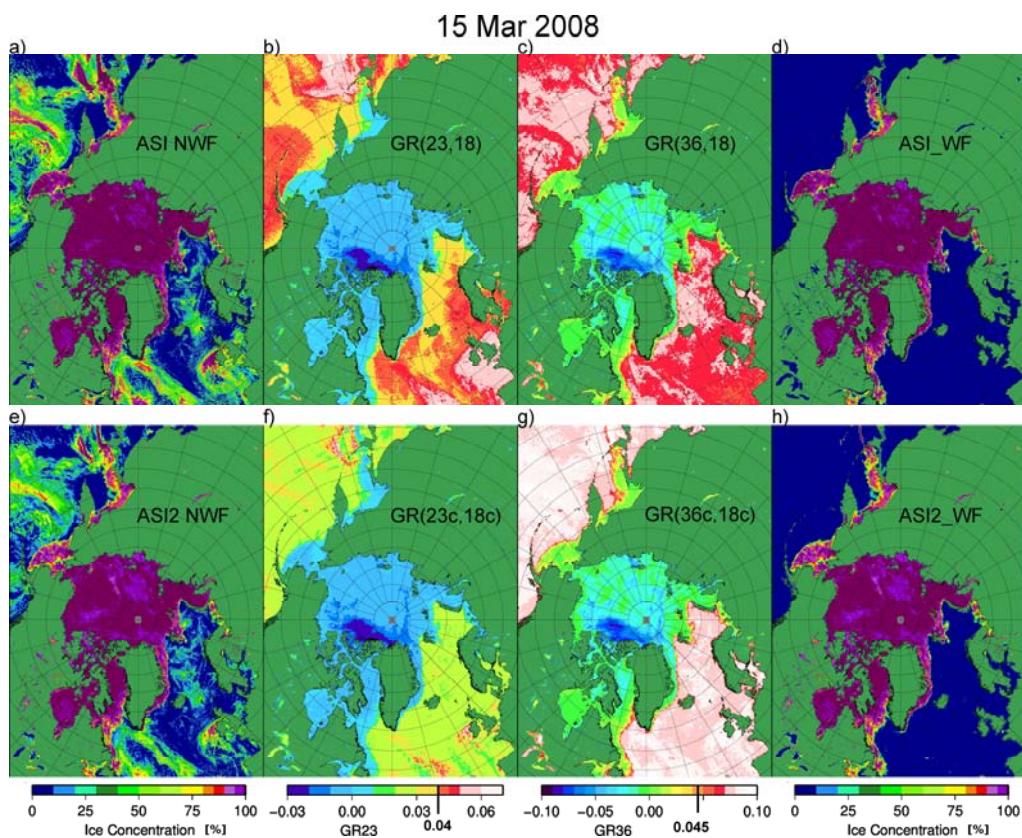


Figure 6-8: Ice concentration retrievals of ASI and ASI2 and weather filters from 15 March, 2008. The top row is based on the original AMSR-E TBs, the bottom row is based on the atmospherically corrected TBs. From left to right column: SIC without any weather filter, $GR(23,18)$, $GR(36,18)$, SIC with external weather filter. The SIC maps are gridded to 6.25 km resolution, and the GR values to 25 km.

Figure 6-9 shows an example scatter plot from 20 January, 2008. The colors represent the data density. The left panels show the original GR values, and the right panels the corrected GR values. The standard thresholds used by ASI_{WF} are marked by blue horizontal lines. In each subplot, the cluster with high GR and PR values represents the open water pixels. In the upper panels, the open water cluster becomes smaller after correction, corresponding to a less scattered distribution of the TBs over open water. Highlighted by the yellow box are data points of high $GR(23,18)$ values, possibly contaminated by TWV . After the

correction, the number of such data points greatly decreases, and almost all data points have $GR(23,18)$ lower than the standard threshold. This confirms the good performance of the water vapor correction. We conclude that no external weather filter is needed to screen out high TWV pixels. In the lower panels, the $GR(36,18)$ of the data points over open water increases by about 0.01. The size of the open water cluster remains unchanged, due to the lack of LWP correction. The new threshold selected for the $GR(36,18)$ filter is 0.07 compared to 0.045 used for ASI_{WF} . Example maps based on the resulting SIC values with external weather filter are shown in Figure 6-8d and h. ASI_{WF} and $ASI2_{WF}$ in general show similar results. $ASI2_{WF}$ SIC retrievals are slightly lower than ASI_{WF} over the ice pack. More differences are only visible at regional maps, and will be discussed in Sections 6.7.2 and 6.7.3.

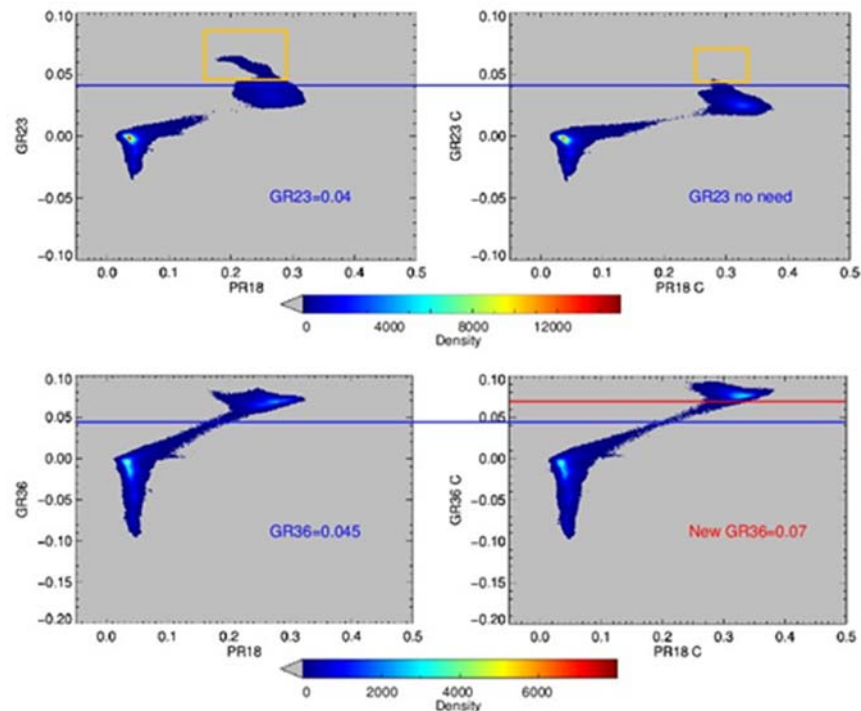


Figure 6-9: Scatter plot of $GR(23,18)$ to $PR18$ (top panels) and $GR(36,18)$ to $PR18$ (bottom panels) based on the original TBs (left panels) and corrected TBs (right panels) using AMSR-E L2A data in the Arctic from 20 Jan, 2008. The original threshold of weather filters used in ASI_{WF} are marked by the blue horizontal lines, and the new threshold denoted by red line.

6.7.2 Comparison to MODIS Image

$ASI2_{WF}$ SIC retrieval is qualitatively compared to a MODIS image near the ice edge. Tie points used for ASI_{WF} and $ASI2_{WF}$ are given in Table 6-1. The MODIS image covers an area of $140 \times 140 \text{ km}^2$ in the Fram Strait from 22 April, 2008. Figure 6-10 shows the MODIS image overlaid with ASI_{WF} and $ASI2_{WF}$ SIC isolines. Sea ice areas appear yellow or brown, clouds are white or grey, and open water appear dark blue/black on the image. SIC isolines of 15%, 30% and 90% are given in green, yellow and red lines respectively. We choose 15%, the common threshold to distinguish ice covered or ice free area as the lowest isoline, to illustrate a qualitative visual comparison between the $ASI2_{WF}$ SIC retrieval and MODIS image near the ice edge. Many ice floes are found outside the range of the

ASI_{WF} 15% SIC isoline. In these cases the weather filters hide real ice. Note that most of these floes are covered by partially transparent clouds. Without atmospheric correction, a more conservative weather filter helps to screen out as much spurious ice as possible at the cost of compromising low ice concentration retrieval. With the weather corrected TBs at 89 GHz and GR(36,18), ASI_{2WF} is able to retrieve low SIC as well while excluding spurious ice. The ASI_{2WF} 15% concentration line is much closer to the actual ice edge, despite the influence from clouds. Comparing the two images, the 30% isoline of ASI_{2WF} overlaps with the 15% isoline of ASI_{WF} in many regions. On the other hand, the area enclosed by the ASI_{2WF} 90% isolines is notably smaller than that by ASI_{WF}. This means that over regions with low or intermediate sea ice, ASI_{2WF} retrieves higher SIC than ASI_{WF}, whereas at close to 100% ice concentration regions, ASI_{2WF} retrieves lower SIC.

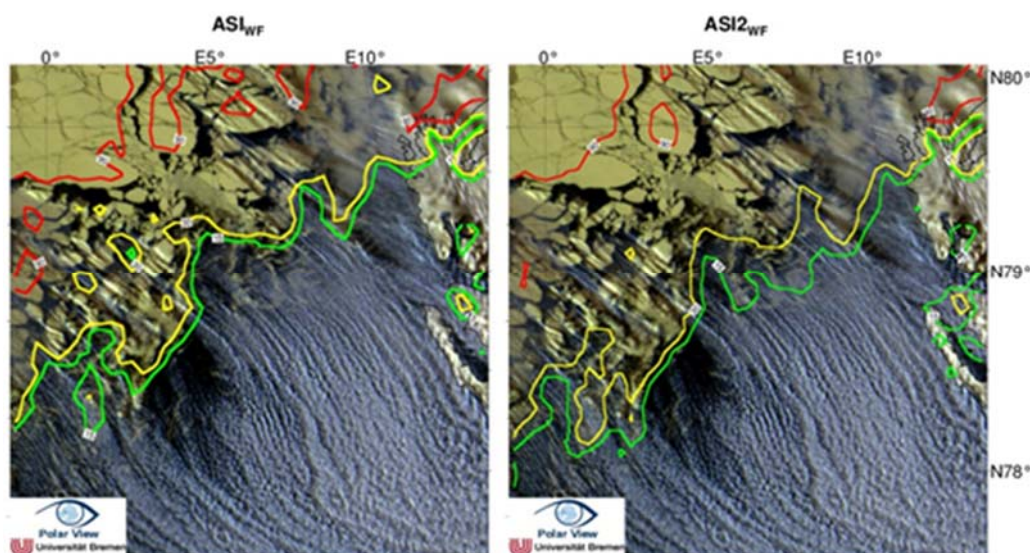


Figure 6-10: Ice concentration retrieved by ASI and ASI 2 overlaid on MODIS image of Fram Strait from 22. April, 2008. SIC of 15%, 30% and 90% are marked by green, yellow and red isolines, respectively.

6.7.3 Comparison to Landsat-5 TM and Landsat-7 ETM+

ASI_{2WF} SIC retrieval is compared to SIC derived from Landsat images. The nine Landsat scenes are acquired from mid-April to late May during the AMSR-E operation time in areas close to ice edge, provided by Stefan Kern from the University of Hamburg. Sea ice and open water are identified using the broadband albedo threshold. All Landsat pixels with albedo below 0.07 is classified as open water, above 0.07 as 100% sea ice. The Landsat images are collocated with ASI_{WF} SIC data and downsampled to the same resolution (6.25 km). Here we only present one scene from 24 May 2005 located near the Davis Strait in Figure 6-11. The other eight scenes show similar behaviour. Figure 6-11 shows: a) the false color Landsat image, b) the Landsat ice concentration at 6.25 km resolution, c) and d) ice concentrations of ASI_{WF} and ASI_{2WF} based on the standard tie points given in Table 6-1 with all weather filters turned on. In areas of Landsat ice concentration above 90%, both ASI_{WF} and ASI_{2WF} show similar SIC distributions as Landsat, with bias ranging from -9.7% to 5.6%. In regions of visually thin and

broken ice floes, ASI_{WF} SIC retrievals are closer to Landsat than ASI_{WF} , yet still underestimates SIC to some extent. Table 6-3 summarizes the average bias and rms errors of ASI_{WF} and ASI_{2WF} compared to Landsat SIC values of all researched scenes. Both ASI_{WF} and ASI_{2WF} show negative bias: -14.4% and -10.7% respectively. ASI_{2WF} gives lower rms error (20.5%) than ASI_{WF} (26.9%). The bias values are considerably higher than the results of [H. Wiebe et. al] (-8.4% to 4.5%). This is probably due to their different albedo threshold (0.1) used for ice/water identification, and different tie points used for ASI_{WF} . In conclusion, ASI_{2WF} improves the SIC retrievals near the ice edge at the cost of underestimating SIC over ice pack.

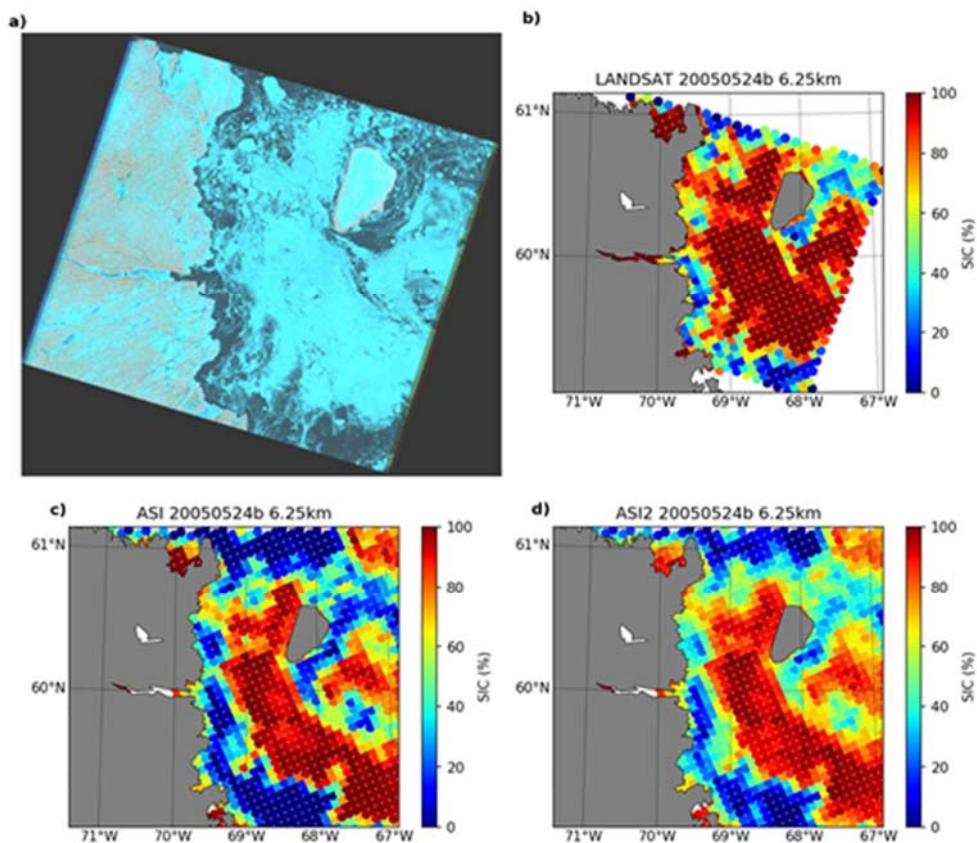


Figure 6-11: ASI_{WF} and ASI_{2WF} SIC compared to Landsat image from 24 May 2005 near Davis Strait.

Table 6-3: BIAS AND RMS ERRORS OF ASI_{WF} -LANDSAT AND ASI_{2WF} -LANDSAT ICE CONCENTRATION.

(%)	ASI_{WF} -Landsat	ASI_{2WF} -Landsat
Bias	-14.4	-10.7
RMS	26.9	20.5

6.7.4 Comparison to other Passive Microwave Algorithms

For a further evaluation of the $ASI2_{WF}$ algorithm, it is applied to a larger data set: the AMSR-E L2A data from 2008. Daily SIC is retrieved by ASI_{WF} and $ASI2_{WF}$, resampled to the polar- stereographic grid at 6.25 km grid cell size which is similar to the native resolution of 89 GHz channel (4×6 km). Daily ice area is computed and compared to other sea ice concentration algorithms: SICCI and NASA Team 2, all gridded to 25 km resolution. The SICCI SIC product is re-sampled to EASE grid, whereas the other algorithms use a polar-stereographic projection. Ice extent is the total area of all grid cells with SIC above 15% in the Arctic. Therefore, ice extent depends on the grid size and we only compare $ASI2_{WF}$ with ASI_{WF} , which both use the same grid resolution of 6.25 km. Ice area is the total area of ice fraction. Figure 6-12 shows the daily ice extent (left panel) and ice area (right panel) retrieved by the aforementioned algorithms. The seasonal variation of ice extent and area of $ASI2_{WF}$ agrees with the other algorithms. Due to the improved weather filter and its ability to retrieve low SIC, the ice extent of $ASI2_{WF}$ (magenta line) is higher than ASI_{WF} throughout the whole year. The ice extent of $ASI2$ is approximately 0.5 million km^2 higher than that of ASI_{WF} (cyan) during winter. The difference rises during the melting season, and reaches about 0.8 million km^2 in the middle of September when the ice minimum occurs. Despite the high bias in ice extent, the ice area of ASI_{WF} and $ASI2_{WF}$ share similar values. This indicates that $ASI2_{WF}$ SIC over ice packs must be lower than ASI_{WF} , especially during melting season. Besides SICCI the ice area of all evaluated algorithms agree well within ± 0.7 million km^2 . The SICCI ice area is more than 1 million km^2 lower than all the other algorithms. The different choice of projection and land mask might partly explain the difference.

Both $ASI2_{WF}$ ice extent and area reveal a higher day to day variability compared to the other algorithms. We explain this feature with the weather influence over ice retrieval. The atmospheric influence over sea ice in general increases the ASI retrieved SIC. As a result, regions of SIC above 90% would be shifted towards 100% especially under heavy weather conditions. The natural variability of the sea ice signal is thus smoothed by atmospheric influence. With a successful weather correction, the retrieved SIC in high SIC regions would decrease, and thus reveal a higher day to day variability.

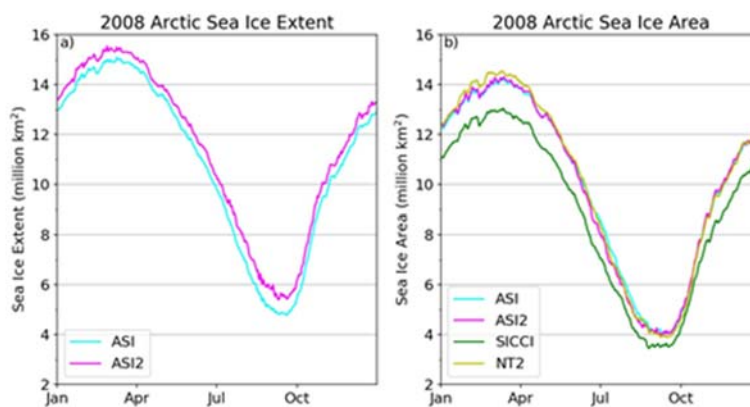


Figure 6-12: Ice extent (a) and ice area (b) retrieved by various empirical SIC retrieval algorithms. ASI and $ASI2$ SIC are gridded to 6.25 km, and all the other algorithms use 25 km grid.

6.8 DISCUSSION AND CONCLUSION

Satellite measurements at 89 GHz have been used for sea ice concentration retrieval to benefit from the high spatial resolution at that frequency compared to the traditionally used lower frequencies at 19 and 37 GHz. However, compared to lower frequencies, atmospheric contamination is particularly challenging at this frequency. The previously used threshold based weather filters remove spurious ice on a statistical basis, yet often at the cost of undermining retrieval of low ice concentration, and do not correct for ice covered surface. In this study, we developed an improved 89 GHz ice concentration retrieval algorithm named ASI2 that includes an individual atmospheric correction for each grid cell and any surface type using NWP data.

The atmospheric correction efficiency depends on the quality of the NWP data, the discrepancy in time and geo-referencing between the NWP and satellite measurement grid cell, and the atmospheric parameters used in the correction. ERA-Interim is chosen as NWP dataset in this study for its complete data coverage in the Arctic, moderate temporal resolution and good consistency with individual geophysical states observations. The influence of major geophysical parameters on the observed TBs at 89 GHz and retrieved SIC were evaluated through a radiative transfer model over open water and consolidated ice (Figure 6-2 and Figure 6-3). Ice reveals much lower sensitivity to any atmospheric influence than open water. The influence of LWP , however, can be significant, especially over multi-year ice. The polarisation difference at 89 GHz decreases with most parameters and results in higher ASI SIC. For open water the reduction in PD is most pronounced with TWV and LWP , the two major parameters that cause spurious ice in the ocean in the retrieval. The observed TBs of consolidated ice on the other hand is less influenced by the atmosphere, but more by the variations in sea ice emissivity which may be caused by surface conditions such as ice age, temperature, snow cover, leads, etc. At frequencies higher than 10 GHz, the volume scattering in snow grain on top of sea ice decreases the emissivity. [R. G. Onstott et. al] found that sea ice emissivity at 90 GHz increases with wet snow. During the melting season, the sea ice emissivity variability can reach up to five times higher than in winter at 85 GHz based on a model study. To account for the background seasonal variability of ice emissivity, we adopted the monthly ice emissivity determined by, and emphasized the study on the winter months when the ice surface conditions are more stable.

The geophysical parameters input (TWV , LWP , T_S , WS) to the correction are selected by testing all single parameters and possible combinations over open water and consolidated ice (Figure 6-4). The best combination, i.e., the one resulting in the lowest standard deviation of TBs and SIC was TWV , WSP and T_{skin} . Although TBs measured from space are sensitive to LWP over both open water and closed ice, LWP is excluded from the correction, because the properties of liquid clouds are not fully represented in the current NWP models, and the disagreement between the 3-hourly model output and the satellite overflight time due to their high spatial and temporal variability. Including LWP in the correction raises the uncertainty.

After the weather correction process is settled, it is integrated into the ASI algorithm. New tie points free of weather contamination are identified, which yield a wider dynamic range in PD and provide a better distinctness between the water and ice signal (Table 6-1 and Figure 6-5). The ASI algorithm based on weather corrected TBs at 89 GHz and tie points is ASI2, and its SIC is validated over 0% and 100% ice concentration with the RRDP database. As the atmospheric influence is corrected, ideally the relationship between the PD at 89 GHz and ice concentration should be linear, because the non-linearity was originally introduced

to statistically account for the atmospheric influence. As shown in Figure 6-1b, the ASI2 retrieval polynomial is almost linear at SIC below 20%, confirming the correction effect at low SIC. As a result, the distribution of retrieved SIC over open water is narrower after the correction, and its peak closer to the reference value 0% (Figure 6-6). At high SIC, the non-linearity of ASI2 is lower than before the correction, leading to a more symmetrical distribution around the 100% SIC. Here bias and standard of SIC compared to ASI remain practically unchanged. The different correction effects over water and ice are consistent with their sensitivity to weather contamination (Figure 6-3).

Even with the new atmospheric correction, residual weather contamination still persists. We attribute this to the influence of liquid water clouds, which the atmospheric correction based on NWP data cannot successfully correct (Sec. 6.6). This problem can in principal be solved by including a better quality *LWP* in the correction which has the exact time and location as the AMSR-E observation. As long as such data is not available, we still need to maintain the *GR(36,18)* weather filter, which is sensitive to the atmospheric liquid water path. The *GR(23,18)* and Bootstrap filters are not needed any more for ASI2. A new higher threshold for the *GR(36,18)* filter based on corrected *TB18 V* and *36 V* was determined. The resulting SIC better outlines the ice edge, and casts less influence near the ice edge compared to the standard *GR(36,18)* filter used in ASI. With this corrected *GR(36,18)* and improved threshold (Figure 6-9), spurious ice is efficiently removed with compromising much less low ice concentration values as with ASI. The distribution of low ice concentrations becomes more realistic. The ASI2 algorithm including the improved *GR(36,18)* filter is called *ASI2_{WF}*.

Comparisons of *ASI_{WF}* and *ASI2_{WF}* SIC to a MODIS image and nine Landsat scenes in marginal ice zones show that *ASI2_{WF}* brings the retrieved boundary of ice/water closer to the actual ice edge, and shows a higher, more realistic horizontal gradient in SIC across the ice edge. Compared to the Landsat SIC values, *ASI2_{WF}* shows lower bias (-10.7%) and rms error (20.5%) than *ASI_{WF}* (bias 14.4%, rms 26.9%).

Finally, *ASI2_{WF}* is applied to AMSR-E L2A data from 2008, and the resulting daily ice extent and ice area are compared with that of *ASI_{WF}*, NASA Team 2 and SICCI algorithm. The daily ice extent retrieved by *ASI2_{WF}* is higher than that of *ASI_{WF}* (Figure 6-12). The daily ice area of *ASI2_{WF}* on the other hand is similar to that of *ASI_{WF}*, lower than NASA Team 2, and higher than SICCI algorithm. This indicates that *ASI2_{WF}* retrieves more sea ice in the low SIC domain, yet lower SIC over the ice pack compared to *ASI_{WF}* due to the removal of atmospheric influences.

In conclusion, weather correction mainly improves SIC retrievals in the low ice concentration domain, and has less influence over ice pack. These features, together with the higher resolution compared to most other SIC algorithms, make it particularly suitable for ship navigation where information about the marginal ice zone and regions of intermediate ice concentrations is required. Under heavy weather contaminations with *ASI_{WF}*, regions of SIC above 90% may appear as 100%. The natural variability of sea ice is thus masked by the atmosphere. Because of that, high SIC with patterns associated with cyclones are observed on the daily SIC maps based on *ASI_{WF}* produced at the University of Bremen (available at www.seaice.uni-bremen.de). With the weather correction, *ASI2_{WF}* SIC over ice pack would decrease, and such patterns are less pronounced on the daily *ASI2_{WF}* SIC maps, yet still persist. To further improve the *ASI2_{WF}* algorithm,

the variability of sea ice emissivity needs to be better accounted for in the weather correction procedure. The remaining challenges in the ASI_{2WF} retrievals are the uncompensated influence of liquid water path and variability of sea ice emissivity. Liquid water path correction requires *LWP* fields better representing the atmosphere at the exact time of satellite overflight. A better knowledge of sea ice emissivity requires an emissivity model and again knowledge about the meteorological history including temperature, precipitation and wind for sea ice drift.

6.9 ACKNOWLEDGEMENT

This work was supported by the ESA Sea Ice Climate Change Initiative 2 (SICCI2) and SFB/TR 172 "Arctic Amplification: Climate Relevant Atmospheric and Surface Processes, and Feedback Mechanisms (AC)3" funded by the German Research Foundation (DFG). The authors would like to thank the SICCI2 and especially Roberto Saldo from the Danish Technical University for constructing and providing the RRDP data set. We would like to express our gratitude to Stefan Kern from the University of Hamburg for providing Landsat images with surface identification. We are very grateful to Leif Toudal Pederson from the Danish Meteorological Institute for his valuable insights and comments on this research. The AMSR-2 Level 1R data is provided by the Earth Observation Research Centre, Japan Aerospace Exploration Agency (JAXA). The ERA-Interim data is provided by the European Centre for Medium-Range Weather Forecasts (ECMWF). The AMSR-E Level 2A data is provided by NASA National Snow and Ice Data Center (NSIDC). The SICCI daily ice concentration data is provided by Integrated Climate Data Center - ICDC of the University of Hamburg.

7 References

A. Beitsch, L. Kaleschke, and S. Kern, "Investigating high-resolution AMSR2 sea ice concentrations during the February 2013 fracture event in the Beaufort Sea," *Remote Sensing*, vol. 6, no. 5, pp. 3841–3856, 2014. [Online]. Available: <http://www.mdpi.com/2072-4292/6/5/3841>

A. Okuyama and K. Imaoka, "Intercalibration of Advanced Microwave Scanning Radiometer-2 (AMSR2) brightness temperature," *IEEE Transactions on Geoscience and Remote Sensing*, vol. 53, no. 8, pp. 4568–4577, 2015.

Andersen, S., Tonboe, R., Kaleschke, L., Heygster, G., and Pedersen, L. T.: Intercomparison of passive microwave sea ice concentration retrievals over the high-concentration Arctic sea ice, *JOURNAL OF GEOPHYSICAL RESEARCH*, 112, 2007.

Andersen, S., Tonboe, R., Kern, S., and Schyberg, H.: Improved retrieval of sea ice total concentration from spaceborne passive microwave observations using numerical weather prediction model fields: An intercomparison of nine algorithms, *Remote Sensing of Environment*, 104, 374–392, 2006.

Andersen, S.: Monthly Arctic Sea Ice Signatures for use in Passive Microwave Algorithms, TECHNICAL REPORT 98-18 DANISH METEOROLOGICAL INSTITUTE, 1998.

ARCGICE: Combination of Spaceborne, Airborne and In-Situ Gravity Measurements in Support of Arctic Sea-Ice Thickness Mapping, (2007). ESA Contract 18753/05/NL/CB.

Bjoergo, E., Johannessen, O. M., and Miles, M. W.: Analysis of merged SMMR-SSMI time series of Arctic and Antarctic sea ice parameters 1978-1995, *Geophysical Research Letters*, 24, 1997.

Cavalieri, D. J., T. Markus, and J. C. Comiso. 2014. *AMSR-E/Aqua Daily L3 12.5 km Brightness Temperature, Sea Ice Concentration, & Snow Depth Polar Grids*. Version 3. June 2002 – October 2011. Boulder, Colorado USA: NASA National Snow and Ice Data Center Distributed Active Archive Center. doi: http://dx.doi.org/10.5067/AMSR-E/AE_SI12.003.

Cavalieri, D. J., Germain, K. S., and Swift, C. T.: Reduction of weather effects in the calculation of sea ice concentration with the DMSP SSM/I, *J. Glaciol.*, 41, 1995.

Cavalieri, D. J., Gloersen, P., and Campbell, W. J.: Determination of Sea Ice Parameters With the NIMBUS 7 SMMR, *Journal of Geophysical Research*, 89, 5355-5369, 1984.

Cavalieri, D.J., C.L. Parkinson, P. Gloersen, J.C. Comiso, and H.J. Zwally. Deriving long-term time series of sea ice cover from satellite passive-microwave multisensor data sets. *Journal of Geophysical Research* 104(C7), 15803-15814, 1999.

Comiso, J. C., and Sullivan, C. W.: Satellite Microwave and In Situ Observations of the Weddell Sea Ice Cover and its Marginal Ice Zone, *Journal of Geophysical Research*, 91, 9663-9681, 1986.

Comiso, J. C., Cavalieri, D. J., Parkinson, C. L., and Gloersen, P.: Passive Microwave Algorithms for Sea Ice Concentration: A Comparison of Two Techniques, *Remote Sensing of Environment*, 60, 357-384, 1997.

Comiso, J. C.: Characteristics of Arctic Winter Sea Ice From Satellite Multispectral Microwave Observations, *Journal of Geophysical Research*, 91, 975-994, 1986.

Comiso, J. C.: SSM/I Sea Ice Concentrations Using the Bootstrap Algorithm, NASA Reference Publication / Goddard Space Flight Center, 1380, 1995.

D. J. Cavalieri, P. Gloersen, and W. J. Campbell, "Determination of sea ice parameters with the NIMBUS 7 SMMR," *Journal of Geophysical Research: Atmospheres*, vol. 89, no. D4, pp. 5355-5369, 1984. [Online]. Available: <http://dx.doi.org/10.1029/JD089iD04p05355>

D. J. Cavalieri, K. M. S. Germain, and C. T. Swift, "Reduction of weather effects in the calculation of sea-ice concentration with the DMSP SSM/I," *Journal of Glaciology*, vol. 41, no. 139, pp. 455-464, 1995.

D. Lubin and R. Massom, "Sea ice," in *Polar Remote Sensing*. Springer Science & Business Media, 2006, vol. 1, ch. 5, pp. 323-331.

D. M. Smith, "Extraction of winter total sea-ice concentration in the Greenland and Barents Seas from SSM/I data," *International Journal of Remote Sensing*, vol. 17, no. 13, pp. 2625-2646, 1996. [Online]. Available: <http://dx.doi.org/10.1080/01431169608949096>

D. K. Perovich, J. Longacre, D. G. Barber, R. A. Maffione, G. F. Cota, C. D. Mobley, A. J. Gow, R. G. Onstott, T. C. Grenfell, W. S. Pegau *et al.*, "Field observations of the electromagnetic properties of first-year sea ice," *IEEE Transactions on Geoscience and Remote Sensing*, vol. 36, no. 5, pp. 1705-1715, 1998.

Eastwood, S. (editor): Ocean & Sea Ice SAF (OSISAF) Sea Ice Product Manual. Version 3.8. May 2012

Emery, W. J., Fowler, C., and Maslanik, J.: Arctic sea ice concentrations from special sensor microwave imager and advanced very high resolution radiometer satellite data, *Journal of Geophysical Research*, 99, 18329 - 18342, 1994.

European Space Agency Envisat RA-2/MWR Product Handbook, Issue2.2, 27 February 2007. Available for download from <http://envisat.esa.int/handbooks>.

E. Svendsen, C. Matzler, and T. C. Grenfell, "A model for retrieving total sea ice concentration from a spaceborne dual-polarized passive microwave instrument operating near 90 GHz," *International Journal of Remote Sensing*, vol. 8, no. 10, pp. 1479-1487, 1987. [Online]. Available: <http://dx.doi.org/10.1080/01431168708954790>

F. J. Wentz, "A well-calibrated ocean algorithm for Special Sensor Microwave/Imager," *Journal of Geophysical Research: Oceans*, vol. 102, no. C4, pp. 8703-8718, 1997.

F. J. Wentz and T. Meissner, "Algorithm theoretical basis document version 2 AMSR ocean algorithm," pp. 10-30, 2000.

Giles, K. A., Laxon, S. W., Wingham, D. J., Wallis, D. W., Krabill, W. B., Leuschen, C. J., McAdoo, D., Manizade, S. S., & Raney, R. K. (2007). Combined airborne
ESA UNCLASSIFIED - For Official Use 167

laser and radar altimeter measurements over the Fram Strait in May 2002. *Remote Sensing of Environment* 111 182 – 194.

Gloersen, P., and Cavalieri, D. J.: Reduction of Weather Effects in the Calculation of Sea Ice Concentration From Microwave Radiances, *Journal of Geophysical Research*, 91, 1986.

G. Spreen, L. Kaleschke, and G. Heygster, "Sea ice remote sensing using AMSR-E 89-GHz channels," *Journal of Geophysical Research: Oceans*, vol. 113, no. C2, 2008. [Online]. Available: <http://dx.doi.org/10.1029/2005JC003384>

H. Wiebe, G. Heygster, and T. Markus, "Comparison of the ASI ice concentration algorithm with Landsat-7 ETM+ and SAR imagery," *IEEE Transactions on Geoscience and Remote Sensing*, vol. 47, no. 9, pp. 3008–3015, Sept 2009.

Ivanova, N., Johannessen, O. M., Pedersen, L. T., and Tonboe, R. T.: Retrieval of Arctic Sea Ice Parameters by Satellite Passive Microwave Sensors: A Comparison between Eleven Sea Ice Concentration Algorithms, submitted to *IEEE Transactions on Geoscience and Remote Sensing*, 2013.

J. C. Comiso, *SSM/I sea ice concentrations using the bootstrap algorithm*. National Aeronautics and Space Administration, Goddard Space Flight Center, 1995, vol. 1380.

J. Comiso, D. Cavalieri, and T. Markus, "Sea ice concentration, ice temperature, and snow depth using AMSR-E data," *IEEE Transactions on Geoscience and Remote Sensing*, vol. 41, no. 2, pp. 243–252, Feb 2003.

J. C. Comiso, T. C. Grenfell, D. L. Bell, M. A. Lange, and S. F. Ackley, "Passive microwave in situ observations of winter weddell sea," *Journal of Geophysical Research: Oceans (1978 - 2012)*, vol. 94, no. C1, 1989.

Kaleschke, L., Lupkes, C., Vihma, T., Haarpaintner, J., Bochert, A., Hartmann, J., and Heygster, G.: SSM/I Sea Ice Remote Sensing for Mesoscale Ocean-Atmosphere Interaction Analysis, *Canadian Journal of Remote Sensing*, 27, 526-537, 2001.

JAXA-EORC (Japan Aerospace Exploration Agency, Earth Observation Research Center), 2015: Status of AMSR2 Level-1 Products (Ver. 2.0).

Kattsov, V. M., Ryabinin, V. E., Overland, J. E., Serreze, M. C., Visbeck, M., Walsh, J. E., Meier, W., and Zhang, X.: Arctic sea-ice change: a grand challenge of climate science, *Journal of Glaciology*, 56, 2010.

Kern, S., and G. Heygster (2001), Sea ice concentration retrieval in the Antarctic based on the SSM/I 85 GHz polarization, *Annals of Glaciology*, 33, 109-114.

Kilic, L. Improving the effective temperature estimation over sea ice using low frequency microwave radiometer data and Arctiv buoys. EUMETSAT OSISAF visiting scientist report, 15pp, June 29, 2017.

Kongoli, C., Boukabara, S.-A., Banghua Yan, F. W., and Ferraro, R.: A New Sea-Ice Concentration Algorithm Based on Microwave Surface Emissivities—Application to AMSU Measurements, *IEEE Transactions on Geoscience and Remote Sensing*, 2010.

Kurtz, N. T., and S. L. Farrell. Large-scale surveys of snow depth on Arctic sea ice from Operation IceBridge. *Geophysical Research Letters*, 38, L20505, 2011. doi: 10.1029/2011GL049216.

L. Kaleschke, G. Heygster, C. Luöpkes, A. Bochert, J. Hartmann, J. Haarpaintner, and T. Vihma, "SSM/I sea ice remote sensing for mesoscale ocean-atmosphere interaction analysis: Ice and icebergs," *Canadian Journal of Remote Sensing*, vol. 27, no. 5, pp. 526–537, 2001.

Laxon, S. W., Peacock, N. R. & Smith, D. M. (2003). High interannual variability of sea ice thickness in the Arctic region. *Nature*, doi:10.1038/nature2050, 947-950.

Lo, R. C.: A comprehensive description of the Mission Sensor Microwave Imager SSM/I environmental parameter extraction algorithm. NRL Memorandum Report 5199, Naval Research Laboratory, Washington D. C., 1983.

L. Klein and C. T. Swift, "An improved model for the dielectric constant of sea water at microwave frequencies," *IEEE Transactions on Antennas and Propagation*, vol. 25, no. 1, pp. 104–111, 1977.

Maass, N., & Kaleschke, L. (2010). Improving passive microwave sea ice concentration algorithms for coastal areas: applications to the Baltic Sea. *Tellus Series A-Dynamic Meteorology and Oceanography*, 62(4), 393-410.

Markus, T. and D.J.Cavaliere. Snow Depth Distribution over Sea Ice in the Southern Ocean from Satellite Passive Microwave Data. *Antarctic Sea Ice: Physical Processes, Interactions and Variability, Antarctic Research Series*, 74, 19-39, 1998.

Markus, T., and Cavaliere, D. J.: An Enhancement of the NASA Team Sea Ice Algorithm, *IEEE Transactions on Geoscience and Remote Sensing*, 38, 2000.

Meier, W., F. Fetterer, K. Knowles, M. Savoie, M. J. Brodzik. (2006, updated quarterly). Sea Ice Concentrations from Nimbus-7 SMMR and DMSP SSM/I-SSMIS Passive Microwave Data, 2002 until present. Boulder, Colorado USA: National Snow and Ice Data Center. *Digital Media*.

N. Ivanova, L. Pedersen, R. Tonboe, S. Kern, G. Heygster, T. Lavergne, A. Srensen, R. Saldo, G. Dybkjr, L. Brucker, and M. Shokr, "Inter-comparison and evaluation of sea ice algorithms: towards further identification of challenges and optimal approach using passive microwave observations," *Cryosphere*, vol. 9, p. 17971817, 2015.

N. Mathew, G. Heygster, and C. Melsheimer, "Surface emissivity of the Arctic sea ice at AMSR-E frequencies," *IEEE Transactions on Geoscience and Remote Sensing*, vol. 47, no. 12, pp. 4115–4124, Dec 2009.

Peacock, N. R. & Laxon, S. W. (2004) Sea surface height determination in the Arctic Ocean from ERS altimetry. *Journal of Geophysical Research*, Vol. 109, No. C7, C07001 10.1029/2001JC001026.

Pedersen, L. T.: Improved spatial resolution of SSM/I products. In: Sandven, S., ed. Development of new satellite ice data products, Nansen Environmental and Remote Sensing Center, Bergen, Norway, 1998.

Pedersen, L. T.: Retrieval of sea ice concentration by means of microwave radiometry. The Technical University of Denmark, 1991.

Pedersen, L. T., R. Saldo. Sea Ice Concentration (SIC) Round Robin Data Package. Sea ice climate change initiative phase 2. Doc Ref: SICCI-RRDP-07-16, v. 1.4, May 07, 2016.

P. Berrisford, D. Dee, P. Poli, R. Brugge, K. Fielding, M. Fuentes, P. Kallberg, S. Kobayashi, S. Uppala, and A. Simmons, "The ERA-Interim archive version 2.0," ECMWF, Technical Report 1, November 2011.

P. Gloersen and D. J. Cavalieri, "Reduction of weather effects in the calculation of sea ice concentration from microwave radiances," *Journal of Geophysical Research: Oceans (1978–2012)*, vol. 91, no. C3, pp. 3913–3919, 1986.

P. Ashcroft and F. J. Wentz., "AMSR-E/Aqua L2A global swath spatially-resampled brightness temperatures, version 3." Boulder, Colorado USA. NASA National Snow and Ice Data Center Distributed Active Archive Center., 2013. [Online]. Available: <http://dx.doi.org/10.5067/AMSR-E/AE L2A.003>

Ramseier, R. O.: Sea Ice Validation. In: Hollinger, J. P., ed. DMSP special sensor microwave/imager calibration/validation, Naval Research Laboratory, Washington, DC, 1991.

Ramseier, R., Rubinstein, I. G., and Davies, A. F.: Operational evaluation of Special Sensor Microwave/Imager by the Atmospheric Environment Service, report from the Centre for Research in Experimental Space Science, York University, North York, Ontario, Canada, 1988.

R. Tonboe, S. Andersen, L. Toudal, and G. Heygster, "Sea ice emission modelling," in *Thermal Microwave Radiation– Applications for Remote Sensing*, C. Matzler, Ed. IET, 2006, vol. 52, pp. 382–400.

Ricker, R., Hendricks, S., Helm, V., Skourup, H., and Davidson, M.: Sensitivity of CryoSat-2 Arctic sea-ice freeboard and thickness on radar-waveform interpretation, *The Cryosphere*, 8, 1607-1622, doi:10.5194/tc-8-1607-2014, 2014.

Rinne, E., and M. Mäkynen. Sea Ice Thickness Round-Robin Data Package: User Manual. ESA Sea Ice Climate Change Initiative: Phase 1, NERSC. Version 1.2, 2013 (access 23.3.2016).

R. Lindsay, M. Wensnahan, A. Schweiger, and J. Zhang, "Evaluation of seven different atmospheric reanalysis products in the Arctic," *Journal of Climate*, vol. 27, no. 7, pp. 2588–2606, 2014.

R. Fuhrhop, T. C. Grenfell, G. Heygster, K.-P. Johnsen, P. Schluessel, M. Schrader, and C. Simmer, "A combined radiative transfer model for sea ice, open ocean, and atmosphere," *Radio Science*, vol. 33, no. 2, pp. 303–316, 1998.

R. G. Onstott, T. C. Grenfell, C. Matzler, C. A. Luther, and E. A. Svendsen, "Evolution of microwave sea ice signatures during early summer and midsummer in the marginal ice zone," *Journal of Geophysical Research: Oceans*, vol. 92, no. C7, pp. 6825–6835, 1987.

Shokr, M., Lambe, A., and Agnew, T.: A New Algorithm (ECICE) to Estimate Ice Concentration From Remote Sensing Observations: An Application to 85-GHz Passive Microwave Data, *IEEE Transactions on Geoscience and Remote Sensing*, 46, 2008.

Smith, D. M., and Barrett, E. C.: Satellite mapping and monitoring of sea ice. Unpublished final report to the Defence Research Agency, RSU, University of Bristol, 1994.

Smith, D. M.: Extraction of winter total sea-ice concentration in the Greenland and Barents Seas from SSM/I data, *International Journal of Remote Sensing*, 17, 2625 - 2646, 1996.

Spreen, G. Meereisfernerkundung mit dem satellitengestützten Mikrowellenradiometer AMSR(-E) – Bestimmung der Eiskonzentration und Eiskante unter Verwendung der 89 Ghz-Kanäle. Diploma Thesis, University of Hamburg, prepared at the University of Bremen, Department of Physics and Electrical Engineering, 2004.

Spreen, G., Kaleschke, L., and Heygster, G.: Operational Sea Ice Remote Sensing with AMSR-E 89GHz Channels, *IEEE International Geoscience and Remote Sensing Symposium Proceedings*, 6, 4033-4036, 2005.

Spreen, G., L. Kaleschke, and G. Heygster. Sea Ice Remote Sensing Using AMSR-E 89 GHz Channels. *Journal of Geophysical Research*, 113, C02S03, doi:10.1029/2005JC003384, 2008.

S. Kern, "A new method for medium-resolution sea ice analysis using weather-influence corrected Special Sensor Microwave/Imager 85 GHz data," *International Journal of Remote Sensing*, vol. 25, no. 21, pp. 4555–4582, 2004.

S. Andersen, R. Tonboe, S. Kern, and H. Schyberg, "Improved retrieval of sea ice total concentration from spaceborne passive microwave observations using numerical weather prediction model fields: An intercomparison of nine algorithms," *Remote Sensing of Environment*, vol. 104, no. 4, pp. 374–392, 2006.

Steffen, K., Cavalieri, D. J., Comiso, J. C., Germain, K. S., Gloersen, P., and Rubinstein, I.: The estimation of geophysical parameters using passive microwave algorithms. In: Carsey, F., ed. *Microwave Remote Sensing of Sea Ice*, American Geophysical Union, Washington, DC, 1992.

Svendsen, E., Kloster, K., Farrelly, B., Johannessen, O. M., Johannessen, J. A., Campbell, W. J., Gloersen, P., Cavalieri, D., and Matzler, C.: Norwegian Remote Sensing Experiment' Evaluation of the Nimbus 7 Scanning Multichannel Microwave Radiometer for Sea Ice Research, *Journal of Geophysical Research*, 88, 2781-2791, 1983.

Svendsen, E., Matzler, C., and Grenfell, T.: A model for retrieving total sea ice concentration from a spaceborne dual-polarized passive microwave instrument operating near 90 GHz, *International Journal of Remote Sensing*, 8, 1479 - 1487, 1987.

Swift, C., Fedor, L., and Ramseier, R.: An Algorithm to Measure Sea Ice Concentration With Microwave Radiometers, *Journal of Geophysical Research*, 90, 1985.

S. Willmes, M. Nicolaus, and C. Haas, "The microwave emissivity variability of snow covered first-year sea ice from late winter to early summer: a model study," *The Cryosphere*, vol. 8, no. 3, pp. 891–904, 2014. [Online]. Available: <http://www.the-cryosphere.net/8/891/2014/>

Tikhonov, V. V., I.A. Repina, M.D. Raev, E.A. Sharkov, V.V. Ivanov, D.A. Boyarskii, T.A. Alexeeva, N.Yu. Komarova, A physical algorithm to measure sea ice concentration from passive microwave remote sensing data, *Advances in Space Research*, Volume 56, Issue 8, 15 October 2015, Pages 1578-1589, ISSN 0273-1177, <http://dx.doi.org/10.1016/j.asr.2015.07.009>.

Tonboe, R. T., G. Dybkjar, J. L. Hoyer. Simulations of the snow covered sea ice surface temperature and microwave effective temperature. *Tellus* 63A, 1028-1037, 2011.

Tonboe, R. T., Eastwood, S., Lavergne, T., Sørensen, A. M., Rathmann, N., Dybkjær, G., Toudal Pedersen, L., Høyer, J. L., and Kern, S.: The EUMETSAT sea ice climate record, *The Cryosphere*, 10, 2275-2290, doi:10.5194/tc-10-2275-2016, 2016.

T. Markus and D. J. Cavalieri, "An enhancement of the NASA Team sea ice algorithm," *IEEE Transactions on Geoscience and Remote Sensing*, vol. 38, no. 3, pp. 1387–1398, May 2000.

T. Maeda, Y. Taniguchi, and K. Imaoka, "GCOM-W1 AMSR2 Level 1R product: Dataset of brightness temperature modified using the antenna pattern matching technique," *IEEE Transactions on Geoscience and Remote Sensing*, vol. 54, no. 2, pp. 770–782, Feb 2016.

T. Meissner and F. J. Wentz, "The complex dielectric constant of pure and sea water from microwave satellite observations," *IEEE Transactions on Geoscience and Remote Sensing*, vol. 42, no. 9, pp. 1836–1849, 2004.

Walters, J. M., Ruf, C., and Swift, C. T.: A Microwave Radiometer Weather-Correcting Sea Ice Algorithm, *Journal of Geophysical Research*, 92, 1987.

Warren, S. G., Rigor, I. G., Untersteiner, N., Radionov, V. F., Bryazgin, N. N., Aleksandrov, Y. I., et al. (1999). Snow depth on Arctic sea ice. *Journal of Climate*, 12

Wentz, F. J. A well-calibrated ocean algorithm for SSM/I. *Journal of Geophysical Research* 102(C4), 8703-8718, 1997.

Wentz, F. J. and T. Meissner. AMSR Ocean Algorithm, Version 2, vol. 121599A-1, p. 66, Remote Sensing Systems, Santa Rosa, CA, 2000.

Wiebe, H., G. Heygster and L. Meyer-Lerbs 2008: Geolocation of AMSR-E Data. *IEEE Trans. Geosci. and Remote Sensing* 46(10), p. 3098-3103, doi:10.1109/TGRS.2008.919272.

Appendix A The SICCI 1 algorithm – Python code

```

# -*- coding: utf-8 -*-
#!/usr/bin/python
import math
import numpy as np
import os
import glob
import datetime

def bootstrap_f(tb18v, tb37v, tiepts):
    # Bootstrap frequency mode

    tw18v = tiepts[6]
    tw37v = tiepts[0]
    tfy18v = tiepts[8]
    tfy37v = tiepts[2]
    tmy18v = tiepts[7]
    tmy37v = tiepts[1]

    if (tb18v-tw18v)==0: #open water
        cf=0.0
    else:

        af = (tfy37v - tmy37v)/(tfy18v - tmy18v)
        bf = (tmy37v - af*tmy18v)
        qf = (tb37v - tw37v)/(tb18v - tw18v)
        wf = (tw37v - qf*tw18v)
        ti18vf = (bf - wf)/(qf - af)
        c_f = (tb18v - tw18v)/(ti18vf - tw18v)
    return c_f

def bristol(tb18v, tb37v, tb37h, tiepts):
    #Bristol

    tw18v = tiepts[6]
    tw37h = tiepts[3]
    tw37v = tiepts[0]
    tfy18v = tiepts[8]
    tfy37h = tiepts[5]
    tfy37v = tiepts[2]
    tmy18v = tiepts[7]
    tmy37h = tiepts[4]
    tmy37v = tiepts[1]

    xa = tmy37v + (1.045*tmy37h) + (0.525*tmy18v)
    xd = tfy37v + (1.045*tfy37h) + (0.525*tfy18v)
    xh = tw37v + (1.045*tw37h) + (0.525*tw18v)
    xt = tb37v +(1.045*tb37h) + (0.525*tb18v)

    ya = (0.9164*tmy18v) - tmy37v + (0.4965*tmy37h)

```

```
yd = (0.9164*tfy18v) - tfy37v + (0.4965*tfy37h)
yh = (0.9164*tw18v) - tw37v + (0.4965*tw37h)
yt = (0.9164*tb18v) - tb37v + (0.4965*tb37h)

a_ht = (yt - yh)/(xt - xh)
b_ht = yh - (a_ht*xh)
a_da = (ya - yd)/(xa - xd)
b_da = yd - (a_da*xd)

xi = (b_da - b_ht)/(a_ht - a_da)
cf = (xt - xh)/(xi - xh)
c_b = cf
return c_b

def sicci(c_f,c_b):
    if c_f<0.7:
        wCF=1.0
    if (c_f >= 0.7 and c_f < 0.9):
        wCF=1.0-(c_f-0.7)/(0.9-0.7)
    if c_f >= 0.9:
        wCF=0.0
    wBR = 1.0-wCF
    c = c_f * wCF + c_b * wBR
    return c
```

Appendix B General structure of SIC RRD

The data are stored in text files with 118 columns:

Nr.	Variable name	Explanation	Data type
1	latitude	of reference point	Float
2	longitude	of reference point	Float
3	time	of reference point	String
4	identification		String
5	SIC	Sea Ice Concentration reference	Float
6	latitude	of NWP	Float
7	longitude	of NWP	Float
8	time	of NWP	String
9	reference-id	of NWP	String
10	upstreamfile	of NWP	String
11	msl	mean sea level pressure	Float
12	u10	u component of 10m wind (E-W)	Float
13	v10	v component of 10m wind (N-S)	Float
14	ws	10m wind speed	Float
15	t2m	2m air temperature	Float
16	skt	Skin temperature	Float
17	istl1	Ice temperature 1	Float
18	istl2	Ice temperature 2	Float
19	istl3	Ice temperature 3	Float
20	istl4	Ice temperature 4	Float
21	sst	Sea surface temperature	Float
22	d2m	2m dew point temperature	Float
23	tcwv	Total columnar water vapour	Float
24	tclw	Total columnar cloud liquid water	Float
25	tciw	Total columnar cloud ice water	Float
26	ssrd	Surface solar radiation downwards	Float
27	strd	Surface thermal radiation downwards	Float
28	e	evaporation	Float
29	tp	Total precipitation	Float
30	sf	Snowfall	Float
31	fal	Albedo	Float
32	ci	Ice concentration from ERA Interim	Float
33	latitude	for AMSR	Float
34	longitude	for AMSR	Float
35	time	for AMSR	String
36	identification	for AMSR	String
37	6.9GHzH	37-50: Brightness Temperatures (K) in the PMW channels	Float
38	6.9GHzV		Float
39	7.3GHzH		Float
40	7.3GHzV		Float
41	10.7GHzH		Float
42	10.7GHzV		Float

43	18.7GHzH		Float
44	18.7GHzV		Float
45	23.8GHzH		Float
46	23.8GHzV		Float
47	36.5GHzH		Float
48	36.5GHzV		Float
49	89.0GHzH		Float
50	89.0GHzV		Float
51	Earth Incidence	AMSR Incidence angle	Float
52	Earth Azimuth	AMSR azimuth angle	Float
53	scanpos	position in AMSR scan	Float
54	upstreamfile	AMSR	String
55	timediff	between AMSR and reference	Float
56	latitude	ASCAT	Float
57	longitude	ASCAT	Float
58	time	ASCAT	String
59	reference-id	ASCAT	String
60	upstreamfile	ASCAT file	String
61	sigma_40	ASCAT sigma nought at 40 degree incidence angle	Float
62	sigma_40_mask	ASCAT sigma-0 masked	Float
63	nb_samples	ASCAT number of samples	Float
64	warning	ASCATwarning flag	Float
65	std	ASCAT standard deviation	Float
66	Near90_lin_dyn	66-114 SIC (%) from the algorithms	Float
67	Near90GHz		Float
68	ASI		Float
69	P90		Float
70	P37		Float
71	Bootstrap_p		Float
72	P18		Float
73	Bristol		Float
74	PR		Float
75	NASA_Team		Float
76	NORSEX		Float
77	Bootstrap_f		Float
78	CalVal		Float
79	UMass_AES		Float
80	P10		Float
81	One_channel		Float
82	TUD		Float
83	bf_nt		Float
84	bf_nt_n90ld		Float
85	p37_n90ld		Float
86	p37_n90ld_bf		Float
87	bf2_n90ld		Float
88	bf3_n90ld		Float
89	bf_n90ld		Float
90	bf_bfn90ld		Float
91	osisaf		Float
92	SICCI		Float
93	comiso_ucorr		Float
94	osisaf_ucorr		Float
95	sicci1_ucorr		Float

96	sicci2lf_ucorr		Float
97	n90lin_ucorr		Float
98	sicci2hf_ucorr		Float
99	sicci2vlf1_ucorr		Float
100	comiso_wRTM		Float
101	osisaf_wRTM		Float
102	sicci1_wRTM		Float
103	sicci2lf_wRTM		Float
104	n90lin_wRTM		Float
105	sicci2hf_wRTM		Float
106	sicci2vlf1_wRTM		Float
107	VASIA1		Float
108	VASIA2		Float
109	VASIA_combo		Float
110	NT2_nocorr		Float
111	NT2_corr		Float
112	alg6GHz		Float
113	ASI1	113-116: Only available for NH (for SH value -999 is used)	Float
114	ASI2		Float
115	LIN1		Float
116	LIN2		Float
117	n_atm_nocorr	Atmosphere number in NT2_nocorr	Float
118	n_atm_corr	Atmosphere number in NT2_corr	Float

The file STD_Bias_AMSRX_[last update].txt contains STDs and Biases for all the algorithms (ASI1, ASI2, LIN1, LIN2 only for the Northern Hemisphere). All years are used to calculate these. For SIC1 only winter months are used: October-May in NH and June-November in SH (April-May are excluded because of the large TBs spread, which has not yet been understood).

< End of Document >